Tracking causes of death in the rainforest p. 454

Tropical cyclones are moving closer to our coasts pp. 458 & 514

Debt relief from China can protect the environment p. 468

Science

$15
29 JANUARY 2021
sciencemag.org

AAAS

MY CHIRP, YOUR CHIRP

Cultural dialects in naked mole-rats pp. 461 & 503

Apply for our exciting research Prize!

SCIENCE-PINS PRIZE FOR NEUROMODULATION

SCIENCE-PINS

$25, 000 Grand Prize!
Get published in *Science*!

The *Science*-PINS Prize is a highly competitive international prize that honors scientists for their excellent contributions to neuromodulation research. For purposes of the Prize, neuromodulation is any form of alteration of nerve activity through the delivery of physical (electrical, magnetic, or optical) stimulation to targeted sites of the nervous system with impications for translational medicine.

For full details, judging criteria and eligibility requirements, visit:

www.sciencemag.org/prizes/pins

Submission Deadline: 15 March 2021

Science AAAS

PINS 品驰

Science Translational Medicine AAAS

Diving deeper into modern scientific questions

World-renowned academics in Hong Kong addressed key academic questions as they participated in the virtual HKIAS Distinguished Lecture series in November 2020. During two lectures delivered as the second half of a four-part series, senior fellows from the Hong Kong Institute for Advanced Study (HKIAS) explored advanced mathematical analysis as well as pioneering approaches to materials science and engineering.

Going beyond the surface

On November 5, 2020, Philippe G. Ciarlet, HKIAS senior fellow and university distinguished professor at the City University of Hong Kong (CityU), delivered a lecture titled "Nonlinear Korn Inequalities on a Surface." The accomplished mathematician moved from past to present as he explained how he began working on this subject when he first came to CityU.

In 2002, Ciarlet built upon the Gauss and Codazzi–Mainardi equations and the fundamental theorem of surface theory and became the first scientist to conclude that a surface varies continuously according to its two fundamental forms for different topologies (*1*). In his talk, he reviewed the results of his work over the past 18 years and highlighted the key question to which he always returns: "As a mathematician, whenever you see a function, you ask, 'Is this function continuous?'"

Ciarlet also noted that the mathematical concepts relating to fundamental surface theory are not new: "They've been around for centuries. What's new is what will follow." Introducing his latest research, Ciarlet explained how nonlinear inequalities on a surface could have applications in nonlinear elastic shell theory, in which the fundamental forms of the unknown deformed middle surface of a shell are taken as the new unknowns.


Philippe G. Ciarlet

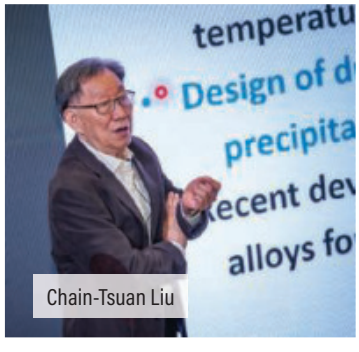

Chain-Tsuan Liu

Materials development

On November 25, 2020, Chain-Tsuan Liu, HKIAS senior fellow and university distinguished professor at CityU, spoke about the importance of advancing the field of materials science. He quoted the late Japanese electronics engineer Tadahiro Sekimoto, who stated that "those who dominate materials, dominate technology." His lecture focused on the technical challenges of developing new structural materials for use at high temperatures, such as in the aerospace industry.

Starting with an overview of the mechanical behavior of different metallic alloys, he noted that most structural alloys lack sufficient strength to be used at elevated temperatures. Design efforts, he said, must focus on enhancing both the strength and ductility of structural materials at different temperatures and working conditions. As an example, he discussed his development of the iridium alloy used as the container material for radioisotope thermoelectric generators on U.S. spacecraft. He went on to highlight the crucial role that steel plays in the global economy and the air pollution problems that are caused by its production, citing as an example the fact that in 2018, the energy used for steel production in China was equivalent to burning 452 million tons of coal. Liu is currently researching ultrahigh-strength steels, which offer an effective way to reduce steel production levels and therefore reduce our fossil-fuel consumption.

Liu concluded his lecture by discussing his research into particle-strengthening, high-entropy alloys for structural applications at all temperatures. "Our development goal is to achieve an effective hardening without any significant loss of ductility in these alloys at ambient and elevated temperatures," he explained. This new class of metallic materials offers scientists a departure from conventional alloy design and has the potential to be used in high-temperature applications in the future, he told his audience.

Supported in part by the Kwang Hua Educational Foundation, the HKIAS Distinguished Lecture series offers scholars the chance to follow the work of internationally renowned academics whose fundamental research will strengthen both our understanding of science and our ability to make scientific advances. HKIAS will continue to organize scientific events, making them available live online to a global audience. In 2021, two new series will be presented: the HKIAS Distinguished Lecture Series on Chemistry and the HKIAS Distinguished Lecture Series on Physics, each to be delivered by three renowned scholars at CityU.

References

1. P. G. Ciarlet, *Comptes Rendus Math.* **355**, 609–614 (2002).

Hong Kong Institute for Advanced Study
Phone: +852-3442-6611
Email: hkias@cityu.edu.hk

PHOTO: HKIAS

CONTENTS

29 JANUARY 2021 • VOLUME 371 • ISSUE 6528

454
In Ivory Coast, veterinarian Fabian Leendertz traps bats to test for Ebola virus.

NEWS

IN BRIEF

IN DEPTH

FEATURES

INSIGHTS

PERSPECTIVES

POLICY FORUM

BOOKS *ET AL.*

PHOTO: PETE MULLER/PRIME FOR NATIONAL GEOGRAPHIC

ON THE COVER

Naked mole-rats (*Heterocephalus glaber*) display rich vocal repertoires. Analysis of their greeting call, the soft chirp, reveals that this sound can be used to communicate social membership. Individuals from different colonies use distinctive dialects that are learned early in life. Dialect usage in naked mole-rats is similar to that in humans, a finding that may shed light on mechanisms of social communication. See pages 461 and 503. *Photo: Felix Petermann, Max-Delbrück Center for Molecular Medicine (MDC)*

SCIENCE (ISSN 0036-8075) is published weekly on Friday, except last week in December, by the American Association for the Advancement of Science, 1200 New York Avenue, NW, Washington, DC 20005. Periodicals mail postage (publication No. 484460) paid at Washington, DC, and additional mailing offices.

Domestic individual membership, including subscription (12 months): $165 ($74 allocated to subscription). Domestic institutional subscription (51 issues): $2148; Foreign postage extra: Air assist delivery: $98. First class, airmail, student, and emeritus rates on request. Canadian rates with GST available upon request, GST #125488122. Publications Mail Agreement Number 1069624. **Printed in the U.S.A.**
Change of address: Allow 4 weeks, giving old and new addresses and 8-digit account number. **Postmaster:** Send change of address to AAAS, P.O. Box 96178, Washington, DC 20090–6178. **Single-copy sales:** $15 each plus shipping and handling available from backissues.sciencemag.org; bulk rate on request. **Authorization to reproduce** material for internal or personal use under circumstances not falling within the fair use provisions of the Copyright Act can be obtained through the Copyright Clearance Center (CCC), www.copyright.com. The identification code for *Science* is 0036-8075. *Science* is indexed in the *Reader's Guide to Periodical Literature* and in several specialized indexes.

CREDITS (LEFT TO RIGHT): NASA; ROBERT NEUBECKER

EDITORIAL

Science, civics, and democracy

Michael J. Feuer is Dean of the Graduate School of Education and Human Development and a professor at The George Washington University and is the Immediate Past President of The National Academy of Education, Washington, DC, USA. mjfeuer@email.gwu.edu

Will the inauguration of President Joe Biden and Vice President Kamala Harris—a transition made "orderly" with barbed wire, National Guard soldiers, and the closure of downtown Washington, D.C.—be remembered as an inflection point? After 4 years of boorish incivility, incendiary nativist extremism, a crippling pandemic, resurgent racism, and riotous mobs incited to attack the Capitol, can the United States rebuild its civic and moral infrastructure? To repair the damage and prepare the next generation of citizens and leaders requires a new spirit of cooperation between the science and civics education communities.

About 30 years ago, the U.S. National Academy of Sciences and the American Association for the Advancement of Science (AAAS, the publisher of *Science*) recommended major overhauls of science education. The drive for reform confronted partisan conflicts along the way, but the good news is that more students today benefit from stimulating instruction in many subjects. Now the country must sustain this momentum for progress in science, technology, engineering, and mathematics (STEM) while heeding the call for more attention to civics, the humanities, and the foundations of democratic pluralism.

> **"...can the United States rebuild its civic and moral infrastructure?"**

This is not a zero-sum competition. STEM priorities can be aligned with—and reinforce—ideals of social responsibility and the public good. The inspired choices of Eric Lander for director of the Office of Science and Technology Policy (OSTP) and Alondra Nelson as OSTP deputy director for science and society can put American science policy back on track. With their leadership and a joint effort of the Department of Education, the National Science Foundation, the National Academy of Education, the National Academies of Sciences, Engineering, and Medicine, and philanthropies, the country can build on the 2013 *Next Generation Science Standards* to promote the needed coordination.

What ingredients should be included in this recipe for reform? Policy-makers and legislators must acknowledge the effects of economic inequality on educational outcomes and invest resources to protect disadvantaged youth. Research on disruptions caused by the pandemic shows that, on average, American students in K–12 experienced less "learning loss" than anticipated, but for disadvantaged and minority children, the setbacks were substantially worse. This is no surprise to researchers who study the effects of poverty and racism on achievement. A strategy to raise average performance in STEM while shrinking the variance would help instill an ethos of the common good—a core aspiration of civics.

Good science education means equitable science education. This principle will require sustained efforts to expunge biases associated with race, gender, and class from curricula and school culture. As the astrophysicist Neil deGrasse Tyson noted, we must work toward a world where students will succeed in science because of—not despite—what happened in school. Research on the origins of bias and its effects is bringing new ideas into the development of methods to combat discrimination in K–12 schools, colleges, and universities. Again, good science and good citizenship are mutually reinforcing.

Americans know that educational opportunity is the ticket to economic and social advancement. In recent polling by PDK International, 70% of parents said that education issues influenced their vote for president in the 2020 election. Let's seize on this evidence and hold government accountable for ensuring that all students learn in safe classrooms with skilled and dedicated teachers, modern lab equipment and digital technologies, experienced school leaders, and a curriculum that logically connects science with social studies, humanities, and language arts.

Certainly, not every young person will become a practicing scientist, but every student should appreciate the processes of scientific inquiry and its uses. In the United States and other countries, relations between the scientific community and government can be tense. But today, the United States is suffering from years of distrust for evidence—about the pandemic, climate change, racism, immigration, and the economy. Let's integrate into hands-on STEM education some hands-on learning about objective inquiry as a cornerstone of American democracy and the preparation of a well-informed citizenry.

President Biden says he is determined to restore dignity to government and trust in science. Miguel Cardona, the nominee for Education Secretary, is a seasoned educator whose path from poverty to leadership exemplifies the possibilities even in the nation's fractured system. The country must work with them toward the inseparable goals of scientific excellence and fulfillment of our noblest egalitarian dreams.

–Michael J. Feuer

10.1126/science.abg7402

PHOTO: GEORGE WASHINGTON UNIVERSITY

Going beyond eloquent words

As the United States steadies itself, recovering from COVID-19 and preparing for future crises, it must draw upon what Eric Lander, the nominee for director of the Office of Science and Technology Policy (OSTP), called "America's greatest asset…our unrivaled diversity." To achieve this goal, OSTP must have the resources and authority to go beyond eloquent words and deliver solid accomplishments for the nation and world.

Diversity is a double-edged sword. When complementary talents and perspectives come together, leaps in understanding are more likely and disruptive technologies are born. But there is also a vulnerability. When seized upon to divide (with talk of quotas in a zero-sum game), diversity can be used to generate fear and stoke division in ways that increase inequities and stifle substantive debate. In the scientific enterprise, explicit acts of racism and sexism still exist and cause harm. However, it is often the less obvious factors—divisive rhetoric, obsolete policies (such as overreliance on standardized tests), and willful blindness to inequitable treatment (such as smaller startup budgets for female academics)—that cement many of the injustices that have sprung from the nation's segregated history. These opaque forces are so ingrained that we scarcely realize their implications for minorities and women in science.

> "Diversity of thought… gives America a critical advantage…"

Over the past year, the American Association for the Advancement of Science (of which I am the chief executive officer; AAAS is the publisher of *Science*) has held a mirror up to its own functions. We have listened carefully to scientists, consulted with experts, and analyzed existing data. Chief among what we have discovered are stark demographic contrasts between programs and awards that are applicant-based and those that are nomination-based. We fall short when it comes to recognizing the contributions of underrepresented members of the scientific community. Transparently sharing these data enables accountability. AAAS and other institutions must be held responsible by the community for meaningful change.

Insisting on inclusion of underrepresented groups neither sacrifices scientific excellence nor diminishes the accomplishments of those who have historically dominated the sciences. Highlighting the previously ignored does not invalidate the already admired. But this change requires that the scientific community increase attention and support for those who have been disadvantaged. I have received letters from scientists attacking AAAS's focus on diversity, stating that race has no scientific basis and scientists should ignore it. But race and patriarchy are powerful social constructs with societal consequences that cannot be overlooked. Alondra Nelson, OSTP deputy director for science and society and former AAAS Board member, stated that "science at its core is a social phenomenon. When we provide inputs to the algorithm; when we program the device; when we design, test and research; we are making human choices…It matters who makes those choices, it matters who they're thinking about when they do." Avoiding these conversations amounts to advocating the status quo—and the United States would be weaker for it.

Institutions also must push for policies that enable diversity across the enterprise. Often, these policies do not seem directly related to diversity, equity, or inclusion. But increasing pay for graduate students and postdocs and providing them with employee-like benefits and protections; achieving open access publishing policies that do not place the financial burden of publishing on authors; improving training and standards for mentorship, and providing safe and supportive workplace cultures—these policies do affect the retention of diverse scientists without sacrificing scientific excellence.

The reasons for ensuring the diversity of science transcend the obvious moral imperative. Diversity of thought derived from diversity of experience gives America a critical advantage in the global competitive landscape. This is key to making the discoveries that will improve everyone's health, inventing the technologies that will grow the economy, and meeting the formidable challenges of this era. Without the innovative boost from a diverse population, the United States will be hard-pressed to compete on sheer numbers of scientists and engineers.

The new OSTP leadership will need the resources and clout to go beyond symbolic gestures. Dr. Lander and Dr. Nelson must receive bipartisan support, funding, and authority to create a national science and technology strategy that ensures a scientific workforce capable of building on the exceptional diversity that is the country's greatest asset.

–Sudip Parikh

PHOTO: ANDY DELGIUDICE

Sudip Parikh
is the chief executive officer of the American Association for the Advancement of Science (AAAS) and executive publisher of the *Science* journals.
sparikh@aaas.org

10.1126/science.abg7406

NEWS

> “Palpable catharsis today. Not realizing how much stress I felt as a civil servant over the last 4 years.”
>
> **Wildlife biologist Jason Ransom** of the U.S. National Park Service, tweeting on his personal account about the inauguration of President Joe Biden. “Now we do the work,” Ransom added.

IN BRIEF

Edited by **Jeffrey Brainard**

President Joe Biden signs his first executive orders in the White House’s Oval Office on 20 January, the day he was sworn in.

POLICY

Biden’s first acts elevate science

In his first week in office, President Joe Biden unleashed an unprecedented flood of executive actions, including many related to science and the environment. He directed agencies to base their decisions on the best available scientific evidence and, reversing decisions made by former President Donald Trump, committed the United States to rejoin the Paris climate pact and the World Health Organization. Biden also ordered federal agencies to take a more active role in administering COVID-19 vaccines in the United States and required mask wearing on federal lands and in interstate transport. He canceled the Keystone XL pipeline, which would have transported oil from Canada’s tar sands, paused oil and gas leasing on federal lands, and ordered agencies to revisit some 100 Trump environmental policies, including those that shrank national monuments, weakened wildlife protections, and relaxed reviews of development projects. He told the Census Bureau to drop Trump’s plan to exclude undocumented residents from its 2020 population count and lifted a de facto ban on visitors from seven Muslim-majority nations that had affected scientists and students. Looking ahead, he asked world leaders to join him at a 22 April summit to discuss climate change.

Memo targets research theft

U.S. POLICY | A memo from the last days of President Donald Trump has offered recommendations on how to ensure foreign adversaries don’t steal federally funded research. Even though it comes from the previous administration, university officials think the measured tone and scope of the 14 January memo, the product of a 2-year exercise by an interagency White House–led panel, could wind up being part of the Biden administration’s policies toward China. The memo and an accompanying report on “promising practices” recommends federal agencies adopt uniform rules for grantees to disclose all foreign ties and impose an escalating series of penalties on those who fail to do so. It also proposes that agencies require universities to conduct rigorous training in research security, and that foreign researchers and students seeking visas receive closer scrutiny.

PHOTO: EVAN VUCCI/AP PHOTO

Trump's power plant reg killed

CLIMATE CHANGE | A federal court ruling last week could help President Joe Biden fulfill a promise to stiffen regulation of greenhouse gas emissions from power plants. The U.S. Court of Appeals for the District of Columbia Circuit struck down a key Environmental Protection Agency rule that would have allowed EPA to require power plants to adopt emissions reduction plans only if the cuts were made at each individual plant. Critics said that policy, enacted by former President Donald Trump's administration, inappropriately ruled out more effective strategies, such as allowing utilities to invest in energy conservation off-site or greener power sources elsewhere. But Biden is likely to face numerous other obstacles, in Congress and the courts, to achieving his goal of ending fossil fuel emissions from electricity production by 2035.

Hypersonic weapons hyped?

MILITARY SCIENCE | Claims that next-generation, superfast gliders and missiles can maneuver through the atmosphere largely invisible to sensors are overblown, a study says. In what some experts compare to the Cold War arms race, China, Russia, the United States, and other nations have been pouring billions of dollars into these hypersonic weapons, which travel at Mach 5 or greater and are meant to dodge defenses. But after assessing public documents on the U.S. military's experimental Hypersonic Technology Vehicle 2 and the open hypersonics literature, authors at the Massachusetts Institute of Technology and the Union of Concerned Scientists concluded the speedy vehicles are "an evolutionary—not revolutionary—development" compared with existing ballistic missiles, they reported this month in *Science & Global Security*. Defense officials told *The New York Times* the critique is based on outdated data.

ILLUSTRATION: DEFENSE ADVANCED RESEARCH PROJECTS AGENCY

A hypersonic U.S. glider carrying a warhead re-enters the atmosphere in this illustration.

COVID-19

Dispatches from the pandemic

Low-income countries get vaccine help

The COVID-19 Vaccines Global Access (COVAX) Facility, an international consortium to distribute COVID-19 vaccines equitably around the world, got a twin boost last week from the manufacturer Pfizer and the new U.S. administration. Pfizer announced it had agreed to sell COVAX up to 40 million doses of its vaccine, starting in the first quarter of 2021. Although the number is small, the deal will allow some of the most vulnerable health care workers in low- and middle-income countries to be vaccinated. The agreement is expected to prime the pump for COVAX to distribute Pfizer vaccine donated by countries. President Joe Biden's administration, meanwhile, pledged that the United States will join COVAX, one of the last countries to do so. The consortium aims to provide 2 billion doses of multiple vaccines to participating countries by the end of this year.

Racial gap in U.S. vaccinations eyed

Although Black Americans die from COVID-19 at a rate nearly three times that of white Americans, Black Americans are receiving vaccines at far lower rates, an analysis this month from Kaiser Health News shows. In 16 states that release data by racial group, Black people made up a smaller proportion of vaccine recipients than their share of the general population and of health care workers, who under guidelines have been receiving the vaccines first. For example, in Pennsylvania as of 14 January, Black people made up only 3% of all who were vaccinated but 11% of residents and 15% of health workers. Factors behind the disparity could include access problems and vaccine mistrust owing to systemic racism, the Kaiser report said. In a January survey by the Harris Poll, only 58% of Black people versus 72% of white people said they are likely to get vaccinated.

Serious allergic reactions to Moderna vaccine are rare

A life-threatening allergic reaction occurred in 10 of more than 4 million people who received a first dose of the Moderna COVID-19 vaccine in recent weeks, the U.S. Centers for Disease Control and Prevention (CDC) reported on 22 January. That's less than one-quarter the rate of the reaction, called anaphylaxis, in people who received a first dose of the Pfizer vaccine in mid-December 2020, which CDC reported was 11.1 cases per million. None of the people who developed anaphylaxis after receiving either vaccine died. The rate of anaphylaxis for all vaccines administered in the United States in 2009, 2010, and 2011 was 1.31 per million, according to a CDC-led study published in 2017. The mortality rate of COVID-19 in the United States is about 16,600 deaths per million cases.

Manufactured antibodies prevent disease symptoms

Two studies have shown that monoclonal antibodies, mass-produced in laboratories, can protect people from developing symptomatic COVID-19. Manufacturer Eli Lilly said in a press release last week that after its antibodies were given to 299 residents of U.S. nursing homes, their risk of becoming ill with COVID-19 fell by 80%. Almost 40% of U.S. COVID-19 deaths have occurred in long-term care facilities. Five days later, Regeneron issued a press release that said its cocktail of two monoclonals given to 186 people living with a person who had COVID-19 conferred 100% protection from symptoms. The companies have already received emergency use authorizations for their monoclonal antibodies to treat infected patients at high risk of developing severe COVID-19—but so far, they are not widely used because they must be infused early in infection in a hospital or clinic. However, the antibodies might be used as a preventive to help protect the elderly and other people with compromised immune systems who do not have vigorous responses to vaccines.

Media reports of preprints often omit lack of peer review

Some 42% of media stories describing preprint papers about COVID-19 posted early in the pandemic failed to mention that the research was unreviewed or otherwise unverified, a study has found. Alice Fleerackers, a Ph.D. student in science communication at Simon Fraser University, and colleagues analyzed 100 papers on the preprint servers medRxiv and bioRxiv that received the most media coverage during the first 4 months of 2020. They found wide variation among 15 outlets in the share of coverage that mentioned the work was unreviewed, they reported this month in *Health Communication*. The pandemic has created an urgent need to share information, but journalists should convey a higher degree of uncertainty for preprints than peer-reviewed work, suggests Abel Gustafson, a science communication researcher at the University of Cincinnati not involved in the study.

Easing author name changes

PUBLISHING | Starting this month, researchers who have published in one of Wiley's 1700 journals may ask the publisher to change their first or last name everywhere it has appeared in author lists, and Wiley will do so without public announcement. In the past, when researchers requested a name change on a publication—to reflect their gender identity, marital status, or religion, for example—Wiley's journals issued a correction notice and notified all coauthors. Wiley's new policy eliminates those practices. "Changing names requires discretion and sensitivity, especially in the case of transgender (including non-binary) authors," Wiley said in an announcement, citing risks of social, psychological, professional, and economic harm if a publisher publicly announces the change. "An inclusive publishing environment doesn't harm people, it supports everyone. And that means empowering authors to own their name change process." Wiley's move follows similar policy changes from smaller scientific publishers over the past 2 years, including the American Chemical Society, Association for Computing Machinery, and Royal Society of Chemistry.

USDA settles animal care lawsuit

ANIMAL RESEARCH | The U.S. Department of Agriculture (USDA) on 19 January settled a lawsuit by animal welfare groups, agreeing to eliminate a rule that had made it easier for research labs and other animal-housing facilities to avoid citations for animal mistreatment and deaths. Stop Animal Exploitation Now and the Missouri Alliance in Animal Legislation had alleged that USDA illegally promulgated, without public notice or comment, a 2017 regulation that allowed animal keepers to avoid penalties and public disclosure for serious violations of animal care rules, including deaths, if they self-reported them. The settlement also requires the agency to toughen the definition of quickly correctable violations called "teachable moments" that remain exempt from citations, and to make information about these violations easily accessible on its website. USDA admitted no wrongdoing but must pay the groups $70,000 to cover legal expenses.

China accused of leniency

RESEARCH INTEGRITY | Authorities last week cleared a prominent Chinese scientist who allegedly manipulated images in dozens of papers, but ordered him to correct "misused images"—a penalty other scholars criticized as light. An investigation of immunologist Cao Xuetao, president of Nankai University, was launched in November 2019 after microbiologist Elisabeth Bik, an independent consultant who specializes in finding doctored figures, questioned several images in a 2009 paper in *The Journal of Immunology* co-authored by Cao. Other scientific fraud sleuths soon raised questions about images in other Cao papers. China's Ministry of Science and Technology said he will be prohibited from applying for national funding for 1 year and must correct the papers. It appears he will keep his job as university president for now. Critics say the investigation report lacked important details and that Cao should resign.

New guidelines recommend that photos show a clear barrier and safe distance between primates and people, as in this one of chimpanzees in France's Beauval zoo.

PHOTO: GUILLAUME SOUVANT/AFP/GETTY IMAGES

ENDANGERED SPECIES

Stop cuddly selfies with apes, conservation group asks

A leading global wildlife protection group wants researchers to quit cuddling monkeys on Instagram, holding hands with orangutans in films, and palling around with chimpanzees in publicity photos. In a new set of guidelines released this month, the International Union for Conservation of Nature (IUCN) called on scientists, students, conservationists, and caretakers to stop publishing images that depict themselves in close contact with nonhuman primates. Although some conservation organizations and sanctuaries rely on such images to help support their fundraising, studies have shown that such pictures lessen people's interest in the animals' status as endangered and boost interest in them as pets—even though such demand helps drive illegal trading of these animals. After habitat loss, this trade and other forms of poaching are a leading cause of dwindling primate numbers; 60% of primate species, including all great apes, are facing extinction.

IN DEPTH

Power plant emission rules could get stricter with a rise in the social cost of carbon.

CLIMATE CHANGE

Trump downplayed the cost of carbon. That's about to change

Biden administration set to update the "social cost of carbon" used in greenhouse regulations

By **Paul Voosen**

Carbon pollution is about to get a lot more expensive. Over the past 4 years, the Trump administration low-balled the "social cost of carbon"—a number representing the burden of carbon emissions on present and future generations, in terms of the cost of floods, droughts, farming losses, and death. The low estimate served to justify permissive regulations for power plant emissions and methane leaks from oil drilling. But now the cost—the price per ton of emitted carbon dioxide, methane, and nitrous oxide—is set to rise radically.

On 20 January, its first day in office, the Biden administration re-created an interagency working group (IWG) Trump had disbanded and ordered it to update the figure within 30 days. Many economists believe the cost, set as low as $1 during the Trump administration, will rise as high as $125 in the next month—and higher still come January 2022, when the IWG is due to provide a final number. The update could lead to tighter greenhouse gas regulations. And it is long overdue, says Tamma Carleton, an economist at the University of California (UC), Santa Barbara. "There's been this huge change in science that hasn't been reflected in policy."

Calculating the social cost of carbon is based on dozens of fiddly knobs that sometimes obscure the value judgments baked into it. Most economists use integrated assessment models (IAMs), first popularized by economist William Nordhaus of Yale University, who in 2018 won a Nobel Prize for his work. IAMs project population, economic growth, and greenhouse gas emissions a few centuries into the future, and use a simple climate model to estimate the warming in those scenarios. Then, they calculate the damage that results from this warming—flooding, heat deaths, and more—and the resulting toll on a nation's gross domestic product (GDP). This economic pain is translated into a present price using a discount rate, which accounts for both the increased buying power expected of future generations (which lowers the current price) and the value we place on avoiding harms to them (which raises it).

The Obama administration's IWG, after accounting for global damage and applying a standard 3% discount rate, came up with a figure of $53 per ton (in 2020 dollars). But in 2017, the Trump administration said the carbon cost would only factor in future damage to the United States. It also increased the discount rate to 7%—a level that devalued much future damage and drastically reduced the social cost figure.

The Biden administration has already said its cost estimate will account for global damages. And many economists favor reducing the discount rate. Inflation-protected 10-year U.S. Treasury bonds now average only a 1% return—a sign that future buying power may not grow as fast as it once did. Surveys of economists have also suggested a 2% discount rate better reflects the need to avoid foisting responsibility on future generations. When New York state set its own carbon cost in late 2020, it used a 2% rate, raising the cost to $125 per ton. The IWG, which will include staff from eight federal agencies, should consider adopting a similar interim standard, says Fran Moore, an economist at UC Davis. "Based on the return to capital we're seeing, there are good reasons those rates should be revised down."

Improvements to other IAM components are also likely to raise the social cost of carbon. Previously, each IAM relied on a simplistic climate simulation, written by an economist, in which the globe warmed more slowly than in more realistic climate models. Now, the IAMs can use models created by climate scientists, which better match current science.

Meanwhile, Resources for the Future, an environmental

Damage to be done

Warming from carbon emissions will impact energy spending, death rates, and crop yields. Estimates of these costs to future generations have changed in the past decade.

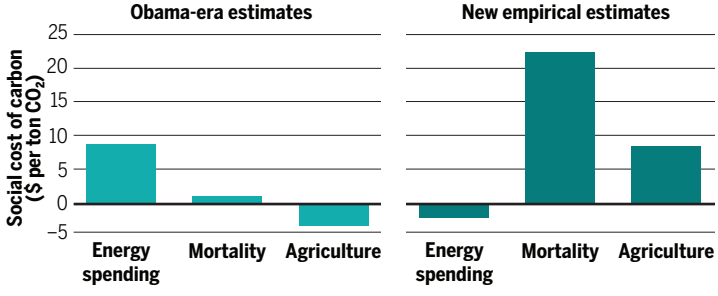

CREDITS: (PHOTO) ISTOCK.COM/HABESEN; (GRAPHIC) N. DESAI/*SCIENCE*; (DATA) T. CARLETON AND M. GREENSTONE, *UPDATING THE UNITED STATES GOVERNMENT'S SOCIAL COST OF CARBON* 2021

think tank that has been a kind of IWG-in-exile, has sponsored work to improve the base economic projections used by IAMs. Teasing out trends from GDP data for 113 countries from 1900 to 2017, researchers can now project economic growth at the country level, albeit with great uncertainty, until 2100. Similar work is being done for population growth and energy use.

Perhaps the biggest improvements, however, have come in estimates of the damage done by global warming. Previously, this "damage function" relied on outdated estimates biased toward wealthy and temperate locations. Now, economists at the Climate Impact Lab, an academic consortium, are making these estimates sector by sector, country by country, based on data sets that capture, for example, how weather swings or heat waves cut agricultural yields or drive up mortality. A flurry of these studies is expected in time to inform the final IWG number. And it's already clear, says Carleton, who works with the lab, that the Obama-era efforts "dramatically misrepresent what we find with the best available tools and data."

Although these damage function studies are likely to raise the social cost of carbon overall, Carleton says the sector-by-sector trends aren't always intuitive. For example, much of the Obama-era carbon cost was tied to increased energy spending on air conditioning as the climate warms. But new estimates suggest overall energy spending is likely to decline slightly, as heating demands decrease and poorer countries adopt cooling devices more slowly than expected. Heat-related mortality is a different story: Previous IWG estimates had it contributing $2 to the overall cost of carbon. But new estimates suggest heating deaths will rapidly outpace the downtick in freezing deaths, adding roughly $23 to the cost figure.

The damage functions are still highly uncertain. Seas could rise faster than anticipated, or emerging technologies could ease adaptation to global change. With their reliance on GDP, the models also don't do a great job of capturing what makes people happy, like the value of nature and biodiversity, Moore says. When she attempted to account for those values, they multiplied the carbon cost fivefold.

A full reckoning of carbon's cost could boost pressure for strict regulations—but there's also a risk of a backlash if the figure shifts too much, says Maureen Cropper, an economist at the University of Maryland, College Park. She hopes the Biden administration returns to the Obama-era standards for its interim figure, saving any drastic changes for the final update. ■

A syringe is filled with Moderna's COVID-19 vaccine at University Hospital Magdeburg.

PHOTO: RONNY HARTMANN/AFP/GETTY IMAGES

COVID-19

Vaccinemakers ponder how to adapt to virus variants

Moderna aims to develop booster shot to counter mutations

By **Kai Kupferschmidt**

News from U.S. manufacturer Moderna that its COVID-19 vaccine is still "expected to be protective" against a virus variant first detected in South Africa came as a relief to scientists and the public. But the 25 January announcement included a caveat: Antibodies triggered by the vaccine appear to be a little less potent against the new variant, named B.1.351, than the one the vaccine was developed for. So researchers were perhaps even more relieved to hear the company will start development of booster shots tailored to B.1.351 and other variants.

"These are exactly the steps that I hoped to see," says virologist Trevor Bedford of the Fred Hutchinson Cancer Research Center. "It may well not be necessary to have a vaccine update in the fall, but taking these steps now is the right course of action." Other vaccinemakers are also contemplating updates.

Scientists have grown increasingly concerned that new coronavirus variants may worsen the pandemic. B.1.1.7, first detected in England and now spreading globally, has been shown to be more transmissible; on 22 January, the U.K. government said it may be deadlier as well. B.1.351 and a very similar variant named P.1 that originated in Brazil's Amazonas state are suspected of evading immunity in people who were vaccinated or previously infected.

Now, researchers from Moderna and the Vaccine Research Center at the U.S. National Institutes of Health have tested the potency of antibodies from eight people who had received the company's vaccine against a retrovirus modified to express the mutated spike proteins of B.1.351 and B.1.1.7. In a preprint, they report that antibodies neutralized the virus in both cases. But for B.1.351, the levels needed were six times higher than for virus expressing the original protein.

A similar study by virologist David Ho of Columbia University, under review at *Nature*, found that the serum of 20 people vaccinated with Moderna's vaccine or a similar one from Pfizer was six to nine times less potent against B.1.351, and serum from 22 previously infected people was 11 to 33 times less potent. Researchers in South Africa, meanwhile, have found that antibodies from six recovered patients were six to 200 times less effective at neutralizing B.1.351.

Such drops sound alarming, but the vaccines produced by Pfizer and Moderna trigger very high levels of antibodies, which likely compensates for the decline in potency, says Florian Krammer, a vaccine researcher at the Icahn School of Medi-

Science's COVID-19 reporting is supported by the Pulitzer Center and the Heising-Simons Foundation.

cine at Mount Sinai. Besides, antibodies are only one part of the immune response; the vaccines also trigger T cells. Krammer is "quite optimistic" that both vaccines will still protect against B.1.351 and P.1. "However, this is worrisome for vaccines that are not as potent in inducing neutralizing antibodies as the two mRNA [messenger RNA] vaccines."

Others agree the results don't spell doom yet. "Given the high starting point, it's conceivable [vaccine efficacy] could drop only slightly," Bedford says. Immunity is not binary, adds Jeremy Farrar, head of the Wellcome Trust: "It doesn't suddenly turn on and turn off." A drop in antibody potency could have more subtle effects, such as immunity waning a bit faster, he says.

Moderna says it will start phase I trials of two booster strategies: a third dose of its current vaccine, or of a slightly different one in which the mRNA has been tweaked to incorporate B.1.351's mutations. They may be given to volunteers 6 to 12 months after the initial immunization. Pfizer, in an email to *Science*, wrote that it, too, is "laying the groundwork to respond quickly if a future variant of SARS-CoV-2 is unresponsive to existing vaccines." Novavax, which is in late-stage trials with a vaccine based the spike protein, says it is "testing sera against the new strains."

Georgetown University virologist Angela Rasmussen says it's "very wise" to start to prepare boosters now. "It's also wise to begin thinking about how they will be distributed," she adds. "For example, will they be allocated to regions with evidence that B.1.351 is circulating?" Regulators still need to spell out what trials they would require for updated vaccines. At a press conference on Monday, World Health Organization official Bruce Aylward said work to define a regulatory pathway was "kicking off right now."

Ho's paper also sheds some light on how B.1.351 escapes the immune response. The team produced retroviruses with spike proteins incorporating each of B.1.351's nine mutations separately, as well as all at once. A mutation named E484K accounted for much of the effect, they found. "E484K is really the bad boy here," says Stephen Goldstein, a virologist at the University of Utah. Brazil's P.1 variant has the same mutation.

Researchers say the plethora of recent changes is a warning sign that the coronavirus may have more surprises in store—and that the world needs to administer existing vaccines as fast as possible. "I think we need to stop the virus from replicating however we can," Ho says. "Otherwise, it will keep accumulating more mutations." ■

COVID-19

Ex–vaccine chief reflects on triumphs, failures, and Trump

Warp Speed's Moncef Slaoui discusses the troubled rollout of COVID-19 vaccines and how to stop the next pandemic

By **Jon Cohen**

PHOTO: JABIN BOTSFORD/*THE WASHINGTON POST*/GETTY IMAGES

Earlier this week, Moncef Slaoui received the fruits of his labor: the first dose of a COVID-19 vaccine, from Moderna. "I feel a joy I am sure every person that has been vaccinated has felt—a form of liberation," says the former scientific head of Operation Warp Speed, the crash U.S. program that invested $11 billion in developing vaccines for the pandemic and purchasing hundreds of millions of doses.

The Moroccan-born immunologist recently resigned from his post, but is "very supportive" of the new Biden administration—he's a Democrat—and has agreed to help its transition team into February. Talking with *Science* from his home in Pennsylvania last week, he reflected on his time with Warp Speed. He described working with former President Donald Trump as challenging, but said he was not subject to political interference and suggested how to better prepare for a future pandemic.

Slaoui refuses to say "I told you so," but about 6 years ago, while head of vaccines at GlaxoSmithKline (GSK), he tried to create a nonprofit Biopreparedness Organization (BPO) that would design and make vaccines to prevent pandemics. GSK even bought a defunct drug manufacturing plant, but the U.S. government and others passed on supporting the idea and it died—a mistake, Slaoui says.

Deeply proud of what he and the Warp Speed team accomplished, Slaoui is chagrined that President Joe Biden has called the vaccine rollout a "dismal failure." Although "sad" and "reflective" about the problems administering the doses, and aware that manufacturing challenges have kept supplies severely limited so far, he attributes most of the troubles to state and local public health systems overwhelmed by the pandemic. This interview was edited for clarity and brevity; a longer version is at http://scim.ag/QASlaoui.

Q: Would the BPO have made a difference with COVID-19?

A: Absolutely. The whole concept—after we went through the flu pandemic, the Ebola outbreak, the Zika outbreak—was to say, "Listen, the problem is always the same, which is there are no manufacturing facilities sitting there idle, waiting to be used. Even if we had one, we would have trouble because we would have to stop manufacturing other vaccines." So why don't we take a dedicated facility and have them work on discovering vaccines against known potential outbreak agents, one after the other? They would become incredibly skilled and trained at going fast, discovering vaccines.

I have already started discussing this with the new administration. This pandemic is costing $23 billion a day to the U.S. economy. Investing $300 million to $500 million a year into such a facility is peanuts and would save countless lives.

Q: What did you think of Trump?

A: I completely disagree with the values that he projects, as a person, in terms of respect, in terms of capacity to listen, accepting diversity. Many of the policy decisions that ended up politicizing this pandemic were wrong, particularly around wearing the mask. But at the same time I do think that Warp Speed was absolutely visionary, to put together science, government, the military, and the private sector and just give us full empowerment.

Q: Trump asserted that Pfizer [the first company to report a successful vaccine] delayed its announcement until after the election to hurt him. What was your reaction?

A: He asked me. And I said, "No, this is

not how it works." It would be the end of the company if they did that.

Q: How did you learn the Pfizer data?
A: [Pfizer CEO] Albert Bourla emailed and then called. I was in my hotel, very close to the White House. I was expecting high efficacy, but it was an unbelievable joy. It may have been 5 a.m., and I remember telling myself, I'm not going to scream. I just realized, oh my God, we're going control this pandemic.

Q: Warp Speed has been heavily criticized for not getting vaccines into more arms. What do you think about that?
A: There has been a huge misunderstanding. Between May 2020 and now, we've moved five vaccines into phase III trials, two have been authorized, two are completing phase III—and one of those could be approved imminently. One other vaccine is in phase IIb. By all standards, this is absolutely exceptional. Our second mission, with my co-leader Gen. [Gustave] Perna, was to distribute the vaccines, take them from point A to the point of immunization. Indeed, the [rollout] definitely is not working appropriately. Overall, we're failing, because the objective is to immunize.

Q: The Trump administration said it would help, but the rollout is up to the states and local jurisdictions. The Biden administration comes in and says the federal government can coordinate this?
A: Frankly I've been caught in the middle of that. But if I am [a state or local official] who is deciding how many doses I need, I should at least say, "Hey guys, I don't have the resources to immunize." We have never been told that.

Q: Do you think Trump's failure to concede made it more difficult to transition vaccine information to the next team?
A: For sure. It was at least very, very unfortunate, to use a polite word.

Q: The Biden administration plans to rename Warp Speed. What do you think of that?
A: I'm surprised we got an email yesterday saying that as of tomorrow, you cannot use the name Operation Warp Speed anymore. I asked myself, why? This is probably why I'm not a politician. It just escapes rationality and understanding. Because in a way, everybody that works under Operation Warp Speed feels like, what did we do wrong? I would redo it in the blink of an eye. But next pandemic virus, please, do not come during an election year. ■

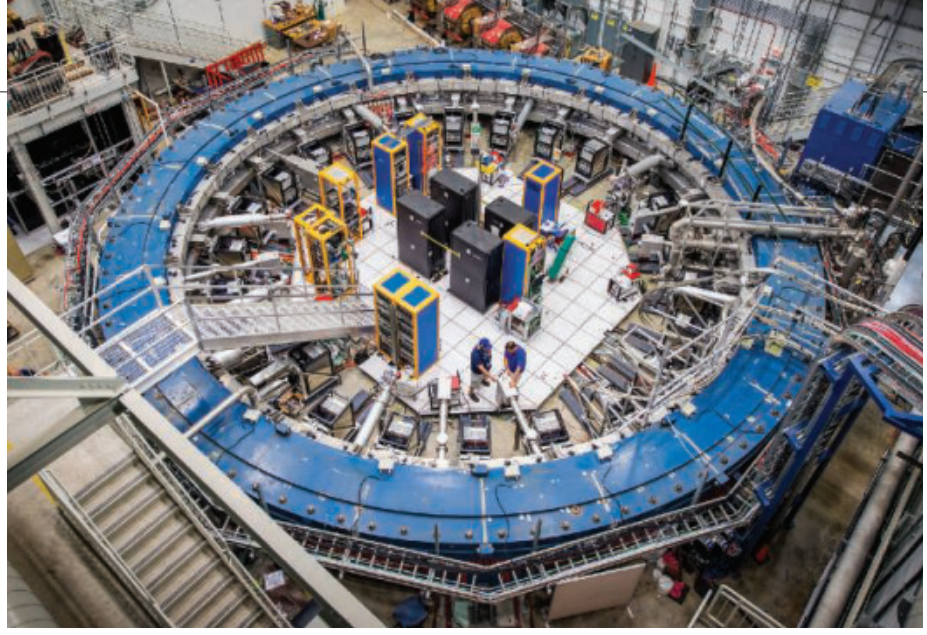

As muons race around a ring at the Fermi National Accelerator Laboratory, their spin axes twirl, reflecting the influence of unseen particles.

PHOTO: FERMI NATIONAL ACCELERATOR LABORATORY

PARTICLE PHYSICS

Once again, physicists ask, how magnetic is the muon?

First new result in 15 years could signal new particles

By **Adrian Cho**

In 1986, the TV journalist Dan Rather was attacked in New York City. A deranged assailant pummeled him while cryptically demanding, "Kenneth, what's the frequency?" The query became a pop culture meme, and the rock band R.E.M. even based a hit song on it. Now, it could be the motto for the team about to deliver the year's most anticipated result in particle physics.

As early as March, the Muon g-2 experiment at Fermi National Accelerator Laboratory (Fermilab) will report a new measurement of the magnetism of the muon, a heavier, short-lived cousin of the electron. The effort entails measuring a single frequency with exquisite precision. In tantalizing results dating back to 2001, g-2 found that the muon is slightly more magnetic than theory predicts. If confirmed, the excess would signal, for the first time in decades, the existence of novel massive particles that an atom smasher might be able to produce, says Aida El-Khadra, a theorist at the University of Illinois, Urbana-Champaign. "This would be a very clear sign of new physics, so it would be a huge deal."

The measures that g-2 experimenters are taking to ensure they don't fool themselves into claiming a false discovery are the stuff of spy novels, involving locked cabinets, sealed envelopes, and a second, secret frequency known to just two people, both outside the g-2 team. "My wife won't pick me for responsible jobs like this, so I don't know why an important experiment did," says Joseph Lykken, Fermilab's chief research officer, one of the keepers of the secret.

Like the electron, the muon spins like a top, and its spin imbues it with magnetism. Quantum theory also demands that the muon is enshrouded by particles and antiparticles flitting in and out of the vacuum too quickly to be observed directly. Those "virtual particles" increase the muon's magnetism by about 0.001%, an excess denoted as g-2. Theorists can predict the excess very precisely, assuming the vacuum fizzes with only the particles in their prevailing theory. But those predictions won't jibe with the measured value if the vacuum also hides massive new particles. (The electron exhibits similar effects, but is less sensitive to new particles than the muon because it is much less massive.)

To measure the telltale magnetism, g-2 researchers fire a beam of muons (or, to be more precise, their antimatter counterparts) into a 15-meter-wide circular particle accelerator. Thousands of muons enter the ring with their spin axis pointing in the direction they travel, like a football thrown by a right-handed quarterback. A vertical magnetic field bends their trajectories around the ring and also makes their spin axis twirl, or precess, like a wobbling gyroscope.

Were it not for the extra magnetism from

the virtual particles, the muons would precess at the same rate that they orbit the ring and, thus, always spin in their direction of travel. However, the extra magnetism makes the muons precess faster than they orbit, roughly 30 times for every 29 orbits—an effect that, in principle, makes it simple to measure the excess.

As they orbit, each muon decays to produce a positron, which flies into one of the detectors lining the ring. The positrons have higher energy when the muons are spinning in the direction they are circulating and lower energy when they are spinning the opposite way. So as the muons go around and around, the flux of high-energy positrons oscillates at a frequency that reveals how much extra magnetism the virtual particles create.

To measure that frequency with enough precision to search for new particles, physicists must tightly control every aspect of the experiment, says Chris Polly, a physicist at Fermilab and co-spokesperson for the 200-member g-2 team. For example, to make the ring's magnetic field uniform to 25 parts in 1 million, researchers have adorned the poles of its electromagnets with more than 9000 strips of steel thinner than a sheet of paper, says Polly, who has worked on the g-2 experiment since its inception in 1989 at Brookhaven National Laboratory in Upton, New York. Each sheet acts as a magnetic "shim" that makes a minuscule adjustment in the field.

At Brookhaven, the experiment collected data from 1997 to 2001. Ultimately, researchers measured the muon's magnetism to a precision of 0.6 parts in 1 billion, arriving at a value about 2.4 parts per billion bigger than the theoretical value at the time. In 2010, they hauled the 700-ton ring 5000 kilometers by barge to Fermilab in Batavia, Illinois (*Science*, 14 June 2013, p. 1277). Using a purer, more intense muon beam, the revamped g-2 ultimately aims to reduce the experimental uncertainty to one-quarter of its current value. The result to be announced this spring won't reach that goal, says Lee Roberts, a g-2 physicist at Boston University. But if it matches the Brookhaven result, it would strengthen the case for new particles lurking in the vacuum.

However, g-2 researchers must ensure they don't fool themselves while making the more than 100 tiny corrections that the various aspects of the experiment require. To avoid subconsciously steering the frequency toward the value they want, the experimenters blind themselves to the true frequency until they've finalized their analysis.

The blinding has multiple layers, but the last is the most important. To hide the true frequency at which the flux of positrons oscillates, the experiment runs on a clock that ticks not in real nanoseconds, but at an unknown frequency, chosen at random. At the start of each monthslong run, Lykken and Fermilab's Greg Bock punch an eight-digit value into a frequency generator that's kept under lock and key. The last step in the measurement is to open the sealed envelope containing the unknown frequency, the key to converting the clock readings into real time. "It's like the Academy Awards," Lykken says.

Any hints of new physics will emerge from the gap between the measured result and theorists' prediction. That prediction has its own uncertainties, but over the past 15 years, the calculations have become more precise and consistent, and the disagreement between theory and experiment is now bigger than ever. The gap between theorists' consensus value for the muon's magnetism and the Brookhaven value is now 3.7 times the total uncertainty, El-Khadra says, not too far from the five times needed to claim a discovery.

Nevertheless, the discrepancy may be less exciting than it was 20 years ago, says William Marciano, a theorist at Brookhaven. At that time, many physicists thought it could be a hint of supersymmetry, a theory that predicts a heavier partner for each standard model particle. But if such partners lurk in the vacuum, the world's largest atom smasher, Europe's Large Hadron Collider, probably would have blasted them out by now, Marciano says. "It's not impossible to explain [the muon's magnetism] with supersymmetry," Marciano says, "but you have to stand on your head to do it."

Still, physicists eagerly await the new measurement because, if the discrepancy is real, *something* new must be causing it. The team is still deciding when it will unblind the data, says Roberts, who has worked on g-2 since it began. "At Brookhaven, I was always sitting on the edge of my chair [during unblinding], and I think I will be here, too." ■

Excess magnetism

As theorists have improved their calculations, the gap between the expected magnetism of the muon and a 2005 measurement has persisted.

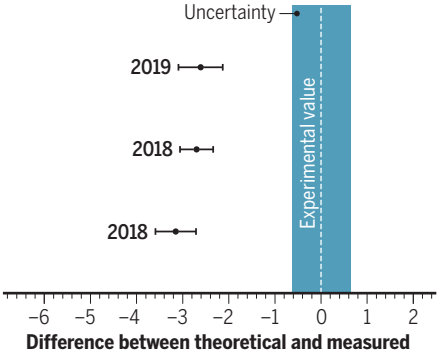

GRAPHIC: P. A. ZYLA *ET AL.* (PARTICLE DATA GROUP), *PROG. THEOR. EXP. PHYS.* 2020, 083C01. ADAPTED BY V. ALTOUNIAN/*SCIENCE*

EVOLUTION

Siberia may be long-sought site of dog domestication

Ancient DNA from people and dogs traces start of long companionship

By **David Grimm**

Sometime toward the end of the last ice age, a group of humans armed with stone-tipped spears stalked their prey in the bitter cold of northeastern Siberia, tracking bison and woolly mammoths across a vast, grassy landscape. Beside them ran wolflike creatures, more docile than their ancestors and remarkably willing to help their primate companions hunt down prey and drag it back to camp. These were the world's first dogs. Their descendants flowed both west and east, populating Eurasia as well as accompanying the ancestors of Native Americans as they spread into the Americas.

That's the scenario laid out in a new study combining DNA data from ancient dogs and humans. The analysis, published this week in the *Proceedings of the National Academy of Sciences*, aims to end years of debate about where and when dogs were domesticated. It may even explain how wary wolves were transformed into faithful companions in the first place.

"I *love* this study," says Jennifer Raff, an anthropological geneticist at the University of Kansas, Lawrence. More genomes from ancient dogs and people will be needed to confirm the findings, she says, but already, "It's amazing to see how the dog story and the human story match up."

The research started over beers in evolutionary biologist Greger Larson's office at the University of Oxford. He was chatting with Angela Perri, a zooarchaeologist at Durham University, about a canine conundrum: the origins of ancient dogs in North America, where evidence suggests they have lived for at least 10,000 years.

Archaeologist David Meltzer, visiting from Southern Methodist University, chimed in to suggest comparing an-

cient DNA from dogs and humans. "Dave started talking about how and when people branched out into different groups first when they were in Siberia and then after they reached North America," Perri recalls. If dog DNA showed similar patterns, that could reveal when the dog and human stories began to match up. "We went to a giant whiteboard and started scribbling arrows in all different directions. It was a hot mess, but it spelled out the story of dog domestication."

To refine their doodling, the researchers analyzed previously sequenced mitochondrial genomes of more than 200 dogs from all over the world. The mitochondrial DNA—short sequences that are more abundant in fossils than nuclear DNA—showed that all ancient American dogs carried a genetic signature, dubbed A2b, and that they splintered into four groups about 15,000 years ago as they spread around North America.

An artist's conception of a Native American and a dog in ancient America.

The timing and location of those splits mirror those of ancient Native American groups, the team found. All of those people descend from a group scientists call ancestral Native Americans, who arose in Siberia about 21,000 years ago. Those people must have brought dogs with them when they entered the Americas about 16,000 years ago, the team concluded. (The ancient American dogs later vanished, wiped out after Europeans came to the Americas with their own canines.)

Going even deeper into the genetic past, the team found that the A2b dogs descended from a canine ancestor that lived in Siberia about 23,000 years ago. That ancestral dog probably lived with people who belonged to a genetic grouping known as the ancient north Siberians, the team speculates. The group, which appeared more than 31,000 years ago, lived in a relatively temperate part of northeastern Siberia for thousands of years, and they shared this refuge with the gray wolf, the direct ancestor of today's dogs.

"These people were probably sleeping on the ground in furs, roasting fresh kills on the fire," Meltzer says. "If you're a hungry carnivore and you smell a mammoth barbecue, you're going to check it out."

The idea fits the leading theory of dog domestication, which holds that gray wolves inched closer and closer to human campsites to scavenge food, with the least timid ones evolving over hundreds or thousands of years into the gentle pups we know today.

What's more, genetic evidence suggests the ancient north Siberians mingled with the ancestral Native Americans before they migrated to the Americas. The ancient dog breeders might have traded animals to the lineage that became Native Americans, as well as to other groups of people, including those traveling farther west into Eurasia. That could explain why dogs appeared in both Europe and North America about 15,000 years ago, a puzzle that had previously sparked speculation that dogs were domesticated more than once. Instead, all dogs descend from roughly 23,000-year-old Siberian pups, the team argues.

Peter Savolainen, a geneticist at the Royal Institute of Technology in Stockholm, is dismissive. He says the A2b signature that the team claims is exclusive to the Americas has been found elsewhere in the world. This invalidates the entire genetic analysis, he argues, and the new study "can't say anything" about dog domestication.

But based on all she knows about ancient people in the Americas, Raff says the study's basic story "rings true." Still, she notes, mitochondrial DNA represents only a tiny fraction of an animal's genome. "You can't fill in the full picture without nuclear DNA." ■

U.S. SCIENCE POLICY

Biden breaks new ground with science team picks

In firsts, science adviser elevated to Cabinet and life and social scientists will hold top White House jobs

By **Jeffrey Mervis**

Days before President Joe Biden was sworn in on 20 January, he took steps to fulfill a campaign promise to draw on the best scientific evidence in making policy. He picked a science team of prominent researchers who have extensive knowledge of the federal government. Biden also signaled that science will play an elevated role in his administration by announcing that his science adviser, for the first time, will also hold a seat in the Cabinet.

At a 16 January press conference, Biden formally introduced mathematician and geneticist Eric Lander to be both director of the White House Office of Science and Technology Policy (OSTP) and his science adviser. If the Senate confirms Lander as OSTP director, he will be the first life scientist to hold the posts. Biden also released a letter that asks Lander to focus on five grand challenges facing the country, including applying lessons from the COVID-19 pandemic to improve public health, dealing more aggressively with climate change, and creating new industries from emerging technologies such as quantum information science and artificial intelligence.

Lander, who will take leave as founding director of the Broad Institute run jointly by Harvard University and the Massachusetts Institute of Technology, is well-versed in those issues and other policies affecting research. He spent the entirety of the Obama administration as co-chair of the President's Council of Advisors on Science and Technology (PCAST), a blue-ribbon group of outside experts, and years earlier helped lead the government's team that sequenced the human genome.

IMAGE: ETTORE MAZZA

Eric Lander (left) and Alondra Nelson were named to top spots at the White House science office.

PHOTOS: (LEFT TO RIGHT) MATT SLOCUM/AP/SHUTTERSTOCK; AP PHOTO/MATT SLOCUM

Biden also introduced sociologist Alondra Nelson, who will fill the new position of OSTP deputy director for science and society. Nelson's title and appointment, which does not require Senate confirmation, appear to reflect Biden's interest in using the federal research machinery to address social inequality. "The benefits of science and technology remain unevenly distributed across racial, gender, economic, and geographic lines," Biden wrote in his 15 January letter to Lander. "How can we guarantee that the fruits of science and technology are fully shared across America and among all Americans?"

Nelson, a faculty member at the Institute for Advanced Study, has spent her academic career wrestling with the societal impacts of technology on marginalized groups. And although she hasn't been a White House insider, she has been interviewing former OSTP staffers for an upcoming book on former President Barack Obama's major science initiatives, including the Cancer Moonshot that Biden personally led as vice president.

Biden also chose Nobel Prize–winning chemist Frances Arnold and pioneering astrophysicist Maria Zuber to lead PCAST. The selection of two women is a first for the panel, which was moribund for most of former President Donald Trump's tenure, but has played a key role in incubating policy initiatives under previous presidents.

Some observers are disappointed Biden didn't pick a scientist of color or a woman to lead his science team. But science advocacy groups generally applaud Biden's moves, viewing him as a desperately needed antidote to his predecessor. "These excellent picks … recognize that science is interwoven into all aspects of federal policy and critical to fueling economic growth and job creation," says Peter McPherson, president of the Association of Public and Land-grant Universities.

As a Cabinet member, Lander will have an easier time providing Biden and his team with the latest scientific findings, believes physicist Neal Lane, who led OSTP and served as science adviser under former President Bill Clinton. "It's the difference between sitting silently along the back wall of the room and engaging the principals in real time," Lane says. He attended Cabinet meetings, he says, but "I never remember being asked to comment during the meeting."

Lane also thinks Lander, as a Cabinet member, will have greater leverage in seeking more staff and a larger budget. (OSTP was seen as too lean under his predecessor, Kelvin Droegemeier, who filled a spot that Trump had left vacant for 2 years.)

But Harvard's John Holdren, who was Obama's science adviser, doesn't see the need for the elevated status. "It wouldn't have made any difference when I was at OSTP," says Holdren, a physicist who has specialized in environmental policy. "I had access to the president whenever I needed it."

Nelson's newly created position, meanwhile, "is the best news I've heard this year," says Dorothy Roberts, a legal scholar and social scientist at the University of Pennsylvania who has interacted with Nelson over the years, and regards her as "a former mentee who has far surpassed me in prominence."

At the press conference, Nelson gave a glimpse of what she expects to tackle. "Science is a social activity," she said. "When we design and carry out experiments, we are making human choices. It matters who makes those choices. And as a Black woman researcher, I'm keenly aware of who has been missing from the room."

Nelson has backed efforts by Roberts and other scholars to push the National Institutes of Health (NIH) and other government agencies to end their use of race as a biological category. But Nelson is no enemy of bench science, Roberts notes. "She is excited by the possibilities that flow from innovation," Roberts says, "but she understands that it also imbeds inequities."

Nelson's research has also highlighted the scientific contributions of activists working with marginalized groups. Her 2011 book examining community health programs run by the Black Panthers "shattered the myth that Black [people] don't believe science is important," Roberts says.

In his letter to Lander, Biden emphasizes the vital role of science in a thriving democracy and mentions a similar letter former President Franklin Roosevelt sent to his science adviser, Vannevar Bush. Bush's response—a 1945 report titled *Science: The Endless Frontier*—became the blueprint for how the U.S. government supports academic research.

But Bush's vision fell short in one crucial aspect that Biden is trying to address, says physicist Rush Holt, a former member of Congress (and former CEO of AAAS, which publishes *Science*). "In the belief that scientific progress ultimately relies on the freedom of scientists to pursue basic research without thought of practical ends, [Bush] promoted a system that has also had the effect of distancing science from the public, and vice versa," Holt writes in a foreword to a new, 75-year-anniversary edition of the report. That separation has resulted in distrust, as well as policies and practices that have failed "to give citizens some important things they need," Holt says, including more effective U.S. responses to the pandemic and climate change.

Biden has already named teams that are expected to work toward closing that gap as they tackle climate change and the COVID-19 pandemic. It's not yet clear how Lander and Nelson will interact with those efforts and, as *Science* went to press, Biden had not announced other key science appointees, including the heads of NASA, the National Oceanic and Atmospheric Administration, and the National Institute of Standards and Technology. But he is retaining at least one familiar face: Francis Collins will continue his tenure as NIH director, working under his third president since taking the job in 2009. ■

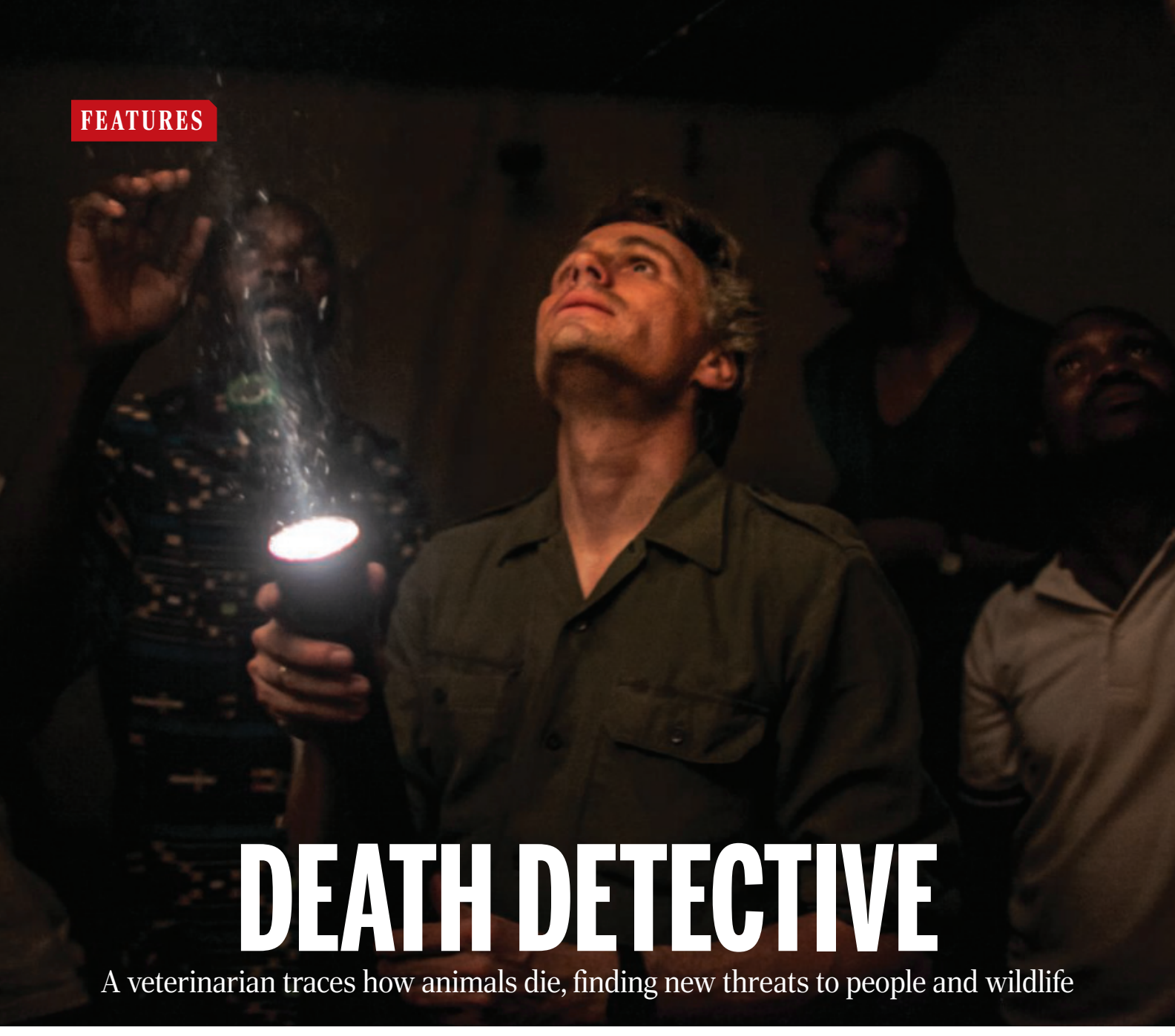

DEATH DETECTIVE

A veterinarian traces how animals die, finding new threats to people and wildlife

By **Kai Kupferschmidt**, *in Taï National Park in Ivory Coast*

The message arrived as Fabian Leendertz was watching what he calls "breakfast TV": a troop of black-and-white colobus monkeys leaping acrobatically through the trees that tower above the remote field camp here near the Liberian border. A colleague had received word that the carcass of a duiker, a kind of antelope, had been spotted in the rainforest some 10 kilometers away.

The notification launched Leendertz, a wildlife veterinarian at the Robert Koch Institute, into a race against time. The jungle is a hungry place, and Leendertz and his team needed to hike to the carcass before it was hauled away by a leopard or consumed by smaller animals. If the researchers beat the scavengers, they could collect tissue and other materials—including maggots feeding on the carrion—that could help answer a fundamental question: What do animals in the jungle die of?

Leendertz and his colleagues have been chasing answers here in the Taï forest for the past 20 years, studying hundreds of carcasses and sampling living animals in one of the only long-term studies of its kind. They've found that poachers and predators aren't the only deadly threat lurking in the rainforest—infectious diseases are a big killer, too.

The findings have implications for both saving endangered animals, especially apes, and protecting human health. Leendertz's work has revealed, for example, that chimpanzees can die from common cold viruses introduced by humans, prompting scientists, conservation groups, and ecotourism firms to impose new requirements on people visiting the apes. His team has also discovered a previously unknown variant of anthrax that appears to pose a major threat to wildlife. And he and colleagues in Guinea-Bissau recently found that wild chimpanzees suffer from leprosy, suggesting apes might be a previously undetected reservoir of that disfiguring disease, which could spill over into human populations.

PHOTO: PETE MULLER

Fabian Leendertz has spent decades studying how diseases flow between humans and wildlife. Here, he and colleagues hunt for bats in Ivory Coast.

"Fabian's work has really changed how we view biosafety and biosecurity around great apes in the wild," says disease ecologist Anthony Goldberg of the University of Wisconsin, Madison.

Now, the 48-year-old Leendertz, who once investigated the animal origins of an Ebola outbreak in West Africa, has been asked to help to solve one of the great disease mysteries of the early 21st century: the origins of SARS-CoV-2, the coronavirus that originated in bats and has killed more than 2 million people worldwide. In November 2020, the World Health Organization (WHO) named him to a 10-person team that is examining how the COVID-19 pandemic emerged. At the same time, Leendertz is worrying about how the coronavirus might affect great apes if it spreads to those vulnerable species.

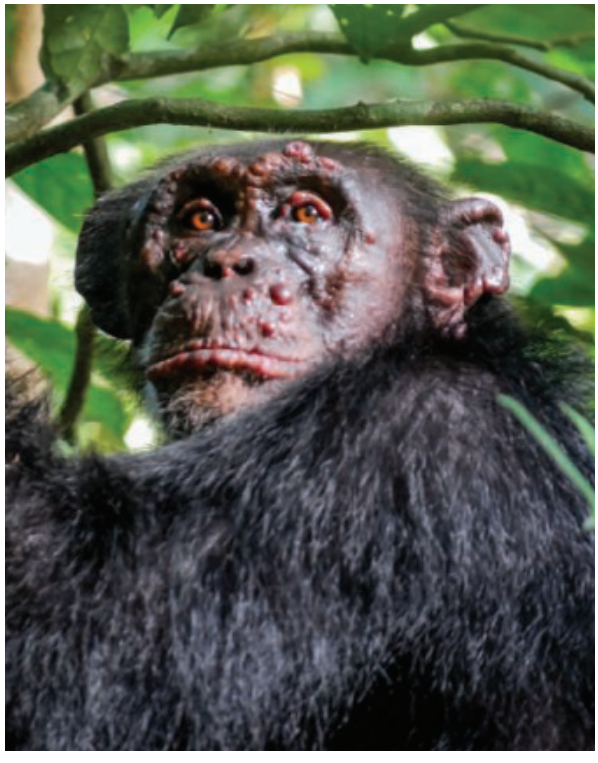

A discovery that leprosy can infect wild chimpanzees broke new ground.

JUST 30 MINUTES after the message arrived, Leendertz and two other veterinarians, Penelope Carlier and Bernard N'gbocho N'guessan, set off to find the carcass. After a kilometer or so, they passed a group of sooty mangabey monkeys lounging on logs. The animals, even a mother hugging a baby to her belly, appeared undisturbed by the hikers. That is because the monkeys had been habituated; researchers followed them for years until they grew used to humans.

In 1979, primatologists Christophe Boesch and Hedwige Boesch-Achermann came to the forest, one of the last large swaths of rainforest in West Africa, to study chimpanzee behavior. Over years, they habituated chimps, mangabeys, and several other kinds of monkeys, and began documenting their lives. But then, in 1994, the chimpanzees started to die. Eight of 43 study animals turned up dead; four more disappeared.

The researchers hauled one chimp's body back to their camp's sturdy dining table for dissection. They wore gloves, but no gowns or masks, and 1 week later one woman fell ill. She recovered, but scientists isolated a virus from her blood. It was a new species of Ebola, a group of viruses already known from human outbreaks elsewhere in Africa, and the dead chimp carried it, too. The discovery of what became known as Taï forest Ebola marked the first time an Ebola outbreak had been documented in nature.

The experience was a wake-up call from both a safety and a scientific perspective, says Boesch, who retired as director of the Max Planck Institute for Evolutionary Anthropology in 2019. "In retrospect it is clear that we ran a risk; we were not prepared at all, we had no equipment." And it made the researchers realize that infectious diseases could be playing a larger role in wildlife mortality than they realized. "We cannot go on like this," Boesch recalls thinking. They needed a trained veterinarian, and in 2001 Leendertz got the job.

It was the kind of position he had long coveted. Growing up in Krefeld, Germany, Leendertz had bred mice and toads and spent a lot of time at the local zoo. (The director was a friend of his parents.) At university, he began to study biology but grew frustrated. "It was just way too much biochemistry," he recalls, including countless hours in the laboratory running polymerase chain reactions (PCRs) to amplify snippets of DNA. "All these PCRs were so far removed from working with actual animals," he says, so he switched to veterinary medicine.

In 1999, after completing his undergraduate studies and working in Namibia for a few months, Leendertz reached out to Boesch, asking whether he could join the Taï project. The reply was yes—if Leendertz found an academic laboratory that would help support his graduate studies.

That wasn't easy. But Beatrice Hahn, a virologist at the University of Pennsylvania, had just published work showing HIV, the virus that causes AIDS in humans, had come from chimpanzees. The discovery ignited scientific interest in zoonoses, diseases that jump from animals to humans. "That was kind of the first big 'aha!' moment about zoonotic disease," Goldberg says. It helped Leendertz find a home at the Robert Koch Institute and ensured that, from the start, he would focus on both veterinary and human medicine.

Starting in 2001, Leendertz spent 14 months at Taï, following chimpanzees through the forest, collecting feces, and conducting necropsies. "That was the real starting point for my work," he says. The conditions didn't bother him. He was content to be outdoors and largely cut off from the world, able to send and receive emails just once a week though a satellite connection. Leendertz didn't see images of the planes hitting New York City's twin towers in 2001 until the year after the attack, after he emerged from his sojourn in the forest.

AFTER A LONG MARCH, the team found what was left of the dead duiker, surrounded by buzzing flies. Leendertz and Carlier suited up: masks, body suits, face shields, layers of gloves. They filled a bucket of bleach to disinfect equipment. Then they began cutting snippets of tissue and collecting blood, even grabbing a few maggots, which would be liquefied and analyzed for any pathogens they carried.

Moving deliberately around the forest in their gleaming white suits, the researchers looked like investigators at a crime scene. They were, in a way, with the added complication that the killer might still be lurking nearby. Leendertz has been following one suspect in particular since his first stint in the Taï forest. He was watching a group of chimpanzees when an alpha male named Leo suddenly vomited. Then, "He climbed on this low branch, toppled over, and died," Leendertz recalls. "I was stunned."

The killer, Leendertz and his group reported in *Nature* in 2004, was anthrax. It later became clear, however, that the cause was not the usual anthrax bacterium, but an unusual variant of *Bacillus cereus*, a soil bacterium that is usually benign. But this variant had acquired two circles of DNA, called plasmids, that had turned it into a formidable killer.

Subsequent work showed the bacterium

PHOTO: TAÏ CHIMPANZEE PROJECT

was attacking other Taï forest mammals, too, including monkeys, mongooses, and porcupines. In 2017, the team published evidence—gathered from bones, carcasses, and even flies—that it appeared to be associated with 38% of 279 deaths the team had investigated from 1996 to 2015. The work was a reminder, Leendertz says, that "we understand very little about what animals really die of in an environment like this."

Most worrying, the *Nature* paper presented simulations showing anthrax could help wipe out the Taï forest's chimpanzees within 150 years. And anthrax is not the only disease threatening the chimps, other work by Leendertz's team has shown. "On top of all of the deforestation, the poaching … they are just getting bashed by these infectious diseases," says primatologist Kimberley Hockings of the University of Exeter.

Before necropsying wild animals, Fabian Leendertz and Kouadio Leonce don protective gear.

Some of those deadly diseases come from humans, Leendertz and colleagues reported in 2008 in *Current Biology*. After investigating five respiratory disease outbreaks that had struck Taï chimpanzees between 1999 and 2006, killing at least 15 individuals, the researchers concluded they were linked to two viruses that commonly cause mild disease in humans: human respiratory syncytial virus and human metapneumovirus. "Our results suggest that the close approach of humans to apes, which is central to both research and tourism programs, represents a serious threat to wild apes," they wrote.

The idea was not new. Jane Goodall, the prominent primatologist, had described a pneumonia outbreak that killed several chimpanzees; researchers believed it was caused by a human-introduced pathogen. But the *Current Biology* study, and a similar viral outbreak documented in Tanzania, highlighted the threat of what Goldberg calls reverse zoonoses. "It's a world of viruses that are crossing species in every direction," he says. "And whenever that happens, it can cause devastating losses." (Goldberg has shown that the most common human cold virus, rhinovirus C, caused a deadly 2013 outbreak among chimpanzees in Uganda.)

The 2008 study also presented a dilemma for primate researchers such as Boesch, who was one of the co-authors. It suggested that even as they studied and worked to protect apes, they might be killing them, too. So, to reduce the risk of future outbreaks, the Taï researchers imposed new restrictions: Incoming staff must quarantine at the camp for 5 days before going into the forest, and everyone must stay at least 7 meters from study animals as well as wear masks while observing. Leendertz, meanwhile, pushed hard for field sites and tourism firms elsewhere to adop similar measures, co-authoring safety guidelines published in 2015.

Such efforts "really … opened people's eyes [that we needed] to be a lot more careful," Hockings says. But, "It was a very controversial thing before COVID," Goldberg adds. "People were afraid that tourists would be angry if you tried to make them wear a mask, that the apes would be afraid of the masks and attack tourists … that foreign governments would get less money from tourism."

Today, Leendertz says helping catalyze such practical, real-world change is among his proudest accomplishments. And he says the experience only underscored the value of long-term, multifaceted studies of wildlife mortality. "The threat that infectious diseases pose to chimpanzees was long underestimated and hardly studied," he says. "They were neglected for a long time."

DESPITE HIS LOVE of fieldwork, Leendertz is spending less time in the Taï forest these days, visiting just once or twice a year. "When my feet are hurting because I'm not used to the long distances anymore, and when I get up in the morning from that moldy mattress, I do think that time is over," he says. Still, he says, "When I arrive it really is that feeling of coming home."

At the Robert Koch Institute, meanwhile, Leendertz's lab is busy with samples shipped by colleagues in the forest. Located in a brand-new building that also houses one of the world's newest biosafety level four high-biosecurity labs, the lab uses state-of-the-art technologies to identify and characterize the pathogens found in the samples. Ironically, Leendertz notes, "I'm back to doing PCRs." Recently, for example, the samples collected from the dead duiker in 2019 were analyzed. The antelope was, as suspected, infected with anthrax.

Such molecular sleuthing isn't just about identifying animal killers. Leendertz notes that, when paired with careful field observations, lab findings can yield important insights into protecting human health. In 2017, for instance, some Taï chimpanzees began to cough and display respiratory distress. Lab work showed the cause was monkeypox, a less deadly relative of smallpox that can move from primates to humans. In humans, monkeypox often announces itself through a skin rash, but Leendertz's work suggests coughing is an "unusual symptom" that health workers working in communities near primate populations should keep in mind.

More recently, Leendertz's team has discovered that leprosy—another disease with the potential to jump to humans—affects wild chimpanzees too. In 2017, Hockings, who studies chimpanzees in Guinea-Bissau's Cantanhez National Park, observed animals with lesions on their

PHOTO: PETE MULLER

A research team heads into Kanankru, Ivory Coast, to search for bats, which have been implicated in outbreaks of Ebola and other deadly diseases.

faces and hands. She shared her observations with Leendertz, and soon afterward he noticed similar lesions on Woodstock, a Taï chimpanzee. By analyzing fecal samples, the researchers confirmed the lesions were caused by leprosy, a disease never before seen in wild chimpanzees.

The discovery has highlighted how little is known about *Mycobacterium leprae*, the bacterium that causes leprosy, says immunologist John Spencer of Colorado State University, Fort Collins. Researchers can't culture the microbe in the laboratory and, although they have found it circulating in armadillos and red squirrels, it hadn't been seen in apes. The chimp find suggests leprosy "has other niches that it has adapted to," Spencer says—and adds one more pathogen to the growing roster of diseases that afflict both humans and other animals.

IF LEENDERTZ HAS BUILT his career on the dual concerns of human and chimpanzee health, then the emergence of SARS-CoV-2 has brought these two issues together with new urgency. The virus now rampaging through human populations is a potential threat to great apes as well, Leendertz and primatologist Tom Gillespie of Emory University warned in a letter published in *Nature* in March 2020. To reduce the risks, they asked governments to suspend ecotourism and researchers to reduce field research, and many complied.

Since then, gorillas at the San Diego Zoo have tested positive for SARS-CoV-2. They showed only mild symptoms, but that is not very reassuring, Gillespie says, because captive animals tend to be well fed and be less burdened with other infections. "It's really hard to say from captive studies what we would see in the wild," he says.

Looking ahead, Leendertz says, "The question is how to get back to a more normal situation" for primate scientists. One concrete step could be to vaccinate researchers and people living around field sites like Taï, he suggests.

In the meantime, WHO has asked Leendertz to join its investigation into the origins of SARS-CoV-2. That appointment makes sense scientifically and politically, colleagues say. Leendertz's years of patient, intensive focus on understanding death in a single rainforest have given him a valuable perspective on how to investigate pathogens hopping from one species to another, as SARS-CoV-2 is believed to have done. And he represents the Robert Koch Institute, Germany's equivalent of the U.S. Centers for Disease Control and Prevention. "I see the WHO mission as about 50% actual science and 50% building bridges with Chinese colleagues," Goldberg says. "I think Fabian will do well on both fronts."

But Leendertz also knows from past experience with virus hunts that definitive answers can be hard to come by. In 2014, he led a team that traveled to Meliandou, Guinea, shortly after the start of an Ebola outbreak that ultimately killed some 1000 people. The researchers interviewed villagers, who told them about a hollow tree where the child who had been the first to get sick had played.

When the team visited the tree, they discovered it had burned (whether by accident or intention wasn't clear). On the blackened stump, they found traces of DNA left behind by bats that had apparently roosted in the tree. Had an encounter between the child and a bat sparked the outbreak? It was a plausible scenario, they concluded, but there would likely never be proof.

The chain of events that led to the COVID-19 pandemic is likely to be far more elusive. And the WHO investigation has gotten off to a bumpy start. When the team first tried to visit China earlier this month, officials barred several members from entering because of pandemic restrictions. Leendertz himself could not join the trip because of a family commitment. So, while his colleagues conducted Zoom meetings from the hotel rooms where they were quarantined after arriving in China, Leendertz joined from his home, where it was 2:30 a.m. It was another kind of breakfast TV, just not the episode he enjoys the most. ■

PHOTO: PETE MULLER

PHOTO: JORGE CABRERA/REUTERS

CLIMATE CHANGE

Increased tropical cyclone risk to coasts

The trends in tropical cyclones point to more frequent strong storms near land

By **Suzana J. Camargo**[1] *and* **Allison A. Wing**[2]

The record-breaking 2020 North Atlantic hurricane season has brought new attention to tropical cyclone (TC) risk. Although the astounding total of 30 named storms is not necessarily a signature of climate change, anthropogenic climate change is increasing the threat posed by TCs in other ways. The most confidently predictable changes in TC activity with warming are an increase in the occurrence and intensity of the most intense TCs, an increase in the precipitation associated with TCs, and an increase in storm-surge flooding due to sea level rise (*1*). On top of these changes, on page 514 of this issue, Wang and Toumi (*2*) provide evidence that TC activity close to land is increasing, with a substantial increase in TC risk to coastal regions.

[1]Lamont-Doherty Earth Observatory, Columbia University, Palisades, NY 10964, USA. [2]Department of Earth, Ocean, and Atmospheric Science, Florida State University, Tallahassee, FL 32306, USA. Email: suzana@ldeo.columbia.edu

TC risk requires a TC to occur, but projections of the number of TCs attributable to warming are uncertain. Because there is no accepted theory for the global number of TCs, projections are based only on modeling studies, which can be sensitive to the type of model used, model convective parameterizations, and the underlying patterns of the projected sea surface temperature forcing of the atmospheric model simulations. Indeed, whereas most models project a decrease in the global number of TCs (*1*), some models instead project an increase in the global TC frequency (*3*–*5*). However, global or even basin-wide TC frequency does not directly drive societal TC risk; landfall does. The 2020 season was also exceptional in this regard: Twelve named storms (six hurricanes) made landfall in the continental United States (see the figure), with devastating social and economic impacts, especially in the central Gulf Coast. Furthermore, in Central America, Eta and Iota dropped huge amounts of rainfall in the same area of Honduras and Nicaragua only 2 weeks apart. Was this a fluke, or is it a worrisome harbinger of future hurricane seasons?

Wang and Toumi analyzed TC activity close to land regions and found that TCs are reaching their lifetime maximum intensity (LMI) closer to land. The distance between the location of LMI and land has decreased by 30 km per decade. More TCs are occurring close to land by about two TCs per decade. The locations at which TCs reach their LMI are intrinsically linked to their tracks.

Many studies have analyzed possible changes in TC tracks, but these changes are not robust across models and projections (*6*). The observed poleward shift of LMI (*7*) is one of the best-known TC location shifts and is thought to be associated with Hadley cell expansion due to anthropogenic climate change. This shift is most notable in the western North Pacific, is also present in the genesis location (*8*), and is expected to continue (*9*). In contrast, Wang and Toumi noted shifts in the east-west direction that are linked to westward shifts in the steer-

A woman stands outside her home in Pimienta, Honduras, that was damaged due to the heavy rains of Hurricane Eta in November 2020.

A busy year for U.S. hurricane landfalls

Tracks of 12 tropical storms and hurricanes that made landfall in the continental United States in 2020 are shown. The colors represent the intensity of the storms: tropical depression (TD, light blue); tropical storm (TS, blue); hurricane categories 1 and 2 (Hur 1-2, pink); and hurricane categories 3 to 5 (Hur 3-5, red).

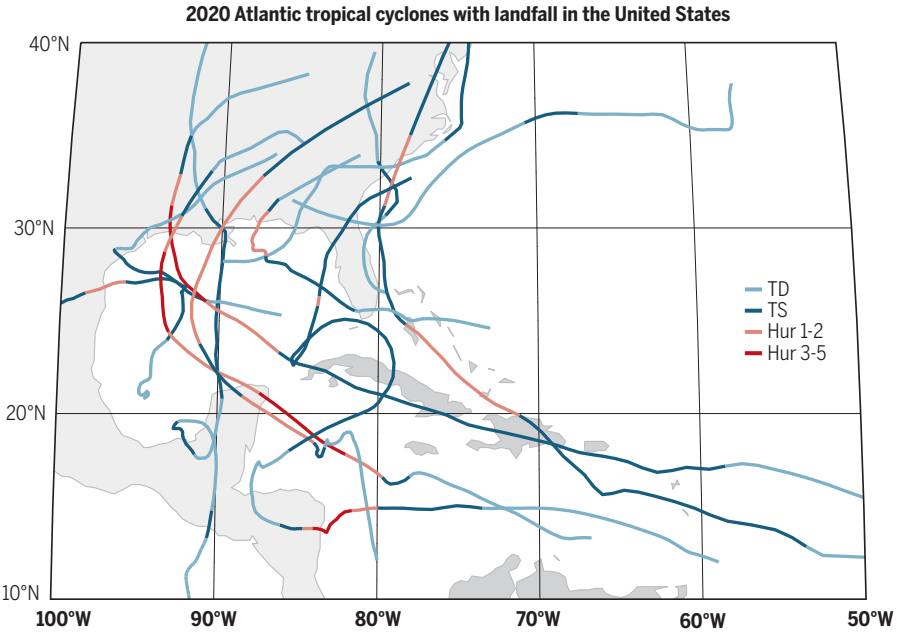

ing flow. Both types of shifts could lead to enhanced landfall impacts.

In the case of the poleward shift, more intense storms could potentially reach and have an impact on unprepared regions typically not affected by intense TCs. Similarly, coastal communities could be affected by TC hazards (winds, precipitation, and storm surge) more often by the westward shift coupled with anthropogenic-driven increases in TC intensity. The impacts of landfalling TCs could potentially become even worse with warming. Li and Chakraborty (*10*) proposed that landfalling TCs take longer to weaken and dissipate over land as the planet warms. Murakami *et al.* (*11*) showed changes in the global spatial distribution of TCs that were attributed to increasing concentrations of greenhouse gases. It remains unknown whether and how these spatial changes in TC activity are related or whether they are independent, as well as which trends are expected to continue.

Wang and Toumi also found that the fraction of time that TCs spend near the coast has been increasing. This could be related to independent observations of a global slowdown of the TC translation speed (*12*) and increased stalling of Atlantic TCs (*13*). Slow-moving hurricanes that spend more time near the coast can lead to large flooding events due to the high amount of precipitation that can fall in one area—as occurred, for example, during Hurricane Harvey (2017) in Houston, Texas, and Hurricane Florence (2018) in the Carolinas.

Changes in TC activity can be difficult to characterize because of the inherent observational limitations and the small magnitude of the changes in comparison to natural variability. Wang and Toumi associated trends with changes in steering flow and ambient vertical wind shear, but they do not discuss reasons for these changes. However, other circulation changes have been outlined. For instance, Kossin (*14*) noticed decadal variability in vertical wind shear along the U.S. Atlantic coast that was associated with a drought of major hurricane landfalls in the United States. However, the protective barrier of wind shear along the Atlantic coast is expected to be eroded in the future as a consequence of increased greenhouse gas concentrations (*15*).

These changes in circulation (i.e., steering flow, vertical shear, and the Hadley cell) are fundamental to determining TC tracks, and thus the locations that will be affected by TCs. A better understanding of future TC risk, and of regional risk assessment in particular, requires a better understanding of spatial changes in TC activity. This requires further research into the causes, projections, and robustness of circulation changes associated with TC occurrence. Nonetheless, all of the discussed changes in TC activity, combined with a continued buildup of coastal population and infrastructure, paint a picture of a future in which coastal cities will be more prone to the occurrence of TC-related disasters. Although continued investigation is important, we already possess an understanding that argues for increased investment in the preparedness of coastal populations in the path of TCs. ■

REFERENCES AND NOTES

1. T. Knutson *et al.*, *Bull. Am. Meteorol. Soc.* **101**, E303 (2020).
2. S. Wang, R. Toumi, *Science* **371**, 514 (2021).
3. K. Bhatia, G. Vecchi, H. Murakami, S. Underwood, J. Kossin, *J. Clim.* **31**, 8281 (2018).
4. C.-Y. Lee, S. J. Camargo, A. H. Sobel, M. K. Tippett, *J. Clim.* **33**, 4815 (2020).
5. K. Emanuel, *J. Clim.* **34**, 57 (2021).
6. J. Nakamura *et al.*, *J. Geophys. Res.* **122**, 9721 (2017).
7. J. P. Kossin, K. A. Emanuel, G. A. Vecchi, *Nature* **509**, 349 (2014).
8. A. S. Daloz, S. J. Camargo, *Clim. Dyn.* **50**, 705 (2018).
9. J. P. Kossin, K. A. Emanuel, S. J. Camargo, *J. Clim.* **29**, 5725 (2016).
10. L. Li, P. Chakraborty, *Nature* **587**, 230 (2020).
11. H. Murakami *et al.*, *Proc. Natl. Acad. Sci. U.S.A.* **117**, 10706 (2020).
12. J. P. Kossin, *Nature* **558**, 104 (2018).
13. T. M. Hall, J. P. Kossin, *npj Clim. Atmos. Sci.* **2**, 17 (2019).
14. J. P. Kossin, *Nature* **541**, 390 (2017).
15. M. Ting, J. P. Kossin, S. J. Camargo, C. Li, *Sci. Rep.* **9**, 7795 (2019).

ACKNOWLEDGMENTS

S.J.C. thanks the Vetlesen Foundation for its generous and sustained support of climate science at the Lamont-Doherty Earth Observatory of Columbia University.

10.1126/science.abg3651

GRAPHIC: KELLIE HOLOSKI/*SCIENCE*; (OPERATIONAL PRELIMINARY DATA) THE NATIONAL HURRICANE CENTER DOWNLOADED FROM IBTRACS

IMMUNOLOGY

Translating viral vaccines into immunity

How adenoviral vaccines orchestrate adaptive immunity from innate responses is uncovered

By **Jennifer A. Juno**[1] and **Shelby L. O'Connor**[2,3]

Viral vector–based vaccines use relatively harmless viruses as delivery vehicles of encoded antigens. Adenovirus vector–based vaccines are popular because they infect a wide variety of cell types, are replication incompetent, and use host cell machinery to produce the foreign protein. Understanding the mechanism by which adenovirus vector–based vaccines generate protective immunity to the expressed foreign antigen is essential for further developing this class of vaccines. On page 521 of this issue, Provine *et al.* (*1*) demonstrate that the generation of antigen-specific $CD8^+$ T cells by adenovirus vector–based vaccines relies on mucosal-associated invariant T (MAIT) cells. Their data provide evidence that MAIT cells act as a link between the innate antiviral immune response and the generation of adaptive antiviral immunity for vaccines, such as the chimpanzee adenovirus Ox1 (ChAdOx1) nCoV-19 vaccine against severe acute respiratory syndrome coronavirus 2 (SARS-CoV-2).

MAIT cells are innate-like T cells that sense foreign pathogens through at least two distinct mechanisms: T cell receptor (TCR)–dependent recognition of major histocompatibility complex (MHC) class I–related protein 1 (MR-1) molecules presenting vitamin B–derived metabolites on a range of antigen-presenting cells (APCs), and TCR-independent activation by cytokines produced during viral infection of APCs (*2*). Acute infections with influenza virus and dengue virus induce host APCs to produce cytokines, such as interleukin-18 (IL-18), IL-15, and type I interferons (IFNs), which activate MAIT cells (*2*–*4*). Acute HIV or simian immunodeficiency virus (SIV) infection also transiently promotes activation and proliferation of MAIT cells (*5*–*7*). These studies demonstrate that viral infections activate MAIT cells, but they do not explain whether MAIT cells subsequently boost the adaptive immune response.

[1]Department of Microbiology and Immunology, The Peter Doherty Institute for Infection and Immunity at the University of Melbourne, Melbourne, VIC, Australia. [2]Department of Pathology and Laboratory Medicine, The University of Wisconsin-Madison, Madison, WI, USA. [3]Wisconsin National Primate Research Center, Madison, WI, USA.
Email: jennifer.juno@unimelb.edu.au; slfeinberg@wisc.edu

Adenovirus vectors have gained momentum as vaccines to elicit antigen-specific immunity against Ebola virus and SARS-CoV-2 (*8*–*10*). Two current SARS-CoV-2 vaccine vector candidates include the rare human adenovirus type Ad26 (*9*, *11*) and the chimpanzee adenovirus vector ChAdOx1 (*10*, *12*). These vaccines are particularly immunogenic because people lack preexisting neutralizing antibodies against these adenovirus serotypes (*13*). Vaccination with these vectors leads to cellular infection and expression of the foreign antigen. A rapid and robust innate immune response is then followed by the generation of T cells and antibodies specific for the foreign antigen (*9*, *10*).

Communicating vaccine immunogenicity

Activation signals from adenoviral vector vaccines to $CD8^+$ T cells occur through mucosal-associated invariant T (MAIT) cells. MAIT cells are activated by the cytokines [interferon-α (IFN-α), interleukin-18 (IL-18), and tumor necrosis factor (TNF)] produced after adenoviral infection of plasmacytoid dendritic cells (pDCs) and monocytes. These activated MAIT cells subsequently induce the expansion of vaccine antigen–specific $CD8^+$ T cells by an unknown mechanism.

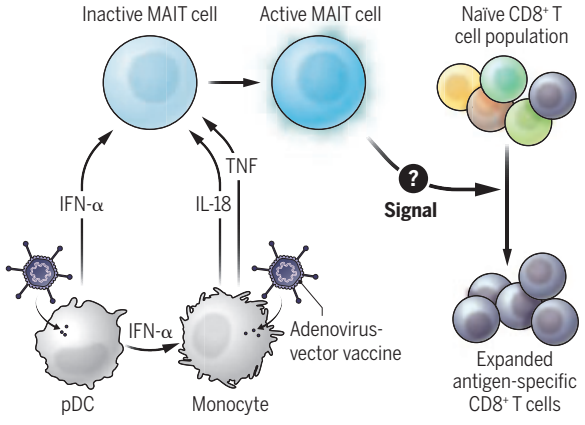

Provine *et al.* isolated specific cell subsets to show that ChAdOx1 virus particles infect plasmacytoid dendritic cells, which in turn produce type I IFN-α. The presence of IFN-α combined with concomitant adenoviral infection of monocytes causes the monocytes to produce IL-18 and tumor necrosis factor (TNF). Together, these three cytokines ultimately drive the activation of MAIT cells. Their activation was required to maximize the production of $CD8^+$ T cells specific for the vector-encoded foreign antigen: for example, the spike protein for the ChAdOx1 nCoV-19 vaccine (see the figure). They found that MR-1–deficient mice (which lack MAIT cells) produce fewer antigen-specific $CD8^+$ T cells upon vaccination compared with wild-type mice. These data provide evidence that the purpose of viral sensing by MAIT cells is to improve the generation of antigen-specific $CD8^+$ T cells elicited by chimpanzee adenoviral vaccine vectors.

The observations of Provine *et al.* are expected to open the door to defining the mechanism by which MAIT cells subsequently promote the expansion of virus-specific $CD8^+$ T cells. This will involve dissecting which MAIT cell–mediated signaling pathways are required to promote the development of antigen-specific $CD8^+$ T cells. Understanding this mechanistic link will reveal fundamental communication mechanisms between innate and adaptive immune responses while also informing the design of future vaccines to maximally produce $CD8^+$ T cells.

High titers of antibodies specific for the spike protein are also elicited by the ChAdOx1 nCoV-19 vaccine, and data suggest that they correlate with protection (*10*, *12*, *14*, *15*). Thus, a future study could explore whether chimpanzee adenoviral vaccines also prime MAIT cells to promote humoral immunity. This would include the production of antigen-specific $CD4^+$ T cells and B cells that produce antibodies directed at a vaccine immunogen, such as the spike protein. Exploring whether the vaccinated wild-type mice produced higher titers of immunogen-specific antibodies when compared to MR-1–deficient mice would be an excellent follow-up experiment.

It would also be exciting to learn whether the role of MAIT cells described by Provine *et al.* is required to protect the host from disease-causing pathogens. Demonstrating that vaccine-mediated induction of MAIT cells maximizes the production of antigen-specific $CD8^+$ T cells only reflects vaccine

GRAPHIC: V. ALTOUNIAN/*SCIENCE*

immunogenicity. Whether MAIT cell activation positively correlates with the production of antibody and $CD8^+$ T cells in vaccinated and protected macaques could complement the immunogenicity studies that Provine *et al.* carried out with wild-type and MR-1–deficient mice.

Notably, macaque MAIT cell signaling and gene expression pathways were not explored, even though Provine *et al.* identified extensive similarities between these features of human and mouse MAIT cells. Macaques are valuable for studying the contributions of MAIT cells to lung immunity. They can be used to define whether adenoviral vector–based vaccines activate MAIT cells in the lungs, which may offer further insight into the immune correlates of protection from viruses, such as SARS-CoV-2.

It is tempting to speculate whether adenovirus-induced MAIT cell activation could offer more generalized protection from viral infections whose antigens are not present in the vaccine. Without knowing the duration of MAIT cell activation or the mechanism by which MAIT cells induce the expansion of antigen-specific $CD8^+$ T cells with these vaccines, it remains possible that MAIT cells have a nonspecific effect on augmenting antiviral immune responses systemically.

The findings of Provine *et al.* further unravel the complex nature of MAIT cells as an integral link between the innate and adaptive arms of the immune system. MAIT cells were originally thought to be an essential component for protecting a host from bacterial infections, but their role in viral infections has become evident (*2*–*4*). Future studies will need to explore whether this role of MAIT cells is required to induce long-lasting protective immunity. ■

REFERENCES AND NOTES

1. N. M. Provine *et al.*, *Science* **371**, 521 (2021).
2. J. E. Ussher, C. B. Willberg, P. Klenerman, *Immunol. Cell Biol.* **96**, 630 (2018).
3. B. van Wilgenburg *et al.*; STOP-HCV consortium, *Nat. Commun.* **7**, 11653 (2016).
4. B. van Wilgenburg *et al.*, *Nat. Commun.* **9**, 4706 (2018).
5. J. A. Juno *et al.*, *J. Immunol.* **202**, 2105 (2019).
6. A. L. Ellis *et al.*, *PLOS Pathog.* **16**, e1008585 (2020).
7. K. G. Lal *et al.*, *Nat. Commun.* **11**, 272 (2020).
8. S. B. Kennedy *et al.*; PREVAIL I Study Group, *N. Engl. J. Med.* **377**, 1438 (2017).
9. J. Sadoff *et al.*, *medRxiv* 10.1101/2020.09.23.20199604 (2020).
10. M. N. Ramasamy *et al.*; Oxford COVID Vaccine Trial Group, *Lancet* **396**, 1979 (2021).
11. N. B. Mercado *et al.*, *Nature* **586**, 583 (2020).
12. N. van Doremalen *et al.*, *Nature* **586**, 578 (2020).
13. F. J. D. Mennechet *et al.*, *Expert Rev. Vaccines* **18**, 597 (2019).
14. P. M. Folegatti *et al.*; Oxford COVID Vaccine Trial Group, *Lancet* **396**, 467 (2020).
15. K. McMahan *et al.*, *Nature* (2020). 10.1038/s41586-020-03041-6

10.1126/science.abf8121

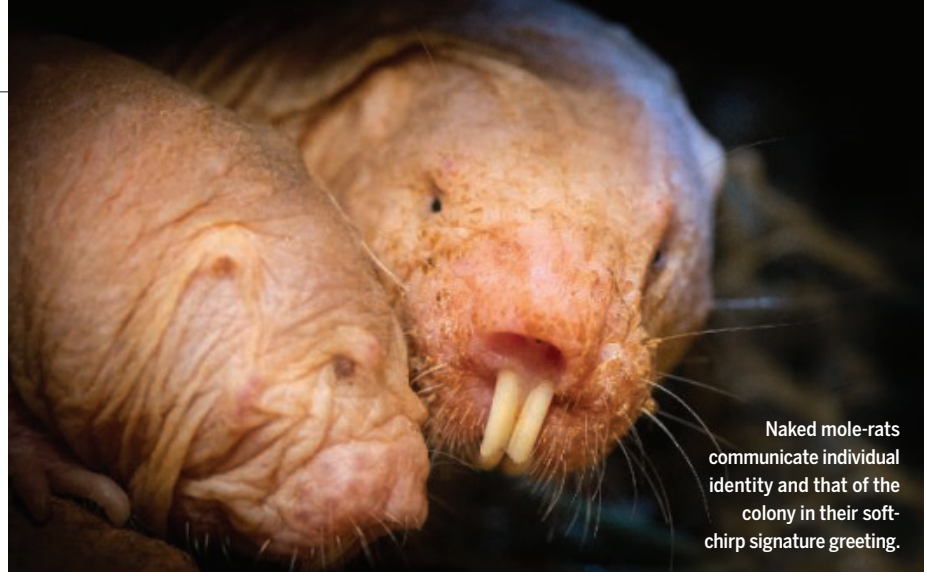

PHOTO: LORNA FAULKES

Naked mole-rats communicate individual identity and that of the colony in their soft-chirp signature greeting.

ANIMAL COMMUNICATION

Colony-specific dialects of naked mole-rats

Colony dialects are learned in early life but are modulated by the reigning queen

By **Rochelle Buffenstein**

Oral communication is an essential component of vertebrate social living. Even so, few animals are vocal learners. Rather, in most species vocalizations are instinctive, immutable, and genetically determined. Humans, whales, and songbirds are well-known exceptions, with elaborate language learned in early life using vocal mimicry, thereby creating distinctive geographic dialects or accents. These vocalizations nevertheless retain acoustic flexibility. On page 503 of this issue, Barker *et al.* (*1*) show that unlike other rodents, the almost blind, highly social, yet xenophobic, naked mole-rat has a colony-specific greeting—the soft chirp—that is learned in early life and facilitates recognition of colony members and thereby helps maintain colony cohesiveness. This soft-chirp signature appears to be modulated by the matriarch, or "queen." Should she die, or new colonies form by fission or outbreeding, after a period of acoustic variability the dialect once again becomes fixed and specific to the colony when a new queen is established.

Naked mole-rats are eusocial, subterranean rodents that live in socially hierarchical groups dominated by the queen. With the evolution of social living came the need to communicate effectively, thereby enabling group recognition, social organization, cooperative division of labor, and conflict avoidance. Similarly, elaborate communication systems are evident in eusocial insects—for example, the waggle dance of bees (*2*). Naked mole-rats, unable to rely on visual cues, have acquired a vocal repertoire (*3*, *4*) that conveys considerable information about the emitters—including size and social status, as well as their intentions. As Barker *et al.* observed, they have a distinctive, colony-specific soft chirp that is used when animals encounter each other in their underground maze. This voice-recognizing, colony-specific dialect is analogous to human regional and ethnic accents and/or dialects. The complexity of naked mole-rat vocalizations and responses suggests sophisticated cognitive comprehensive abilities, requiring intricate neural control and coordination of vocal motor structures and breathing.

Naked mole-rats are extremely xenophobic (*5*) and readily attack and kill animals from other colonies if they are mistakenly returned to a wrong colony in captivity (*6*); they likely respond similarly to intruders in the wild. This intolerance of foreign conspecifics assists in maintaining their unusual lifestyle that is heavily reliant on kin selection and altruistic behaviors (e.g., shared pickings from foraging bouts) for the needs of the entire colony. The colony-specific greeting enables mole-rats to recognize intruders immediately, and thereafter, elicit appropriate colony defenses. Alien recognition prevents colony

Calico Life Sciences LLC, 1170 Veterans Boulevard, South San Francisco, CA 94080, USA. Email: rbuffen@calicolabs.com

mixing, particularly foiling foreign males from mating with the queen and reducing genetic relatedness among colony members. Such xenophobic actions are a corollary of kin selection and concomitant altruistic behavior (*7*). Although vocal learning is an expensive trait, colony-identifying greetings are vital for their species fitness, survival, and colony cohesion.

Like human language, whale calls, and bird songs, the soft-chirp dialect appears to be learned, probably by vocal mimicry, and requires memorization of sensory inputs stored as an acoustic template and subsequently translated into template-matching vocal outputs (*8*). This is an astonishing feat for a rodent and is in stark contrast to the majority of mammalian vocalizations, which are innate, immutable, and genetically inherited (*9*). The colony-specific dialect, like that of human infants, is attained in early life by repeatedly hearing the sounds emitted by adults in the colony. Again, analogous to humans, there appears to be a critical period in which refinement of pup babbles can occur—a process requiring considerable practice to mold vocalizations until these precisely recapitulate adult sounds. Presumably, this life cycle–dependent, learned vocalization also reflects developmental changes in the anatomy of vocal and auditory tracts, as well as active sensory motor learning processes. It has been recently reported that in the wild, small colonies of naked mole-rats allegedly may invade neighboring colonies and "kidnap" young pups (*10*). Integrating this observation with the cross-fostering findings of Barker *et al.*, it is likely that these "enslaved" pups would learn the colony vocalizations of their captors. In turn, this would facilitate their acceptance into a genetically unrelated colony and thus expand its workforce by engaging them in burrow maintenance and food location, albeit at the expense of their own fitness (*10*). Although the colony-specific dialect is learned during the critical period of pup maturation, Barker *et al.* showed that dialects of fostered offspring may be slightly imperfect, suggesting that these were not accurately learned, possibly because learning may have started a little later in their life cycle.

Barker *et al.* observed that the naked mole-rat soft-chirp signature retains acoustic flexibility. The precise dialect of the colony is greatly influenced by the matriarch, whose chirps may be critical for indicating her continued presence, dominance, and suppression of reproduction in other colony members. This raises several interesting possibilities: Does her more precise chirp constantly retune and calibrate the dialect sound architecture through active template matching? More parsimoniously, could colony members be matching their dialect to the average sound features encountered within the colony environment? In this case, could the presence of the queen serve to restrict individual variability? Regardless, these possibilities would require sophisticated neural computations for sensorimotor processing and provide a detectable vocal signal of nonconformity. Dialect nonconformity by a particular individual within the colony might be met with intracolony conspecific aggression to uphold colony stability.

Only breeding males show considerable variability in the soft chirp. Although this may reflect a hormonal role in vocal plasticity, it is possible that this more varied chirp may contribute to mate selection by the queen and that she chooses the male she mates with on the basis of his beguiling voice, in much the same way that songbirds do (*11*). Should the queen die, colony vocalizations become less precise and the colony less cohesive, leading to dispersal or fights for reproductive dominance. Mole-rats modify their dialects when a new colony is formed, regardless of whether this is due to the rise of a new dominant female within an existing colony, colony fission, or pairing of unrelated individuals. Establishment of a new dialect distinguishes the newly formed colony as an independent, distinct social unit. Dialect plasticity highlights that memorization-based vocal learning can and does also occur in adults.

Barker *et al.* have revealed marked similarities between the learned, and complex vocalizations of naked mole-rats, songbirds, and humans, and many intriguing questions follow. For example, do these very disparate taxa all employ the same developmental trajectory, brain mechanisms, and regulatory genes to regulate vocal learning? Clearly such evolutionary convergence in learned vocalizations offers a valuable opportunity to decode the shared mechanistic and neurogenetic basis of vocal learning and get a little closer to understanding the origins of human language. ■

REFERENCES AND NOTES

1. A. J. Barker *et al.*, *Science* **371**, 503 (2021).
2. A. B. Barron, J. A. Plath, *J. Exp. Biol.* **220**, 4339 (2017).
3. K. Okanoya *et al.*, *J. Comp. Physiol. A Neuroethol. Sens. Neural Behav. Physiol.* **204**, 905 (2018).
4. S. Yosida, K. Okanoya, *Ethology* **115**, 823 (2009).
5. M. O'Riain, J. Jarvis, *Anim. Behav.* **53**, 487 (1997).
6. K. N. Lewis, R. Buffenstein, in *Handbook of the Biology of Aging*, M.R. Kaeberlein, G.M. Martin, Eds. (Academic Press, 2016), pp. 179–204.
7. T. Kay, L. Keller, L. Lehmann, *Proc. Natl. Acad. Sci. U.S.A.* **117**, 28894 (2020).
8. P. L. Tyack, *Philos. Trans. R. Soc. B* **375**, 20180406 (2020).
9. A. Nieder, R. Mooney, *Philos. Trans. R Soc. B* **375**, 20190054 (2020).
10. S. Braude *et al.*, *J. Zool.* 10.1111/jzo.12834 (2021).
11. J. H. Bruno *et al.*, *Annu. Rev. Linguist.* **7**, 10.1146/annurev-linguistics-090420-121034 (2021).

10.1126/science.abf7962

AGING

Targeting enzyme aging

Age-associated changes in enzyme activity drive aging in mice and are possible drug targets

By **Friedrich Becker**[1] *and* **K. Lenhard Rudolph**[1,2]

Therapeutic targeting of certain enzyme activities has been exploited to improve health at old age. These approaches have mainly focused on reducing damage-promoting metabolic and growth activities [such as by targeting mammalian target of rapamycin (mTOR)] or on the activation of damage-resolving mechanisms (for example, targeting sirtuins or autophagy). Additionally, however, there is emerging evidence that aging-associated alterations in enzyme activity per se can drive tissue and organism aging. On page 483 of this issue, Palla *et al.* (*1*) reveal that an aberrant activation of the prostaglandin-degrading enzyme 15-hydroxyprostaglandin dehydrogenase (15-PGDH) in aging muscle leads to impaired prostaglandin signaling, resulting in a reduced ratio of protein synthesis versus degradation and in the development of muscle atrophy (sarcopenia). Notably, inhibition of 15-PGDH restores prostaglandin signaling and prevents muscle atrophy in aged mice. These results support the concept that an aging-associated change to enzyme activity by itself represents a druggable, active contributor to tissue aging.

During organism aging, profound changes in enzyme activity occur (*2*), including changes in enzyme expression levels (*3*), conformational changes of enzymes through oxidative damage (*4*), decline in essential cofactors, such as nicotinamide adenine dinucleotide (NAD) (*3*), shifts in cellular or tissue pH (*5*), and the accumulation of molecules that inhibit enzyme activity (*6*). Some studies have shown that the reversal of aging-associated alterations in enzyme activities can improve cellular and organismal functions during aging. For example, replenishing aging-associated decrease of NAD, which is an essential

[1]Leibniz Institute on Aging–Fritz Lipmann Institute, Jena, Germany. [2]University Hospital Jena, Friedrich Schiller University, Jena, Germany.
Email: lenhard.rudolph@leibniz-fli.de

cofactor for mitochondrial enzymes and metabolic regulators such as sirtuins, rescues aging-associated decline in stem cell function and organ maintenance in aged mice (*7*). Similar effects were seen after inhibition of aging-associated increases in the expression of the NAD-degrading enzyme CD38 (*8*). Together, these studies provide experimental proof in mice that reversal of aging-associated changes in enzyme activity by repletion of an enzyme cofactor could be a viable strategy to ameliorate aging, which should be tested in further studies, including in humans.

Still, it remains poorly understood whether the aging-associated dysregulation of specific enzymes causally contributes to the decline in maintenance and regenerative capacity of distinct tissues during aging. Prostaglandin E_2 (PGE_2) is an extracellular signaling molecule derived from arachidonic acid in cell membranes. Cyclooxygenases and prostaglandin E synthases (PTGESs) convert arachidonic acid into PGE_2, which binds to cell surface receptors and activates intracellular signal transduction. To limit prostaglandin signaling, 15-PGDH degrades PGE_2. PGE_2-mediated signaling is an important activator of anabolic metabolism, which is essential for regeneration and stem cell function in various tissues, including skeletal muscle (*9*). Palla *et al.* delineated enzymatic reactions that control prostaglandin signaling in skeletal muscle of old versus young mice, hypothesizing that impairments in prostaglandin signaling could contribute to muscle aging. They found that aging-associated increases in the expression and activity of 15-PGDH are a causative factor for the development of skeletal muscle atrophy with age (see the figure).

Specifically, increased 15-PGDH activity reduces local PGE_2 availability in aging muscle, which leads to impairment of protein synthesis and induction of muscle atrophy–associated protein degradation by activation of E3-ubiquitin ligases, called "atrogenes." Targeting 15-PGDH activity with a selective inhibitor rescued PGE_2 signaling, induced protein synthesis, impaired the induction of atrogenes, and improved mitochondrial quality and function, thereby ameliorating muscle atrophy in aging mice. The authors show that the up-regulation of 15-PGDH activity in aging tissues occurs at the messenger RNA (mRNA) level. The transcription of *15-PGDH* is induced by c-Jun N-terminal kinases (JNKs) and the transcription factor complex activating protein 1 (AP1) (*10*). Two pathways that lead to JNK activation were implicated in driving the development of aging-associated muscle atrophy: the decline in testosterone signaling (*11*) and the activity of Tribbles homolog 3 (TRB3) (*12*). Of note, the reduction of JNK-AP1 activity either by *Trb3* deletion or by testosterone application ameliorates muscle atrophy in aging mice (*11, 12*). It is conceivable that 15-PGDH activity represents a downstream factor of these pathways inducing age-associated muscle atrophy.

It remains to be delineated whether aging-associated decline of NAD availability affects the activity of 15-PGDH, which is an NAD-dependent enzyme. Thus, aging-associated reduction of NAD may counteract transcriptionally driven increases in 15-PGDH expression during aging. However, replenishing NAD in aged mice improves muscle stem cell function (*7*), suggesting that the positive effects of NAD repletion on sirtuin 1 and mitochondrial metabolism outweigh possible negative effects of NAD on 15-PGDH activation.

Palla *et al.* provide important evidence that targeting an aging-associated dysregulation of a single enzyme can improve muscle maintenance. Delineating an atlas of aging-associated changes in enzyme activities, with respect to tissue-, cell-, and compartment-specific differences, could generate a basis for the development of future therapies to improve healthy aging across tissues. In this context, it could also be important to delineate aging-associated changes in the capacity of enzymes to react to stress. Early studies on aging-associated changes in enzyme activities documented that the response of enzymes to stress, such as nutrient starvation, is greatly attenuated during aging (*2*). Low levels of stress induce adaptive responses that improve cellular functions and protect the organism from age-associated functional decline. One of the most prominent examples is the increase in life expectancy across species by dietary restriction (*13*), which can also improve health parameters in humans. In nematode worms, dietary restriction requires the induction of stress signaling to mediate health benefits (*14*). Therefore, aging-associated defects in enzymatic stress responses could contribute to the failure of dietary restriction to reduce mortality when applied at old versus young age in mice (*13*).

Palla *et al.* provide a proof of concept that reversing aging-associated dysregulation of a single enzyme can ameliorate aging-associated muscle atrophy in mice. Next-generation inhibitors targeting 15-PGDH have been developed and should now be tested to reverse aging of muscle and other tissues affected by age-associated up-regulation of 15-PGDH activity (*1*, *15*). Given that enzyme activities can be targeted at multiple levels, the reversal of enzyme dysregulation in aging may have a high therapeutic potential. It is thus anticipated that an understanding of aging-associated enzyme activity changes will identify drivers of the aging process and will also accelerate the development of therapeutic approaches aiming to improve the maintenance of organ function and ameliorate the induction of aging-associated diseases. ■

Improving muscle maintenance

In aging mice, reduced testosterone concentrations and increased Tribbles homolog 3 (*Trb3*) expression induce c-Jun N-terminal kinases (JNKs) and activating protein 1 (AP1)–dependent transcription, which could contribute to age-associated up-regulation of 15-hydroxyprostaglandin dehydrogenase (15-PGDH) activity. This leads to degradation of prostaglandin E_2 (PGE_2) and impairment of muscle homeostasis, involving phosphorylated AKT (pAKT) and forkhead box O (FOXO).

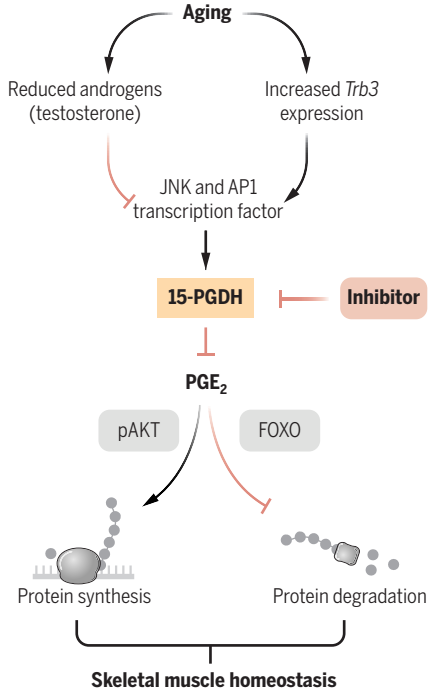

GRAPHIC: N. DESAI/*SCIENCE*

REFERENCES AND NOTES

1. A. R. Palla *et al.*, *Science* **371**, eabc8059 (2021).
2. R. C. Adelman, G. W. Britton, *Bioscience* **25**, 639 (1975).
3. C. C. S. Chini *et al.*, *Nat. Metab* **2**, 1284 (2020).
4. L. J. Yan, R. L. Levine, R. S. Sohal, *Proc. Natl. Acad. Sci. U.S.A.* **94**, 11168 (1997).
5. T. Wilms *et al.*, *PLOS Genet.* **13**, e1006835 (2017).
6. N. Sitte *et al.*, *FASEB J.* **14**, 1490 (2000).
7. H. Zhang *et al.*, *Science* **352**, 1436 (2016).
8. M. G. Tarragó *et al.*, *Cell Metab.* **27**, 1081 (2018).
9. Y. Zhang *et al.*, *Science* **348**, aaa2340 (2015).
10. J.-M. Park, H.-K. Na, *J. Cancer Prev.* **24**, 183 (2019).
11. E. L. Kovacheva *et al.*, *Endocrinology* **151**, 628 (2010).
12. G. K. Shang *et al.*, *J. Cachexia Sarcopenia Muscle* **11**, 1104 (2020).
13. O. Hahn *et al.*, *Nat. Metab* **1**, 1059 (2019).
14. T. J. Schulz *et al.*, *Cell Metab.* **6**, 280 (2007).
15. A. Desai *et al.*, *Haematologica* **103**, 1054 (2018).

ACKNOWLEDGMENTS

K.L.R. is funded by the German Research Foundation (DFG, CRC-PolyTarget, project B01).

10.1126/science.abf9566

VIEWPOINT: COVID-19

Lessons in antiviral immunity

Immune responses to SARS-CoV-2 reveal regulation and dynamics of lymphocytes

By **Jennifer L. Hope** and **Linda M. Bradley**

The adaptive branch of the immune system can kill virally infected cells and generate protective immune memory, which is the basis of vaccination strategies. Both T cell and B cell responses are important in controlling viruses and the development of immunity. However, the COVID-19 pandemic is revealing widely varying immune responses and diverse clinical outcomes with severe acute respiratory syndrome coronavirus 2 (SARS-CoV-2) infection, raising questions about how antiviral responses are orchestrated, factors that influence the longevity of immunological memory, and approaches that mediate robust protection from viral infections.

Viruses are responsible for many diseases, with effects on human health ranging from mild infections to those that are potentially fatal. Viruses infect host cells and then take over the cellular machinery to replicate and spread to susceptible cells. Viral infections, which can be localized or systemic, elicit innate immune responses (such as inflammation) that in turn activate the adaptive immune system. Viral proteins and particles are taken up by dendritic cells (DCs) that transport them into lymphoid organs, where they are specifically recognized by T and B cells. Ultimately, the cellular (T cell) and humoral (B cell) branches of adaptive immunity work together to enable highly specific defenses against diverse viruses with the following general features.

T cell recognition of viral peptides and B cell recognition of viral proteins both begin in lymphoid tissues, where DCs present peptides to T cells, and B cells sample viral proteins, together initiating the development of effector cells to eliminate the virus. The magnitudes of the T and B cell responses are determined by such factors as the pathogenicity of the virus, the extent of inflammation, the frequencies of virus-specific T and B cells, and the kinetics of viral replication. $CD8^+$ T cells differentiate into effector cells that limit viral replication through production of cytokines and direct killing of infected cells. For $CD4^+$ T cells, viral recognition elicits cytokine-producing effector cells, such as T helper 1 (T_H1) cells, which inhibit viral replication and support $CD8^+$ T cell as well as B cell differentiation. Effector T cells can enter the circulation and relocate to tissue sites of infection, where they mediate local antiviral responses. $CD4^+$ T cells also differentiate into T follicular helper (T_{FH}) cells that are crucial for the development of antibody-producing B cells (plasma cells) in lymphoid tissues and support memory B cell development. Antibodies can neutralize viruses by preventing host cell entry or promoting the lysis of infected cells. As a result of the coordinated interplay of innate and adaptive responses, the peak T and B cell responses lead to decreasing viral load (see the figure) and subsiding inflammation, often within 1 week of infection.

After viral clearance, the majority of effector T and B cells contract and die. Small pools of resting memory T cells form while persisting B cells generate either long-lived antibody-producing plasma cells or resting memory B cells. These heterogeneous memory cell populations are capable of rapid responses upon reinfection. Virus-specific T cells responding when viral titers are high can retain effector properties as memory cells (effector memory cells), whereas those responding as a viral infection becomes contained typically generate memory cells with a capacity for self-renewal (central memory cells) that serve as a reservoir for protection during future reinfections. T cells located in sites of infection can become specialized tissue-resident memory (T_{RM}) cells. However, when adaptive immune responses to infection are suboptimal or a virus has evolved means to evade immune responses (including the induction of host immune suppression), chronic infection or widespread illness and death can ensue, especially in at-risk individuals. SARS-CoV-2 infection demonstrates varied disease severity and highlights the need for greater understanding of the factors that determine effective adaptive immune responses and long-lasting protective immunity, particularly in vulnerable populations, such as older people or immunocompromised individuals.

A key factor in eliminating virus infections is whether robust, high-affinity T and B cell antiviral responses are elicited. Naïve T and B cell pools demonstrate a wide range of viral recognition due to the highly diverse T cell receptor (TCR) and B cell receptor (BCR) repertoires established during cellular development. Clones with high-affinity TCRs are selected during infection because of their greater ability to bind viral peptides. By contrast, BCR affinity continues to increase for viral proteins over the course of infection through the processes of somatic hypermutation and clonal expansion. Additionally, B cells undergo antibody class switching from early immunoglobulin M (IgM) production to higher-affinity IgG and IgA subtypes, which have specialized immune functions and are all detected in the sera of convalescent COVID-19 patients. The magnitude of early antibody responses may be indicative of the severity of infection, because higher IgM and IgG antibody titers are associated with more severe disease (*1*). Similar to other viral infections, the overall serum titers of SARS-CoV-2–specific antibodies wane following clearance of the active infection. However, long-lived memory B cells can remain and produce circulating, virus-neutralizing antibodies. A recent study showed that 6 to 8 months after COVID-19 disease onset, SARS-CoV-2 neutralizing antibodies were found in 90% of recovered patients (*2*). It is also important to track and compare the duration of memory B cell responses from natural SARS-CoV-2 infection and from vaccines.

Adaptive immune responses to viruses can also be influenced by the history of previous virus encounters. For example, T_{RM} cells residing in the lungs can recognize conserved internal structural proteins of influenza viruses and subsequently can reduce the severity of infection by new strains of influenza virus (*3*). T cells reactive to SARS-CoV-2 proteins have been detected in individuals previously infected with SARS-CoV and in nonexposed healthy individuals (*4*, *5*). These findings indicate that memory T cells are generated by infections with other human coronaviruses (HCoVs), including "common cold" coronaviruses. Similarly, IgG antibodies from COVID-19 patients were found to strongly react to proteins conserved among common cold HCoVs. Conversely, SARS-CoV-2–reactive antibodies specific for conserved HCoV proteins were detected in sera from people who had not had COVID-19 (*6*); these may be broadly neutralizing antibodies. It is not yet clear whether these preexisting SARS-CoV-2–reactive T and B cells can contribute to better disease outcomes. If they can, their high reactivity suggests that it may be desirable to expand such T and B cell populations through vaccination.

The extent of infection and inflammation engendered by viruses, including SARS-CoV-2, is important because excessive in-

Tumor Microenvironment and Cancer Immunology Program, NCI-Designated Cancer Center, and Immunity and Pathogenesis Program, Infectious and Inflammatory Diseases Center, Sanford Burnham Prebys Medical Discovery Institute, La Jolla, CA 92037, USA.
Email: lbradley@sbpdiscovery.org

nate immune responses, such as hyperinflammation [increased interleukin-6 (IL-6) and C-reactive protein], can promote pronounced T cell activation that further amplifies inflammation and disease severity (*7*). Extensive T cell activation during COVID-19 can lead to lymphopenia (reduced numbers of lymphocytes), altered subset differentiation, and loss of function, which together can limit viral clearance, prolong infection, and increase morbidity (*8*). SARS-CoV-2–specific $CD4^+$ and $CD8^+$ T cells are detectable in circulation in both actively infected and recovered patients, revealing the potential capacity for the development of protective cell-mediated immunity (*7*, *8*).

Differences in the magnitude and breadth of individual adaptive immune responses to SARS-CoV-2, and correlations with patient morbidity, highlight the need to identify factors that predict disease severity. It remains unclear why some infected individuals are asymptomatic whereas others experience severe COVID-19 symptoms. The underlying factors that promote resolution of infection are still unknown, as is the extent of residual pathology. Our current understanding of the immune correlates of disease severity is limited by sample size and diverse patient study populations, but some factors—such as impaired type I interferon innate immune responses (*9*), or cytomegalovirus (CMV) and herpes simplex virus 1 (HSV-1) seropositivity (*6*)—are beginning to be linked to severe COVID-19.

Factors such as gender and age must also be considered, because men hospitalized with COVID-19 have stronger antibody responses and increased disease severity compared to women hospitalized with COVID-19 (*6*). In older individuals (>65 years), who have the greatest risk for severe disease, dysregulated adaptive responses were more often observed during acute SARS-CoV-2 infection than in younger individuals (*10*). Early differences in antibody profiles for the SARS-CoV-2 spike protein (S) versus its nucleocapsid protein (N) tended to predict mild or severe disease, respectively, further underscoring the importance of the specificity of the humoral response for viral control (*11*). By contrast, robust T cell responses against S, N, and the membrane protein (M) were not associated with better recovery in critically ill COVID-19 patients (*12*). The possibility of identifying predictive factors would be enhanced by the inclusion of SARS-CoV-2–infected asymptomatic individuals.

There remains uncertainty as to whether some SARS-CoV-2–specific adaptive responses can be detrimental. Although clinical validation is needed, recent TCR and BCR repertoire profiling of active and convalescent COVID-19 patients defined signatures associated with disease severity (*7*, *13*). In actively infected patients, highly mutated BCRs and decreased clonal expansion were associated with more severe clinical outcomes, whereas a larger pool of virus-specific naïve B cells in patients correlated with the development of a more effective antiviral immune response (*7*). Enhanced T_H1 differentiation, loss of the T_{FH} compartment, and associated lack of germinal center formation were recently observed in postmortem analysis of lymph nodes and spleens from patients who rapidly succumbed (within 10 days of respiratory symptom onset) to COVID-19 (*14*). Altered proportions of peripheral blood $CD4^+$ T cell subsets, $CD8^+$ T cell activation status, and B cells have also been observed in patients across a broad spectrum of disease severity. In-depth analysis of ~200 immune parameters revealed that disease severity, including severe inflammation and organ failure, correlated with overall lymphopenia (likely due to multifactorial immune dysregulation), with the remaining lymphocytes reflective of highly activated (and potentially hyperactivated) $CD4^+$ and $CD8^+$ effector T cells, low $CD4^+$ T_{FH} cells, and antibody-producing plasmablasts (short-lived plasma cells) expressing the transcription factor T-bet (*15*).

The underlying determinants of diverse responses to SARS-CoV-2 remain unclear. One potential avenue for future investigation is to evaluate whether prior infection by other respiratory infections, or preexisting immune-mediated conditions such as asthma, may enhance susceptibility to SARS-CoV-2 infection. Most studies evaluating adaptive responses to SARS-CoV-2 infection have analyzed infected adults, whereas such studies in children are more limited. Understanding differences in adaptive immune responses between children and adults is an important concern with respect to SARS-CoV-2 because children appear to be less at risk for severe respiratory complications compared to adults, yet they can develop a life-threatening multisystem inflammatory syndrome. This may reflect altered virus recognition by the immune system in children: A recent study comparing antibody specificity in adults and children with SARS-CoV-2 infection observed reduced antibody diversity in children and a skewed response toward S-protein–specific IgG antibodies (*1*). Studies evaluating the adaptive immune response, clarifying the interplay between T and B cells as well as innate immune responses, and determining correlates of protection will be key to developing strategies aimed at establishing or boosting T and B cell antiviral immunity. ■

Adaptive immune responses to viral infections

Adaptive immune responses control and eliminate viral infections that have outpaced innate immune control. Days after infection, virus-specific cytotoxic $CD8^+$ T cells migrate to the site(s) of infection, where they kill virally infected cells. Early-responding B cells produce and release virus-specific immunoglobulin M (IgM) antibodies; $CD4^+$ T helper cells promote class-switching of germinal center B cells from IgM to IgG or IgA virus-specific antibody production. After virus clearance, a pool of memory IgG/IgA B cells and T cells remain (virus-specific memory) and are rapidly reactivated upon reinfection with the same virus. Vaccination aims to generate protective adaptive immune memory without the need for a bona fide primary infection.

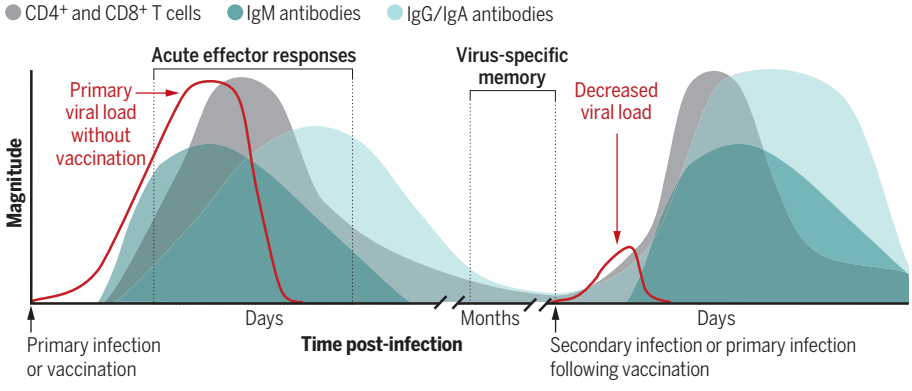

GRAPHIC: N. CARY/*SCIENCE*

REFERENCES AND NOTES

1. S. P. Weisberg *et al.*, *Nat. Immunol.* **22**, 25 (2021).
2. J. M. Dan *et al.*, *Science* **371**, eabf4063 (2021).
3. I. Uddbäck *et al.*, *Viral Immunol.* **33**, 201 (2020).
4. A. Grifoni *et al.*, *Cell* **181**, 1489 (2020).
5. N. Le Bert *et al.*, *Nature* **584**, 457 (2020).
6. E. Shrock *et al.*, *Science* **370**, eabd4250 (2020).
7. C. Schultheiß *et al.*, *Immunity* **53**, 442 (2020).
8. Z. Chen, E. J. Wherry, *Nat. Rev. Immunol.* **20**, 529 (2020).
9. Q. Zhang *et al.*, *Science* **370**, eabd4570 (2020).
10. C. Rydyznski Moderbacher *et al.*, *Cell* **183**, 996 (2020).
11. C. Atyeo *et al.*, *Immunity* **53**, 524 (2020).
12. C. J. Thieme *et al.*, *Cell Rep. Med.* **1**, 100092 (2020).
13. L. Kuri-Cervantes *et al.*, *Sci. Immunol.* **5**, eabd7114 (2020).
14. N. Kaneko *et al.*, *Cell* **183**, 143 (2020).
15. D. Mathew *et al.*, *Science* **369**, eabc8511 (2020).

10.1126/science.abf6446

VIEWPOINT: COVID-19

Insights from SARS-CoV-2 sequences

Analysis of viral sequences can tell us how SARS-CoV-2 spreads and adapts

By **Michael A. Martin[1,2], David VanInsberghe[1], Katia Koelle[1,3]**

As severe acute respiratory syndrome coronavirus 2 (SARS-CoV-2) has spread across the globe, so have efforts to sequence its RNA genome. More than 260,000 sequences are now available in public databases, about a year after the viral genome was first sequenced (*1*). These sequences and their associated metadata have allowed researchers to estimate the timing of SARS-CoV-2 spillover into humans, characterize the spread of the virus, and gauge virus adaptation to its new host. Such analyses rely on interpreting patterns of nucleotide changes that have occurred in the virus population over time and are brought into focus through the reconstruction of genealogical relationships between sampled viruses that are depicted in phylogenetic trees.

Analysis of phylogenetic trees allows for conclusions to be drawn about epidemic and pandemic viruses that are important for public health (see the figure). After the emergence of a new virus, viral sequence data and sampling dates can be used to infer the rate at which the virus population evolves, along with the time of the most recent common ancestor (TMRCA) of all sampled viruses. For SARS-CoV-2, these analyses have revealed that the virus evolves at a rate of ~1.1×10^{-3} substitutions per site per year (*2*)—corresponding to one substitution every ~11 days—and a TMRCA of around late November 2019. However, owing to limited sampling early in the COVID-19 outbreak, this date likely lags behind the spillover into humans by several weeks.

Once virus circulation becomes widespread, phylodynamic analyses can give insight into how a virus spreads both spatially and temporally. Viruses from a given region can be placed in the context of those circulating globally, allowing for the number of independent virus introductions into a region to be estimated through phylogeography. These methods rely on assigning geographical states to unsampled ancestral viruses through a process called ancestral state reconstruction. Multiple applications of this approach have consistently shown that regional SARS-CoV-2 spread was ignited not by one, but by many independent introductions. This is likely due to slow or imperfect implementation of screening efforts at borders in the early stages of the pandemic. Similar types of analyses are conducted in local outbreak investigations, in what is often called genomic epidemiology. This has been used, for example, to link multiple transmission chains to a motorcycle rally in South Dakota (*3*).

Care must be taken, however, when interpreting phylogeographic analyses of this virus owing to the limited extent of its circulating genetic diversity. Given the evolutionary rate of SARS-CoV-2, viruses sampled weeks apart on different continents can have identical nucleotide sequences, making robust inferences more challenging. Additionally, sampling efforts are geographically heterogeneous, which can bias phylogeographic analyses. Methods have recently been developed to better accommodate the degree of undersampling across regions and the known travel history of sampled cases (*4*). Application of these methods has shown that later, rather than earlier, virus introductions established the first sustained transmission networks in the United States and Europe (*5*), highlighting the utility of genomic data in epidemiological investigations.

Once viral lineages have been introduced into a region, phylodynamic methods can also be used to infer the rate of viral spread through a host population and the basic reproduction number R_0, defined as the average number of infections generated by an infected host in a susceptible host population. This inference can be done using coalescent-based methods, which infer changes in the underlying population size of infected individuals using the time points at which viral lineages "coalesce" (merge) backward in time. Epidemiological models can also be fit directly to viral phylogenies based on the timing of coalescent events (*6*). Another approach to infer R_0 from sequence data relies on a forward-in-time birth-death process, with a "birth" corresponding to a transmission event (resulting in the birth of an infected individual) and a "death" corresponding to a removal of an infected individual (*7*). Both methods have been applied to SARS-CoV-2 sequence data, with relatively consistent results across methods and regions: At the beginning of the pandemic, R_0 fell between 2 and 3.5 (*8*, *9*) but decreased substantially after the implementation of nonpharmaceutical interventions. Although R_0 can be, and usually is, estimated from epidemiological case data, these estimates can be biased by changes in reporting rates. The relative contributions of new introductions versus local spread are often also indistinguishable in tabulated case data. Thus, analysis of sequence data provides an alternative approach to infer R_0 that may be particularly useful in the early stages of virus circulation when a large proportion of identified cases may be new introductions and when reporting rates are likely to be low. The development of methods that integrate both epidemiological time series and sequence data is an area of active research that will improve parameter estimation.

Phylodynamic analyses can also be used to identify instances of viral adaptation. Adaptation is a particular concern because SARS-CoV-2 only recently spilled over into humans and thus may still adapt to its new host through substitutions that facilitate its spread. One emerging variant that has been implicated as being more transmissible is 614G, which replaces aspartic acid (D) with glycine (G) at amino acid site 614 in the cellular entry (spike) protein of SARS-CoV-2. This variant likely arose in China in January 2020 and has since become dominant worldwide. The D-to-G substitution results in more efficient infection and replication in vitro and enhances transmission in animal models (*10*). Coalescent-based phylodynamic analyses using densely sampled genomes from infections in London found trends toward higher transmissibility of 614G clusters relative to 614D clusters (*11*). More recently, a new SARS-CoV-2 lineage, B.1.1.7, has rapidly spread from southeast England around the globe, and early analyses indicate that it has a substantial fitness advantage over other currently circulating lineages. These recent evolutionary events indicate that SARS-CoV-2 still has the capacity to develop more efficient transmission between human hosts.

When considering viral adaptation, a commonly held fear is that a virus may evolve to become more virulent, that is, cause more severe disease and host mortality. However, natural selection acts on variation in viral transmission potential, not variation in virulence per se. More virulent strains could have

[1]Department of Biology, Emory University, Atlanta, GA, USA. [2]Population Biology, Ecology, and Evolution Graduate Program, Laney Graduate School, Emory University, Atlanta, GA, USA. [3]Emory–University of Georgia Center of Excellence for Influenza Research and Surveillance (CEIRS), Atlanta, GA, USA. Email: katia.koelle@emory.edu

higher transmission potential if infection with a more virulent strain resulted in infected hosts shedding more virus. However, a more virulent infection may reduce contact rates of infected individuals, limiting the opportunity for viral transmission. Therefore, it is not clear whether more virulent SARS-CoV-2 strains are likely to evolve.

As SARS-CoV-2 continues to spread, the virus will begin to face new evolutionary pressures. Other respiratory viruses can provide insight into how SARS-CoV-2 evolution may manifest. For example, the 2009 pandemic H1N1 influenza virus started to evolve antigenically a couple of years after its emergence (*12*) and recent work has identified signatures of adaptive evolution in the spike protein of seasonal coronaviruses, consistent with antigenic evolution (*13*). Emerging evidence suggests that some SARS-CoV-2 variants may already be exhibiting antigenic evolution, and this is likely to continue as population immunity (through natural infection or vaccination) builds. Efforts by public health agencies to monitor emergent SARS-CoV-2 lineages, particularly those that may escape vaccine or natural immunity, are under way. Additionally, widespread infection of farmed mink has recently been observed, and there is evidence of transmission of mink lineages back into humans (*14*). Animal reservoirs may therefore contribute to the dynamics of SARS-CoV-2 evolution and adaptation.

For viral adaptation to be possible, be it through the evolution of immune escape or other viral traits, genetic (and phenotypic) variation needs to be present. Although nucleotide substitutions are the primary source of genetic variation in SARS-CoV-2, insertions and deletions of nucleotides have also been observed. Furthermore, recombination is common in coronaviruses and may potentially give rise to new SARS-CoV-2 lineages. A small number of SARS-CoV-2 recombinant genomes have already been detected (*15*). Because of their potential phenotypic effects, circulation of genomic insertions, deletions, and recombinants should be monitored.

The number of available SARS-CoV-2 sequences is, like many things during this pandemic, unprecedented. Gaining understanding from these data does not come without challenges. Many current methods rely not just on the sequence itself but on associated metadata that provide additional information about viral samples. Research laboratories are often limited in the metadata that can be released owing to patient privacy regulations. For similar reasons, some government health agencies, such as the U.S. Centers for Disease Control and Prevention (CDC), receive only limited metadata from state health departments. Although privacy is an important concern, the routine release of more detailed metadata would improve the power of phylodynamic methods to describe viral dynamics and evolution. Notably, sequences are often released with only coarse sampling location data. However, viral dynamics may be heterogeneous even between locations that are geographically close. Furthermore, the incorporation of travel history can improve the accuracy of phylogenetic methods (*4*), but this information is not commonly reported. Because phylodynamic methods often require an assumption of random sampling, when samples from individuals belonging to the same transmission chain are sequenced, it is crucial that this information be labeled in the sequence metadata to avoid biasing analyses. Despite these challenges, a tremendous amount of SARS-CoV-2 sequence data is publicly available on GISAID's EpiCov database. Phylogenetic analyses of these sequences are conducted in near–real time and available on platforms such as Nextstrain and Microreact, allowing the ongoing evolution of SARS-CoV-2 genomes to be viewed in detail.

In many ways, the SARS-CoV-2 pandemic offers a distinct opportunity for the field of phylodynamics. Methods development over the past 10 to 15 years, the widespread availability of sequencing technologies, open data sharing, and the tireless efforts of clinicians and scientists who collect these data mean that more can be learned from viral genomes than ever before. As viral diversity continues to accumulate, SARS-CoV-2 sequence data and associated metadata can be used to answer questions focused on the longer-term evolution and adaptation of SARS-CoV-2. The volume of sequence data also presents an opportunity for methods development, because most current methods are computationally intractable when applied to hundreds of thousands of genomes. Continued efforts to collect viral sequence data and the development of efficient and scalable computational inference methods will help to further cement evolutionary analyses as a cornerstone of the public health response to viral spread and adaptation. ■

Uses for viral sequence data

Viral phylogenies, rooted at the most recent common ancestor (TMRCA), are inferred on the basis of genetic differences. These phylogenies can be used to estimate viral emergence, characterize the geographic spread of the virus, reconstruct epidemiological dynamics of viral spread within a region, and identify instances of adaptation.

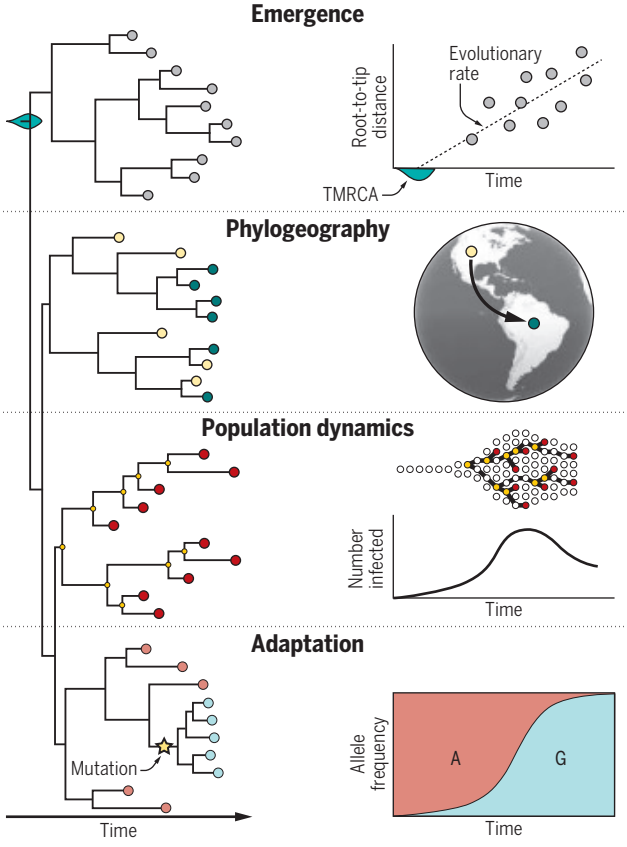

GRAPHIC: A. KITTERMAN/*SCIENCE*

REFERENCES AND NOTES

1. F. Wu *et al.*, *Nature* **579**, 265 (2020).
2. S. Duchene *et al.*, *Virus Evol.* **6**, veaa061 (2020).
3. M. J. Firestone *et al.*, *MMWR* **69**, 1771 (2020).
4. P. Lemey *et al.*, *Nat. Commun.* **11**, 5110 (2020).
5. M. Worobey *et al.*, *bioRxiv* 10.1101/2020.05.21.109322 (2020).
6. E. M. Volz, I. Siveroni, *PLOS Comput. Biol.* **14**, e1006546 (2018).
7. T. Stadler *et al.*, *Mol. Biol. Evol.* **29**, 347 (2012).
8. D. Miller *et al.*, *Nat. Commun.* **11**, 5518 (2020).
9. S. A. Nadeau *et al.*, *medRxiv* 10.1101/2020.06.10.20127738 (2020).
10. Y. J. Hou *et al.*, *Science* **370**, 1464 (2020).
11. E. Volz *et al.*, *Cell* **184**, 64 (2021).
12. Y. C. F. Su *et al.*, *Nat. Commun.* **6**, 7952 (2015).
13. K. E. Kistler, T. Bedford, *bioRxiv* 10.1101/2020.10.30.352914 (2020).
14. B. B. Oude Munnink *et al.*, *Science* **371**, 172 (2021).
15. D. VanInsberghe *et al.*, *bioRxiv* 10.1101/2020.08.05.238386 (2020).

ACKNOWLEDGMENTS

This work was supported by National Institute of Allergy and Infectious Diseases (NIAID) Centers of Excellence for Influenza Research and Surveillance (CEIRS) grant HHSN272201400004C and an Emory University MP3 seed grant. We thank G. Armstrong, T. Bedford, and two anonymous reviewers for feedback.

10.1126/science.abf3995

POLICY FORUM

FINANCE AND ENVIRONMENT

China can help solve the debt and environmental crises

China could implement debt-for-nature and debt-for-climate swaps to protect the environment and reduce global debt

By **B. Alexander Simmons, Rebecca Ray, Hongbo Yang, Kevin P. Gallagher**

Many developing countries are experiencing mounting external debt distress owing to the economic consequences of COVID-19. G20 Finance Ministers were swift to adopt the Debt Service Suspension Initiative (DSSI) in 2020, suspending bilateral debt payments through July 2021 for 73 low-income countries. Globally, Chinese government–sponsored banks have emerged as the largest bilateral creditors (*1*). For the 46 participating DSSI countries thus far, payments due to China constitute 68% ($8.4 billion) of all official bilateral payments originally due by the end of 2020 (*2*). G20 countries have now come to realize that they will need to go beyond debt suspension to include the cancellation of some portion of debt. Without substantial debt relief, developing countries will face pressure to exploit natural capital to pay short-term debt, placing conservation and climate change ambitions aside. It is therefore of paramount importance to align debt restructuring efforts with climate, biodiversity, and development goals. Although China has only recently become a major creditor, it has already built a strong record of bilateral debt relief and has begun to advocate for linking biodiversity, climate change, and international finance (*3*). Here, we conduct an exploratory analysis of opportunities for China to alleviate debt burdens in exchange for debtor nation commitments to climate change mitigation and/or adaptation and environmental protection through "debt-for-climate" and "debt-for-nature" swaps.

China's two "policy banks" that operate abroad—the China Development Bank and the Export-Import Bank of China—have committed $464 billion in finance to governments around the world since 2008, only $3 billion of which has gone to high-income countries (*4*). Many countries with substantial debt exposure to China are increasingly vulnerable to tension between the priorities of economic recovery, public health, and environmental protection. Without immediate action to tackle this debt crisis, developing countries will have to service external debt payments at the expense of fighting the virus, protecting vulnerable communities, and honoring sustainability commitments. These low- and lower-middle-income countries are more vulnerable to the impacts of climate change (*5*) and have lost two to five times more intact landscapes since 2000 compared with upper-middle- and high-income countries (*6*). Unsustainable long-term recovery strategies further jeopardize climate change mitigation and biodiversity conservation in these countries.

THE PROMISE OF CHINESE DEBT SWAPS

Debt swaps are quickly becoming part of the international dialogue surrounding innovative approaches to achieving climate change mitigation and biodiversity conservation targets amid the COVID-19 economic crisis (*7*, *8*). Early debt-for-nature efforts, where organizations and/or government creditors negotiated with government debtors to cancel or reduce debts in return for binding commitments to achieve conservation targets (*9*), focused on low-hanging fruit, where debt was cheap on the secondary markets and enforcement was limited. Contemporary debt-for-nature swaps establish funds to ensure investment over longer periods of time, greater involvement of numerous stakeholders, and sufficient enforcement. New frontiers of debt restructuring continue to emerge that envision debt swaps for "nature performance bonds" or "green recovery bonds" that link economic activity to environmental performance. Incentive-based climate mitigation and adaptation strategies—like the emerging debt-for-climate swaps—will also be necessary for reducing countries' contributions and vulnerability to climate change. Given that the mantra for the response to the COVID-19 economic crisis has been to do "whatever it takes," serious consideration of debt-for-nature or climate swaps is warranted as part of the COVID-19 global economic toolkit.

With China's emergence as the world's largest source of bilateral credit, it has come under scrutiny in some quarters for creating "debt traps" in developing countries, supposedly seeking to saddle borrowers with massive debt to increase political leverage. Yet this perception is in contrast to empirical evidence of China's history in lending and debt relief (*10*). Across Africa—where China has a long history with sovereign lending—China has frequently engaged with various forms of bilateral debt relief (*11*), including additional promises during the 2020 Extraordinary China-Africa Summit on Solidarity Against COVID-19. China also joined the DSSI in 2020, marking its first participation in any multilateral debt relief effort, and it is currently the largest single contributor to the DSSI. To date, China has not engaged in debt-for-nature or debt-for-climate swaps, but as a pioneer of green bonds, the country is now considering including these swaps in their policy toolkit (*8*).

To maximize return on investment, countries participating in debt swaps could jointly target debt relief, conservation, and climate mitigation and/or adaptation (*7*, *12*). Of 87 low- to middle-income countries that received more than $25 million in development finance commitments from China's two policy banks since 2008 (*4*), we identify 25 countries under the greatest possible Chinese debt stress; we define these as countries whose Chinese development finance commitments constitute more than 4.80% (median) of their most recent gross domestic product (GDP) (*4*) and whose total outstanding external debts constitute more than 38.47% (median) of their GDP. We also considered payments due for 62 DSSI countries and identify the 27 countries at greatest risk of defaulting on China payments due in 2020, defined as countries whose China payments constitute more than 51.30% (median) of all bilateral payments due in 2020 and more than 13.17% (median) of all external (bilateral and multilateral) payments due in 2020 (*2*). In total, Chinese debts were considered for 102 countries, and 41 low- and middle-income countries met one or both indicators of substantial Chinese debt concern (fig. S1), representing up to $179 billion in maximum Chinese debt and $9.7 billion in payments originally due by the end of 2020 [see supplementary materials (SM) for country-level data].

Traditionally, debt-for-nature swaps target reducing deforestation and protecting threatened species (*9*), and debt-for-climate

Global Development Policy Center, Boston University, Boston, MA, USA. Email: blakeas@bu.edu

swaps can target climate change mitigation and/or adaptation strategies (*7*). To gauge the prominence of these respective threats for debt-stressed countries, we score the 41 countries on two climate threat metrics (average annual carbon emissions and climate vulnerability) and two biodiversity threat metrics (threatened species density and annual tree cover loss) (fig. S2). Scores for each metric are distinguished as relatively "high threat" (1 point) or "low threat" (0 points) based on the median of all 102 low- and middle-income countries considered in this analysis (see SM for data sources and calculations).

Recent studies have considered countries' "creditworthiness" (*7*) and implementation or management costs (*12*) as barriers in debt swap opportunities. Here, we take a more direct and globally comparative approach to estimate opportunities for success, based on climate commitments and natural capital. Under the Paris Climate Agreement, several countries have proposed ambitious nationally determined contributions (NDCs) for renewable energy (*13*), and high debt stress may jeopardize these commitments. We consider countries whose renewable energy investment costs (associated with their existing NDC commitments) are more than 5.50% (median) of their GDP to have greater opportunity for success in meeting the terms of debt-for-climate swaps, because they may have stronger political will for climate action. Given the rapid decline of intact landscapes in developing countries and the frequency with which protected areas have been key features of traditional debt-for-nature swaps, we consider countries with more than 78.39% (median) of remaining intact lands currently unprotected to have greater opportunity for implementing traditional debt-for-nature swaps. We add an additional point to countries' climate and/or biodiversity threat scores if they have greater debt swap opportunity, for a total score ranging from 0 to 3 for debt-for-climate and debt-for-nature potential (see the figure and SM).

GLOBAL OUTLOOK

Several countries under greatest China debt stress show great promise for debt-for-nature and debt-for-climate swaps. Angola, Cambodia, Myanmar, and the Solomon Islands score highest across simultaneous climate and biodiversity threats and opportunities (see the figure). Angola—where China has extended a total of $29.6 billion (31% of GDP) in finance commitments—could greatly benefit from debt-for-climate swaps incorporating both climate mitigation and adaptation initiatives, freeing up capital for their $15.7 billion commitment to renewable energy investments. In addition, nearly 91% of Angola's remaining intact areas are unprotected, providing an opportunity for debt-for-nature swaps to protect these landscapes and reduce relatively high rates of tree cover loss. Cambodia ($5 billion in China finance commitments) faces similar potential benefits, but the majority of its intact landscapes (84%) are already under protection, limiting the opportunity to find suitable locations to efficiently and ethically implement traditional debt-for-nature swaps.

For countries like Senegal, Sudan, and Zimbabwe, where carbon emissions and climate vulnerability are high and renewable energy commitments span 15 to 39% of their GDP, debt-for-climate swaps could be prioritized to simultaneously reduce carbon emissions and facilitate investment in building climate-resilient communities. By contrast, debt-for-nature swaps show greater promise for smaller countries like Fiji and Togo. These nations with a smaller carbon footprint have some of the highest concentrations of threatened species and minimal existing protection of their remaining intact landscapes. Together, these two countries owed China $58 million by the end of 2020—a relatively small figure compared with most other debt-stressed countries; such small debt-for-nature investments could serve as lower-risk pilot programs and lead to positive biodiversity outcomes.

LEAD BY EXAMPLE

Debt swaps provide both practical and reputational incentives for China. Many of China's debtors will not be able to repay the full amount of their debt, which could leave China with stranded assets across the globe. Restructuring would simultaneously help countries recover from the pandemic and increase the likelihood that the remainder of the debt will be repaid. Furthermore, the implementation of debt swaps could allow China to still receive something in return in terms of reputation (e.g., favorable political scores, evidence of investing in the public good). As China is set to host the Conference of the Parties (COP) to the Convention on Biological Diversity (CBD) in 2021, opportunities abound to advance debt swap mechanisms and lead by example in the post-2020 era of conservation. China has also pledged to be carbon neutral by 2060; as the "Rule Book" for Article 6 of the Paris Climate Agreement becomes clearer, China and other creditors may even be able to obtain "credits" for such swaps moving forward.

Because biodiversity and climate change are intrinsically linked, debt swaps should be designed to maximize dual benefits to

A promising avenue for debt-stressed countries

An assessment of the potential for debt-for-nature and debt-for-climate swaps in countries under greatest China debt stress is shown. The relative potential for debt-for-nature and debt-for-climate swaps based on threats and opportunity for implementation, with maximum (max.) total China debts and China payments due in 2020, is highlighted for select countries (see supplementary materials for data and calculations). Countries under lower China debt stress (light gray) are excluded.

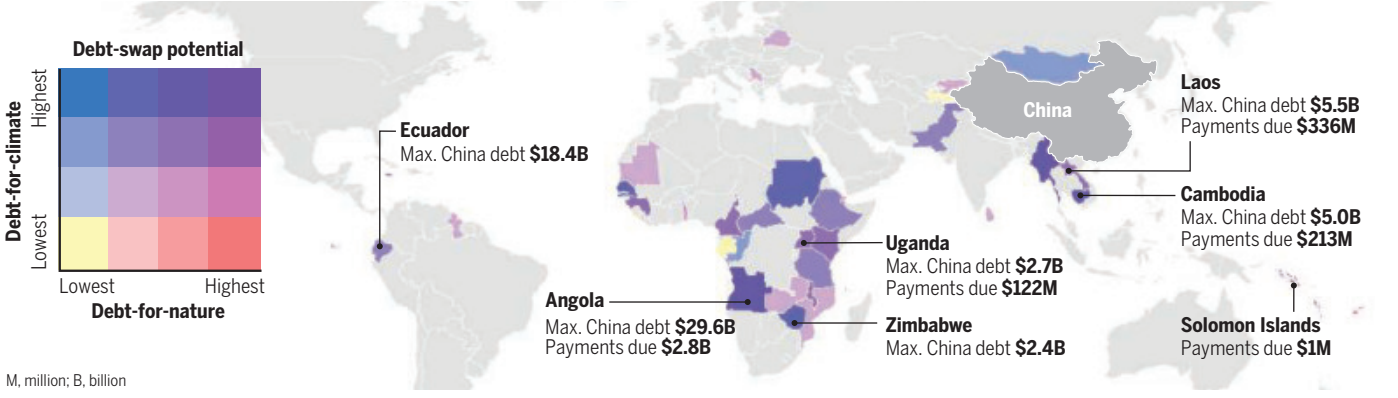

M, million; B, billion

GRAPHIC: ADAPTED FROM B. A. SIMMONS *ET AL.* BY N. DESAI/*SCIENCE*

biodiversity and climate mitigation, such as preserving carbon sinks by reducing deforestation. This would provide an additional tool for China to deliver on its own policy priorities, such as the Beijing Call for Biodiversity and Climate Change (*3*) and a "green" Belt and Road (*8*).

China and its borrowers can work bilaterally and multilaterally to make these swaps part of their toolkit. As China considers creating a new biodiversity fund ahead of the CBD COP in 2021, some of those funds could be earmarked for debt-for-nature or debt-for-climate swaps, enhancing the environmental performance of new or replaced financing from China. On a bilateral level, numerous countries are engaged in debt relief negotiations. China could signal that it is willing to expand those discussions to include possible debt swaps, and borrowers could propose swaps as well. More ambitiously, China could expand multilateral debt relief options. There is an increasing recognition that the DSSI does not include all the countries that will need debt relief, including several climate-vulnerable countries. China should join these calls to expand the DSSI to include climate-vulnerable countries and to use debt swaps as a tool for reducing these countries' debt burdens.

Ecuador's Villonaco wind farm was financed by the China Development Bank in 2011. Plans to expand it are key to the country's renewable energy goals, as reflected in the 2016–2025 Electricity Master Plan.

As China develops debt swaps as part of its toolkit, it should be mindful to avoid pitfalls of such swaps in the past, such as inadequate provision of resources, misalignment with the debtor country's policies, and offering too little debt restructuring to sufficiently reduce debt stress (*14*). However, there is compelling evidence that debt-for-nature swaps can lead to positive biodiversity outcomes if designed and implemented to avoid these pitfalls (*15*), and these successful examples can guide the design of debt-for-climate swaps and other emerging nature and climate performance-linked finance instruments that have yet to gain widespread adoption.

This global outlook is just the first step in propelling proenvironmental debt restructuring into the next decade. We have used new data on Chinese overseas lending to highlight debt-distressed countries and just a few overarching indicators of climate and biodiversity threat to highlight heterogeneities and synergies between two types of debt swaps. Going forward, debt swaps will need to be designed according to the specific threats and priorities for biodiversity and climate change in the debtor countries, and a greater suite of indicators will be necessary for identifying global debt swap priorities. For example, countries considered to have relatively low biodiversity threat from tree-cover loss in this analysis may still face considerable challenges with pollution, coastal development, endemic species decline, or marine habitat loss. Prioritizations will also benefit from more explicit considerations of the direct costs and feasibility of debt swaps and the relationship between threats and opportunity for success (*12*), which was not possible in this global comparison (see SM for additional considerations for future research). These priorities must be guided by climate and conservation scientists in collaboration with policy experts and community stakeholders to maximize environmental benefits while stimulating economic growth and increasing human well-being. Implementing a strategic, effective, and socially responsible framework for debt-for-nature and debt-for-climate swaps could ultimately allow China to lead on global financial stability, a recovery from the COVID-19 pandemic, and simultaneous reductions of climate and biodiversity risks. ■

REFERENCES AND NOTES

1. S. Horn, C. Reinhart, C. Trebesch, "China's overseas lending" (Kiel Working Paper No. 2132, Kiel Institute for the World Economy, 2019); www.ifw-kiel.de/fileadmin/Dateiverwaltung/IfW-Publications/Christoph_Trebesch/KWP_2132.pdf.
2. World Bank, "COVID-19 debt service suspension initiative" (2021); www.worldbank.org/en/topic/debt/brief/covid-19-debt-service-suspension-initiative.
3. Xinhua, "Beijing call for biodiversity conservation and climate change," *China Daily*, 6 November 2019; www.chinadailyhk.com/articles/3/219/67/1573024746231.html.
4. R. Ray, K. P. Gallagher, W. Kring, J. Pitts, B. A. Simmons, Geolocated dataset of Chinese overseas development finance, OSF (2020); https://osf.io/7wuxv.
5. S. A. Sarkodie, V. Strezov, *Sci. Total Environ.* **656**, 150 (2019).
6. B. A. Williams *et al.*, *One Earth* **3**, 371 (2020).
7. P. Steele, S. Patel, "Tackling the triple crisis: Using debt swaps to address debt, climate and nature loss post-COVID-19" (Issue Paper, International Institute for Environment and Development, 2020).
8. China Council for International Cooperation on Environment and Development (CCICED), "Special policy study on Green Belt and Road and 2030 agenda for sustainable development" (Policy Report, CCICED, 2019).
9. T. B. Hamlin, *Ecol. Law Q.* **16**, 1065 (1989).
10. D. Brautigam, *Area Dev. Policy* **5**, 1 (2020).
11. K. Acker, D. Brautigam, Y. Huang, "Debt relief with Chinese characteristics" (Working Paper No. 2020/39, China Africa Research Initiative, School of Advanced International Studies, Johns Hopkins University, 2020).
12. J. McGowan *et al.*, *Conserv. Biol.* **34**, 1065 (2020).
13. M. M. Cabré, K. P. Gallagher, Z. Li, *China World Econ.* **26**, 27 (2018).
14. D. Cassimon, M. Prowse, D. Essers, *Glob. Environ. Change* **21**, 93 (2011).
15. J. M. Sommer, M. Restivo, J. M. Shandra, *J. Dev. Stud.* **56**, 748 (2020).

ACKNOWLEDGMENTS

Funding for this paper comes from the Climate and Land Use Alliance, David and Lucile Packard Foundation, and Rockefeller Brothers Fund. K.P.G. conceived the concept; B.A.S. and H.Y. collected the data; B.A.S. performed the analysis; B.A.S. and K.P.G. wrote the manuscript. R.R. and H.Y. revised and provided crucial comments on the manuscript. The authors declare no competing interests. All primary data is publicly available (see references for original data sources). Country-level data used for analysis is available in the supplementary materials. An interactive version of the map shown in the figure is available at www.bu.edu/gdp/china-debt-sustainability-environment.

SUPPLEMENTARY MATERIALS

science.sciencemag.org/content/371/6528/468/suppl/DC1

10.1126/science.abf4049

PHOTO: AGUSTIN0915/SHUTTERSTOCK

HUMAN BIOLOGY

The human voice, in all its idiosyncratic glory

A deep dive into voice research covers lyrical lilts, gargled rasps, and everything in between

BOOKS *et al.*

Packed with subtle clues about the speaker, the voice often leads listeners to make inaccurate inferences.

PHOTO: ISTOCK.COM/CARLOSDAVID.ORG

By **Elizabeth Erickson DiRenzo**

The larynx is critical for two broad functions: one life-sustaining, aiding in respiration and preventing the aspiration of food into the lungs; and the other life-enhancing, contributing to phonation, an essential component of communication. There was a time when the latter was largely ignored by researchers. However, in recent years, there has been an explosion of interest in the voice by investigators from a diverse range of disciplines. In his new book, *This Is the Voice*, journalist John Colapinto creates a compelling narrative surrounding this vast and complex topic and investigates what makes the voice uniquely human.

Colapinto creatively describes the structure of the book as "a little like the vocal signal itself." He starts at the beginning of a human life, examining how the voice is first exhibited in the cry of a newborn baby and then, remarkably rapidly, shaped into speech, eventually allowing communication partners to engage in conversation. The scope of the book then "radiates outward like a soundwave" to explore how the voice functions in society, including as a prominent marker of status and class, as an indicator of gender and racial identity, and sometimes as a signal of sexual orientation. It also addresses the distinctive voices of religious leaders and those involved in mass broadcast and finally the voices of political leaders who have shaped our society. Colapinto concludes, appropriately, by recognizing that even though the complex biological processes associated with aging do not spare the voice, they also impart a wisdom that can only be achieved with life experience.

This Is the Voice
John Colapinto
Simon and Schuster, 2021. 320 pp.

The voice is a vital part of the uniquely human attribute known as speech, and while the focus of the book is not necessarily on language, Colapinto does consider voice and speech in the broader context of communication. He argues that the voice was selectively advantageous in evolutionary history and emphasizes the role the voice played in creating language in humans. Here, Colapinto draws on the pioneering work of Philip Lieberman, whose theory asserts that "Language, far from being a purely mental phenomenon, is a physical act whose first stirrings can be traced back, hundreds of millions of years, to the oldest, air-breathing vertebrate (the lungfish), as voice." Colapinto goes on to provide compelling evidence that in our early hominin history, a series of advantageous genetic mutations changed the respiratory and vocal apparatuses and basal ganglia to give rise to speech and prime the brain for language.

"Just as every human speaker emits vocal signals whose shape, rhythm, and tune offer strong clues about their geographic origins, socioeconomic background, and education level, all of us, as listeners, parse other people's pronunciation for such clues and draw instant inferences, often quite inaccurate, about the speaker," observes Colapinto. In one notable example, he describes how simple alterations in vowel and consonant pronunciations as well as prosody cause us to rapidly stigmatize speakers from the south as "backwards, undereducated," northerners as "elitist," and Californians as "hopeless flakes."

The voice can also express emotion and produce song, thus illuminating the inner self. Colapinto explores the emotional power of song and how the singer, with delicate control of the vocal instrument, can bring immense pleasure to the listener. While discussing the voice of American operatic soprano Renée Fleming, Colapinto muses: "How she shapes that sound into something we deem 'beautiful,' so that each note hangs for a moment in the air, as present as an abstract Brancusi sculpture—shaped and shimmering in space, textured, polished, and conforming to all the criteria of proportion and harmony that Plato said embody perfection in the arts—well, that's another question entirely."

Colapinto begins his book by detailing his personal experience with a voice injury, stating: "I took for granted the sounds that emerged from between my lips." As a voice scientist and rehabilitation expert, I regularly hear this same sentiment from my clients. As the book concluded, I was surprised to learn that after years of living with a voice injury, he ultimately decided against pursuing surgical vocal fold treatment. I was ultimately satisfied, however, that he had found peace and genuine appreciation for his unique voice. ■

The reviewer is at the Department of Otolaryngology, Stanford University School of Medicine, Stanford, CA 94305, USA. Email: edirenzo@stanford.edu

10.1126/science.abf7191

ARCHAEOLOGY

Exploring the origins of urban living

Ancient human settlements are brought vividly to life in an engaging new analysis

By **B. R. Hassett**

In *Four Lost Cities*, Annalee Newitz—a technology journalist and author of popular genre fiction—has unexpectedly turned their attention to the archaeology of the urban past. Each of the four sections of this volume describes a different case study.

Çatalhöyük, the first case Newitz describes, is a fascinating example of a very early experiment in settled living some 10,000 years ago in a region now encompassed by the country of Turkey. Newitz captures the intricacies of the formation of Çatalhöyük: layer upon layer of building, the construction of its members' private lives, and the shift from wild to domestic foods. Their discussion, in the second chapter, of the notorious "Mother Goddess" theory, which posits a unified prehistoric matriarchy and has earned a present-day cult following, is particularly deft. Adding to fairly well-established evidence of climatic and environmental changes that led to the abandonment of the site, Newitz offers an interesting discussion of how a lack of social buy-in might have doomed this early experiment in group living.

Despite weaving together disparate expert commentary into an eminently readable and coherent whole, this is the weakest of the book's four sections. With its fairly flat social structure—mirroring the fairly flat Konya plain on which it was located—Çatalhöyük does not match the traditional description of a city. It may not have been very different at all from the mobile existence that preceded it. Central Anatolia is littered with other settlements that, while they may not have been as long-lived, would have introduced concepts such as "privacy" long before Çatalhöyük.

Newitz's discussion of Pompeii, the city famously destroyed by the eruption of Vesuvius in 79 CE, is a far smoother ride, perhaps because the Roman cities of the first century are so closely in tune with what we think of as urbanism today. They write with an excellent eye for relatable detail about the lives of the liberti (freed slaves), about female entrepreneurs, and about the many ways in which Pompeii confounds our expectations. The section's second chapter on the myriad uses of public space would be very on-trend in an archaeological volume but is presented far more interestingly here, in vignettes about the activities of the city's inhabitants, from bad drivers to sex workers. The section's third chapter covers the city's destruction, a well-tread subject, but offers much more than most accounts do, discussing the lives of the survivors and the contemporary perception of the tragedy.

Monks and visitors mingle in the ruins of Cambodia's Angkor Wat.

Moving to Cambodia and the sprawling temple complex known as Angkor Wat, in the book's third section, Newitz discusses distinctive southeastern Asian subsistence strategies and explains how modern researchers have used remote-sensing technologies to uncover the ancient landscape of urban life around the famous temple complex. This section's examination of the big public works projects that defined Angkor—including the economics of debt-slavery, or debt-labor—reveals Newitz's ability to parse academic arguments into something worth arguing about. It closes with a discussion of the not-quite-collapse of this urban polity into its current genteel retirement as a spiritual center.

The reviewer is at the Institute of Archaeology, University College London, London WC1H OPY, UK, and is the author of *Built on Bones: 15,000 Years of Urban Life and Death* (Bloomsbury, 2017). Email: b.hassett@ucl.ac.uk

Four Lost Cities: A Secret History of the Urban Age
Annalee Newitz
Norton, 2021. 320 pp.

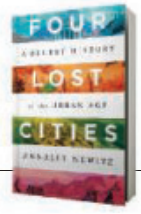

Cahokia, on the banks of the Mississippi River, is discussed in the book's final section and is clearly very close to Newitz's heart. Introducing the site as more a spiritual than a commercial center, Newitz includes critical perspectives and curated histories from Indigenous groups with a stake in the story, something that not even all professional archaeologists manage. This section finishes with a discussion of "survivance" of Cahokian themes, motifs, and practices from the settlement's heyday a millennium ago to the modern day. The book concludes with a nuanced proposal that we reconsider "collapse" as a multifaceted thing and reject strict environmental determinism for disasters that are often intertwined with social factors.

There are a few missteps in this book that will likely give professional archaeologists a tremor or two: some are obscure errors of attribution, and some are just too-sharp observations (it is true, we really do always talk about space). Other errors, including Newitz's misidentification of what are probably seasonal laborers or ethnic Yörük outside of Konya as Bedouin or the gross misnumbering of the Maya (in the thousands, when their actual number is closer to six million), are less forgivable. Overall, however, Newitz has achieved something remarkable, taking a very personal drive to understand the way we live and using it to enliven the past, at each turn letting expert voices guide a clear-sighted discussion of the lives of marginalized populations, the potential held by new scientific methods of analysis, and—perhaps most importantly—the self-awareness that what we see of the past is very much a product of how we understand the present. ■

10.1126/science.abg1045

PHOTO: ISTOCK.COM/NIKADA

China's plan to protect the Asian giant softshell (*Pelochelys cantorii*) focuses on captive breeding.

PHOTO: JACK FOLKERS/BUITEN-BEELD/ALAMY STOCK PHOTO

Edited by **Jennifer Sills**

China's turtles need protection in the wild

In Chinese mythology, giant softshell turtles are important symbols of longevity and strength. The two extant species, the Yangtze giant softshell (*Rafetus swinhoei*) and the Asian giant softshell (*Pelochelys cantorii*), are among the largest and rarest freshwater turtles in the world (*1*–*3*). After the death of a female *R. swinhoei* during artificial insemination in 2019, there is only one male left in captivity (*2*). The status of *P. cantorii* is less publicized, but this species is also disappearing (*3*). There are 15 adult *P. cantorii* kept in captivity in China, and the Chinese conservation plan for the species focuses on their captive breeding (*4*). However, based on China's past record, conservation efforts that exclude habitat protection will likely provide no benefit to wild populations.

A singular focus on conservation in captivity guarantees there will be no place for reintroduction of *P. cantorii* into the wild [as occurred in the case of the Yangtze alligator (*Alligator sinensis*) (*5*)]. So far, the farming of other turtles in China has been little help to wild populations. Paradoxically, this approach increases poaching because captured animals can be sold to breeders (*6*). Breeding programs also result in genetically compromised individuals of reduced conservation value, as exemplified by the mass release of farmed Chinese giant salamanders (*Andrias davidianus*), which provided few benefits and likely introduced new threats to the native population (*7*). Three sites have bred *P. cantorii* from wild-caught individuals, but they have not demonstrated a sustainable breeding program. The origin of most captive turtles is unknown because they were bought in markets or seized from smugglers (*3*, *4*).

Thirteen reserves were designed to protect *P. cantorii* in southern China, but just six are staffed and only half of those have recorded the presence of *P. cantorii* in recent years (*3*). The effectiveness of the reserves is questionable given that they have been constantly flooded since the construction of hydroelectric dams, destroying the essential sand banks habitat the turtles use to bask and nest (*8*). After losing the Baiji dolphin (*Lipotes vexillifer*) (*9*) and Chinese paddlefish (*Psephurus gladius*) (*10*), the Chinese government banned all fishing in the Yangtze river system for 10 years (*11*). China should expand this strict fishing ban to all rivers and prohibit dams within turtle reserves to protect their habitats. Furthermore, the reserves should be adequately supported and effectively managed. We may fail to save *R. swinhoei*, but we can save other giants in the wild rivers of China if we do not focus exclusively on breeding programs.

Jian Wang[1], James F. Parham[2], Haitao Shi[3]*
[1]College of Life Science and Technology, Honghe University, Mengzi 661199, China. [2]Department of Geological Sciences, California State University, Fullerton, CA 92834, USA. [3]Ministry of Education Key Laboratory for Ecology of Tropical Islands, College of Life Sciences, Hainan Normal University, Haikou 571158, China.
*Corresponding author. Email: haitao-shi@263.net

REFERENCES AND NOTES

1. P. C. H. Pritchard, *Chelon. Conserv. Biol.* **4**, 5 (2001).
2. H. Liu, X. Li, C. Zhang, *Science* **364**, 1144 (2019).
3. X. Hong *et al.*, *Chelon. Conserv. Biol.* **18**, 68 (2019).
4. Ministry of Agriculture and Rural Affairs of the People's Republic of China, "Action Plan for the Rescue of *Pelochelys cantorii* (2019–2035)" (2019); www.moa.gov.cn/nybgb/2019/201912/202004/t20200410_6341174.htm [in Chinese].
5. S. Lu *et al.*, *Croco. Special. Group Newsl.* **34**, 29 (2015).
6. H. Shi *et al.*, *Conserv. Biol.* **21**, 5 (2007).
7. F. Yan *et al.*, *Curr. Biol.* **28**, R590 (2018).
8. D.-M. Ruan *et al.*, *Chin. J. Zool.* **36**, 42 (2001) [in Chinese].
9. S. T. Turvey *et al.*, *Biol. Lett.* **3**, 547 (2007).
10. H. Zhang *et al.*, *Sci. Total Environ.* **710**, 136242 (2020).
11. Z. Mei *et al.*, *Science* **367**, 1314 (2020).

COMPETING INTERESTS

J.W. and H.S. receive funding from the National Natural Science Foundation of China (31401983 and 31772486, respectively).

10.1126/science.abg3541

Social distancing remains key during vaccinations

A global effort to develop vaccines against severe acute respiratory syndrome coronavirus 2 (SARS-CoV-2) began early in 2020. In mid-December, the U.S. Food and Drug Administration approved emergency use authorization for two vaccines that successfully concluded their phase 3 trials (*1*), and vaccine distribution in the United States began shortly afterwards. As vaccinations progress, the public must continue to social distance, limit large gatherings, wear masks, and engage in other non-pharmaceutical interventions (NPIs) to curb the spread of COVID-19.

Both the Pfizer/BioNTech and Moderna vaccines use mRNA technology and require two doses administered 3 and 4 weeks apart, respectively, to reach the full 90 to 95% efficacy (*2*). In light of limited supply, the Centers for Disease Control and Prevention has provided preliminary guidance indicating that vaccination should be prioritized first for health care workers and long-term care facility residents, then for other essential workers, and next for people at higher risk for severe illness (*3*). Subsequently, vaccination will reach most sectors of the population, though inoculation of children under 16 has yet to be recommended.

Globally, vaccination uptake over the coming year could prevent disease for the sizeable portion of the population that has yet to be infected with SARS-CoV-2 and move the world to a post-pandemic

phase; however, this potential benefit of averted infections, hospitalizations, and deaths depends considerably on societal maintenance of NPIs during vaccine deployment. Relaxing NPIs before attaining adequate distribution would enable infection of many more people before their vaccination than would occur if NPIs were to be maintained or increased. Locally, relaxation of NPIs increases the reproduction number, R_t, which enables greater transmission of the virus and a larger overall attack rate. These changes lead to a faster and larger accumulation of infections that could greatly outpace vaccination distribution efforts. Thus, maintaining NPIs throughout the upcoming SARS-CoV-2 vaccination campaign is essential for maximizing the health benefit. In the coming months, public health messaging is critically needed to encourage continued compliance with NPI control measures.

Marta Galanti[1], Sen Pei[1], Teresa K. Yamana[1], Frederick J. Angulo[2], Apostolos Charos[3], David L. Swerdlow[2], Jeffrey Shaman[1]*
[1]Department of Environmental Health Sciences, Mailman School of Public Health, Columbia University, New York, NY 10032, USA. [2]Medical Development and Scientific/Clinical Affairs, Pfizer Vaccines, Collegeville, PA 19426, USA. [3]Patient Health Impact, Pfizer Vaccines, Walton Oaks, Tadworth, KT20 7NS, UK.
*Corresponding author. Email: jls106@cumc.columbia.edu

REFERENCES AND NOTES

1. U.S. Food and Drug Administration, "COVID-19 vaccines" (2020); www.fda.gov/emergency-preparedness-and-response/coronavirus-disease-2019-covid-19/covid-19-vaccines.
2. C. Zimmer, J. Corum, S.-L. Wee, "Coronavirus vaccine tracker," *The New York Times* (2020).
3. Centers for Disease Control and Prevention, "How CDC is making COVID-19 vaccine recommendations" (2020); www.cdc.gov/coronavirus/2019-ncov/vaccines/recommendations-process.html.

COMPETING INTERESTS

Pfizer Inc. reviewed this manuscript and approved the decision to submit the manuscript for publication. F.J.A., A.C., and D.L.S. own Pfizer stock. J.S. and Columbia University disclose partial ownership of SK Analytics. J.S. has done paid consulting work for Business Network International and receives funding from Pfizer Inc., National Science Foundation grant DMS-2027369, and a gift from the Morris-Singer Foundation.

10.1126/science.abg2326

Disinfection spreads antimicrobial resistance

During the COVID-19 pandemic, the use of disinfectants, alcohol-based hand sanitizers, and antiseptic hand wash has surged. As a precaution, many authorities have also increased chlorine dosage in wastewater disinfection to achieve a free chlorine residual concentration greater than 6.5 mg/liter (*1*), despite evidence that a free chlorine residual of just above 0.5 mg/liter can completely inactivate human coronavirus (*2*). These chemicals can reach aquatic and terrestrial environments through direct discharge of wastewater into receiving waters. Disinfection protocols put in place to prevent COVID-19 should be limited to the minimum required to kill severe acute respiratory syndrome coronavirus 2 (SARS-CoV-2) and weighed against their potential to increase antimicrobial resistance (AMR).

Disinfectants facilitate the bacterial acquisition of AMR, potentially the biggest global health challenge next to the COVID-19 pandemic (*3*). For example, antiseptic ingredients quaternary ammonium compounds (*4*), triclosan (*5*), chlorhexidine (*6*), and ethanol (*7*); chlorine-based disinfectants (*8*); and disinfection by-products (*9*) can promote the spread of AMR through mutation or horizontal gene transfer. Thus, current increases in disinfection practices may pose an environmental and public health risk by accelerating the spread of AMR.

Unlike human viruses, which cannot independently reproduce and rarely survive in the environment, bacteria can proliferate and persist, conceivably inheriting AMR over generations. The health of humans and animals is inextricably connected to the environment, potentially creating a cycle of AMR dissemination. Indeed, humans and animals can acquire AMR from the environment through food (*10*), water (*11*), and air (*12*).

From the One Health perspective, a robust risk assessment is necessary to evaluate the environmental and public health risks of increased disinfection and its role in mediating the spread of AMR, particularly in the long term. To reduce the release of disinfectants into the environment, policies should be enacted to reduce unnecessary fomite disinfection, reduce the chlorine load to maintain a free chlorine residual of just above 0.5 mg/liter (*2*), and dechlorinate treated effluent before discharge. These approaches may be critical to protecting the public from future health threats by slowing down the dissemination of AMR.

Ji Lu and Jianhua Guo*
Advanced Water Management Centre, The University of Queensland, St Lucia, Brisbane, QLD 4072, Australia.
*Corresponding author.
E-mail: j.guo@awmc.uq.edu.au

REFERENCES AND NOTES

1. J. Wang *et al.*, *Environ. Pollut.* **262**, 114665 (2020).
2. X. W. Wang *et al.*, *J. Virol. Methods* **126**, 171 (2005).
3. J. O'Neill, A.R. Board, Eds., "Tackling drug-resistant infections globally: Final report and recommendations" (Review on Antimicrobial Resistance, 2016).
4. M. Tandukar *et al.*, *Environ. Sci. Technol.* **47**, 9730 (2013).
5. J. Lu *et al.*, *Environ. Int.* **118**, 257 (2018).
6. M. Wand *et al.*, *Antimicrob. Agents Chemother.* **61**, e01162-16 (2017).
7. S. J. Pidot *et al.*, *Sci. Transl. Med.* **10**, eaar6115 (2018).
8. M. Jin *et al.*, *ISME J.* **14**, 1847 (2020).
9. D. Li *et al.*, *Environ. Sci. Technol.* **50**, 3193 (2016).
10. T. P. Van Boeckel *et al.*, *Science* **365**, eaaw1944 (2019).
11. A. F. C. Leonard *et al.*, *Environ. Int.* **114**, 326 (2018).
12. J. Li *et al.*, *Environ. Sci. Technol.* **52**, 10975 (2018).

COMPETING INTERESTS

J.L. was funded by the Advance Queensland Industry Research Fellowship (grant no. RM2020001500). J.G. was funded by the Australian Research Council (grant no. FT170100196).

10.1126/science.abg4380

Former AAAS Entry Point! intern, Kelly Gilkey, working at NASA.

PHOTO: MICHELLE M. MURPHY/NASA GLENN RESEARCH CENTER

Diversity in STEM includes scientists with disabilities

Now in its 25th year, Entry Point! has placed more than 500 STEM majors in summer internships

By **Becky Ham**

When Kelly Gilkey was in high school, she sent an email to astronaut Pamela Melroy, asking if it might be possible for a person with a hearing loss like Gilkey to become a NASA astronaut.

"Amazingly, she responded and said the sky was the limit," Gilkey recalled. "If NASA could fly astronauts who needed glasses to see clearly, who was to say what might be possible some day?"

Gilkey got her first chance to work for NASA as a participant in Entry Point!, the American Association for the Advancement of Science's internship program for undergraduate and graduate students with disabilities in science, engineering, mathematics, and computer science. As an Entry Point! intern, she worked at NASA Glenn Research Center and NASA contractor Wyle Laboratories.

Today, Gilkey is a biomedical engineer and manager at Glenn and credits her internship with introducing her to a network of "highly capable and intelligent peers with various forms of disabilities," she said. "Being aware that there were others like me who were passionate about working in a STEM career and who had overcome the unique challenges of being other-abled was very empowering."

The goal of the program has always been to discover and develop scientific talent among people with disabilities and increase their representation in the scientific workforce. Highly qualified STEM majors with outstanding academic records are placed in companies, agencies, and universities that partner with Entry Point! Eighty-five percent of the program's alumni have been or are current working scientists and engineers.

Participants contribute more than technical expertise during their 10-week summer internships, according to Laureen Summers, project director for Entry Point!. "They represent a great opportunity to expand the science and engineering community, and the students are bringing their unique experiences and coping skills that can have a great effect on the research they do," she said.

Entry Point! debuted in 1996 with a grant from NASA to conduct a nationwide recruitment effort and to refer qualified students with disabilities for placement in a NASA summer program. It became the signature program of the AAAS Project on Science, Technology, and Disability, as a broker for talented STEM students with disabilities seeking opportunities to showcase their skills and interest to prospective employers.

NASA is one of Entry Point!'s first and most consistent partners. Other companies and institutions have come and gone during the project's life span, said Summers. Last year, interns worked at Mayo Clinic College, Cornell University, the University of Tennessee, the University of Arkansas, the University of Virginia Medical School, and The Ohio State University.

There are fewer partners now than in past years, Summers said, because companies are no longer willing to pay the annual administrative fee of $5000 when other organizations offer free recruitment and referrals of student candidates. As Entry Point! looks for more partners and funding, Summers is ramping up her efforts to encourage AAAS programs to consider more people with disabilities as part of the association-wide effort to increase and support diversity.

For the AAAS Committee on Diversity, Equity, and Inclusion, Summers wrote and performed a skit about disability for the organization, while reaching out to individual programs at AAAS such as the Science & Technology Policy Fellowships, the Mass Media Science & Engineering Fellowships, and the Human Rights, Law & Ethics program and awards such as the L'Oréal USA Fellowships for Women in Science "to encourage them to think about reaching out to people with disabilities."

"It does take time and an extra effort to reach people with disabilities, and people are busy," she said. "I think they don't always know where to go to find talent."

One program with strong outreach and significant inclusion of people with disabilities has been the Emerging Researchers National Conference, Summers said, noting that the conference regularly features workshops for students and keynote speakers with disabilities. Last year, conference lead and AAAS STEM Program Director Iris Wagstaff added a Students in STEM with Disabilities Working Group to the conference.

"Entry Point! students have been an invaluable component of the ERN Conference, as they provide a lens and perspective to aid us in viewing the world from a broader perspective, which is critical for innovation," said Wagstaff.

AAAS elections open in February

AAAS elections for the offices of President-Elect, Board of Directors, and Committee on Nominations will open on 8 February 2021. Please visit www.aaas.org/governance/annual-election for more information on candidates and the voting process.

The Entry Point! interns have gained more than job experience and networking opportunities from their time in the program, according to responses from a survey Summers sent to alumni last summer. Participants said that the experience helped them succeed in interviews and negotiations and encouraged them in new adventures.

The internship helped convince Jeremy Johansen that he could still pursue his dream of becoming an engineer after he lost his sight, he said, "boosting my confidence in living and working independently."

"A year after my first successful internship on the opposite end of the country, I participated in an international research exchange in Japan, an opportunity I only took because Entry Point! showed me that I could survive living far from home," said Johansen, who now works as a software engineer at OSIsoft.

The program maintains Facebook and LinkedIn pages for alumni, but one of Summers's goals is to find funding for more alumni connections. For some, the pandemic has exacerbated the sense of isolation that many scientists with disabilities already experience, she said.

At a recent conference, Summers overheard company representatives say, "'Okay, we know about accommodations [for disabilities], we know it's the right thing to do. But how do you act around a person with a disability?'"

"For people who are hesitant to be with disabled people or employ them, I think it comes from their own experiences," she said. "Relationships are key to understanding who a person with a disability really is, and the creativity, skills, and life experiences that contribute to innovation and new advances within the STEM enterprise."

Through Entry Point!, numerous companies have learned how to build these relationships, providing more opportunities and diminishing bias against scientists with disabilities.

Call for nomination of 2021 Fellows

Fellows who are current members of AAAS are invited to nominate members for election as Fellows. A member whose efforts on behalf of the advancement of science or its applications are scientifically or socially distinguished, and who has been a continuous member for the 4-year period leading up to the year of nomination, may by virtue of such meritorious contribution be elected a Fellow by the AAAS Council. A nomination must be sponsored by three previously elected AAAS Fellows (who are current in their membership), two of whom must have no affiliation with the nominee's institution. Nominations undergo review by the steering groups of the Association's sections (the chair, chair-elect, retiring chair, secretary, and four members-at-large of each section). Each steering group reviews only those nominations designated for its section. Names of Fellow nominees who are approved by the steering groups are presented to the Council in the fall for election.

NEW FOR 2021: The AAAS Executive Office is using a new submission portal to accept all nominations this cycle, which means we will no longer be accepting nomination packets via email. Nominations with complete documentation must be received by 28 April 2021 at 11:59 p.m. EDT. Nominations received after that date or nominations that are incomplete as of the deadline will not move forward. Complete instructions are available at https://www.aaas.org/programs/fellows/current-nomination-cycle. Questions may be directed to fellownomination@aaas.org.

RESEARCH

IN *SCIENCE* JOURNALS

Edited by **Michael Funk**

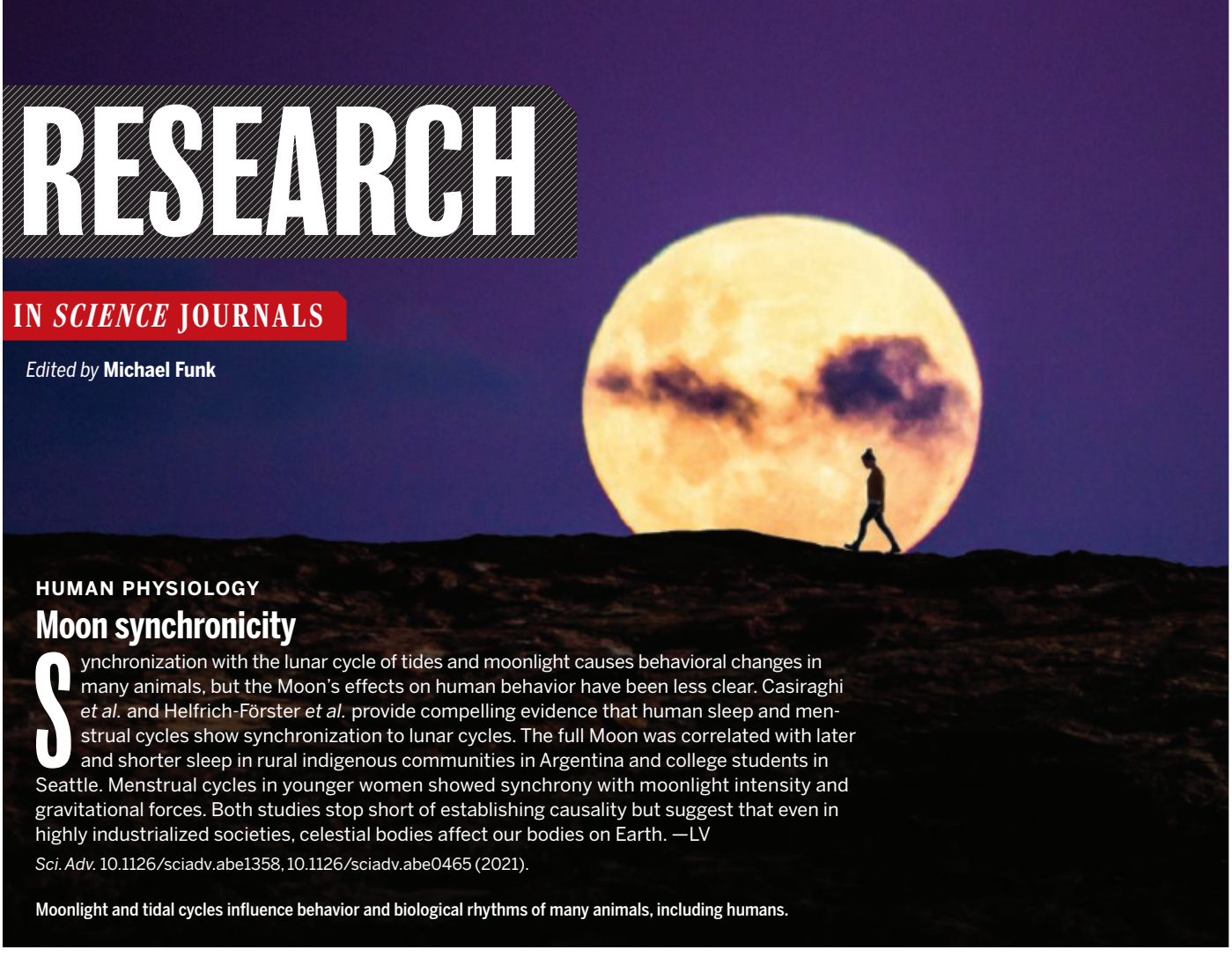

HUMAN PHYSIOLOGY

Moon synchronicity

Synchronization with the lunar cycle of tides and moonlight causes behavioral changes in many animals, but the Moon's effects on human behavior have been less clear. Casiraghi *et al.* and Helfrich-Förster *et al.* provide compelling evidence that human sleep and menstrual cycles show synchronization to lunar cycles. The full Moon was correlated with later and shorter sleep in rural indigenous communities in Argentina and college students in Seattle. Menstrual cycles in younger women showed synchrony with moonlight intensity and gravitational forces. Both studies stop short of establishing causality but suggest that even in highly industrialized societies, celestial bodies affect our bodies on Earth. —LV

Sci. Adv. 10.1126/sciadv.abe1358, 10.1126/sciadv.abe0465 (2021).

Moonlight and tidal cycles influence behavior and biological rhythms of many animals, including humans.

PHOTOS (FROM TOP): JOEL SHARPE/GETTY IMAGES; NASA

CRYSTALLIZATION

Watching early stage nucleation

In classic nucleation theory, a metastable disordered dense liquid or amorphous solid cluster spontaneously and irreversibly transforms into a crystalline nucleus. Jeon *et al.* observed the formation of gold crystals on a graphene substrate through the reduction of a precursor using an electron beam. Rather than the classic view, they instead observed a nucleation pathway that involves dynamic and reversible fluctuations of developing nuclei between disordered and crystalline states. The lifetime in the disordered state decreases with increasing cluster size, and at sufficiently small sizes, the binding energy per atom is large enough relative to the energy required to induce melting that the heat imparted upon binding is enough to drive partial collapse of an ordered cluster into the disordered state. —MSL

Science, this issue p. 498

CLIMATE

Making tracks

The magnitude of the effect of anthropogenic aerosols on the formation of clouds is an important unknown about how humans are affecting climate. Studies of stratocumulus cloud tracks that are formed by ship exhaust have been used to estimate the radiative impact of this process, but Glassmeier *et al.* now show that this approach overestimates the cooling effect of aerosol addition by up to 200%. These findings underscore the need to quantify stratocumulus cloud responses to anthropogenic aerosols to understand the climate system. —HJS

Science, this issue p. 485

The climate-cooling effect of clouds seeded by ship exhaust has been overestimated.

VACCINES

Vaccines get a help-MAIT

Mucosal-associated invariant T (MAIT) cells are a T cell subset important for mucosal homeostasis. These cells recognize derivatives of microbiota-derived vitamin B2 precursors but can also be activated by certain cytokines in the context of viral infections. Provine *et al.* report that a leading adenoviral vector vaccine, ChAdOx1, activated MAIT cells in immunized mice (see the Perspective by Juno and O'Connor). This activation required interferon-α produced by plasmacytoid dendritic cells as well as monocyte-derived interleukin-18 and

tumor necrosis factor. MAIT cell activation positively correlated with vaccine-mediated T cell responses in human subjects, and mice deficient in MAIT cells showed impaired $CD8^+$ T cell immunity to target antigens after vaccination. This work suggests an additional pathway that could be exploited to enhance the efficacy of vaccines. —STS

Science, this issue p. 521; see also p. 460

ORGANIC CHEMISTRY

Shuttling halide pairs back and forth

The transfer of adjacent hydrogens from a saturated to an unsaturated organic compound is a fairly common reaction. However, analogs that shuttle two heavy atoms back and forth are much harder to catalyze. Dong *et al.* report an electrochemical approach that transfers a pair of adjacent chlorines or bromines from an alkyl compound to an olefin. The method could help to remediate halogenated pollutants while concurrently producing fine chemicals. —JSY

Science, this issue p. 507

CATALYSIS

Rotation during reaction

Determining changes in heterogeneous catalysts under reaction conditions can provide insight into mechanisms. Under reaction conditions, not only can metal nanoparticles change shape but their interaction with the oxide support could also be affected. Yuan *et al.* used aberration-corrected environmental transmission electron microscopy to study gold nanoparticles on titanium surfaces at low electron beam doses. During carbon monoxide (CO) oxidation at total pressures of a few millibars and 500°C, they observed that gold nanoparticles rotated by about 10° but returned to their original position when CO was removed. Density function theory calculations indicated that rotation was induced by changes in the coverage of adsorbed molecular oxygen at the interface. —PDS

Science, this issue p. 517

GEOLOGY

What matters for mudrocks

Rock such as slate and shale, which form from mud, suddenly start appearing in the geologic record around 450 million years ago. Their appearance at about the same time as certain plants seems to implicate plant roots in the formation of these ubiquitous rocks. Zeichner *et al.* found a different route for creating the flocculation required for mudrock. Using analog experiments, the authors found that organic matter from plants alone was sufficient for the formation of flocs—aggregates of small silt and clay particles—which are required to deposit mudrock. This observation could explain the appearance of these rocks in places where the plants did not have deep roots. —BG

Science, this issue p. 526

GENE THERAPY

The sooner, the better

Gene therapy approaches hold promise for the treatment of spinal muscular atrophy (SMA). However, these therapies show variable clinical response, and treatment at earlier ages is associated with better outcome. Using tissues from patients and a mouse model, Kong *et al.* found that motor neuron axons were already developmental delayed in the fetus and experienced early postnatal death. In utero therapeutic intervention prevented motor neuron degeneration and improved axonal function and motor behavior in mice. The results suggest that fetal treatment might increase the efficacy of current therapies for SMA. —MM

Sci. Transl. Med. **13**, eabb6871 (2021).

IN OTHER JOURNALS

Edited by **Caroline Ash** *and* **Jesse Smith**

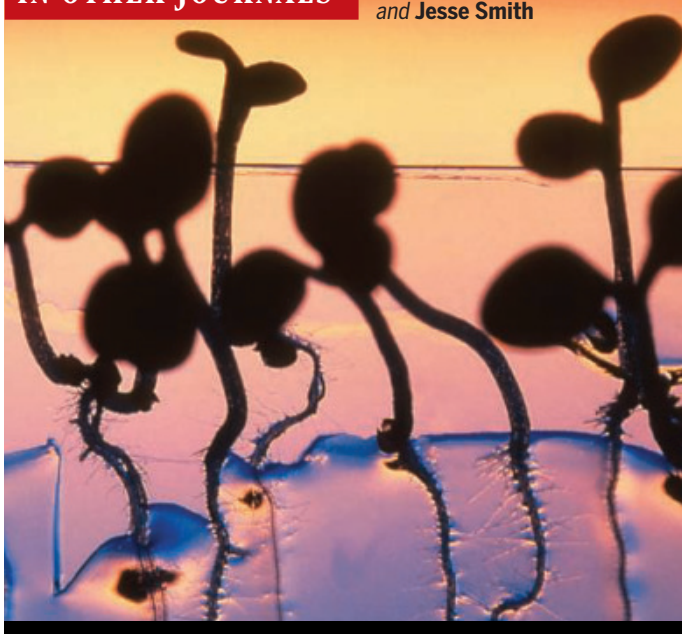

PLANT SCIENCE

Roots hunt nutrients

Soil nutrients such as nitrogen sources are not uniformly distributed. Neither are plant roots. Nonetheless, roots of *Arabidopsis* seedlings seek out pockets of soil ammonium and nitrate. Ötvös *et al.* clarify how root growth and branching are regulated to optimize nitrogen uptake. The auxin efflux carrier PIN-FORMED 2 (PIN2) is regulated posttranscriptionally by phosphorylation at its serine-439 in response to shifts in ammonium or nitrate availability. Phosphorylation in turn triggers changes in PIN2 subcellular localization, which drives changes in auxin distribution between root cortex and epidermis, causing altered root growth rate or direction. —PJH *EMBO J.* e106862 (2020).

In *Arabidopsis*, hormone localization in roots directs root growth toward pockets of nutrients.

PHOTO: DAMIEN LOVEGROVE/SCIENCE SOURCE

PROTEIN DESIGN

Function-focused protein design

De novo design allows the creation of new types of stable folds in proteins; however, building in successful function remains challenging. Yang *et al.* describe a bottom-up approach in which they conceived structures around functional motifs and then used targeted screening to optimize their composition. Based on thousands of blueprints, they screened yeast libraries in which most residues were restricted to those found most frequently in the designs, but critical core residues were allowed limited variability constrained by these designs. This approach enabled the authors to discover five folds that accommodated four different binding motifs, including a protein that displays two motifs. They then built proteins that are functional as biosensors of specific antibody epitopes and others that act as ligands to regulate synthetic receptors in mammalian cells. —VV

Nat. Chem. Biol. 10.1038/s41589-020-00699-x (2020).

MICROBIOTA

Transmissible bone mass

Human skeletal mass tends to be genetically determined, but there is an unexplained component. The occurrence of segmented filamentous bacteria (SFB; spore-forming organisms in the class Clostridiales) in the mouse gut is associated with physiological effects, including potent induction of T helper cell 17 (T_H17) cells. Tyagi *et al.* transferred SFB from mouse to mouse in various ways, including from mother to offspring, by cohousing, or by fecal transplantation. They found that skeletal maturation was impaired and that young animals were predisposed to osteoporosis as they aged. Antibiotic treatments that removed the SFB were also associated with changes in bone volume, structure, and turnover. Interleukin-17 from T_H17 cells is known to increase expression of a cytokine (TNFSF11) involved in osteoclast differentiation. Therefore, that members of the gut microbiota seem to be communicable regulators of bone development in mice implies that similar effects in humans are possible. —CA

eLife **10**, e64237 (2021).

ECONOMICS

Environmental bias in trade policy

"Dirty" industries that emit large amounts of carbon dioxide per output value enjoy hundreds of billions of dollars of implicit annual subsidies because trade policies in most countries impose higher tariffs and trade barriers on "clean" industries. Shapiro suggests that this is because firms lobby for low tariffs on their inputs but protections for their outputs, because "downstream" industries in the value chain (for example, selling pans), which generally have lower emissions, also typically have higher tariffs than "upstream" industries (for example, coal, which is used to create steel to make pans). Global emissions would decrease, with little change in real income, if trade policies treated clean and dirty goods similarly. —BW

Q. J. Econ. 10.1093/qje/qjaa042 (2020).

NANOMATERIALS

Less strength but greater toughness

Although two-dimensional materials such as molybdenum disulfide (MoS_2) can exhibit high strength, their usefulness is limited by ready propagation of cracks through the lattice that limits their fracture toughness. To create nanometer-scale holes, Manzaneres-Negro *et al.* irradiated suspended monolayers of MoS_2 with argon ions to introduce single-atom lattice vacancies and gallium ions. Mechanical testing showed that a defect density of 0.2% reduced the breaking strength by as much as 50% and decreased the crack propagation length by a factor of 5. Increasing the defect density such that the mean distance between defects decreased by about 50% increased a measure of fracture toughness by about 40%. —PDS.

ACS Nano. 10.1021/acsnano.0c08235 (2021).

OZONE POLLUTION

Oh, Oh, Oh

Tropospheric zone (O_3) is a secondary pollutant (meaning that it is formed by reaction rather than being directly emitted) that has major impacts on climate, human health, crops, and ecosystems. Zhang *et al.* show how emissions of a range of anthropogenic pollutants contributed to the growth of the global O_3 burden from 1980 to 2010. Methane concentration increases caused more than one-fourth of the rise of global ozone. Pollutant emission increases in Southeast Asia, East Asia, and South Asia drove most of the increase in ozone, whereas emission reductions in North America and Europe helped to decrease ozone abundance. —HJS

Geophys. Res. Lett. 10.1029/2020GL089184 (2020).

PARASITISM

Sniffing out the enemy

Immune cells are generated and activated to fight injury and disease. Curiously, environmental odors can mediate cellular response in the immune system. Madhwal *et al.* studied the *Drosophila* larval olfactory system during attack by parasitoid wasps. They show that olfactory stimulation results in the release of γ-aminobutyric acid (GABA) from neurons, which is then used by blood progenitor cells to stabilize a protein called Sima/HIFa. This then promotes differentiation in cells known as lamellocytes that are involved in encapsulating and eliminating wasp eggs. When flies live in wasp-infected areas, they enhance survival by using this olfactory-immune mechanism to protect against parasitic wasp infection. —BAP *eLife* **9**, e60376 (2020).

Fruit fly larvae can detect the smell of the parasitoid wasp *Leptopilina boulardi* and initiate defensive responses.

PHOTO: DR. CHIA-HUA LUE, IN COLLABORATION WITH USDA AND SMITHSONIAN NMNH

REVIEW SUMMARY

NANOPHOTONICS

Miniaturization of optical spectrometers

Zongyin Yang*, Tom Albrow-Owen*, Weiwei Cai†, Tawfique Hasan†

BACKGROUND: Optical spectrometry is one of the most powerful and widely used characterization tools in scientific and industrial research. Benchtop laboratory spectrometer systems—characterized by bulky optical components, moving parts, and long path lengths—can deliver unparalleled, ultrafine resolution and wide spectral ranges. However, a rapidly growing application space exists for spectral analysis where the need for reduced physical dimensions, cost, or power consumption takes precedence over the need for high performance. The demand for portable or handheld spectral analysis devices requires shrinking of these systems down to centimeter-scale footprints. More extreme miniaturization to submillimeter length scales would open a range of opportunities for in situ analysis, with potential for integration into lab-on-a-chip systems, smartphones, or even spectrometer-per-pixel snapshot hyperspectral imaging devices. Toward this aim, an approach that involves simply scaling down benchtop systems (with miniaturized gratings and reflective optics) becomes constrained as a result of the complex fabrication involved and the inherent proportionality of resolution to path length in dispersion-based systems.

ADVANCES: A wide variety of miniaturized spectrometer systems have emerged since the early 1990s. These can be grouped into four broad categories according to the underlying strategies they use for spectral characterization: (i) those that have tried to push the boundaries of miniaturization using a conventional benchtop strategy, where light interacts with miniaturized dispersive optics such that different spectral components are spatially separated when arriving at a detector array; (ii) narrowband filters, which can be used to selectively transmit light with specific wavelengths, such that analysis of complete spectra can be achieved either with a single filter (the transmissive properties of which can be varied over time) or by passing light through an array of multiple unique narrowband filters, each mounted onto its own detector; (iii) Fourier transform systems, where integrated interferometers [such as those based on microelectromechanical systems (MEMS) components] can be used to produce temporal or spatial interferograms, which are then computationally converted to a readable spectrum; and (iv) a newly emerging paradigm of microspectrometers, in which computational techniques are used to approximate or reconstruct an incident light spectrum from precalibrated spectral response information encoded within a set of broadband detectors or filters.

OUTLOOK: We now stand at a watershed where this field is yielding ultracompact microspectrometer systems with performance and footprint near those viable for integrated applications such as lab-on-a-chip systems, smartphones, and spectral imagers. Until recently, advancement has been inspired by and has benefited from wider technological trends in the production of hardware. For instance, earlier dispersion-based strategies have been improved through optimization of high-precision microfabrication, lithographic, and etching techniques to produce ever more scaled-down gratings and optics. In parallel, the development of MEMS components has enabled ultracompact, electronically driven moving parts for miniaturized Fourier transform interferometer–based devices. However, as the physical size and cost of processing power have fallen sharply over the past 15 years, the emergence of reconstructive microspectrometers has heralded a fundamental shift in the field, where developments in the software will shoulder much of the burden for enhancing device performance while footprints continue to shrink. Maturation of the algorithmic strategies behind these devices will likely see the incorporation of machine learning–based techniques, which increasingly will be able to compensate for the compromises in detector performance necessitated by further miniaturization. This represents a promising route toward ultracompact high-performance systems and the emergence of spectral analysis in a host of previously inaccessible platforms in scientific research, industry, and consumer electronics. ■

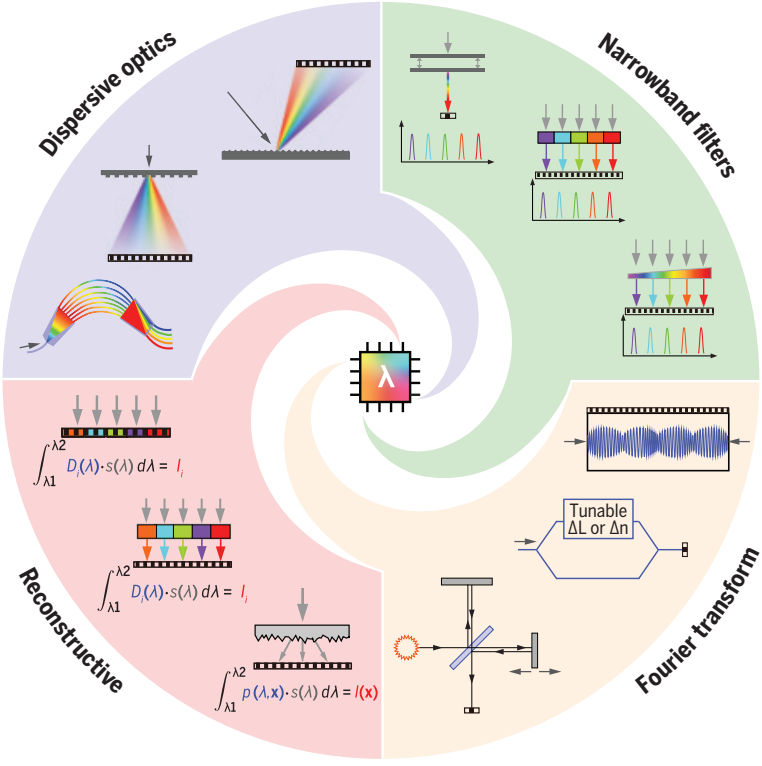

Strategies toward ultracompact microspectrometers. Schemes for miniaturized spectral sensing systems based on dispersive optics, narrowband filters, Fourier transform interferometers, and computational spectral reconstruction schemes have all emerged over the past three decades.

The list of author affiliations is available in the full article online.
*These authors contributed equally to this work.
†Corresponding author. Email: cweiwei@sjtu.edu.cn (W.C.); th270@cam.ac.uk (T.H.)
Cite this article as Z. Yang *et al.*, *Science* **371**, eabe0722 (2021). DOI: 10.1126/science.abe0722

READ THE FULL ARTICLE AT
https://doi.org/10.1126/science.abe0722

RESEARCH ARTICLE SUMMARY

IN SITU SEQUENCING

Expansion sequencing: Spatially precise in situ transcriptomics in intact biological systems

Shahar Alon*, Daniel R. Goodwin*, Anubhav Sinha*, Asmamaw T. Wassie*, Fei Chen*, Evan R. Daugharthy†, Yosuke Bando, Atsushi Kajita, Andrew G. Xue, Karl Marrett, Robert Prior, Yi Cui, Andrew C. Payne, Chun-Chen Yao, Ho-Jun Suk, Ru Wang, Chih-Chieh (Jay) Yu, Paul Tillberg, Paul Reginato, Nikita Pak, Songlei Liu, Sukanya Punthambaker, Eswar P. R. Iyer, Richie E. Kohman, Jeremy A. Miller, Ed S. Lein, Ana Lako, Nicole Cullen, Scott Rodig, Karla Helvie, Daniel L. Abravanel, Nikhil Wagle, Bruce E. Johnson, Johanna Klughammer, Michal Slyper, Julia Waldman, Judit Jané-Valbuena, Orit Rozenblatt-Rosen, Aviv Regev, IMAXT Consortium, George M. Church‡§, Adam H. Marblestone§, Edward S. Boyden‡§

INTRODUCTION: Cells and tissues are made up of diverse molecular building blocks, organized with nanoscale precision over extended length scales. Newly developed techniques that enable highly multiplexed, nanoscale, and subcellular analysis of such systems are required. Although much progress has been made on methods for multiplexed RNA imaging, these methods have been limited in their spatial precision, especially in the context of three-dimensional systems such as tissues. Because of this limitation, interrogation of tissues has been performed with either high spatial resolution or high molecular multiplexing capacity, but not both.

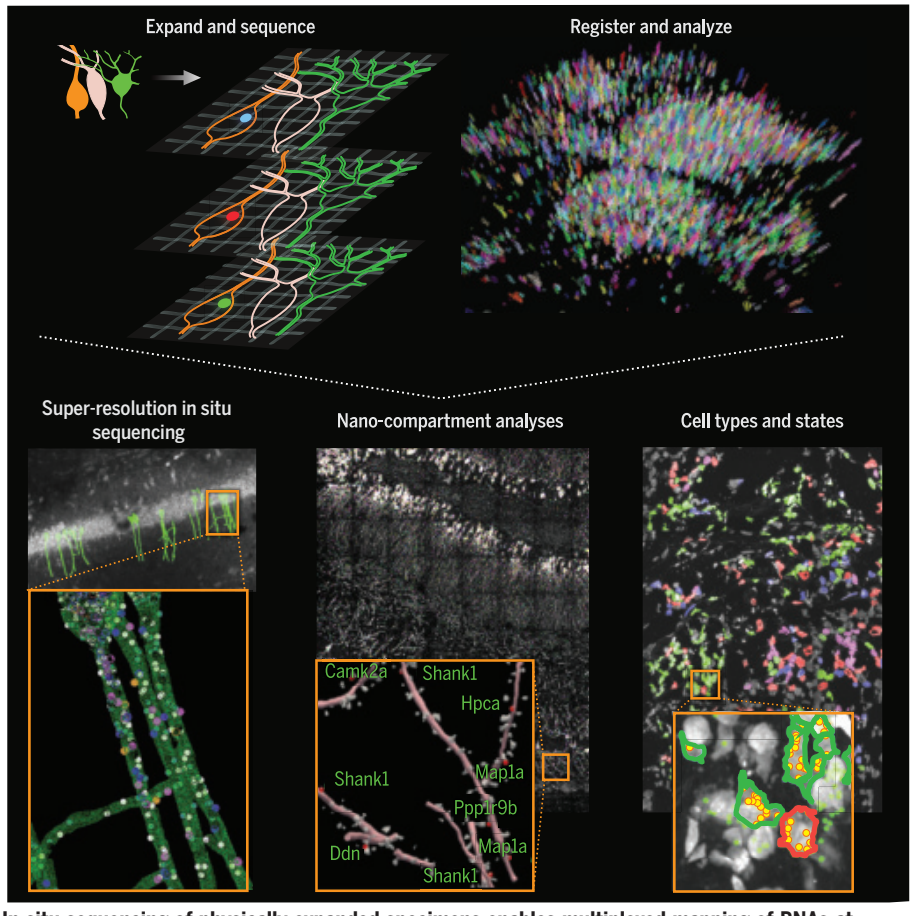

In situ sequencing of physically expanded specimens enables multiplexed mapping of RNAs at nanoscale, subcellular resolution throughout intact tissues. (Top) Schematics of physical expansion and in situ sequencing (left) and image analysis (right). (Bottom) Characterization of nanoscale transcriptomic compartmentalization in mouse hippocampal neuron dendrites and spines (left and middle) and maps of cell types and states in a metastatic human breast cancer biopsy (right).

RATIONALE: We reasoned that physically expanding specimens by adapting expansion microscopy could help support spatially precise in situ sequencing. The physical expansion of specimens provides two benefits: First, it enables ordinary microscopes to achieve nanoscale effective resolution. Second, by anchoring RNA molecules to a polymer network, digesting away other molecules, and then expanding the polymer in water, RNAs become more accessible. By creating a chemical process that enables enzymatic reactions to proceed in expanded specimens, we enabled in situ fluorescent sequencing of RNA with high spatial precision, which we term expansion sequencing (ExSeq). We developed both untargeted (i.e., not restricted to a predefined set of genes) and targeted versions of ExSeq.

RESULTS: Using untargeted ExSeq, we showed the presence of transcripts that retain their introns, transcription factors, and long noncoding RNAs in mouse hippocampal neuron dendrites. Using targeted ExSeq, we observed layer-specific cell types across the mouse visual cortex and RNAs in nanoscale compartments of hippocampal pyramidal neurons, such as dendritic spines and branches. We found that spines could exhibit distributions of mRNAs different from those exhibited by adjacent dendrites. Moreover, we found patterns of similarity between the dendritic profiles of RNAs in different types of hippocampal neurons. In a human metastatic breast cancer biopsy, we mapped how cell types expressed genes differently as a function of their distance from other cell types, identifying, for example, cellular states of immune cells specific to when they were close to tumor cells.

CONCLUSION: ExSeq enables highly multiplexed mapping of RNAs—from nanoscale to system scale—in intact cells and tissues. We explore how RNAs are preferentially targeted to dendrites and spines of neurons, suggesting RNA localization principles that may generalize across different cell types. We also examine gene expression differences in cell types as a function of their distance from other cell types in the context of a human cancer, which may yield insights into future therapeutic approaches that take cellular interactions into account. ■

The list of author affiliations is available in the full article online.
*These authors contributed equally to this work.
†This author made key and essential contributions to the early stages of the project.
‡Corresponding author. Email: gchurch@genetics.med.harvard.edu (G.M.C.); edboyden@mit.edu (E.S.B.)
§These authors contributed equally to this work.
Cite this article as S. Alon *et al.*, *Science* **371**, eaax2656 (2021). DOI: 10.1126/science.aax2656

READ THE FULL ARTICLE AT
https://doi.org/10.1126/science.aax2656

RESEARCH ARTICLE SUMMARY

INNATE IMMUNITY

Human NLRP1 is a sensor for double-stranded RNA

Stefan Bauernfried, Matthias J. Scherr, Andreas Pichlmair, Karl E. Duderstadt, Veit Hornung*

INTRODUCTION: The innate immune system constitutes the first line of host defense. To detect pathogens, it uses a set of germline-encoded pattern recognition receptors (PRRs) that have evolved to sense the presence of non-self. PRRs can either directly sense pathogens or they can indirectly respond to the perturbation of cellular homeostasis during the course of pathogen infection. One group of cytosolic PRRs are inflammasome-forming nucleotide-binding domain leucine-rich repeat (NLR) proteins. After activation, they form high-molecular-weight signaling complexes that result in the direct or ASC-dependent engagement and activation of caspase-1. Active caspase-1, in turn, cleaves and thereby activates the highly proinflammatory cytokine interleukin-1β (IL-1β). In addition, caspase-1 cleaves gasdermin D (GSDMD), which results in the activation of a lytic cell death pathway known as pyroptosis. NLRP1 was one of the first inflammasome-forming PRRs to be identified, yet its role in pathogen defense in the human system remains poorly defined.

RATIONALE: NLRP1 is highly expressed and functional in epithelial barrier tissues, e.g., in keratinocytes. Unlike myeloid immune cells, keratinocytes appear to express only a limited set of inflammasome sensors, which makes them an interesting model system in which to study the role of NLRP1. To identify a potential NLRP1 stimulus, we used an immortalized keratinocyte cell line to screen a panel of viral pathogens for their potential inflammasome activation.

RESULTS: Screening different types of viruses, we found that Semliki Forest virus (SFV) triggered inflammasome activation in keratinocytes in an NLRP1-dependent fashion. As a positive-strand RNA virus, SFV generates ample amounts of double-stranded (ds) RNA during its life cycle, and the production of dsRNA coincided with the activation of NLRP1. We therefore tested poly(I:C), a synthetic dsRNA analog, and in vitro transcribed dsRNA molecules for inflammasome activation. These experiments revealed that NLRP1 was indeed stimulated by dsRNA, yet long dsRNA was required to trigger activation. These findings could be recapitulated in primary keratinocytes and immortalized bronchial epithelial cells. To determine whether this phenotype was specific for human NLRP1, we reconstituted NLRP1-deficient keratinocytes with transgenes for either human *NLRP1* or murine *Nlrp1b*. Indeed, only keratinocytes expressing human NLRP1 were responsive to dsRNA. dsRNA-induced inflammasome activation was independent of other known dsRNA sensors, because their depletion did not decrease NLRP1 activation after dsRNA delivery. Because of these findings, we then investigated whether NLRP1 directly interacted with dsRNA. Pull-down studies revealed that human NLRP1, but not murine NLRP1B, could be immunoprecipitated by dsRNA. Using recombinant proteins, we found that NLRP1 bound nucleic acids with high affinity, predominantly through its leucine-rich repeat (LRR) domain. To ascertain whether dsRNA binding activated NLRP1 in vitro, we subsequently studied ATP hydrolysis of NLRP1 as a proxy for its activation. These studies revealed that dsRNA, but not dsDNA, triggered ATPase activity.

CONCLUSION: In 2002, human NLRP1 became the first inflammasome-forming sensor to be characterized. However, no direct ligand had been identified so far. Our work demonstrates that human NLRP1 is a bona fide nucleic acid sensor. NLRP1 directly interacts with dsRNA, a typical intermediate of viral replication, which subsequently results in the activation of the inflammasome pathway. ■

*Corresponding author. Email: hornung@genzentrum.lmu.de
Cite this article as: S. Bauernfried *et al.*, *Science* **371**, eabd0811 (2021). DOI: 10.1126/science.abd0811

READ THE FULL ARTICLE AT
https://doi.org/10.1126/science.abd0811

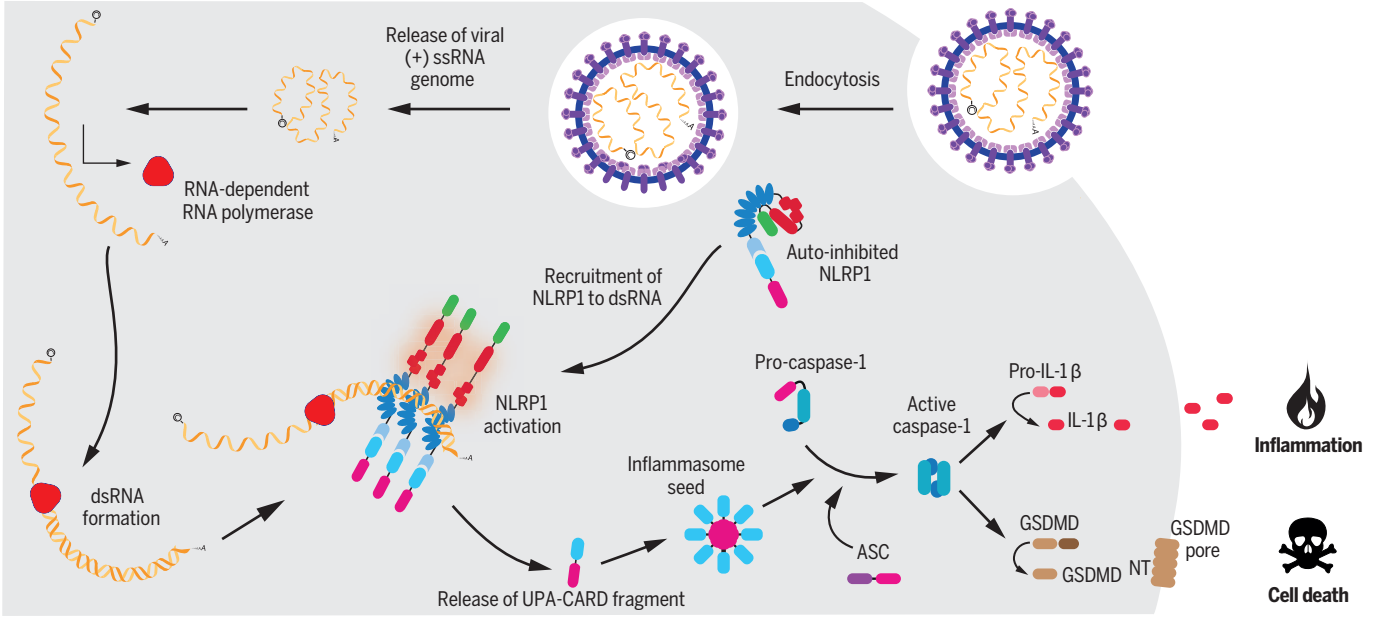

The pathogen-associated molecular pattern dsRNA interacts with human NLRP1 and leads to inflammasome activation. Infection with a positive-strand RNA virus leads to the formation of dsRNA, and the generated dsRNA recruits human NLRP1. This results in the activation of NLRP1, which leads to the formation of an inflammasome complex. Inflammasome activation results in IL-1β maturation and the induction of pyroptosis.

RESEARCH ARTICLE SUMMARY

AGING

Inhibition of prostaglandin-degrading enzyme 15-PGDH rejuvenates aged muscle mass and strength

A. R. Palla, M. Ravichandran, Y. X. Wang, L. Alexandrova, A. V. Yang, P. Kraft, C. A. Holbrook, C. M. Schürch, A. T. V. Ho, H. M. Blau*

INTRODUCTION: Currently there are no approved treatments for sarcopenia, the age-dependent loss of skeletal muscle mass and strength that constitutes a major public health problem affecting ~15% of individuals aged 65 or older. This dysfunction is due to aberrant protein and organelle turnover, inflammation, neuromuscular degeneration, and reduced mitochondrial function. Owing to its multifactorial etiology, untangling the causal molecular pathways to identify therapeutic targets to delay or reverse sarcopenia has proven challenging. Here we identify increased accumulation of the prostaglandin-degrading enzyme, 15-hydroxyprostaglandin dehydrogenase (15-PGDH), as a hallmark of aged tissues, including skeletal muscle, and show that it can be therapeutically targeted to enhance muscle mass and strength.

RATIONALE: Previously we determined that in young mice, prostaglandin E_2 (PGE_2), a lipid metabolite generated from membrane fatty acids, stimulates muscle stem cells and is required to repair damaged muscles, in agreement with reports of PGE_2's function in hematopoietic, bone, colon, and liver regeneration. However, there is a paucity of knowledge regarding the role of PGE_2 in muscle aging. We hypothesized that PGE_2 concentration and signaling go awry in aged tissues. In accordance, we found that PGE_2 is reduced as a result of increased amounts of 15-PGDH and that short-term inhibition of this catabolic enzyme suffices to rejuvenate mitochondrial function, induce hypertrophy, and increase aged muscle strength.

RESULTS: Using liquid chromatography coupled to tandem mass spectrometry (LC-MS/MS) to distinguish closely related prostaglandin family members, we determined that concentrations of PGE_2 are reduced in aged murine skeletal muscles. We found that the decrease in PGE_2 is due to increased prostaglandin catabolism by elevated 15-PGDH. By using multiplex tissue imaging (CODEX, co-detection by indexing) to visualize localization of multiple markers together with 15-PGDH, we identified myofibers and tissue-resident macrophages as the source of 15-PGDH in the aged muscle microenvironment. Inhibition of 15-PGDH, either by localized genetic knockdown using a short hairpin RNA or systemic delivery of a small-molecule inhibitor, countered muscle atrophy and markedly increased the cross-sectional area of myofibers, muscle mass, strength, and endurance in aged mice after 1 month of treatment. The potency of 15-PGDH in mediating an aging phenotype is underscored by the atrophy and loss of muscle mass and strength, observed after 1 month of ectopic expression of the enzyme in muscles of young mice. Genetic loss-of-function experiments confirmed that PGE_2 and its receptor EP4 mediate these effects. Mechanistically, inhibition of 15-PGDH in aged muscles affects several signaling pathways: decreasing transforming growth factor–β (TGF-β) signaling and the ubiquitin proteosome pathway and increasing mitochondrial biogenesis and function. Transmission electron microscopy (TEM) of muscles after 15-PGDH inhibition revealed an increase in the number of intermyofibrillar mitochondria and restoration of mitochondria morphology similar to that of young muscles. In accordance with the increase in mitochondrial function, we observed an increase in autophagy flux. These synergistic interactions culminate in a marked increase in muscle mass and strength in sarcopenic aged mice.

CONCLUSION: We identified the prostaglandin-degrading enzyme, 15-PGDH, as a driver of muscle atrophy. Overexpression of this enzyme in young mice induced muscle loss, and short-term inhibition overcame the muscle wasting associated with aging. A major advantage of our approach is that it restores PGE_2 in aged muscles to physiological levels characteristic of young muscles. The augmented PGE_2 orchestrates several complementary signaling pathways, leading to increased mitochondrial numbers and function. Our findings have broad relevance, as elevated 15-PGDH expression is detected in a multiplicity of aged tissues. The pleiotropic beneficial effects leading to the muscle rejuvenation seen upon inhibition of 15-PGDH identify the enzyme as a pivotal molecular determinant of aging that can be therapeutically targeted to surmount the muscle weakness associated with sarcopenia. ■

The list of author affiliations is available in the full article online.
*Corresponding author. Email: hblau@stanford.edu
Cite this article as A. R. Palla *et al.*, *Science* **371**, eabc8059 (2021). DOI: 10.1126/science.abc8059

READ THE FULL ARTICLE AT
https://doi.org/10.1126/science.abc8059

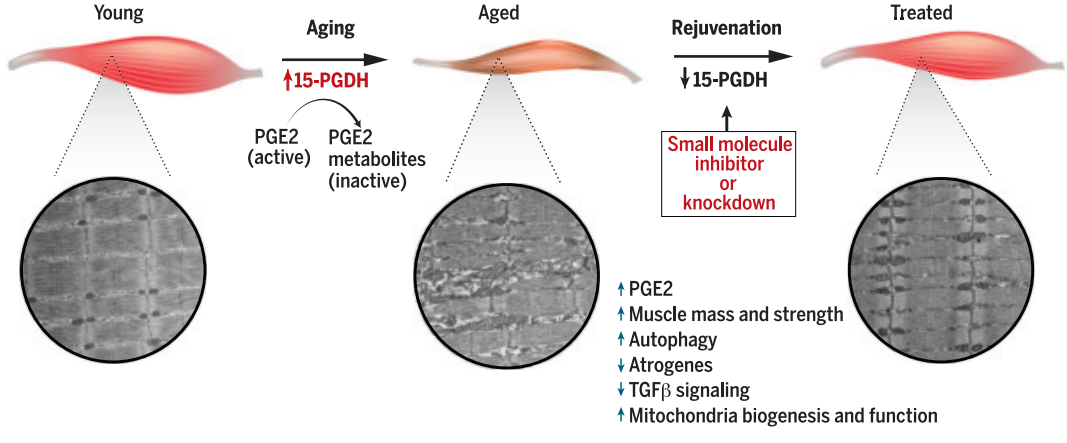

15-PGDH inhibition in aged mice leads to increased skeletal muscle mass and strength. The prostaglandin-degrading enzyme, 15-PGDH, is increased in aged muscles and drives age-related muscle atrophy. Inhibition of 15-PGDH by a small molecule or genetic depletion (knockdown) in aged mice leads to increased PGE_2, decreased atrogene expression and TGF-β signaling, and increased autophagy and mitochondrial biogenesis and function, culminating in muscle hypertrophy and increased force.

RESEARCH ARTICLE SUMMARY

NEURODEVELOPMENT

Postnatal connectomic development of inhibition in mouse barrel cortex

Anjali Gour, Kevin M. Boergens, Natalie Heike, Yunfeng Hua, Philip Laserstein, Kun Song, Moritz Helmstaedter*

INTRODUCTION: The establishment of neuronal circuits in the cerebral cortex of mammals is an important developmental process extending over embryonic and postnatal periods, from the first occurrence of differentiated neurons to the final formation of precise synaptic innervation patterns, which are further shaped by experience. Of special interest is the establishment of inhibitory circuits, constituted by nerve cells that produce γ-aminobutyric acid as a neurotransmitter (GABAergic interneurons), which are known to form intricate neuronal networks with a distinctive degree of synaptic preference for the types of postsynaptic structures to innervate. While the time course of neuronal migration and integration of interneurons is beginning to be understood and the first molecular cues for selectively enhancing and suppressing synaptic innervation have been identified, a comprehensive mapping of cortical inhibitory innervation during postnatal development is missing.

RATIONALE: With the development of high-throughput three-dimensional electron microscopy (3D EM) imaging and analysis of nervous tissue, the goal of systematically mapping neuronal connectivity in ever-increasing volumes of brain tissue has become possible. This methodological approach, connectomics, has so far been primarily aimed at comprehensive circuit mapping in complete smaller animals' brains or parts of larger brains. An additional advantage of higher-throughput connectomic analysis, however, is the opportunity to repeat similar experiments under many experimental conditions. This advantage is particularly relevant for the study of developmental processes, which naturally require the measurement of multiple time points. In this study, we made use of these technological advances to map neuronal connectivity in 13 3D EM datasets with a focus on the primary somatosensory cortex of mouse during postnatal development.

RESULTS: We acquired and analyzed data from layers 4 and 2/3 of mouse cortex over the period during which synaptic networks are formed within the neocortex. We studied data from mice at 5, 7, 9, 14, 28, and 56 days of age, corresponding to the development from baby to adult. We analyzed the formation of interneuronal synaptic preference for subsections of neurons, their cell bodies, their initial part of the axon, and apical dendrites. We found that only axons with preference for apical dendrites already show high target preference in the early time points measured. By contrast, preference for innervation of cell bodies was gradually established, with a peak in developmental change between postnatal days 7 and 9. During this time, preference for cell bodies increased almost threefold, and the density of synapses along these axons dropped by almost twofold. With this, we found that while for apical dendrite–preferring interneurons, mechanisms of ab initio target choice are plausible, cell body innervation could be established by the removal of inadequately placed synapses along the presynaptic axon. For the innervation of the initial section of axons, we found that axo-axonic innervation initially constitutes only a minor fraction of the innervation and develops to provide ~50% of the synaptic input to the axon initial segment. Our data indicate that synaptic preference for axon initial segments develops before the formation of special vertically oriented axonal configurations called cartridges.

CONCLUSION: The first comprehensive mapping of inhibitory circuit development in mammalian cortex provides quantitative insights into the formation of circuits and the precise time course for the establishment of synaptic target preference. The approach of connectomic screening also may prove useful for future studies of experimental interference with relevant genetic and environmental conditions of circuit formation in the mammalian brain. ■

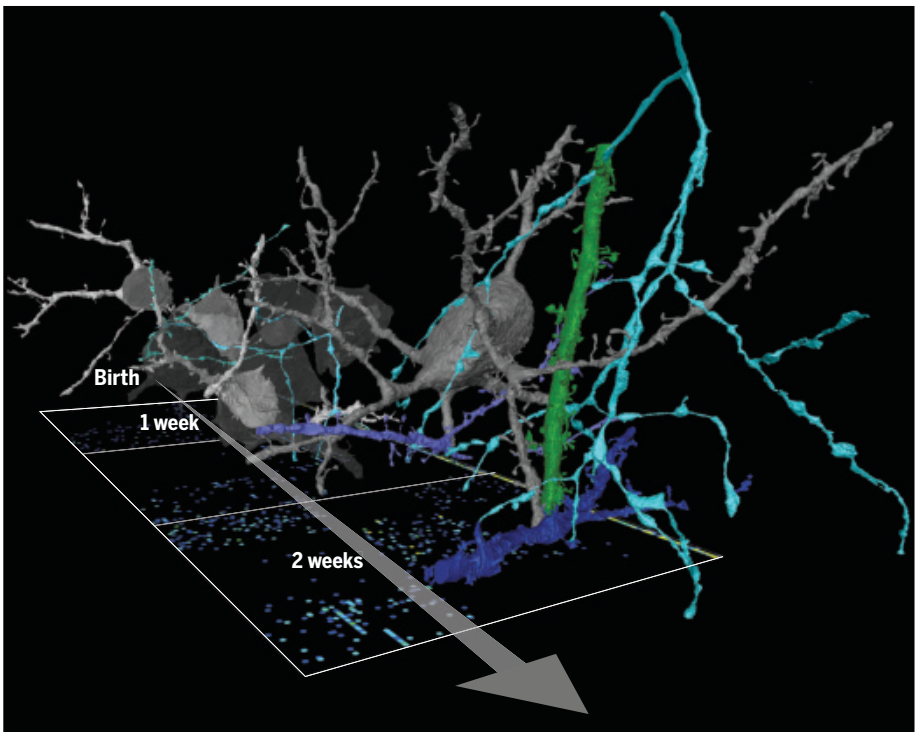

Connectomic mapping of inhibitory circuits during postnatal development. Data from 7, 9, and 14 days of age are shown, with cell bodies, axons, and dendrites reconstructed. Under the datasets, matrices describing the neuronal connectivity ("connectomes") are displayed. Synaptic preference for cell bodies, dendrites, and axon initial segments is a hallmark of circuit structure in the cerebral cortex, and this connectomic developmental screening study uncovers precise timelines of the synaptic preference development in the cortex.

Department of Connectomics, Max Planck Institute for Brain Research, Frankfurt, Germany.
*Corresponding author. Email: mh@brain.mpg.de
Cite this article as A. Gour *et al.*, *Science* **371**, eabb4534 (2021). DOI: 10.1126/science.abb4534

READ THE FULL ARTICLE AT
https://doi.org/10.1126/science.abb4534

RESEARCH ARTICLE

CLIMATE

Aerosol-cloud-climate cooling overestimated by ship-track data

Franziska Glassmeier[1,2,3]*, Fabian Hoffmann[3,4,5], Jill S. Johnson[6], Takanobu Yamaguchi[3,4], Ken S. Carslaw[6], Graham Feingold[4]

The effect of anthropogenic aerosol on the reflectivity of stratocumulus cloud decks through changes in cloud amount is a major uncertainty in climate projections. In frequently occurring nonprecipitating stratocumulus, cloud amount can decrease through aerosol-enhanced cloud-top mixing. The climatological relevance of this effect is debated because ship exhaust only marginally reduces stratocumulus amount. By comparing detailed numerical simulations with satellite analyses, we show that ship-track studies cannot be generalized to estimate the climatological forcing of anthropogenic aerosol. The ship track–derived sensitivity of the radiative effect of nonprecipitating stratocumulus to aerosol overestimates their cooling effect by up to 200%. The offsetting warming effect of decreasing stratocumulus amount needs to be taken into account if we are to constrain the cloud-mediated radiative forcing of anthropogenic aerosol.

Clouds interact with atmospheric radiation and therefore play an important role in the planetary energy balance. Their net effect is to cool the planet by reflecting incoming solar radiation (*1*). Covering large parts of the subtropical oceans, stratocumulus (Sc) clouds are by far the largest contributor to this cooling (*2*). Effects on cloud reflectivity caused by the production of atmospheric aerosol particles are the most uncertain anthropogenic forcing of the climate system (*3*, *4*). As an illustration of this effect, exhaust from ships can create "ship tracks" that manifest as bright linear features in Sc decks. This brightening arises because exhaust-aerosol particles act as nuclei of cloud droplets. A greater abundance of particles means that a cloud consists of more, but smaller, droplets, which enhances the radiant energy reflected to space (*5*). Changes in the number and size of cloud droplets also influence cloud physical processes (*6*–*11*); for the example of ship tracks, this means that the amount of cloud water inside and outside of a track may evolve differently. Globally, the large uncertainty in the cloud-mediated aerosol forcing arises from the unknown magnitude of such adjustments of cloud water in response to aerosol-induced perturbations (*3*, *12*, *13*). Here, we show that despite providing a illustration of aerosol-cloud interactions, ship tracks do not provide suitable data to estimate the magnitude of cloud liquid-water adjustments in a polluted climate, in contrast with the common assumption that ship-track data can quantify those adjustments (*14*–*17*).

In nonprecipitating Sc with their approximately full cloud cover, cloud response to aerosol perturbations is commonly quantified by the sensitivity (*4*, *18*, *19*)

$$S = \frac{\mathrm{d}A_\mathrm{c}}{\mathrm{d}N} = \frac{A_\mathrm{c}(1-A_\mathrm{c})}{3N}\left(1+\frac{5}{2}\frac{\mathrm{dln LWP}}{\mathrm{dln}N}\right) \quad (1)$$

of cloud albedo A_c to cloud droplet number N. The first term on the right-hand side of Eq. 1 quantifies the albedo effect of changing droplet number when keeping the vertically integrated amount of liquid water, or liquid-water path (LWP), constant; the second term accounts for cloud water adjustments as quantified by the relative sensitivity dlnLWP/dln$N$ of LWP to N. Numerical values for LWP adjustments dlnLWP/dln$N$ have been derived from detailed modeling and satellite studies (*8*, *14*–*17*, *20*–*25*). Both approaches have recently converged on the insight that the sign of LWP adjustments is regime-dependent (Fig. 1). Adjustments tend to be positive under precipitating conditions where the addition of particles decreases drop size, increases colloidal stability, and allows for an accumulation of liquid water (*6*). A positive LWP adjustment thus implies thicker, more reflective clouds that have a stronger cooling effect. In the current work, we focus on nonprecipitating Sc. Morphologically, this regime features an approximately hexagonal arrangement of cloudy (closed) cells, whereas the precipitation-dominated regime tends to occur as an inverse pattern of open cells (*14*, *26*). Occurring in 50 to 80% of observations, the nonprecipitating regime is at least as common as the precipitating regime (*25*, *27*). Nonprecipitating Sc feature negative adjustments, indicating a decrease in LWP for higher aerosol concentrations. The decrease in LWP stems from the accelerated and stronger evaporation of cloud liquid in higher aerosol conditions as the Sc mixes with dry air from above the cloud (entrainment). Smaller droplets evaporate more efficiently because they provide a larger surface (for a given total amount of liquid) and reside closer to the entrainment interface than larger droplets owing to reduced gravitational settling, which increases the potential for evaporation (*7*–*11*, *28*). Negative LWP adjustment values indicate thinner, less reflective clouds and a weaker cooling effect. When the darkening effect of cloud thinning is stronger than the brightening of increased N, negative LWP adjustments can even imply a warming effect. In nonprecipitating Sc, this is the case when dlnLWP/dln$N$ < −2/5 such that Eq. 1 becomes negative (orange shading in Fig. 1).

In addition to the distinction between the entrainment- and precipitation-dominated regimes, satellite studies have identified above-cloud moisture as an important control on the magnitude of LWP adjustments in Sc (*15*, *25*, *29*). This is consistent with process understanding from detailed cloud modeling studies [large-eddy simulation (LES)], where drier above-cloud conditions correspond to a stronger aerosol effect on entrainment (Fig. 1). As another factor behind the variability of adjustment estimates, the effects of N-LWP covariability that results from large-scale covariability of aerosol and moisture are discussed in (*15*, *30*). As an example of this confounding effect, compare a maritime situation with a clean and moist atmosphere to a polluted and drier continental case. Observations from these two cases will likely show that higher N is correlated with lower LWP, suggesting a negative LWP adjustment. Clearly, the "adjustment" quantified here is not related to the effect of aerosol on cloud properties driven by entrainment or precipitation formation that we seek to capture but rather to large-scale conditions.

A special appeal of ship tracks has been that they are not affected by external covariability because the large-scale meteorological conditions are the same inside and outside of the track. Accordingly, results from targeted satellite analyses of ship tracks (*14*, *16*, *20*) have been assigned higher credibility than climatological satellite studies, for which external covariability cannot be ruled out. In particular, the comparably large absolute adjustment values found in the latter studies have been attributed to aerosol-moisture covariability, assuming that weak-to-almost absent LWP adjustments identified by ship-track studies

[1]Department of Geoscience and Remote Sensing, Delft University of Technology, P.O. Box 5048, 2600 GA Delft, Netherlands. [2]Department of Environmental Sciences, Wageningen University, P.O. Box 47, 6700 AA Wageningen, Netherlands. [3]Cooperative Institute for Research in Environmental Sciences, University of Colorado Boulder, Boulder, CO 80309, USA. [4]NOAA Chemical Sciences Laboratory, 325 Broadway, Boulder, CO 80305, USA. [5]Institut für Meteorologie, Ludwig-Maximilians-Universität, Theresienstrasse 37, 80333 München, Germany. [6]School of Earth and Environment, University of Leeds, Woodhouse Lane, Leeds LS2 9JT, UK.
*Corresponding author. Email: f.glassmeier@tudelft.nl

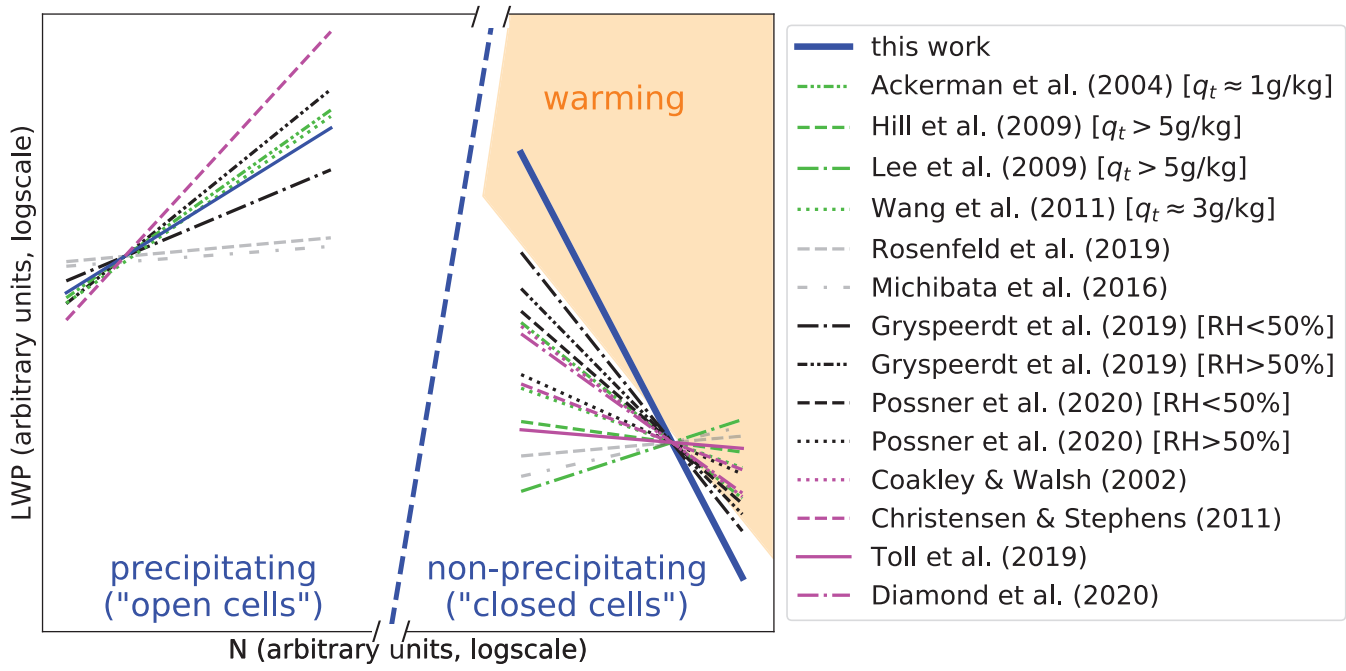

Fig. 1. Reported log-log-linear relationships between LWP and *N* in comparison to this work. Lines are based on reported slopes (table S1), and axis intercepts have been added as suitable for illustration. The dashed blue line indicates a critical droplet radius for precipitation formation (based on a mean droplet radius of 12 μm at cloud top for an adiabatic condensation rate of 2.5 × 10^{-6} kg m^{-4}), which separates the precipitation-dominated regime on the left from the nonprecipitating, entrainment-dominated regime on the right. The latter is the focus of this study. Colors distinguish results from LESs (green), climatological satellite studies (black), and satellite studies of ship tracks (magenta). Results in gray are shown for completeness but are not directly comparable, owing to differences in methodology. For simulation and climatological studies, above-cloud absolute humidity (q_t) or ranges of relative humidity (RH) are indicated. Solid blue lines show values derived in this work (tables S1 and S4; in particular, dlnLWP/dln*N* = −0.64 in the entrainment regime). The orange shading indicates where LWP adjustments are sufficiently negative to lead to climate warming rather than cooling based on the sign of albedo sensitivity *S* (Eq. 1).

(*14*, *16*, *20*) provide the best estimate for LWP adjustment. In contrast to this assumption, a recent study of a shipping lane reports considerably negative adjustment values (*17*).

We show that the current emphasis on satellite studies of ship tracks to estimate LWP adjustments leads to an overestimation of the cooling effect of aerosols in Sc. We furthermore reconcile the broad range of reported adjustment estimates and discuss implications of our results for identifying alternatives to ship-track studies. Our argument is illustrated in Fig. 2 and builds on two key results: (i) LWP adjustments become more negative as Sc decks evolve toward a steady state, and (ii) in ship tracks, this temporal evolution does not proceed long enough to be representative of Sc decks in a polluted climate.

Effect of cloud field evolution toward steady state on adjustment strength

Climatological satellite studies derive LWP adjustments dlnLWP/dln*N* as slopes of linear regression lines through median LWP values in *N*-bins. We apply this methodology to an ensemble of 12-hour-long LES time series that resembles the scope of a satellite dataset (supplementary materials). To discuss the time dependence of adjustments, we separately derive LWP adjustments per time step. Figure 3A and fig. S1A illustrate this for t = 2 hours (magenta) and t = 12 hours (green). Considering all time steps 2 hours ≤ t ≤ 12 hours shows that the LWP adjustment becomes increasingly negative over time (Fig. 3B). This behavior results from the sampling of the *N*-LWP space by our simulations, which evolves over time. By construction, our dataset initially features an uncorrelated sampling (supplementary materials). This explains the almost horizontal regression line and corresponding vanishing adjustment observed at t = 2 hours. An initial covariability of *N* and LWP values would have imprinted an initial correlation and corresponding adjustment value between *N* and LWP.

As our simulations collectively evolve further from the initial state, they approach a steady-state LWP line (blue curve in Fig. 3A and fig. S1) and the sampling of the *N*-LWP space features an increasingly negative correlation. This relationship replaces the initial relationship because the evolution speed of Sc systems scales with their distance to the steady-state line (fig. S3). Had we run our simulations beyond 12 hours, all ensemble members would eventually have reached their steady-state LWP. This means that for $t \to \infty$ only the steady-state line is sampled and the LWP adjustment is quantified by the slope of this line. Because the slope of the steady-state LWP line reflects the *N*-dependence of entrainment (*31*), the LWP adjustment at $t \to \infty$, $\mathrm{dlnLWP}_\infty/\mathrm{dln}N$, is a direct quantification of *N*—or more generally aerosol—effects on cloud processes.

Using Gaussian-process emulation, we determine the location of this steady-state line in *N*-LWP space from limited-duration time series (supplementary materials). For nonprecipitating Sc, we obtain $\mathrm{dlnLWP}_\infty/\mathrm{dln}N = -0.64$ (Fig. 3A; uncertainty quantification in table S4). This value constitutes a lower bound; a more negative adjustment value would require a stronger *N*-dependent entrainment and therefore drier above-cloud conditions than prescribed for our simulations. This is not realistic because our simulations feature very dry conditions already (fig. S5 and table S2). Figure 1 also supports −0.64 ≤ dlnLWP/dln*N* as a lower bound on previous estimates from the literature. We contrast this value with the positive value of the precipitation-dominated branch, for which we determine a slope of 0.21 (table S4) that lies well within the reported range (Fig. 1).

The equilibration of adjustments to the steady-state value is the collective result of the equilibration of individual Sc systems.

This allows us to derive that the observed time dependence of LWP adjustments is well described as an exponential decay toward $d\ln LWP_\infty/d\ln N$ (Fig. 3B)

$$\mathrm{adj}(\Delta t) = \frac{d\ln LWP_\infty}{d\ln N}\left[1 - \exp\left(-\frac{\Delta t}{\tau_{adj}}\right)\right],$$

$$\tau_{adj} \approx \tau\left(1 - 1.6\,\frac{d\ln LWP_\infty}{d\ln N}\right) = 2.0\,\tau = 20 \text{ hours} \quad (2)$$

with an adjustment equilibration time scale τ_{adj} that scales with the equilibration time scale of an individual system, τ = 9.6 hours, and with adjustment strength (supplementary materials). The time dependence of LWP adjustments on a time scale of almost a day is in marked contrast to the radiative effect of an increased cloud droplet number, which takes full effect in 5 to 10 min (supplementary materials).

The extent and interpretation of LWP adjustments in a Sc field depends on the proximity of the system's LWP to its steady-state LWP. Adjustments based on sampling transient LWP, far from steady state, reflect *N*-LWP covariability that is externally prescribed on the system, i.e., a mere association; LWP adjustments diagnosed from steady systems reflect aerosol-dependent cloud processes, i.e., a causal relationship; intermediate degrees of proximity result in a mixture of both.

Insufficient time for evolution of ship tracks toward steady state

The degree of proximity of an ensemble, or sampling, of Sc systems to its steady-state LWP adjustment can be estimated by comparing the duration of its evolution under an aerosol perturbation, Δt, to the characteristic adjustment equilibration time scale, τ_{adj} = 20 hours (Eq. 2). From a Lagrangian perspective, a Sc system is exposed to an aerosol background throughout its lifetime: In the absence of precipitation, the aerosol coevolves with the boundary layer height (*25*), i.e., on a multiday-long time scale (*32*). Typical Sc trajectories in the subtropics persist on time scales of days, Δt_{clim} > 48 hours, before they transition into the shallow cumulus regime owing to advection toward higher sea-surface temperatures (*33*). Because $\Delta t_{clim} \gg \tau_{adj}$, the climatological sampling of Sc is dominated by strongly equilibrated LWPs. Although not necessarily composed of steady-state LWPs, we can assume that the LWP climatology of nonprecipitating Sc is better characterized as a sampling of steady-state LWPs than as one of highly transient LWPs. Steady-state values as a feasible approximation for Sc properties are in line with previous theoretical studies (*34*). A substantial probability of Sc being observed close to their steady state is also consistent with relatively narrow climatological distributions of Sc LWPs (*15*, *35*) that indicate dominant sampling of a steady-state line. The scatter around this line corresponds to transient LWPs.

Sc decks being strongly adjusted to the aerosol background in which they evolve has implications for constraining the anthropogenic radiative forcing; LWP adjustments need to compare Sc that are strongly adjusted to an aerosol background typical of an industrial-era aerosol climatology (cyan circle in Fig. 4) to Sc decks that are strongly adjusted to a preindustrial aerosol background (orange circle). Climatological satellite studies are suitable for this quantification because they predominantly sample strongly adjusted LWPs close to steady state. As discussed in the previous section, this specifically means that such studies capture cloud processes and are only weakly confounded by externally induced *N*-LWP covariability.

Ship-track data are obtained throughout the life of the track, with fresh tracks more likely to be sampled owing to their better visibility. With a typical lifetime for ship tracks of 6 to 7 hours (*36*, *37*), this corresponds to an average evolution time until sampling of $\Delta t_{ship} \approx 3$ hours. Because the characteristic equilibration time exceeds the typical evolution time at sampling, $\Delta t_{ship} \ll \tau_{adj}$, we conclude that LWPs sampled from ship tracks are not representative of the aerosol-cloud interaction processes, specifically entrainment, that manifest as a Sc system approaches a steady-state LWP. Instead, their sampling of transient LWPs carries a strong imprint of their specific initial conditions. To characterize these conditions, we describe ship-track studies as a sampling within two different *N*-bins, one representing out-of-track conditions and the other in-track conditions (Fig. 4). Because LWP adjustments are not instantaneous, the LWP distributions within these two bins are identical when the ship exhaust first makes contact with the cloud. As for the idealized initial conditions in our dataset, this corresponds to an initial adjustment of zero (purple regression line in Fig. 4). After the perturbation, the in-track distribution evolves toward an asymptotic LWP value that is different from that of the out-of-track LWP. Owing to the short duration of this evolution until sampling, adjustment values diagnosed from ship tracks remain small. Indeed, evolution according to Eq. 2 corresponds to an adjustment value of

$$\mathrm{adj}(\Delta t_{ship} = 3 \text{ hours}) = -0.1$$

which matches reported values ranging from −0.2 to 0.0 (table S1). By contrast, when

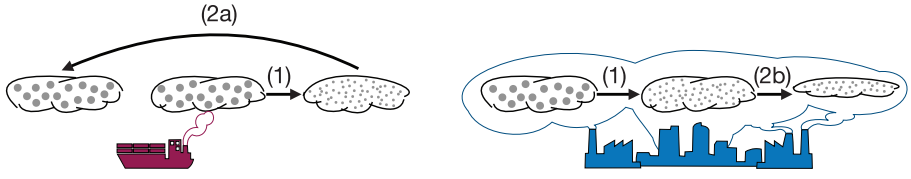

Fig. 2. LWP adjustments in ship tracks as compared with industrial-era pollution. As an initial response to the aerosol perturbation, both situations feature cloud brightening through more, but smaller, cloud droplets at constant LWP (step 1). The ship track then returns to its original state because the perturbation ceases after a few hours (step 2a). An aerosol background that is enhanced because the climatological aerosol background is perturbed, by contrast, persists for days and allows for LWP to equilibrate toward a new steady state that is characterized by increased entrainment efficiency and a lower LWP (step 2b).

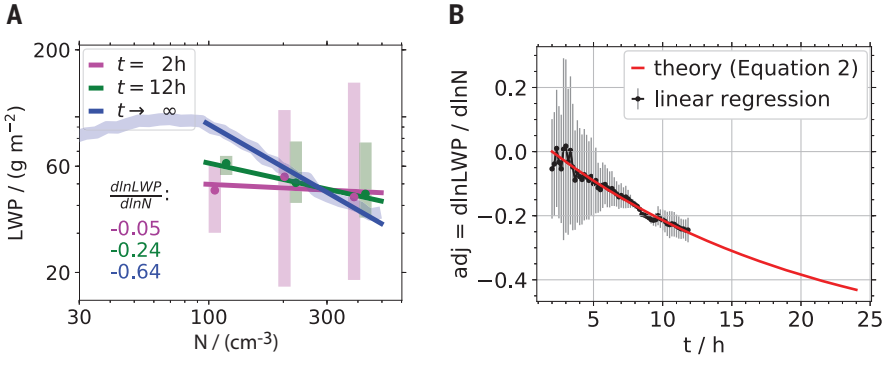

Fig. 3. Time dependence of LWP adjustments. (**A**) Data points with error bars show median and 25th-75th percentile of simulated LWP at t = 2 hours (magenta) and t = 12 hours (green) for the *N*-bins indicated in fig. S1A. The light blue curve indicates the steady-state LWP as in Fig. S1. Regression lines with slopes $d\ln LWP/d\ln N$ are indicated. (**B**) Each data point indicates an adjustment slope obtained as in (A), with error bars for 2 hours ≤ t ≤ 12 hours. The red line shows the theoretically expected exponential decay (Eq. 2).

sampling a climatologically polluted situation, adjustments can evolve toward more negative values before being sampled and values of adj(Δt_{clim} = 48 hours) = −0.6, close to the asymptotic value of −0.64 (Fig. 3A), are obtained.

Although ship exhaust may, at first glance, seem to be an intriguing proxy for aerosol conditions typical of the industrial-era aerosol climatology, it does not perturb the pristine background for a sufficiently long time (Fig. 2). In other words, typical LWPs in ship tracks are not comparable to LWPs in Sc that experience a higher aerosol background owing to an anthropogenic shift of the aerosol climatology (cyan circle versus triangle in Fig. 4).

Implications for the cloud-mediated radiative forcing of anthropogenic aerosol

Ship track–derived LWP adjustments are less negative than the LWP adjustment exhibited by a Sc deck under climatologically polluted conditions. Because negative adjustments mean that an increased aerosol load leads to cloud thinning and reduced reflectivity, they imply a warming effect that offsets the cooling associated with cloud brightening (Eq. 1). Ship-track studies underestimate this offsetting warming effect of LWP adjustments (Fig. 2). We contend, therefore, that using ship track–derived adjustment values to estimate the cloud-mediated radiative forcing of anthropogenic aerosol underestimates the absolute effect of LWP adjustments on the radiative forcing. With −0.64 ≤ dlnLWP/dln$N$ as a lower bound (Fig. 3), this underestimation corresponds to an overestimation of the cooling effect of aerosols on nonprecipitating Sc of up to 200% (supplementary materials). Because nonprecipitating Sc occur frequently (*25*, *27*), this warming effect may offset the cooling effect of positive LWP adjustments in precipitating Sc in the overall climate effect of Sc.

Our results are consistent with recent satellite estimates of LWP adjustments in Sc (*15*, *25*). Our insight that the effects of external covariability fade as a Sc system evolves toward its internal steady state refutes N-LWP covariability as the likely explanation for the strongly negative adjustment values reported. At the same time, our modeling results show that strongly negative adjustment values are consistent with process understanding. In combination with the limitations of ship track–derived adjustment values discussed above, we therefore conclude that climatological satellite studies should be assigned more weight for estimating LWP adjustments than ship-track studies. Specifically, values of dlnLWP/dln$N$ = −0.3 (*25*) to −0.4 (*15*) should be considered possible central values rather than lower bounds, as in a recent review (*4*). Our analysis establishes the steady-state adjustment dlnLWP$_\infty$/dln$N$ = −0.64 as a new lower bound for LWP adjustments in nonprecipitating Sc.

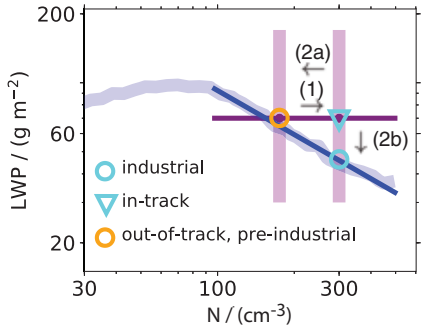

Fig. 4. Conceptual illustration of LWP adjustments as derived from ship tracks in comparison to climatological satellite studies. (Pre)industrial climatological conditions are strongly adjusted and represented by circles close to the steady state (blue). LWPs within ship tracks are weakly adjusted (triangle) such that ship-track studies are based on comparing almost identical LWP distributions (purple dots with error bars; illustration in analogy to Fig. 3A, no actual data), which implies vanishing LWP adjustments (purple regression line). Labeled arrows correspond to steps shown in Fig. 2.

Our results are moreover consistent with a recent study that derived LWP adjustments from climatological observations of a heavily frequented shipping lane (*17*). This setup provides more persistent pollution than an individual ship track while still suffering from a certain intermittency of pollution as compared with a climatological perturbation. We estimate an effective lifetime of ship tracks in a shipping lane of $\Delta t_{lane} \gtrsim 9$ hours (supplementary materials). With an evolution time that is longer than that for individual ship tracks but shorter than Sc lifetime, it is not surprising that the shipping lane provides a numerical adjustment value that lies in between those derived from single-ship-track studies and fully climatological studies (Fig. 1). Our results therefore reconcile and explain the differing LWP adjustments that have recently been reported (*15*–*17*, *25*).

Satellite remote sensing of thin and broken clouds remains a challenge, with large uncertainties in retrieved values. Despite the support for climatological satellite studies that our results provide, it therefore seems desirable to identify alternatives to ship-track studies that allow for a direct observation of aerosol effects. Our analysis shows that suitable natural experiments should feature temporally continuous pollution. Spatial continuity of pollution is another criterion, which excludes biases from boundary effects as described for ship tracks (*38*, *39*). Effusive volcanic emission and oceanic outflows of continental air are examples of such continuously polluting natural experiments. Existing datasets do not sample the subtropical Sc regions, however (*16*). In addition to adjustments being cloud-regime specific, higher extratropical above-cloud moisture may bias toward less-negative values. Undersampling of the subtropics may also exacerbate the time-scale effect, leading to underestimation of negative anthropogenic LWP adjustments by ship-track data.

Deliberate experiments could, by design, provide suitable aerosol perturbations. Such experiments have been suggested to assess the feasibility of marine cloud brightening (MCB) (*40*), i.e., the advertent mitigation of climate forcing by injecting aerosol into extensive Sc decks. In contrast to a setup with persistent pollution as needed to estimate the climatological aerosol effect, MCB rests on the notion of weak LWP adjustments as observed in ship tracks. Our results indicate that an intermittent aerosol perturbation may maximize the cooling effect by limiting the magnitude of compensating adjustments. To be feasible, MCB strategies will therefore have to balance the potential for LWP adjustments discussed here with the total aerosol perturbation obtainable with a given installation.

There is an urgent need to quantify the albedo and LWP responses in both precipitating and nonprecipitating Sc cloud systems to successfully quantify the cloud-mediated effect of anthropogenic aerosol on the climate system. This will require careful assessment of the frequency of occurrence and areal coverage of these regimes, with attendant consideration of the temporal nature of the LWP responses. Estimates of aerosol-cloud forcing that ignore the nonprecipitating regime are likely to substantially overestimate climate cooling.

REFERENCES AND NOTES

1. G. L. Stephens *et al.*, *Nat. Geosci.* **5**, 691–696 (2012).
2. T. S. L'Ecuyer, Y. Hang, A. V. Matus, Z. Wang, *J. Clim.* **32**, 6197–6217 (2019).
3. O. Boucher *et al.*, *Climate Change 2013: The Physical Science Basis. Working Group I Contribution to the Fifth Assessment Report of the Intergovernmental Panel on Climate Change*, T. F. Stocker *et al.*, Eds. (Intergovernmental Panel on Climate Change, 2013).
4. N. Bellouin *et al.*, *Rev. Geophys.* **58**, RG000660 (2020).
5. S. Twomey, *Atmos. Environ.* **8**, 1251–1256 (1974).
6. B. A. Albrecht, *Science* **245**, 1227–1230 (1989).
7. S. Wang, Q. Wang, G. Feingold, *J. Atmos. Sci.* **60**, 262–278 (2003).
8. A. S. Ackerman, M. P. Kirkpatrick, D. E. Stevens, O. B. Toon, *Nature* **432**, 1014–1017 (2004).
9. C. S. Bretherton, P. N. Blossey, J. Uchida, *Geophys. Res. Lett.* **34**, L03813 (2007).
10. J. D. Small, P. Y. Chuang, G. Feingold, H. Jiang, *Geophys. Res. Lett.* **36**, L16806 (2009).
11. F. Hoffmann, G. Feingold, *J. Atmos. Sci.* **76**, 1955–1973 (2019).
12. B. Stevens, G. Feingold, *Nature* **461**, 607–613 (2009).
13. J. Mülmenstädt, G. Feingold, *Curr. Clim. Change Rep.* **4**, 23–40 (2018).
14. M. W. Christensen, G. L. Stephens, *J. Geophys. Res.* **116**, D03201 (2011).
15. E. Gryspeerdt *et al.*, *Atmos. Chem. Phys.* **19**, 5331–5347 (2019).
16. V. Toll, M. Christensen, J. Quaas, N. Bellouin, *Nature* **572**, 51–55 (2019).
17. M. S. Diamond, H. M. Director, R. Eastman, A. Possner, R. Wood, *AGU Advances* **1**, e2019AV000111 (2020).
18. S. Platnick, S. Twomey, *J. Appl. Meteorol.* **33**, 334–347 (1994).
19. R. Boers, R. M. Mitchell, *Tellus A* **46**, 229–241 (1994).

20. J. A. Coakley Jr., C. D. Walsh, *J. Atmos. Sci.* **59**, 668–680 (2002).
21. A. A. Hill, G. Feingold, H. Jiang, *J. Atmos. Sci.* **66**, 1450–1464 (2009).
22. S. S. Lee, J. E. Penner, S. M. Saleeby, *J. Geophys. Res.* **114**, D07204 (2009).
23. H. Wang, P. J. Rasch, G. Feingold, *Atmos. Chem. Phys.* **11**, 4237–4249 (2011).
24. D. Rosenfeld *et al.*, *Science* **363**, eaav0566 (2019).
25. A. Possner, R. Eastman, F. Bender, F. Glassmeier, *Atmos. Chem. Phys.* **20**, 3609–3621 (2020).
26. F. Glassmeier, G. Feingold, *Proc. Natl. Acad. Sci. U.S.A.* **114**, 10578–10583 (2017).
27. D. C. Leon, Z. Wang, D. Liu, *J. Geophys. Res.* **113**, D00A14 (2008).
28. H. Xue, G. Feingold, B. Stevens, *J. Atmos. Sci.* **65**, 392–406 (2008).
29. Y.-C. Chen, M. W. Christensen, G. L. Stephens, J. H. Seinfeld, *Nat. Geosci.* **7**, 643–646 (2014).
30. F. A.-M. Bender, L. Frey, D. T. McCoy, D. P. Grosvenor, J. K. Mohrmann, *Clim. Dyn.* **52**, 4371–4392 (2019).
31. F. Hoffmann, F. Glassmeier, T. Yamaguchi, G. Feingold, *J. Atmos. Sci.* **77**, 2203–2215 (2020).
32. W. H. Schubert, J. S. Wakefield, E. J. Steiner, S. K. Cox, *J. Atmos. Sci.* **36**, 1308–1324 (1979).
33. I. Sandu, B. Stevens, *J. Atmos. Sci.* **68**, 1865–1881 (2011).
34. C. S. Bretherton, J. Uchida, T. N. Blossey, *J. Adv. Model. Earth Syst.* **2**, 20 (2010).
35. R. Wood, *Mon. Weather Rev.* **140**, 2373–2423 (2012).
36. M. W. Christensen, K. Suzuki, B. Zambri, G. L. Stephens, *Geophys. Res. Lett.* **41**, 6970–6977 (2014).
37. P. A. Durkee *et al.*, *J. Atmos. Sci.* **57**, 2542–2553 (2000).
38. H. Wang, G. Feingold, *J. Atmos. Sci.* **66**, 3257–3275 (2009).
39. Y.-C. Chen, M. W. Christensen, D. J. Diner, M. J. Garay, *J. Geophys. Res. Atmos.* **120**, 2819–2833 (2014).
40. R. Wood, T. Ackerman, P. Rasch, K. Wanser, *Earths Futur.* **5**, 659–663 (2017).

ACKNOWLEDGMENTS

F.G. thanks A. Possner and T. Goren for helpful discussions about the interpretation of satellite literature. M. Khairoutdinov graciously provided the System for Atmospheric Modeling (SAM) model. The University of Wyoming, Department of Atmospheric Science, is acknowledged for archiving the radiosonde data. We thank three anonymous reviewers for their helpful comments. **Funding:** F.G. acknowledges support from The Branco Weiss Fellowship – Society in Science, administered by the ETH Zürich, and from a Veni grant of the Dutch Research Council (NWO). F.H. held a visiting fellowship of the Cooperative Institute for Research in Environmental Sciences (CIRES) at the University of Colorado Boulder, and the NOAA Earth System Research Laboratory, and is supported by the German Research Foundation under grant HO 6588/1-1. J.S.J. and K.S.C. were supported by the Natural Environment Research Council (NERC) under grant NE/I020059/1 (ACID-PRUF) and the UK-China Research and Innovation Partnership Fund through the Met Office Climate Science for Service Partnership (CSSP) China as part of the Newton Fund. K.S.C. is currently a Royal Society Wolfson Research Merit Award holder. This research was partially supported by the Office of Biological and Environmental Research of the U.S. Department of Energy Atmospheric System Research Program Interagency Agreement DE-SC0016275 and by an Earth's Radiation Budget grant, NOAA CPO Climate & CI #03-01-07-001. **Author contributions:** F.G., G.F., and F.H. conceived the study; F.G. developed the emulator with support from J.S.J. and K.S.C.; T.Y. performed the simulations. All authors contributed to the final product. **Competing interests:** All authors declare that they have no competing interests. **Data and materials availability:** Simulation data are available from https://esrl.noaa.gov/csl/groups/csl9/datasets/data/cloud_phys/2020-Glassmeier-etal/. Radiosonde data can be acccessed at http://www.weather.uwyo.edu/upperair/sounding.html.

SUPPLEMENTARY MATERIALS

science.sciencemag.org/content/371/6528/485/suppl/DC1
Materials and Methods
Supplementary Text
Figs. S1 to S6
Tables S1 to S4
References (*41*–*45*)

23 June 2020; accepted 22 December 2020
10.1126/science.abd3980

REPORTS

SPECTROSCOPY

Sub-7-femtosecond conical-intersection dynamics probed at the carbon K-edge

Kristina S. Zinchenko[1]*†, Fernando Ardana-Lamas[1]*†, Issaka Seidu[2]*, Simon P. Neville[2]*, Joscelyn van der Veen[2]*, Valentina Utrio Lanfaloni[1], Michael S. Schuurman[2,3]‡, Hans Jakob Wörner[1]‡

Conical intersections allow electronically excited molecules to return to their electronic ground state. Here, we observe the fastest electronic relaxation dynamics measured to date by extending attosecond transient-absorption spectroscopy (ATAS) to the carbon K-edge. We selectively launch wave packets in the two lowest electronic states (D_0 and D_1) of $C_2H_4^+$. The electronic $D_1 \rightarrow D_0$ relaxation takes place with a short time constant of 6.8 ± 0.2 femtoseconds. The electronic-state switching is directly visualized in ATAS owing to a spectral separation of the D_1 and D_0 bands caused by electron correlation. Multidimensional structural dynamics of the molecule are simultaneously observed. Our results demonstrate the capability to resolve the fastest electronic and structural dynamics in the broad class of organic molecules. They show that electronic relaxation in the prototypical organic chromophore can take place within less than a single vibrational period.

Electronically excited molecules can decay through a variety of channels, including fluorescence, bond dissociation, or nonradiative electronic relaxation to lower-lying states. The key to defining the relative importance of these decay channels is the associated time scales. Electronic relaxation is known to be particularly fast when mediated by conical intersections (*1*, *2*), enabling the photostability of DNA bases (*3*), the quantum yield of retinal isomerization in vision (*4*, *5*), and the efficiency of charge separation in organic semiconductors (*6*).

But how fast electronic relaxation really is has remained elusive in many molecular systems owing to experimental limitations, particularly temporal resolution. This situation has changed with the advent of attosecond science that has redefined the frontiers of time-resolved measurements on molecules (*7*–*14*). Attosecond transient-absorption spectroscopy (ATAS) is a particularly powerful technique for accessing both electronic and structural dynamics (*15*–*21*). With respect to dynamics at conical intersections (*22*), the methods of attosecond science provide the ultimate time resolution that is required to unambiguously monitor and dissect the intimately coupled electronic and nuclear dynamics that take place in their vicinity. Pioneering ATAS work in the extreme-ultraviolet domain has followed curve-crossing dynamics in diatomic molecules (*20*) and monitored dynamics induced by conical intersections through the appearance time of atomic fragments (*23*).

Here, we demonstrate ATAS at the carbon K-edge, which extends its applicability from systems containing specific reporter atoms to the general class of organic molecules. We studied ethylene, the most important organic chromophore involved in the photochemistry and photophysics of a majority of molecular systems (*24*–*32*). Rather than using one-photon excitation as in typical femtochemistry experiments, we used a carrier-envelope-phase (CEP)–stable sub-two-cycle pulse (*33*) to prepare the first electronically excited state (D_1) of $C_2H_4^+$ and probed its relaxation to the electronic ground state (D_0) using transient absorption of an attosecond soft x-ray (SXR) continuum covering the carbon K-edge. The experimental results were compared with ab initio multiple spawning (AIMS) quantum dynamics simulations (*34*) coupled to x-ray absorption calculations (*35*, *36*). This technique has the distinctive advantage of not requiring any assumptions regarding the dynamics or precomputed potential-energy surfaces and is thus truly predictive. The recent extension of the combined density functional theory and multireference configuration interaction (DFT-MRCI) method to calculate transient x-ray spectra on the fly (*37*) was validated here against experimental data. The strong-field-ionization step was described using the time-dependent first-order algebraic diagrammatic construction [TD-ADC(1)] method, including the complete state-specific molecular-orientation dependence of the strong-field ionization rates.

This joint experimental and theoretical study provided a comprehensive view of the coupled electronic and nuclear dynamics of the ethylene

[1]Laboratorium für Physikalische Chemie, ETH Zürich, 8093 Zürich, Switzerland. [2]National Research Council of Canada, Ottawa, ON, Canada. [3]Department of Chemistry and Biomolecular Sciences, University of Ottawa, Ottawa, ON, Canada.
*These authors contributed equally to this work. †Present address: European XFEL GmbH, Schenefeld, Germany.
‡Corresponding author. Email: michael.schuurman@nrc-cnrc.gc.ca (M.S.S.); hwoerner@ethz.ch (H.J.W.)

cation. The structural dynamics driven by the vibrational wave packet in the D_0 state was identified through its modulation of the line positions in both pre-edge and post-edge transitions. These spectral fingerprints simultaneously revealed the electronic character of the involved core-level transitions and the electronically adiabatic structural dynamics occurring in the ionized molecule. The nonadiabatically coupled electronic and nuclear wave packet prepared in the D_1 state was found to electronically relax with a fast time constant of 6.8 ± 0.2 fs, representing the fastest electronic relaxation measured to date.

These results demonstrate the potential of ATAS at the carbon K-edge to resolve the fastest chemical processes in the general class of organic molecules (*38*, *39*). They moreover demonstrate the existence of electronic relaxation on time scales far below vibrational periods, which is likely to be a general phenomenon of relevance to the photochemistry and photophysics of most molecular systems.

The experimental setup is schematically illustrated in Fig. 1A, with details given in the supplementary materials (SM, section S1). Strong-field ionization of ethylene was initiated by a passively CEP-stable sub-two-cycle (10.4 ± 1.5 fs) laser pulse centered at 1.6 μm. Transient-absorption spectra were acquired by measuring the transmission of an x-ray supercontinuum extending to above 450 eV (with an estimated sub-200-as duration), thus covering the carbon K-edge with a nearly constant photon flux (fig. S2). In this experiment, the time resolution is thus limited by the pump pulse.

Figure 1B shows the experimental x-ray absorption spectrum of neutral ethylene in its electronic ground state (S_0). It is dominated by the carbon 1s (C1s) → π^* transition, followed by two weaker excitations and the onset of continuum absorption (see also fig. S3). The change in optical density induced by the pump pulse (ΔOD) is shown in Fig. 1C, obtained by integrating the transient data over time delays longer than 20 fs. This spectrum is characterized by the appearance of an additional absorption band at 281 eV, corresponding to the 1s → π transition into the singly occupied π molecular orbital and a shift of the 1s → π^* transition to higher energies.

Figure 1D shows ΔOD as a function of the pump-probe delay, where a positive delay means that the mid-infrared (mid-IR) pulse preceded the SXR pulse. The transient spectra are dominated by the 1s → π band centered at 281 eV that undergoes a periodic oscillation of its central position and the 1s → π^* band at 286 eV. Both bands are characteristic of the D_0 state, as revealed by comparison with the calculated spectrum shown in Fig. 1F. The oscillations of the band positions revealed the detailed structural dynamics in the D_0 state and are further discussed below.

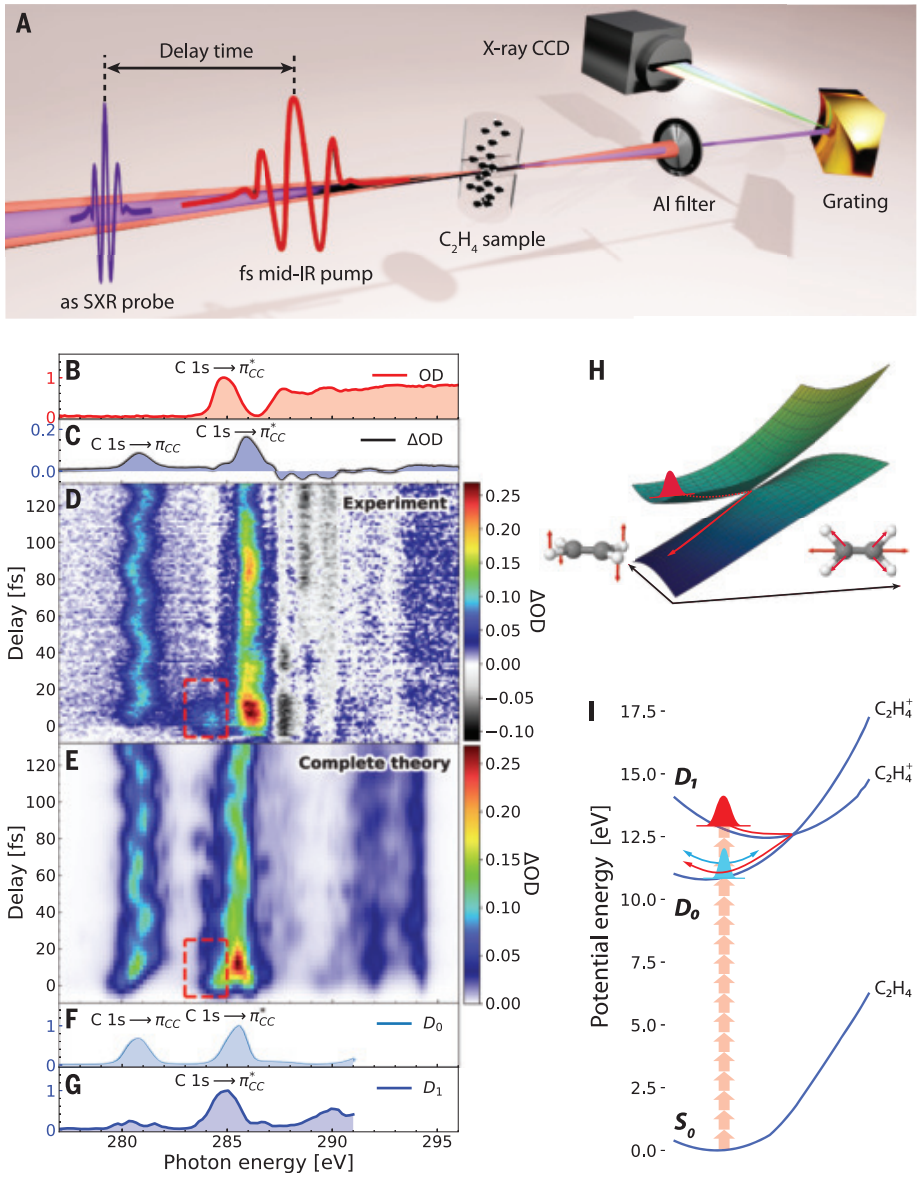

Fig. 1. Attosecond transient-absorption spectroscopy of ethylene at the carbon K-edge. (**A**) Experimental setup. CCD, charge-coupled device. (**B** and **C**) Overview of measured data showing (B) the optical density (OD) of the unexcited target and (C) its change under the action of the pump pulse (ΔOD). (**D** to **G**) The (D) experimental and (E) calculated (complete simulation) ΔOD as a function of pump-probe delay. The dashed red boxes indicate the signal assigned to the D_1 state of $C_2H_4^+$. Shown at the bottom are the calculated x-ray absorption spectra of $C_2H_4^+$ in its (F) electronic ground state (D_0) and (G) excited state (D_1). (**H** and **I**) Illustration of the conical intersection between the D_1 and D_0 states of $C_2H_4^+$ that mediates the electronic relaxation.

The most notable feature in Fig. 1D is a short-lived transient centered at 284 eV (dashed red box). This feature was assigned to the D_1 state through comparison with the calculated spectrum in Fig. 1G and the detailed time-resolved calculations shown in Fig. 1E.

The experimental results are in excellent agreement with the calculations described above. Details on the theoretical methods are given in SM section S3. Figure 1, F and G, shows the transient spectra of the D_0 and D_1 electronic states of $C_2H_4^+$. They were obtained by integrating the transient spectra shown in Fig. 1E over pump-probe delays longer than 21.6 fs or from −9.6 to 21.6 fs, respectively.

These results enabled us to draw a comprehensive picture of the prepared dynamics (Fig. 1, H and I). Strong-field ionization prepares coupled electronic and nuclear wave packets in both the D_0 and the D_1 states. The wave packet prepared in D_1 undergoes a fast electronic relaxation through a planar conical intersection accessed by stretching of the C=C bond. The dynamics are gradient directed (i.e.,

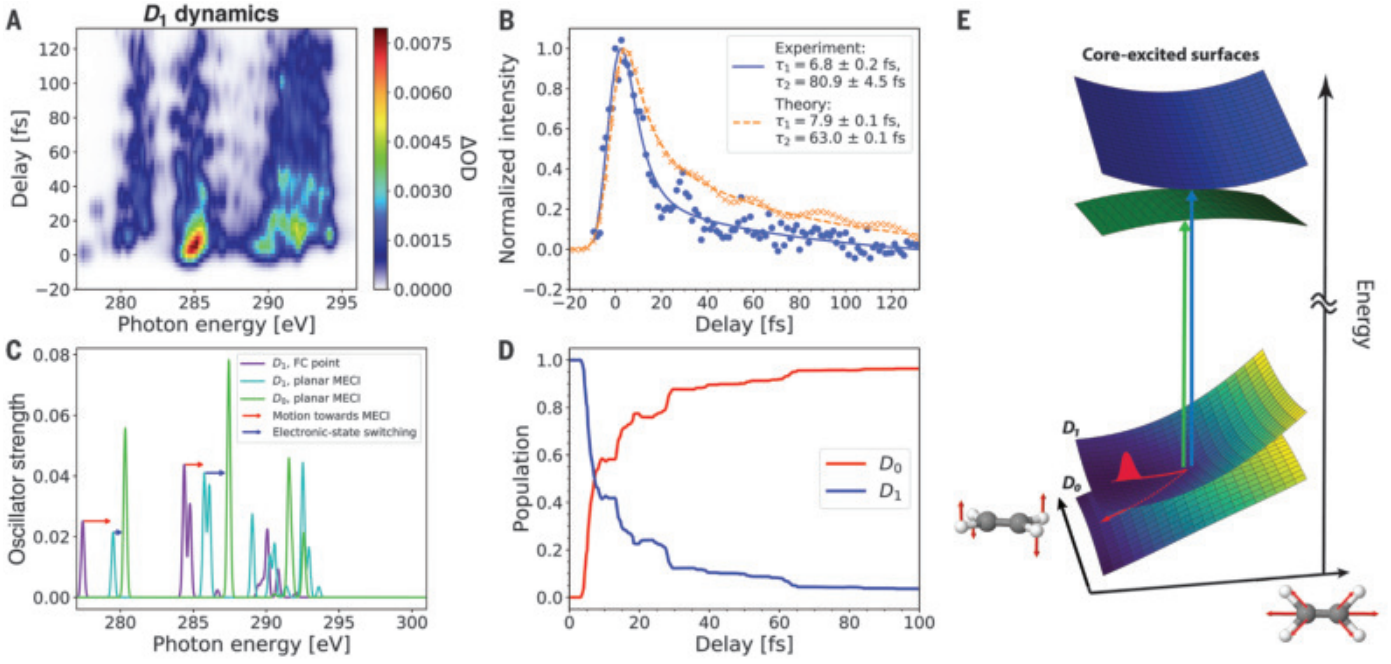

Fig. 2. Electronic relaxation probed by carbon K-edge ATAS. (**A**) The calculated ΔOD contributions from AIMS simulations in which trajectories were initialized on the D_1 electronic state. (**B**) The evolution of the experimental and calculated [from (A)] ΔOD with pump-probe delay, integrated over the band centered between 284 and 285 eV. (**C**) Calculated x-ray absorption spectra (XAS) for geometries and electronic states of interest. All calculations were performed at the CVS-DFT–MRCI/aug-cc-pVDZ level of theory. (**D**) Adiabatic state populations from AIMS simulations in which trajectory basis functions were initialized on the D_1 electronic state. (**E**) Illustration of the mechanism resolving the electronic-state switching: The core-excited surfaces accessed from the D_0 and D_1 states (blue and green, respectively) are energetically separated at the location of the MECI between D_0 and D_1.

ballistic) and involve points of electronic degeneracy that lie close to the nuclear configuration in the vicinity of the S_0 minimum energy surface. Whereas earlier calculations (*40*, *41*) and less direct measurements (*41*) qualitatively agree with our results, they associated time scales of 30 to 60 fs to the $D_1 \rightarrow D_0$ electronic relaxation. Both our measurements and our calculations showed that the onset of this process is observed to occur even earlier than that. As we further detail below, the electronic relaxation was both extremely rapid and exceptionally efficient, occurring in less than a single C=C stretch vibrational period [22.4 fs (*42*)]. Details of the dynamical simulations are presented in SM sections S3 and S4.

The ultrafast decay of the characteristic D_1 absorption band was further analyzed in Fig. 2. Figure 2A shows the contribution of all 24 AIMS trajectory basis functions initiated in the D_1 state to the transient spectra. The dominant ($1s \rightarrow \pi^*$) absorption band centered between 284 and 285 eV decays on an ultrashort time scale. Figure 2B compares the measured ΔOD signal (blue dots) integrated over the spectral width of the D_1 band (dashed red boxes in Fig. 1, D and E) with the calculated spectra (orange crosses). A bi-exponential fit to the experimental data (solid line) yielded time constants of 6.8 ± 0.2 and 80.9 ± 4.5 fs. The bi-exponential fit (dashed line) of the theoretical data was in excellent agreement with the short time constant (7.9 ± 0.1 fs) and in reasonable agreement with the longer time constant (63.0 ± 0.1 fs). The small differences in the time scales were attributed to the approximation of the initial phase-space distribution of the D_1 wave packet with that of the S_0 ground state. The statistical analysis of the results is shown in figs. S4 and S5.

Figure 2C shows static x-ray absorption spectra calculated at the equilibrium geometry of the neutral molecule [Franck-Condon (FC) point] for the D_1 state of $C_2H_4^+$ and at the geometry of the minimum-energy conical intersection (MECI) for both the D_1 and D_0 states. These static absorption spectra were calculated for a randomly oriented sample of ethylene, whereas the anisotropic axis distribution induced by strong-field ionization was included in the dynamic calculations (Fig. 2A and SM section S4). The comparison of Fig. 2A with Fig. 2C showed that the shift of the D_1 band toward higher photon energies was the signature of wave-packet motion from the FC point to the MECI.

Notably, the calculations revealed a sudden shift of this band by >1 eV as the electronic character switches from D_1 to D_0 without change of the molecular structure. This sudden shift, confirmed by the experimental observations, is explained by the difference in the $1s \rightarrow \pi^*$ transition energies from the D_0 and D_1 states (Fig. 2E). This large splitting is the consequence of electron correlation, i.e., it results from the different occupations of the two orbitals lying below the π^* orbital (see Fig. 3D). This direct spectroscopic mapping of electronic-state switching at a conical intersection can be expected to be a general feature of ATAS. A similar effect was also observed in the case of the $1s \rightarrow \pi$ transition (lines centered at 281 eV), but its contribution to the dynamic (and experimental) D_1 spectra is suppressed by the axis distribution created by strong-field ionization (SM section S4).

This sudden shift of the $1s \rightarrow \pi^*$ transition energy with the change in electronic character is indeed key to unambiguously observing the ultrafast $D_1 \rightarrow D_0$ relaxation. Figure 2D shows the populations of the adiabatic D_1 and D_0 states as a function of the delay after preparation of the D_1 state. The D_1 population decays by 70% at the first encounter with the conical intersection, which begins to occur within 5 fs. The combination of this short time with the highly efficient population transfer explains the observed electronic-relaxation time scale of 6.8 ± 0.2 fs. The slower time constant of the bi-exponential decay is caused by a residual

population in the D_1 state that decays at later returns of the excited-state wave packet to the conical intersection, causing the later steps in the population curves.

In addition to the nonadiabatically evolving wave packet in the D_1 state, the pump pulse also prepared a wave packet in the D_0 state that evolved adiabatically with respect to its electronic character. This fact is most clearly visible through the periodic oscillation of the absorption band centered at 281 eV in Fig. 1, D and E. The contribution of the D_0 wave packet to the observed dynamics is further detailed in Fig. 3A. The transient spectra are dominated by the $1s \rightarrow \pi$ and $1s \rightarrow \pi^*$ bands that display opposite energy shifts as a function of delay. This observation is explained by static x-ray spectra (Fig. 3C) calculated at

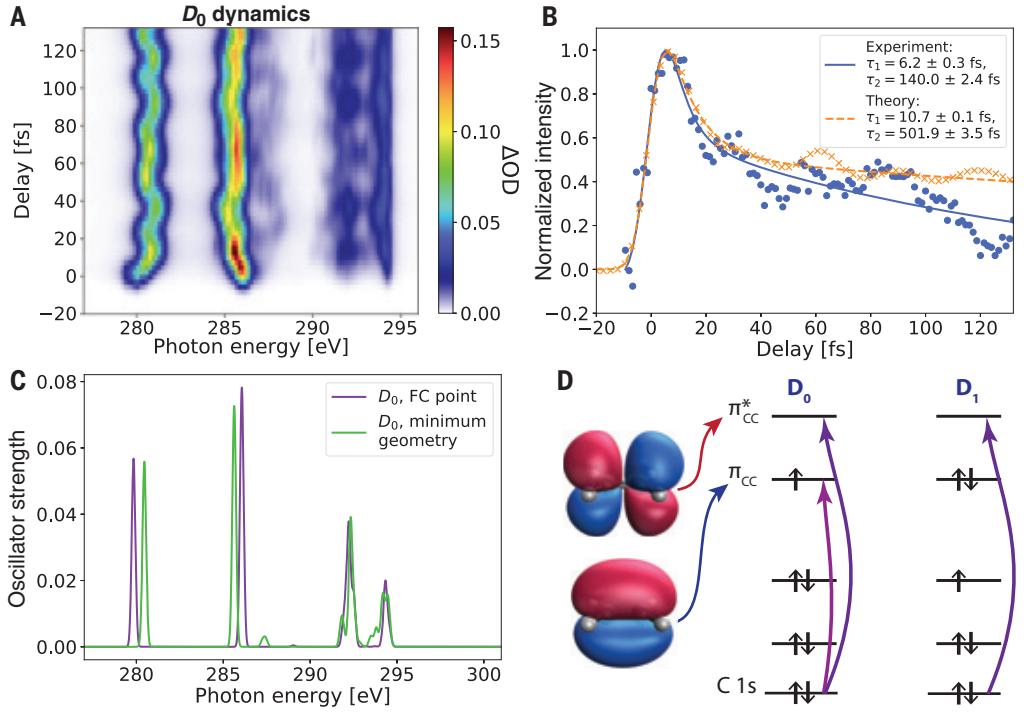

Fig. 3. Structural and electronic relaxation probed by carbon K-edge ATAS. (**A**) Calculated ΔOD contributions from AIMS simulations in which trajectories were initialized on the D_0 electronic state. (**B**) The evolution of the experimental and calculated ΔOD (from complete dynamics, Fig. 1E). (**C**) Calculated isotropic XAS for the D_0 state at both S_0 and D_0 minimum-energy geometries. All calculations were performed at the CVS-DFT–MRCI/aug-cc-pVDZ level of theory. (**D**) Schematic representation of the frontier molecular orbitals of $C_2H_4^+$ in its D_0 and D_1 electronic states.

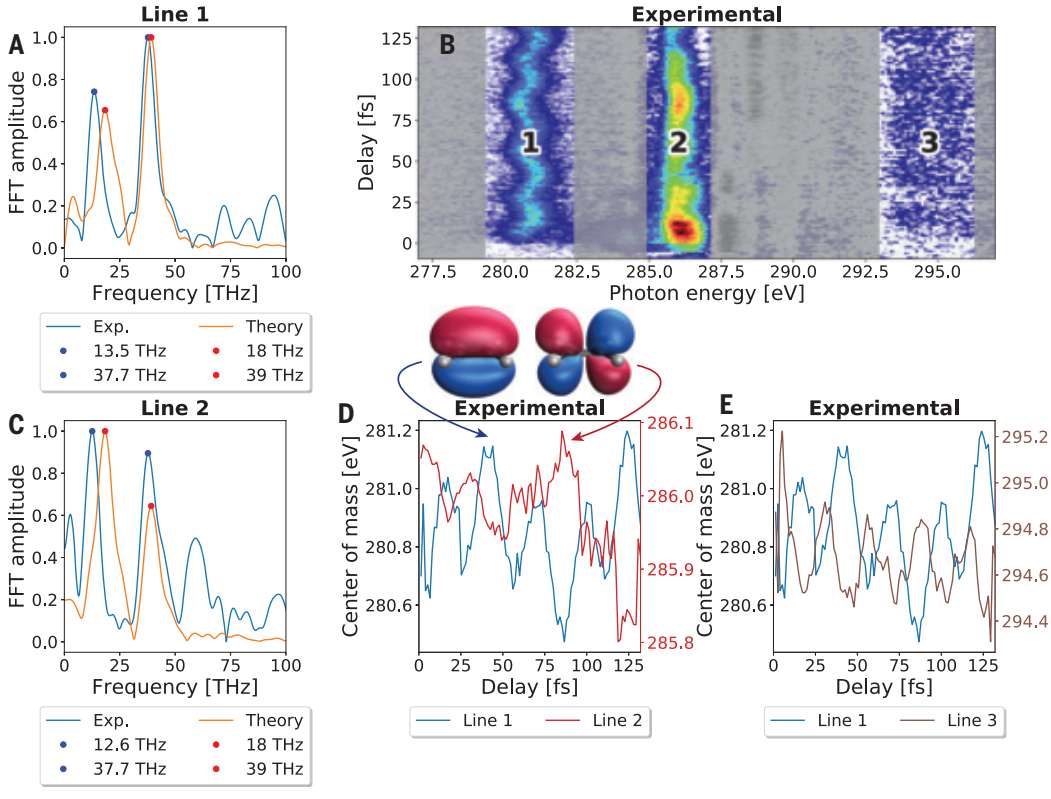

Fig. 4. Electronic-structure encoding in vibrational dynamics probed by ATAS. (**A** and **C**) Fourier transforms of the center of mass of the absorption (A) band 1 centered at 281 eV and (C) band 2 centered at 286 eV. FFT, fast Fourier transform. (**B**) Overview of the transient-absorption spectra. (**D**) Time-dependent shifts in the center positions of bands 1 and 2, assigned in terms of the (particle) NTOs dominating the corresponding positions. (**E**) Same as (D) for the center positions of bands 1 and 3.

the FC point and the equilibrium geometry of the D_0 state. These spectra confirm the opposite energy shifts of the two absorption bands caused by the structural-relaxation dynamics in the D_0 state. The spectral intensities of the 1s → π* band in measurements and calculations are compared in Fig. 3B. Here, the contributions of both the D_1 and the D_0 states to the 1s → π* band were included because of their spectral overlap in the calculations. A bi-exponential fit to these data again yielded short time constants of 6.2 ± 0.3 fs (experiment) and 10.7 ± 0.1 fs (theory), which were dominated by the $D_1 \rightarrow D_0$ electronic relaxation.

These results suggest that x-ray absorption spectroscopy might also be directly sensitive to structural dynamics, in addition to the electronic dynamics discussed above. A Fourier transform of the center position of the 1s → π and 1s → π* bands (Fig. 4, A and C) indeed revealed two dominant frequencies (37.7 ± 3.3 and 13.5 ± 3.3 THz). These values were assigned to the fundamental CH_2 scissor mode (v_3 = 1) and the overtone of the CH_2 torsion (v_4 = 2), respectively. The analysis of calculations performed over longer delays suggested the population of a third vibrational mode, the symmetric C=C stretch vibration, with a frequency of 45 THz (SM section S2.6), which explained the high-frequency shoulder observed in the experimental data in Fig. 4C. The dominant population of these three vibrational modes reflected the change in equilibrium geometry from the electronic ground state of ethylene to that of its cation. Whereas neutral ethylene is planar, its cation has a twisted equilibrium geometry with an angle of ~29.2° between the two planes defined by the CH_2 units (*24*, *42*), a stretched C=C bond length and an increased H–C–H angle (fig. S7). Our dynamical simulations showed that vertical ionization of S_0 to D_0 resulted in a pronounced excitation of all three vibrational modes (fig. S10). These three vibrational frequencies were indeed also observed in the Fourier transform of the measured line positions, which illustrated the direct mapping of structural dynamics into SXR-ATAS spectra. We note that it is not the fundamental of the torsional mode that was excited but its overtone, because the former has A_u symmetry in the $D_{2h}(M)$ symmetry group and thus a vanishing Franck-Condon factor, whereas the latter is totally symmetric.

The direct mapping of structural dynamics into the spectral position of x-ray absorption lines is a useful property for tracing ultrafast structural dynamics with element sensitivity. In the present case, this sensitivity originates from a strong variation of the energy of the 1s → π and 1s → π* transitions with the excited vibrational modes (see figs. S18 and S19). The mapping of structural dynamics to x-ray absorption line positions thus simultaneously provides information on the electronic character of the states involved in the x-ray transition.

This electronic-structure encoding is further illustrated by the fact that the central positions of the 1s → π and 1s → π* bands modulated out of phase, both in the experimental (Fig. 4B) and the theoretical data (Fig. 3A). These observations were related to the electronic-structure properties through the calculated (particle) natural transition orbitals (NTOs), shown in Fig. 4D. Whereas the NTO for the 1s → π band has bonding character without nodal planes perpendicular to the C=C bond, the NTO for the 1s → π* band has antibonding character and one nodal plane perpendicular to the C=C axis. Hence, the out-of-phase modulation observed in the experiment directly reflects the different electronic properties of the final states of the core-level excitation. Notably, this property is not limited to the two discussed bands. Figure 4E shows that the central position of band 3, centered at 295 eV, also modulates out of phase with the 1s → π band. Highly accurate calculations in this spectral domain remain challenging because transitions to both (high) Rydberg states and the continuum may contribute. The experimental results, however, suggest that the electronic-structure encoding demonstrated for the lower-lying transitions also extends to the Rydberg and continuum part of the spectrum, which offers interesting perspectives for time-resolved near- and extended-edge x-ray absorption fine-structure studies.

We have demonstrated attosecond transient-absorption spectroscopy at the carbon K-edge and have used it to reveal the fastest electronic relaxation process in molecular systems measured to date. We have shown that the technique is particularly powerful in revealing electronic-state switching at conical intersections, a property that we traced back to electron correlation. Moreover, the technique simultaneously displays a pronounced sensitivity to multidimensional structural dynamics, including electronic-structure encoding. This study shows that electronic relaxation can take place on time scales below the shortest vibrational periods, extending previous results from frequency-domain spectroscopy (*43*). This finding supports the feasibility of electronic coherent control over conical-intersection dynamics (*44*) because electronic coherence might be sufficiently long lived (*45*). It further reveals the crucial importance of subfemtosecond spectroscopies for fully understanding excited-state dynamics in molecules through a clean separation of electronic and structural dynamics. The extension of ATAS from the extreme-ultraviolet domain to the carbon K-edge generalizes the considerable potential of this method to the broad class of organic molecules and thereby opens a wide range of opportunities, such as access to the ultimate time scale of the retinal isomerization reaction (*46*, *47*). It will also enable studies of solvated molecules (*48*) that can now be extended from the femtosecond (*49*) to the attosecond time scale, giving access to the effects of solvation on the time scales of conical intersection dynamics and electronic decoherence.

REFERENCES AND NOTES

1. W. Domcke, D. R. Yarkony, H. Köppel, Eds., *Conical Intersections: Electronic Structure, Dynamics and Spectroscopy* (Advanced Series in Physical Chemistry, vol. 15, World Scientific, 2004).
2. M. S. Schuurman, A. Stolow, *Annu. Rev. Phys. Chem.* **69**, 427–450 (2018).
3. A. L. Sobolewski, W. Domcke, C. Hättig, *Proc. Natl. Acad. Sci. U.S.A.* **102**, 17903–17906 (2005).
4. R. W. Schoenlein, L. A. Peteanu, R. A. Mathies, C. V. Shank, *Science* **254**, 412–415 (1991).
5. D. Polli *et al.*, *Nature* **467**, 440–443 (2010).
6. S. M. Falke *et al.*, *Science* **344**, 1001–1005 (2014).
7. G. Sansone *et al.*, *Nature* **465**, 763–766 (2010).
8. P. M. Kraus *et al.*, *Science* **350**, 790–795 (2015).
9. F. Calegari *et al.*, *Science* **346**, 336–339 (2014).
10. M. Huppert, I. Jordan, D. Baykusheva, A. von Conta, H. J. Wörner, *Phys. Rev. Lett.* **117**, 093001 (2016).
11. J. Vos *et al.*, *Science* **360**, 1326–1330 (2018).
12. S. Biswas *et al.*, *Nat. Phys.* **16**, 778–783 (2020).
13. V. Loriot *et al.*, *J. Phys. Photon.* **2**, 024003 (2020).
14. I. Jordan *et al.*, *Science* **369**, 974–979 (2020).
15. E. Goulielmakis *et al.*, *Nature* **466**, 739–743 (2010).
16. A. Wirth *et al.*, *Science* **334**, 195–200 (2011).
17. C. Ott *et al.*, *Nature* **516**, 374–378 (2014).
18. S. M. Teichmann, F. Silva, S. L. Cousin, M. Hemmer, J. Biegert, *Nat. Commun.* **7**, 11493 (2016).
19. A. S. Johnson *et al.*, *Struct. Dyn.* **3**, 062603 (2016).
20. Y. Kobayashi, K. F. Chang, T. Zeng, D. M. Neumark, S. R. Leone, *Science* **365**, 79–83 (2019).
21. N. Saito *et al.*, *Optica* **6**, 1542 (2019).
22. H. J. Wörner *et al.*, *Science* **334**, 208–212 (2011).
23. H. Timmers *et al.*, *Nat. Commun.* **10**, 3133 (2019).
24. H. Köppel, W. Domcke, L. S. Cederbaum, W. Niessen, *J. Chem. Phys.* **69**, 4252–4263 (1978).
25. C. Sannen, G. Raşeev, C. Galloy, G. Fauville, J. Lorquet, *J. Chem. Phys.* **74**, 2402–2411 (1981).
26. M. Ben-Nun, T. J. Martínez, *Chem. Phys. Lett.* **298**, 57–65 (1998).
27. J. Quenneville, T. J. Martinez, *J. Phys. Chem. A* **107**, 829–837 (2003).
28. T. J. Martínez, *Acc. Chem. Res.* **39**, 119–126 (2006).
29. K. Kosma, S. A. Trushin, W. Fuss, W. E. Schmid, *J. Phys. Chem. A* **112**, 7514–7529 (2008).
30. H. Tao *et al.*, *J. Chem. Phys.* **134**, 244306 (2011).
31. T. K. Allison *et al.*, *J. Chem. Phys.* **136**, 124317 (2012).
32. T. Kobayashi, T. Horio, T. Suzuki, *J. Phys. Chem. A* **119**, 9518–9523 (2015).
33. S. Pabst, M. Lein, H. J. Wörner, *Phys. Rev. A (Coll. Park)* **93**, 023412 (2016).
34. M. Ben-Nun, T. J. Martínez, *Ab Initio Quantum Molecular Dynamics* (Wiley, 2002), pp. 439–512.
35. S. P. Neville *et al.*, *Faraday Discuss.* **194**, 117–145 (2016).
36. S. P. Neville, M. Chergui, A. Stolow, M. S. Schuurman, *Phys. Rev. Lett.* **120**, 243001 (2018).
37. I. Seidu *et al.*, *J. Chem. Phys.* **151**, 144104 (2019).
38. Y. Pertot *et al.*, *Science* **355**, 264–267 (2017).
39. A. R. Attar *et al.*, *Science* **356**, 54–59 (2017).
40. B. Joalland, T. Mori, T. J. Martínez, A. G. Suits, *J. Phys. Chem. Lett.* **5**, 1467–1471 (2014).
41. A. Ludwig *et al.*, *J. Phys. Chem. Lett.* **7**, 1901–1906 (2016).
42. S. Willitsch, U. Hollenstein, F. Merkt, *J. Chem. Phys.* **120**, 1761–1774 (2004).
43. M. Oku *et al.*, *J. Phys. Chem. A* **112**, 2293–2310 (2008).
44. M. F. Kling, P. von den Hoff, I. Znakovskaya, R. de Vivie-Riedle, *Phys. Chem. Chem. Phys.* **15**, 9448–9467 (2013).
45. M. Vacher, M. J. Bearpark, M. A. Robb, J. P. Malhado, *Phys. Rev. Lett.* **118**, 083001 (2017).
46. P. J. Johnson *et al.*, *Nat. Chem.* **7**, 980–986 (2015).
47. R. A. Mathies, *Nat. Chem.* **7**, 945–947 (2015).
48. C. Kleine *et al.*, *J. Phys. Chem. Lett.* **10**, 52–58 (2019).
49. A. D. Smith *et al.*, *J. Phys. Chem. Lett.* **11**, 1981–1988 (2020).
50. K. S. Zinchenko *et al.*, Data for "Sub-7-femtosecond conical-intersection dynamics probed at the carbon K-edge" Zenodo (2020); https://doi.org/10.5281/zenodo.4293679.

ACKNOWLEDGMENTS

We thank A. Schneider, M. Seiler, and M. Kerellaj for their technical support. H.J.W. thanks J.-P. Wolf (Geneva) for discussions. **Funding:** H.J.W. acknowledges funding from an ERC Consolidator Grant (project no. 772797-ATTOLIQ) and the Swiss National Science Foundation through project 200021_172946 and the NCCR-MUST. M.S.S. acknowledges the support of the Natural Sciences and Energy Research Council (Canada) through the Discovery Grants program. **Author contributions:** K.S.Z. and F.A.-L. built the experimental setup, performed the measurements, and analyzed the data; V.U.L. contributed to the measurements; S.P.N. and M.S.S. developed the theoretical methods; I.S., S.P.N., J.v.d.V., and M.S.S. carried out the calculations; and H.J.W. supervised the experimental part of the project and wrote the manuscript with input from all co-authors. **Competing interests:** None declared. **Data and materials availability:** All data needed to evaluate the conclusions in the paper are present in the paper or the supplementary materials, as well as online at Zenodo (*50*).

SUPPLEMENTARY MATERIALS

science.sciencemag.org/content/371/6528/489/suppl/DC1
Materials and Methods
Figs. S1 to S20
Tables S1 and S2
References (*51*–*57*)

8 October 2020; accepted 22 December 2020
10.1126/science.abf1656

ARTIFICIAL MUSCLES

Unipolar stroke, electroosmotic pump carbon nanotube yarn muscles

Hetao Chu[1,2]*, Xinghao Hu[1,3]*, Zhong Wang[1,4]*, Jiuke Mu[1]*, Na Li[1,5], Xiaoshuang Zhou[6], Shaoli Fang[1], Carter S. Haines[1,7], Jong Woo Park[8], Si Qin[9], Ningyi Yuan[6], Jiang Xu[3], Sameh Tawfick[10], Hyungjun Kim[11,12], Patrick Conlin[11], Maenghyo Cho[11,12], Kyeongjae Cho[11], Jiyoung Oh[1], Steven Nielsen[4], Kevin A. Alberto[4], Joselito M. Razal[9], Javad Foroughi[13], Geoffrey M. Spinks[14], Seon Jeong Kim[8], Jianning Ding[3,6]†, Jinsong Leng[2]†, Ray H. Baughman[1]†

Success in making artificial muscles that are faster and more powerful and that provide larger strokes would expand their applications. Electrochemical carbon nanotube yarn muscles are of special interest because of their relatively high energy conversion efficiencies. However, they are bipolar, meaning that they do not monotonically expand or contract over the available potential range. This limits muscle stroke and work capacity. Here, we describe unipolar stroke carbon nanotube yarn muscles in which muscle stroke changes between extreme potentials are additive and muscle stroke substantially increases with increasing potential scan rate. The normal decrease in stroke with increasing scan rate is overwhelmed by a notable increase in effective ion size. Enhanced muscle strokes, contractile work-per-cycle, contractile power densities, and energy conversion efficiencies are obtained for unipolar muscles.

With the growing need for artificial muscles for diverse applications (*1*–*3*), major increases in muscle stroke, cycle rate, work capacity, power density, and energy conversion efficiency are required. Electrochemically driven muscles are especially important because their efficiencies are not restricted by the Carnot limit of thermal muscles and they can have a natural latching state, meaning that they can maintain stroke with low input energy.

The initially investigated electrochemical carbon nanotube (CNT) artificial muscles had a small stroke (~0.2%) (*4*, *5*), like that for many piezoelectrics, and their actuation was slow. Transitioning to twisted yarn electrochemical CNT muscles increased muscle stroke to 0.8% (*6*), and using coiled CNT yarns increased the contractile stroke for an organic electrolyte to up to 16.5% (*7*–*9*). Although muscle stroke can be amplified by mandrel coiling to make a muscle with a high spring index (the ratio of average coil diameter to yarn diameter) (*10*), this reduces the muscle's work capacity by disproportionally reducing load-lifting capability.

We provide solutions to a major problem for present electrochemical CNT yarn muscles. During a scan from extreme negative to extreme positive potentials, there is first an efflux of positive ions and then an influx of negative ions for the electrochemical double layer. Therefore, these muscles are bipolar, meaning that they first expand and then contract during this potential scan so that the net effect is a reduced overall stroke. By contrast, the stroke of a unipolar artificial muscle monotonically changes during a potential scan over the entire electrochemical window. Some of these unipolar muscles provide the strange property of increasing stroke with increasing potential scan rate, which we call scan rate–enhanced stroke (SRES).

Unlike bipolar electrochemical actuation, tensile actuation monotonically increases with temperature increases for thermally powered muscles (*11*–*13*) or weight increases for sorption-powered muscles (*14*). Unipolar tensile actuation is observed for Faradaic electrochemical muscles in which only one sign ion participates in an intercalation-based process over the available potential range (*15*, *16*). However, Faradaic intercalation generally suffers from rate and cyclability limitations, as seen by comparing battery and supercapacitor performance (*17*).

The artificial muscles were fabricated by inserting twist into a stack of forest-drawn or guest-containing CNT sheets (figs. S1 to S4) (*18*). The reported work capacities and power densities are for muscle contraction. For an optimized step potential change, the full-cycle power density is the ratio of contractile work-per-cycle to the cycle time, and the maximum average power density is the ratio of contractile work to actuation time for an optimized time (*19*). Unless otherwise noted, tensile actuation was characterized under constant load while the yarn was torsionally tethered, a large capacitance counter electrode was used, current densities are relative to the weight of dry muscle, and capacitances and injected charges are relative to the weight of CNTs. The performance metrics for bipolar muscles include only potential ranges where stroke cancellation does not occur.

The first investigated polymer guest was poly(sodium 4-styrenesulfonate) (PSS), which is approved for drug use and inexpensive enough for use in water softening. A CNT yarn containing PSS guest is called a PSS@CNT yarn. The dependence of measured strokes on the applied potential is shown in Fig. 1, A and B, for a bipolar neat CNT yarn and a unipolar PSS@CNT yarn, respectively, in 0.1 M aqueous LiCl electrolyte. About 30 weight

[1]Alan G. MacDiarmid NanoTech Institute, University of Texas at Dallas, Richardson, TX 75080, USA. [2]Center for Composite Materials and Structures, Harbin Institute of Technology (HIT), Harbin 150080, China. [3]Institute of Intelligent Flexible Mechatronics, Jiangsu University, Zhenjiang 212013, China. [4]Department of Chemistry and Biochemistry, University of Texas at Dallas, Richardson, TX 75080, USA. [5]MilliporeSigma, Materials Science, Milwaukee, WI 53209, USA. [6]Jiangsu Collaborative Innovation Center of Photovoltaic Science and Engineering, Changzhou University, Changzhou 213164, China. [7]Opus 12 Incorporated, Berkeley, CA 94710, USA. [8]Center for Self-Powered Actuation, Department of Biomedical Engineering, Hanyang University, Seoul 04763, South Korea. [9]Institute for Frontier Materials, Deakin University, Waurn Ponds, Victoria 3216, Australia. [10]Department of Mechanical Science and Engineering, University of Illinois Urbana-Champaign, Urbana, IL 61801, USA. [11]Department of Materials Science and Engineering, University of Texas at Dallas, Richardson, TX 75080, USA. [12]Department of Mechanical and Aerospace Engineering, Seoul National University, Gwanak-gu, Seoul 08826, The Republic of Korea. [13]Faculty of Engineering and Information Sciences, University of Wollongong, Australia, Wollongong, New South Wales 2500, Australia. [14]Intelligent Polymer Research Institute, Australian Institute for Innovative Materials, University of Wollongong, Wollongong, New South Wales 2522, Australia.
*These authors contributed equally to this work.
†Corresponding author. Email: dingjn@ujs.edu.cn (J.D.); lengjs@hit.edu.cn (J.L.); ray.baughman@utdallas.edu (R.H.B.)

percent (wt %) PSS was used to optimize performance. Piezoelectrochemical spectroscopy (PECS) indicates the origin of this transition from bipolar to unipolar actuation. During PECS, a cyclic voltammetry (CV) scan is conducted while the yarn is sinusoidally stretched (*20*). The potential of zero charge (pzc) is the potential at which the stretch-induced current change becomes zero (Fig. 1, C and D). PECS shows (figs. S5 and S6) that the pzc shift monotonically increases with increasing PSS concentration and converts to fully unipolar behavior for >5 wt % PSS because of a polymer-induced shift of the pzc from −80 mV to more than +1 V (which is outside the electrolyte's electrochemical stability window).

Although previous electrochemical yarn muscles decreased stroke with increasing potential scan rate (Fig. 1A), the stroke of this unipolar muscle containing 30 wt % PSS (Figs. 1B and 2A) increased (by a factor of 3.8 for a scan rate increase from 0.01 to 1 V/s, which is called the SRES enhancement). To evaluate the effects of scan rate on effective ion size (Fig. 2B), we measured the scan rate dependence of the stroke-charge ratio (SCR), the ratio of muscle stroke to the change in charge per CNT weight for a given potential scan range. These results show that the SCR of the neat CNT yarn is very low for both electron and hole injection and even slightly decreases in magnitude with increasing potential scan rate. However, the SCR for the PSS@CNT yarns generally increases with increasing scan rate (Fig. 2B). This result shows that the effective ion size increases with increasing potential scan rate because of the electroosmotic pumping of solvent. This effective ion size includes the ion hydration observed at low scan rates as well as the water dragged by the hydrated ion at high scan rates. Figure S17 shows that the coulombic efficiency is sufficiently high that charge loss minimally affects the SCR.

These results are like those known for electrochemically pumping water between ionomer membrane–separated reservoirs (*21*, *22*). Analogous water pumping has been observed for ionic polymer-metal composite (IPMC) bending actuators (*23*). Upon increasing the charge transfer rate, the hydrated ion drags additional water. If no ion solvation can occur, then SRES cannot result. This is demonstrated by the absence of SRES for actuation of PSS@CNT in an ionic liquid (figs. S18 and S19) and in water-in-salt electrolytes (fig. S18), where little water is available (*24*).

Further evidence for increasing effective ion size with increasing scan rate was obtained from electrochemical quartz crystal microbalance measurements of the scan rate dependence of weight increase per injected charge for a CNT sheet stack containing 40 wt % PSS. The transported water increased monotonically with increasing potential scan rate from 10 to 100 mV/s for the PSS@CNT sheet stack, whereas it was approximately constant for a neat CNT sheet stack (fig. S8). These weight change measurements during CV scans (fig. S7) also show unipolar weight pickup for the 40 wt % PSS@CNT sheet stack and bipolar weight pickup for the neat CNT sheet stack.

The effect of SRES can also be seen for actuation of a 30 wt % PSS@CNT yarn in 0.1 M aqueous LiCl electrolyte when using the large square-wave potentials enabled by unipolar behavior (Fig. 2C). The small stroke observed for a neat CNT yarn rapidly decreased with frequency increase because of capacitance decrease. The existence of SRES means that an increase in effective ion size partially compensates for this capacitance decrease. The maximum contractile work capacity for the unipolar PSS@CNT muscle is 0.73 J/g (Fig. 2D), which is 3.1 times that reported (*4*) for a CNT yarn operated in an aqueous electrolyte. These PSS@CNT unipolar muscles provided 10,000 largely reversible cycles (fig. S13) and a natural latching state (fig. S14). This SRES-enhanced contractile work capacity can be further increased to 3.5 J/g in an organic electrolyte because of its larger electrochemical window (fig. S9).

Because of the high rate capability of the unipolar PSS@CNT muscles, they can function at lower temperatures than prior-art electrochemical muscles. More specifically, the results of figs. S15 and S16 show that a 35 wt % PSS@CNT muscle can usefully operate down to −30°C while providing a contractile stroke of ~2.5%.

Unipolar actuation and SRES also occur for Nafion@CNT (Fig. 3A and fig. S29). The contractile work capacity of the Nafion@CNT reached 1.04 J/g (Fig. 3B), and the contractile efficiency (Fig. 3B) was 6.1% for a scan rate of 200 mV/s. An anion-exchange ionomer [poly (diallyldimethylammonium chloride), PDDA] shifts the pzc in an opposite direction (to below −1 V; fig. S5) to cation-exchange ionomers, but unipolar strokes and SRES are still obtained. A potential change from +1 to −1 V generates a −4.5% stroke for PDDA@CNT and a 5.8% stroke for PSS@CNT (fig. S30 and Fig. 2D). Unless the polymer in a CNT yarn contains a charged group, the pzc is little changed and no unipolar or SRES behavior is observed (fig. S21).

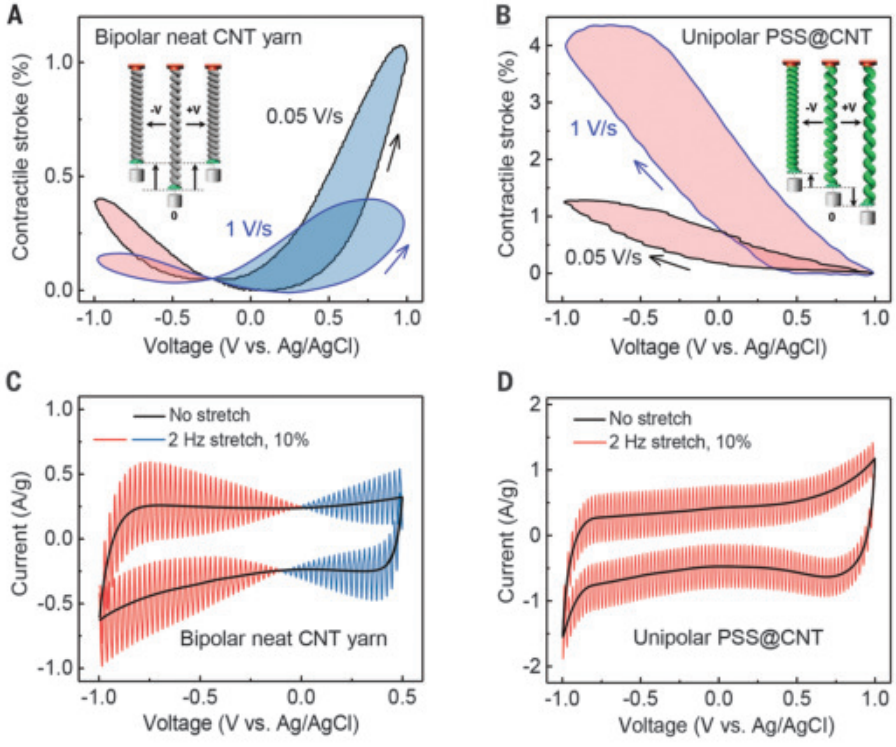

Fig. 1. Comparisons of unipolar and bipolar muscles. (**A** and **B**) Tensile stroke measurements under 10.9 MPa stress for different cyclic voltammetry scan rates for a neat CNT yarn muscle and a 30 wt % PSS@CNT yarn muscle, respectively, in 0.1 M aqueous LiCl. Insets are illustrations of bipolar and unipolar stroke actuation. (**C** and **D**) Piezoelectrochemical spectroscopy for a scan rate of 50 mV/s for a neat CNT yarn muscle and a 30 wt % PSS@CNT yarn muscle, respectively, in the above electrolyte. A sinusoidal tensile strain of 10% at 2 Hz was applied. The potential at which the stretch-induced current change vanishes indicates that the pzc of the neat CNT yarn is −80 mV and that the pzc of the unipolar PSS@CNT yarn is outside the electrochemical window of the electrolyte.

The capacitance (per CNT weight) of the PSS@CNT muscle substantially increases with increasing PSS content, which increases muscle stroke (figs. S6 and S32). Also, the concentration dependence of capacitance of the fully coiled PSS@CNT muscle is close to that for the precursor PSS@CNT sheet stack. The most reasonable explanation for this is that infiltration of PSS between nanotube bundles interferes with capacitance losses because of electrolyte wetting–induced and twist-induced increases in bundling.

Because PSS@CNT and PDDA@CNT yarns actuate in-phase when used as opposite electrodes, they can be mechanically coupled to provide a single muscle that uses the SRES-enhanced strokes of both yarns to increase the force output and eliminate the need for a passive counter electrode. An all-solid-state PSS@CNT/PDDA@CNT muscle coupled with gel electrolyte was realized (figs. S1 and S30), the contractile stroke of which (3.9%) was comparable to that for a PSS@CNT muscle (5.8%) and a PDDA@CNT muscle (4.5%). This elimination of an electrolyte bath is important for many applications. We used these coiled PSS@CNT and PDDA@CNT muscles to make an actuating two-layer textile (fig. S31), which shows a 3.9% contractile stroke in the warp direction (the muscle direction) for a 0.05-Hz square wave between −2 and +2 V (movie S1).

A unipolar stroke, SRES, and 8000 largely reversible cycles were observed for a coiled CNT yarn muscle coated with a surfactant, sodium dodecyl sulfate (SDS) (figs. S22 and S24). The work capacity for square-wave excitation reached 0.79 J/g, and the maximum average power density during contraction and the full cycle power density were 2.7 and 2.0 W/g, respectively (Fig. 3C). Using this approach for a sheath-run artificial muscle (*19*), we obtained a usable muscle stroke (1.3%) when operating at 10 Hz in a 0.2 M LiCl aqueous electrolyte containing 0.6 wt % SDS (fig. S25B). This high frequency capability results from the combination of SRES behavior and the short diffusion distance for actuating the sheath compared with the diffusion distance for actuating a CNT yarn that has the same mass of CNTs per muscle length. Results for an aqueous LiCl electrolyte (Fig. 3D) show that the SCR is similarly enhanced with increasing potential scan rate for PSS@CNT and SDS@CNT muscles.

We also made unipolar muscles that provided 10,000 largely reversible cycles by biscrolling graphene oxide (GO) into a CNT yarn (figs. S26 and S27). During biscrolling, a GO-coated CNT sheet stack is twisted so that this guest is trapped within the helical corridors of the yarn (*25*). An organic electrolyte (0.2 M TBA·PF_6 in acetonitrile, where TBA is tetrabutylammonium) was used. With increasing GO content, the stroke of a CNT yarn muscle gradually changed from bipolar to unipolar (fig. S27). The peak equilibrium tensile contraction and work capacity were 21% and 4.1 J/g, respectively, compared with 16% and 3.2 J/g for the neat yarn in this electrolyte (Fig. 3E).

The contractile stroke of a unipolar GO@CNT muscle at 1 Hz was 8.0% (Fig. 3F) compared with 2.5% for the neat CNT muscle and the previous 4.7% for a sheath-run CNT muscle (*18*) at 1 Hz. The full-cycle contractile power and the maximum average power during contraction were 2.08 and 8.17 W/g, respectively, for the GO@CNT muscle, compared with 1.02 and 2.52 W/g, respectively, for a neat CNT yarn muscle (Fig. 3F). The highest previously reported full-cycle contractile power and maximum contractile average power for operation in an organic electrolyte were 0.99 and 3.71 W/g, respectively, for a sheath-run artificial muscle (*18*). Oxidizing the surfaces of the CNTs in a yarn using boiling nitric acid also results in unipolar behavior (with the maximum stroke twice that of the neat bipolar CNT yarn), but SRES was absent (fig. S28). Additional examples of unipolar strokes without SRES are found for Faradaic muscles (*15*, *16*) and those based on CNTs (fig. S20).

Our density functional theory (DFT) calculations show that the work function shift of the positive groups $[N^+(CH_3)_2]$ in PDDA and the negative groups (SO_3^-) in PSS are identical in magnitude for the same ratio of charge to electrochemically accessible surface carbon atoms. Using the previously predicted linear correlation between pzc and work function (*26*), good agreement was obtained between the measured and calculated dependence of pzc on surface charge density (fig. S35). We found that coiled muscles containing electronically contacting neat CNT- and PSS-infiltrated yarns have a measured pzc that is the average of the component structures (figs. S33 and S34).

The variation of current density with potential for constant scan-rate actuation partially explains why muscle strokes are additive for galvanostatic stroke changes for different potential ranges (figs. S12 and S23), but they are not additive for fast constant scan-rate actuation or for square-wave actuation (fig. S10). Also, the sum of the charge injected at high potential scan rates for a potential scan from

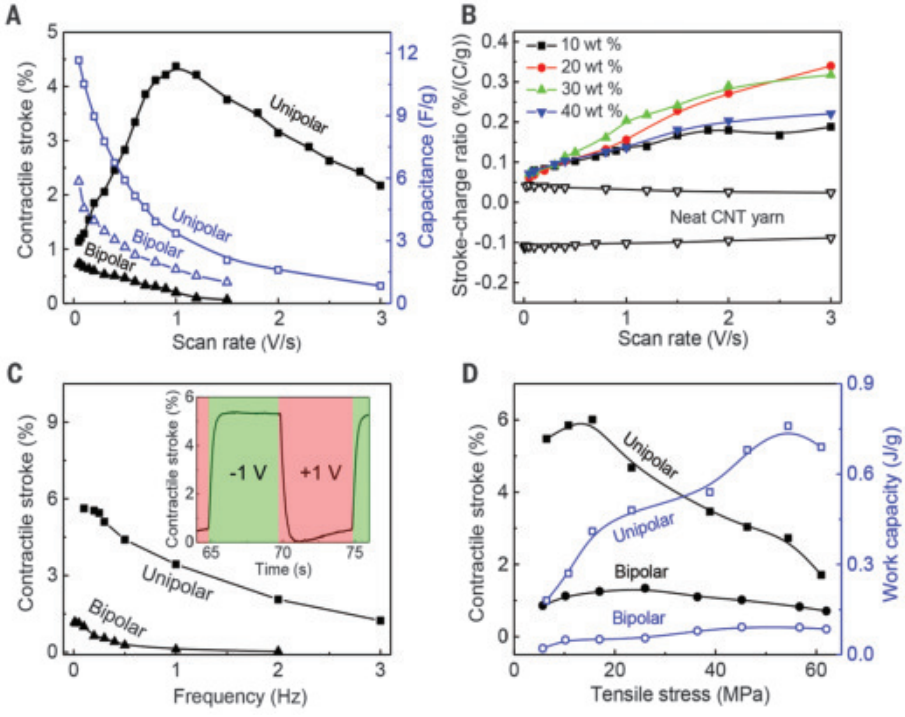

Fig. 2. Scan rate–enhanced strokes for PSS@CNT unipolar muscles. (**A**) Dependence of tensile stroke and capacitance on scan rate for a unipolar PSS@CNT and a bipolar neat CNT muscle in 0.1 M aqueous LiCl. Upon increasing the scan rate from 20 to 1000 mV/s, for the potential range of +1 to −1 V, the contraction of the unipolar muscle was amplified by a factor of 3.8. (**B**) Effect of polymer content on the stroke-charge ratio for a PSS@CNT unipolar muscle (for the potential range of −0.95 to 0.90 V) and for a bipolar CNT muscle (between −1.00 and 0.00 V and between 0.00 and 1.00 V). (**C**) Frequency dependence of contractile stroke for square-wave pulses, which is maximized by using a potential range between +1 V and −1 V for the above unipolar muscle and between 0 and +1 V for the bipolar muscle. The inset shows the dependence of stroke on square-wave pulses for the PSS@CNT muscle. (**D**) Dependence of equilibrium stroke and work capacity on applied tensile stress for a unipolar PSS@CNT muscle and a bipolar neat CNT muscle, when 0.1-Hz square-wave pulses are applied for the potential range in (C).

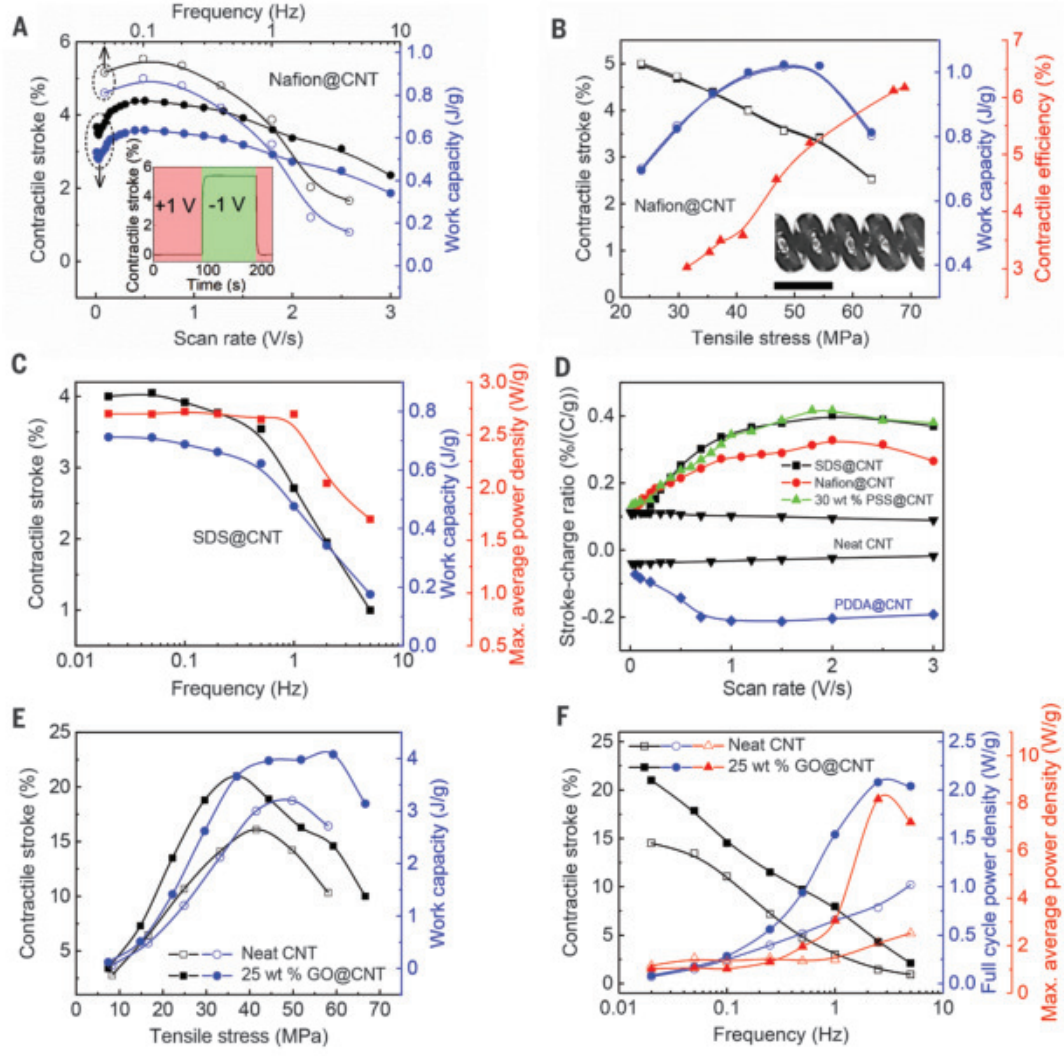

Fig. 3. Other unipolar muscles. (**A**) Dependence of muscle stroke and work capacity on scan rate (bottom axis) and on square-wave frequency (top axis) for a potential change between −1 and +1 V for a Nafion@CNT muscle operated in 0.2 M aqueous LiCl under 21 MPa tensile stress. The inset shows the dependence of stroke on square-wave pulses for the Nafion@CNT muscle. (**B**) Contractile stroke, work capacity, and contractile efficiency versus tensile stress for the Nafion@CNT muscle, when 0.1-Hz square-wave pulses are applied for the potential range and electrolyte in (A). The inset shows a microscope image of the Nafion@CNT muscle. Scale bar, 150 μm. (**C**) Dependence of contractile stroke, work density, and maximum average power density on square-wave frequency for an SDS@CNT muscle having 48 MPa applied load. (**D**) Stroke-charge ratio versus potential scan rate for unipolar muscles having SRES and a bipolar neat CNT muscle that does not have SRES. The electrolyte used was 0.1 M LiCl for PSS@CNT, PDDA@CNT, and the neat CNT yarn and 0.2 M LiCl for Nafion@CNT and SDS@CNT. (**E**) Contractile stroke and work capacity versus applied tensile stress for neat CNT yarn and 25 wt % GO@CNT yarn when actuated in 0.2 M TBA·PF_6 in acetonitrile at a square-wave frequency of 0.02 Hz and a potential change from −2.75 to +1 V. (**F**) Contractile stroke, full-cycle power density, and maximum average power density versus square-wave frequency for actuation of a neat CNT yarn and a 25 wt % GO@CNT yarn using the above electrolyte and potential range and 36 MPa applied load.

V_1 to V_3 is larger than the sum for a potential scan from V_1 to V_2 and from V_2 to V_3, where $V_3 > V_2 > V_1$ (fig. S11). Likewise, for high-frequency square-wave actuation, the charge injected for a potential change between V_1 and V_3 is larger than the sum of the charge injected for potential changes between V_1 and V_2 and between V_2 and V_3. This aspect has not been previously described because previous electrochemical muscles had such a low tensile stroke for fast actuation that it could not be investigated.

Performance improvements resulted from using coiled CNT yarns containing pzc shift agents such as ionomers, oxidized graphene platelets, and surfactants. These include avoiding stroke cancelation caused by bipolar actuation, enabling operation down to at least −30°C, realizing large strokes at high frequencies, and increasing efficiencies, work capacities, and power densities. These result from replacement of bipolar behavior with unipolar behavior and a marked increase in effective ion size caused by electroosmotic solvent pumping. The advantages of these unipolar muscles having SRES are also demonstrated for all-solid-state muscles and muscle textiles that eliminate the need for an electrolyte bath.

REFERENCES AND NOTES

1. S. M. Mirvakili, I. W. Hunter, *Adv. Mater.* **30**, 1704407 (2018).
2. J. D. Madden, *Science* **318**, 1094–1097 (2007).
3. G.-Z. Yang *et al.*, *Sci. Robot.* **3**, eaar7650 (2018).
4. R. H. Baughman *et al.*, *Science* **284**, 1340–1344 (1999).
5. Y. Yun *et al.*, *Nano Lett.* **6**, 689–693 (2006).
6. J. Foroughi *et al.*, *Science* **334**, 494–497 (2011).
7. J. Qiao *et al.*, *Small* **14**, e1801883 (2018).
8. J. A. Lee *et al.*, *Adv. Mater.* **29**, 1700870 (2017).
9. K. J. Kim *et al.*, *ACS Appl. Mater. Interfaces* **11**, 13533–13537 (2019).
10. C. S. Haines *et al.*, *Science* **343**, 868–872 (2014).
11. J. Fan, G. Li, *RSC Advances* **7**, 1127–1136 (2017).
12. M. Kanik *et al.*, *Science* **365**, 145–150 (2019).
13. M. Hiraoka *et al.*, *Sci. Rep.* **6**, 36358 (2016).
14. P. Chen *et al.*, *Nat. Nanotechnol.* **10**, 1077–1083 (2015).
15. W. Lu, E. Smela, P. Adams, G. Zuccarello, B. R. Mattes, *Chem. Mater.* **16**, 1615–1621 (2004).
16. K. Mukai, K. Yamato, K. Asaka, K. Hata, H. Oike, *Sens. Actuators B Chem.* **161**, 1010–1017 (2012).
17. A. González, E. Goikolea, J. A. Barrena, R. Mysyk, *Renew. Sustain. Energy Rev.* **58**, 1189–1206 (2016).
18. Materials and methods are available as supplementary materials.
19. J. Mu *et al.*, *Science* **365**, 150–155 (2019).
20. S. H. Kim *et al.*, *Science* **357**, 773–778 (2017).
21. T. Okada, H. Satou, M. Okuno, M. Yuasa, *J. Phys. Chem. B* **106**, 1267–1273 (2002).
22. M. D. Bennett, D. J. Leo, G. L. Wilkes, F. L. Beyer, T. W. Pechar, *Polymer (Guildf.)* **47**, 6782–6796 (2006).
23. S. Nemat-Nasser, Y. Wu, *J. Appl. Phys.* **93**, 5255–5267 (2003).
24. L. Suo *et al.*, *Science* **350**, 938–943 (2015).
25. M. D. Lima *et al.*, *Science* **331**, 51–55 (2011).
26. S. Trasatti, *J. Electroanal. Chem. Interfacial Electrochem.* **33**, 351–378 (1971).

ACKNOWLEDGMENTS

We thank B. J. Carlson, H. L. Hansen, and X. Li for sample preparation and measurements. **Funding:** Support in the United States was from Air Force Office of Scientific Research grant no. FA9550-18-1-0510, Robert A. Welch Foundation grant no. AT-0029, and DARPA SHRIMP program contract no. HR001119C0042.

Support in Korea was from the Creative Research Initiative Center for Self-Powered Actuation of the National Research Foundation of Korea and the Ministry of Science and ICT and the National Research Foundation of Korea (grant nos. 2012R1A3A2048841 and 2015M3D1A1068062). Support in China was from the Program of Introducing Talents of Discipline to Universities (grant no. G20212006001), the National Key Research and Development Program (grant no. 2017YFB0307001), the National Natural Science Foundation (grant no. 91648109), the Harbin Institute of Technology program for short-term PhD visits, and the China Scholarships Council. Support in Australia was from the Alfred Deakin Postdoctoral Research Fellowship and the Australian Research Council (grant no. FT130100380). **Author contributions:** R.H.B. conceived and initiated the project. All authors contributed to experimental design, planning, and execution; data analysis; and manuscript writing. H.K., P.C., M.C., K.C., S.N., and K.A.A. conducted theoretical analysis. **Competing interests:** H.C., J.L., X.H., N.L., C.S.H., S.F., Z.W., J.M., and R.H.B. are listed as the inventors on a PCT patent application (PCT/US2020/016391) describing unipolar muscle. **Data and materials availability:** All data needed to evaluate the conclusions in the study are present in the main text or the supplementary materials.

SUPPLEMENTARY MATERIALS

24 April 2020; accepted 17 December 2020
10.1126/science.abc4538

CRYSTALLIZATION

Reversible disorder-order transitions in atomic crystal nucleation

Sungho Jeon[1]*, Taeyeong Heo[1]*, Sang-Yeon Hwang[2]*†, Jim Ciston[3], Karen C. Bustillo[3], Bryan W. Reed[4], Jimin Ham[1], Sungsu Kang[5,6], Sungin Kim[5,6], Joowon Lim[1], Kitaek Lim[1], Ji Soo Kim[5,6], Min-Ho Kang[5,6], Ruth S. Bloom[4], Sukjoon Hong[1], Kwanpyo Kim[7,8], Alex Zettl[9,10,11], Woo Youn Kim[2], Peter Ercius[3]‡, Jungwon Park[5,6]‡, Won Chul Lee[1]‡

Nucleation in atomic crystallization remains poorly understood, despite advances in classical nucleation theory. The nucleation process has been described to involve a nonclassical mechanism that includes a spontaneous transition from disordered to crystalline states, but a detailed understanding of dynamics requires further investigation. In situ electron microscopy of heterogeneous nucleation of individual gold nanocrystals with millisecond temporal resolution shows that the early stage of atomic crystallization proceeds through dynamic structural fluctuations between disordered and crystalline states, rather than through a single irreversible transition. Our experimental and theoretical analyses support the idea that structural fluctuations originate from size-dependent thermodynamic stability of the two states in atomic clusters. These findings, based on dynamics in a real atomic system, reshape and improve our understanding of nucleation mechanisms in atomic crystallization.

Nucleation is a critical phenomenon in the formation of many solid materials (*1*–*3*). Classical nucleation theory describes a pathway to crystal formation (*4*, *5*) in which direct assembly of monomers occurs by density fluctuations over the surface and volume free-energy barrier. Notably, the nucleation process in diverse systems of colloidal particles (*6*, *7*), proteins (*8*, *9*), and small molecules (*10*) has been shown to incorporate nonclassical processes (*1*) such as a two-step nucleation mechanism (*2*, *3*). In those systems, metastable intermediate clusters form and then transform to stable crystals, thereby circumventing the high energy barrier of direct crystallization.

Atomic crystallization is affected by diverse metastable states, which inherently appear in small atomic clusters (~1 nm), with sizes equivalent to the nucleation stage (*11*). A few experimental studies have identified fully or partially disordered states in the early stage of atomic crystallization in solution (*12*, *13*), on surfaces (*14*, *15*), or in nanomaterials (*16*, *17*). Because of multiple local minima with similar energy levels originating from diverse metastable states (*1*, *11*), we hypothesize that the contribution of metastable states provides a dynamic nature to the early stage of crystallization. Additionally, surfaces of small clusters fluctuate because of recurrent collisions of incoming atoms and desorption of surface atoms, and thus, the free-energy barrier defining nuclei can be perturbed dynamically. These energetic interactions suggest that the early stage of atomic crystallization may exhibit nonclassical processes governed by atomistic dynamics. In this work, we investigated the heterogeneous nucleation process of gold nanocrystals on a graphene surface with atomic spatial resolution and millisecond temporal resolution.

We used three aberration-corrected transmission electron microscopes (TEMs)—one with a direct electron detector, the second with a scintillator-coupled camera combined with an electrostatic subframing system that further improved temporal resolution (*18*), and the third with a low-noise, scintillator-coupled camera for low-dose imaging (supplementary materials section 1 and fig. S1). For in situ imaging of crystal nucleation, we prepared single-layered graphene support films on which gold(I) cyanide (AuCN) nanoribbons were synthesized (fig. S2) (*19*, *20*). The electron beam acted as an imaging source as well as a reducing agent to decompose AuCN nanoribbons (~2- to 5-nm thick) to zerovalent Au atoms and $(CN)_2$ gas (*19*, *21*). The concentration of Au adatoms increased locally near the imaged nanoribbon, and the atoms aggregated to form Au nanocrystals (fig. S1A). This process occurred on the two-dimensional (2D) surface of free-standing graphene in vacuum, which minimized electron scattering from the substrate. To investigate the process from the beginning, the recording of a high-speed TEM movie was synchronized with the illumination of the high-intensity electron beam on a pristine sample area (fig. S1D). The advanced imaging detectors and sample geometry enabled us to achieve millisecond temporal resolution (1.6 and 10 ms) with atomic-scale observations.

Movie S1, with snapshots included in Fig. 1A, presents a typical high-speed TEM movie (temporal resolution: 10 ms; accelerating voltage: 300 kV; current density: 7.0×10^6 A/m^2, equivalent to an electron dose-rate of 4.4×10^5 e$^-$/Å^{2}s) of the crystal nucleation and growth processes—the overall characteristics of which are presented in the supplementary materials section 2 and fig. S3. Time-resolved investigation of each nucleation path (movie S2) elucidates that the crystal nucleation proceeds through a mechanism in which an atomic cluster transforms reversibly between disordered and crystalline states many times. As shown in the first notable events of movie S2 (Fig. 1B; seven successive frames from 140 to 200 ms), the first lattice fringe abruptly appears at 150 ms and disappears at 170 ms. Then, the second lattice fringe appears (190 ms) with a different lattice orientation and disappears at some point between 200 and 230 ms (fig. S4 and

[1]Department of Mechanical Engineering, BK21 FOUR ERICA-ACE Center, Hanyang University, Ansan, Gyeonggi 15588, Republic of Korea. [2]Department of Chemistry, Korea Advanced Institute of Science and Technology (KAIST), Daejeon 34141, Republic of Korea. [3]National Center for Electron Microscopy, Molecular Foundry, Lawrence Berkeley National Laboratory (LBNL), Berkeley, CA 94720, USA. [4]Integrated Dynamic Electron Solutions, Inc., Pleasanton, CA 94588, USA. [5]School of Chemical and Biological Engineering and Institute of Chemical Processes, Seoul National University, Seoul 08826, Republic of Korea. [6]Center for Nanoparticle Research, Institute for Basic Science (IBS), Seoul 08826, Republic of Korea. [7]Department of Physics, Yonsei University, Seoul 03722, Republic of Korea. [8]Center for Nanomedicine, IBS, Seoul 03722, Republic of Korea. [9]Department of Physics, University of California, Berkeley, CA 94720, USA. [10]Materials Sciences Division, LBNL, Berkeley, CA 94720, USA. [11]Kavli Energy NanoSciences Institute, Berkeley, CA 94720, USA.
*These authors contributed equally to this work. †Present address: Samsung Advanced Institute of Technology (SAIT), Samsung Electronics, Suwon 16678, Republic of Korea.
‡Corresponding author. Email: wonchullee@hanyang.ac.kr (W.C.L.); jungwonpark@snu.ac.kr (J.P.); percius@lbl.gov (P.E.)

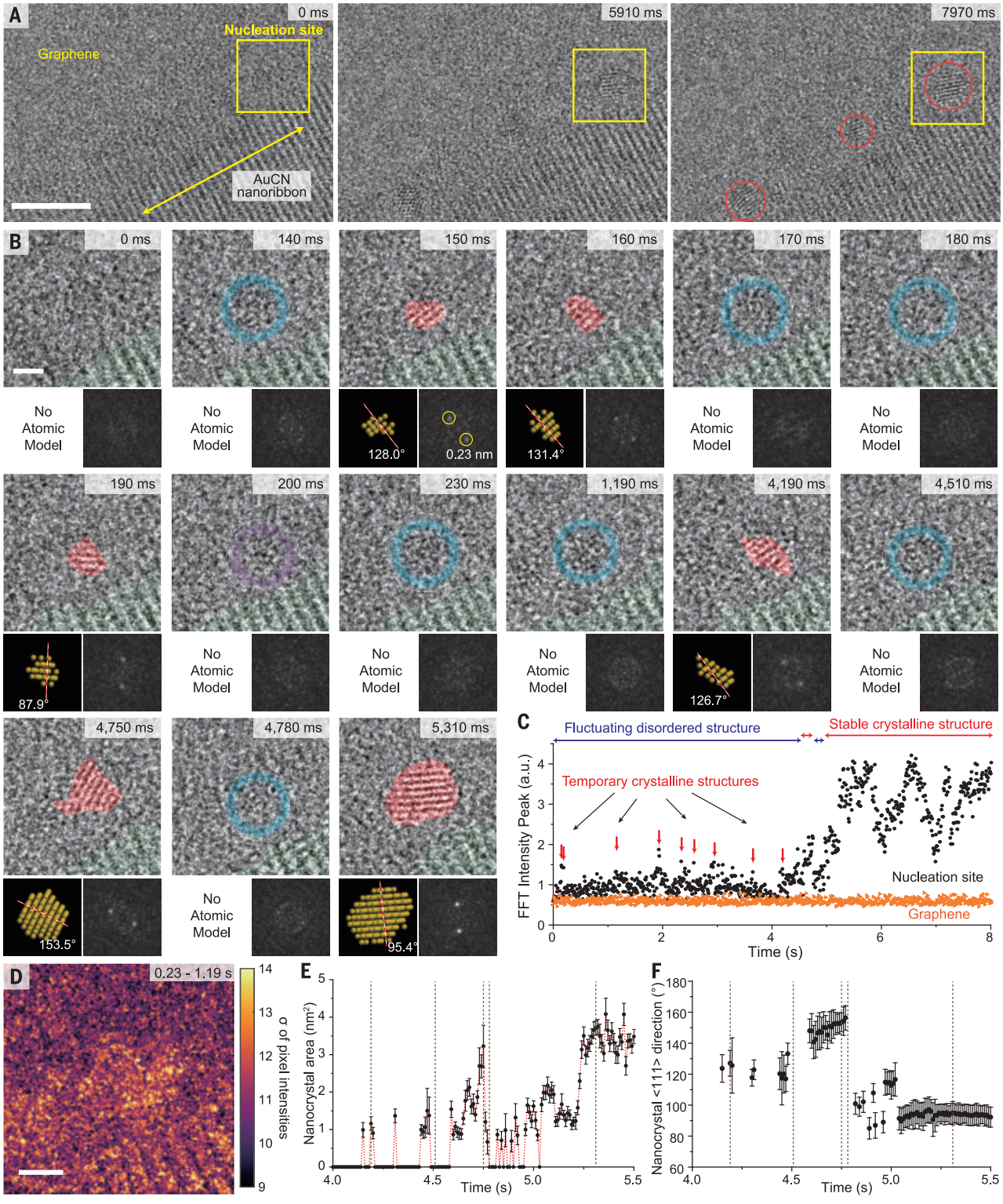

Fig. 1. Direct observation of the formation of an Au nanocrystal. (**A**) TEM image frames from the high-speed in situ movie (movie S1). Scale bar, 5 nm. Au nanocrystals in the final image are marked with red circles. (**B**) Individual frames from movie S2 showing a nucleation process [from the yellow box in (A); temporal resolution, 10 ms]. Beneath each frame on the left side, an atomic model of the nanocrystal is shown. Red dashed lines indicate nanocrystal <111> directions. Beneath each frame on the right, an FFT image is shown. Scale bar, 1 nm. The areas of Au lattices and AuCN nanowires in the frames are pseudocolored in red and light-green, respectively. Blue circles indicate nanoclusters in the disordered state, and purple circles indicate the undefinable state (where the crystalline versus disordered classification is unclear). (**C**) Maximum intensity of the FFT image as a function of time. The signals from a graphene area represent ground noise levels (negative control) of this analysis. a.u., arbitrary units. (**D**) A color map obtained from standard deviations of intensities from 230 to 1190 ms for each pixel. Scale bar, 1 nm. (**E**) Nanocrystal area from 4.00 to 5.50 s. (**F**) Direction of <111> lattices from 4.00 to 5.50 s. Vertical dotted lines in (E) and (F) correspond to the time-labeled images in (B). Related images and detailed methods are presented in figs. S3 to S10.

supplementary materials section 3.2). From 230 to 1190 ms, no lattice fringe is observed while strong fluctuations of pixel intensities in the center indicate the presence of an atomic cluster (Fig. 1D). Similar processes are repeated during the early stage of crystallization from 0 to ~4 s (fig. S5). Short-lived lattice fringes appear and disappear repeatedly, whereas no lattice fringe is observed in most of the frames. This phenomenon is also confirmed with multiple small peaks observed by tracking maximum intensities in 2D fast Fourier transforms (FFTs) of TEM frames over time (Fig. 1C). After ~4 s, the lattice fringe starts to grow laterally and becomes stable in the next stage of the nucleation process. Notably, this growth is not gradual, but many transitions between images that show lattice and no lattice are observed multiple times (Fig. 1, B and E). During these transitions, abrupt changes of the lattice orientation occur only when lattice fringes disappear and reappear (Fig. 1, E and F). In the final stage (after ~5 s), a stable lattice fringe gradually grows without any further abrupt changes.

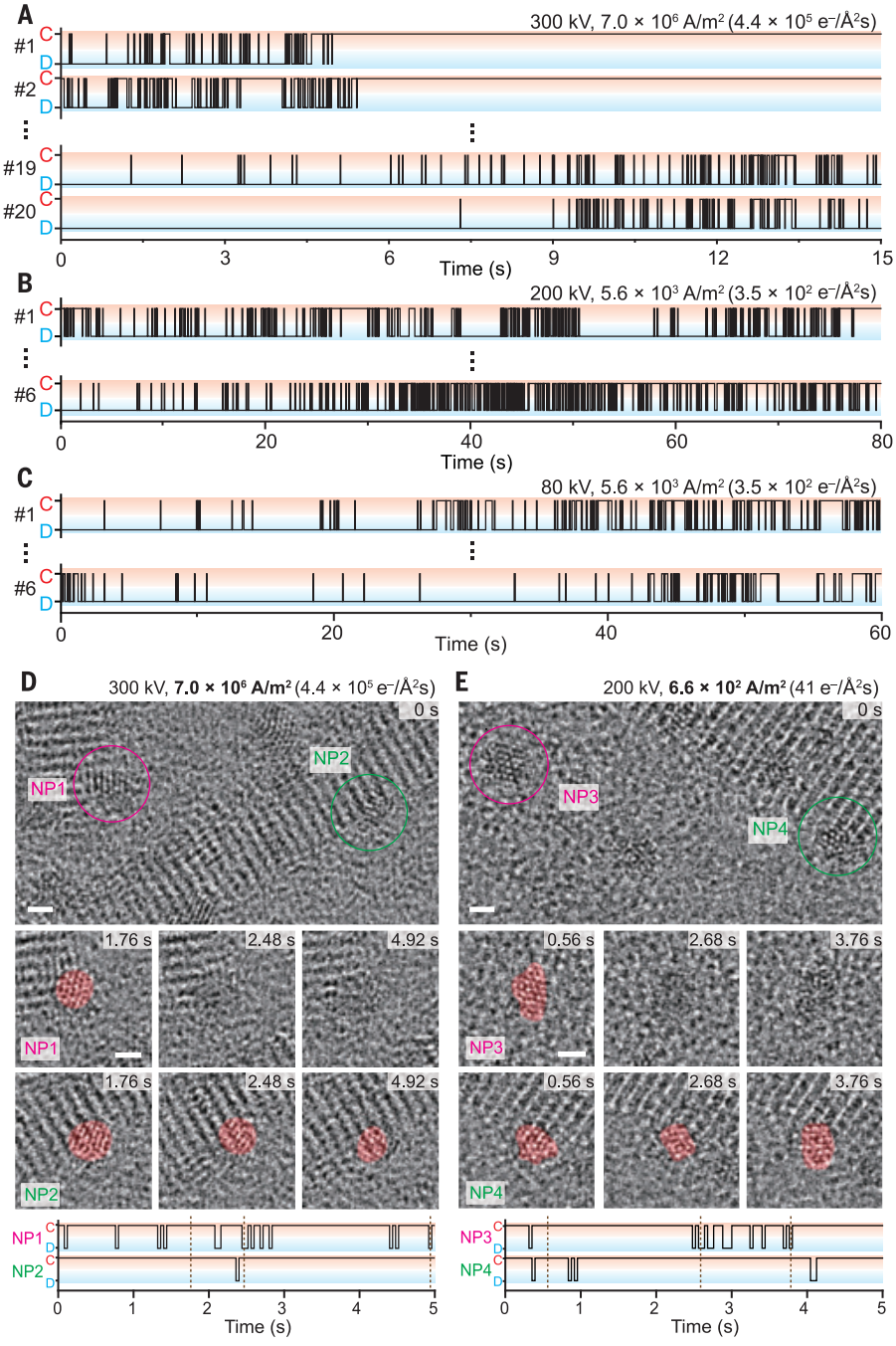

Fig. 2. Multiple nucleation paths of Au nanocrystals. (**A** to **C**) Trajectories of structural transitions between disordered and crystalline states in multiple nucleation paths observed at 300 kV and 7.0 × 10^6 A/m^2 (A), at 200 kV and 5.6 × 10^3 A/m^2 (B), and at 80 kV and 5.6 × 10^3 A/m^2 (C). Red and blue shadings are visual guides for indicating crystalline (labeled C) and disordered (labeled D) states, respectively. The first nucleation path (#1) in (A) is the dataset in Fig. 1. (**D** and **E**) TEM images and trajectories of structural transitions showing asynchronized structural fluctuations of two neighboring nanoclusters observed at 300 kV and 7.0 × 10^6 A/m^2 (D) and at 200 kV and 6.6 × 10^2 A/m^2 (E). The two cases have four orders of magnitude difference in current density. Scale bars, 1 nm. NP, nanoparticle.

The observed lattice fringes in the TEM images indicate crystalline Au nanoparticles (fig. S11). The 2D projected areas covered by lattice fringes mostly have noncircular and irregular shapes (Fig. 1B), which implies that the early-stage crystalline nuclei have nonequilibrium geometries (*16*). The frequent disappearances of existing lattice fringes, a distinguishing observation in this study, can be interpreted as a transformation of crystalline atomic structures to a disordered state. This analysis is derived from previous works which have identified fluctuating disordered (*22*, *23*) or quasi-melting (*24*) states of nanoclusters. TEM frames without a lattice fringe instead show continuous fluctuations of granular features with sizes commensurate with those of Au atoms (Fig. 1D, fig. S10, and movie S2, 0.23 to 1.19 s), and similar series of TEM frames were presented as evidence of previous identifications of disordered states (*22*–*24*). Previous x-ray diffraction (XRD) analyses confirmed disordered atomic structures of small Au nanoparticles (less than ~2 nm) (*25*). The presence of disordered atomic clusters in our case is also supported by Fig. 1, E and F, which shows that lattice orientations abruptly changed only after they disappeared and reemerged. We can rule out other explanations for the lattice disappearance (supplementary materials section 3.1), such as the tilting of nanocrystals away from low-index zone axes or the fast rotation of nanocrystals within our exposure time (~10 ms). Small nanocrystals (less than ~2 nm) always present lattice fringes in high-resolution TEM images regardless of viewing orientations (*22*, *26*), confirmed by TEM image simulations (fig. S12). The fast rotation of a nanocrystal inherently changes lattice orientations (fig. S13), but our TEM movies show that lattice orientations are fixed in successive frames during which crystalline domains decrease in size and then disappear (fig. S14).

On the basis of the above analysis, the process shown in Fig. 1 can be described as a trajectory of recurrent structural transformations between disordered and crystalline states, which is nucleation path 1 in Fig. 2A. In the early stage, a gold nanocluster is mostly in the

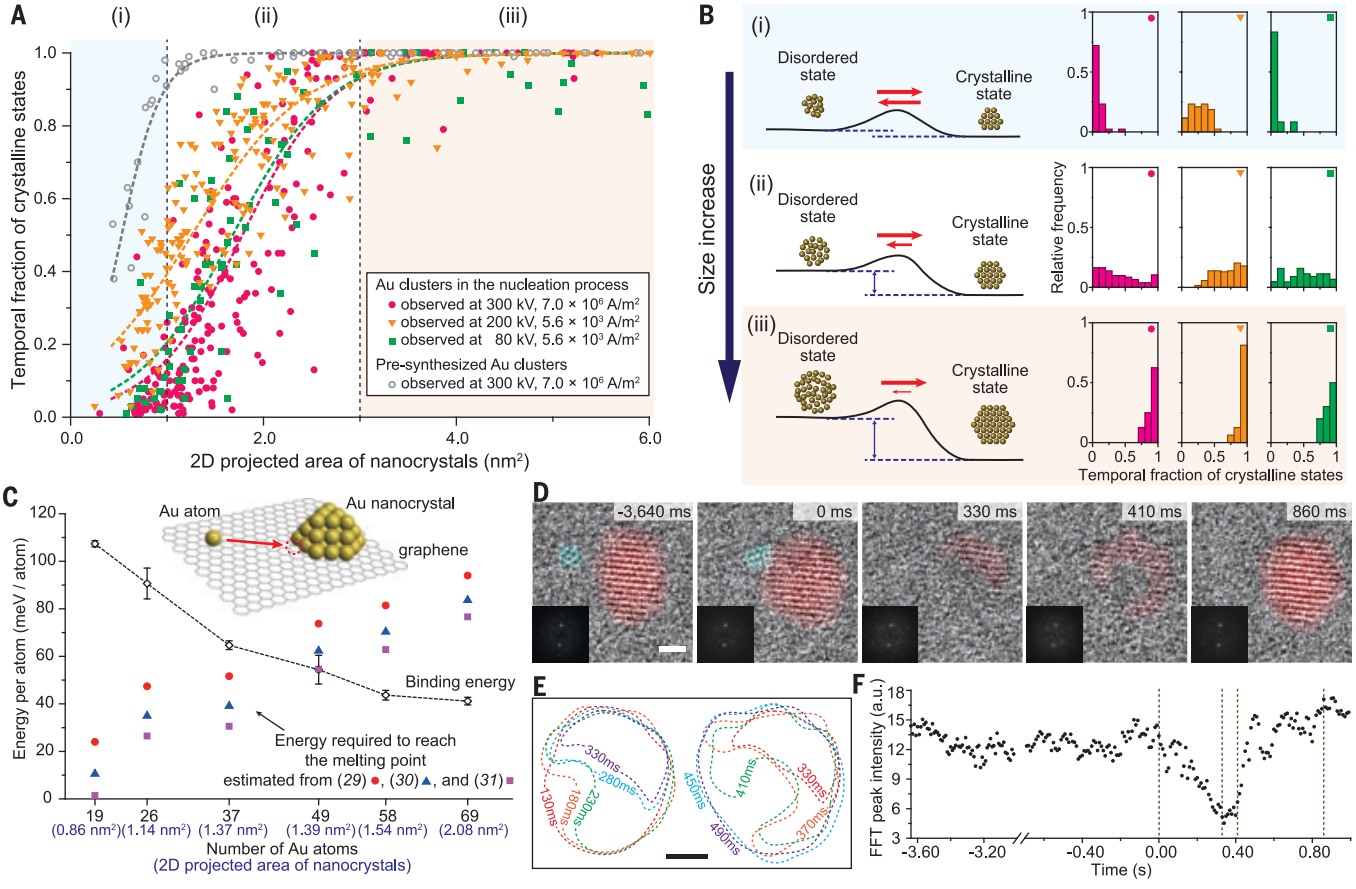

Fig. 3. Experimental and theoretical investigations of the crystalline-to-disordered transformations during the nucleation process. (**A**) Temporal fraction of crystalline states versus 2D projected area of Au nanocrystals observed during the nucleation processes (solid symbols) and observed using presynthesized Au nanoclusters (gray circles). The dashed curves represent fitting lines to the data with sigmoid (logistic) functions. (**B**) Size-dependent characteristics of nanoclusters during the nucleation process. (Left) Schematic energy diagrams showing the nucleation mechanisms of nanocrystals from small (i) to large (iii) sizes. (Right) Histograms of the temporal fractions of crystalline states for three size ranges (0 to 1.0 nm^2, 1.0 to 3.0 nm^2, and 3.0 to 6.0 nm^2) and three different imaging conditions indicated in (A). (**C**) First-principles calculations of the binding energy between an Au atom and hemispheroidal Au_n nanocrystals. The binding energy is compared with the energy required to reach the melting point of Au_{n+1} nanocrystals. (Inset) Binding model at n = 37. (**D**) Sequential TEM images showing the binding of a small nanocluster (colored in blue) to a large nanocrystal (colored in red). (Insets) FFT images of the nanocrystal. (**E**) Time-labeled contour plots of crystalline areas during partial collapse (left) and recrystallization (right). (**F**) Maximum intensities of the FFT images. Vertical dotted lines and axis in (F) correspond to the time-labeled images in (D), respectively. Scale bars, 1 nm.

disordered state and fluctuates continuously, while a few short-lived crystalline states appear with a relatively short lifetime. Repeated transformations between the two states are observed for an extended period, and ultimately a stable crystalline particle is formed. Slowing down the effective frame rate of movie S1 with frame-averaging to the previously achievable level of conventional TEM (fig. S3; 0.5 s per frame) greatly improves the signal-to-noise ratio of each TEM image, but the frame-averaged movie incorrectly suggests that the process follows a sequence of irreversible steps: A blurry or granular spot forms at the nucleation site (0.5 to 1.0 s), then the spot transforms into a lattice fringe (4.5 to 5.0 s), and the lattice fringe gradually grows. However, our high-speed in situ observations reveal that the process includes dynamic and reversible transformations between the two states.

The characteristics discovered in Fig. 1 are consistently observed in all nucleation paths investigated in this study (figs. S15 to S29 and movies S3 to S5). We modified the electron beam conditions (fig. S15) to control kinetic factors and affect the nucleation process. For example, the rate of Au adatom supply determined by radiolysis of AuCN was found to be sensitive to accelerating voltage and current density. Radiolysis of AuCN was highest at 80 kV and decreased with lower current densities (fig. S30 and supplementary materials section 4.2). We performed in situ imaging under seven different conditions (fig. S15) with accelerating voltages of either 80, 200, or 300 kV and current densities ranging from 6.6×10^2 A/m^2 (41 e^-/$Å^2$s) to 6.1×10^7 A/m^2 (3.8×10^6 e^-/$Å^2$s). The best temporal resolution achieved was 1.6 ms (at 200 kV and 6.1×10^7 A/m^2) using a subframing system (fig. S1C and fig. S25). Thus, we investigated nucleation paths in a wide range of the averaged growth rate of Au nanoclusters, from ~0.5 atoms per second (at 200 kV and 6.6×10^2 A/m^2) to ~50 atoms per second (at 80 kV and 5.9×10^5 A/m^2; at 200 kV and 6.1×10^7 A/m^2). Regardless of the different conditions, the existence of dynamic structural fluctuations during the nucleation process is confirmed in all 68 nucleation paths, as shown in the nucleation paths under three representative conditions in Fig. 2, A to C. Additionally, structural fluctuations of neighboring nanoclusters occur asynchronously in each of the in situ movies, and these phenomena are consistently observed under substantially different conditions (Fig. 2, D and E). It further supports that stochastic structural fluctuations are universal in the observed nucleation process (supplementary materials section 4.4).

Using the multiple nucleation paths presented in Fig. 2, A to C, we performed a statistical analysis for the relative population between the disordered and crystalline states, which is indicative of the relative stability of the two states. For example, from the 20 nucleation paths in Fig. 2A and fig. S22, we calculated temporal fractions of the crystalline state (fig. S31) and investigated their relation to the sizes of nanocrystals (magenta dots in Fig. 3A). The other two cases (Fig. 2, B and C), which had current densities 10^{-3} times that of the first case, were also analyzed with the identical method (orange triangles and green squares in Fig. 3A). The results from different conditions follow a similar trend, and the difference is relatively small, as seen in the scattering of the data points. In all three cases, a nascent small nanocluster has a high probability of retaining the disordered state (top part in Fig. 3B). Then, the relative population of the crystalline state increases while the nanocluster grows from ~1.0 to ~3.0 nm^2 (middle part in Fig. 3B; equivalent circular diameters: ~1.1 to ~2.0 nm). Eventually, the enlarged nanocluster maintains the crystalline state (bottom part in Fig. 3B). This implies that the observed process is an evolution of atomic structures through stochastic and dynamic fluctuations between two states with size-dependent relative stability. Figure 3A also indicates that the observed structural fluctuations are mainly directed by the formation and early-stage growth of nanoclusters and are not an artifact induced by the electron beam. The electron beam can transfer a certain amount of energy to Au atoms and clusters elastically and/or inelastically, which may generate the crystalline-to-disordered transformations of clusters. To confirm that this was not the case in our study, Au nanoclusters smaller than 2 nm were prepared by a typical colloidal synthesis and observed under the same imaging condition for a prolonged time (supplementary materials section 4.1). Small-sized presynthesized clusters occasionally show disordered structures (fig. S32), consistent with previous studies (*22*–*28*). However, Fig. 3A indicates that the presynthesized clusters (gray circles) were mostly in the crystalline state throughout imaging for cluster sizes larger than ~1 nm, which is clearly different from the other cases (solid symbols) observed during the nucleation process. Additionally, extensive discussion regarding the electron beam effects is provided in the supplementary materials section 4 (figs. S15, S16, and S25 to S34).

The free-energy change for the transition from disordered to crystalline states is usually negative and large enough to make the transition spontaneous. However, statistical observations of the reversible and dynamic transformations in Fig. 3, A and B, imply that the energy difference and the barrier between the two states are small when the cluster size is small in the early stage of nucleation (top part in Fig. 3B). As nanoclusters grow, the energy difference gradually increases, and the nanoclusters present the crystalline state more frequently. From a certain nanocluster size (~2.0 nm in our study), nanoclusters are trapped in the crystalline state because of the increased energy difference (bottom part in Fig. 3B). Many theoretical and experimental studies (*22*–*28*) have reported that small (less than ~2 nm) nanoparticles can have disordered atomic structures even in ambient conditions. Melting-point depression (*29*–*31*) also means that crystalline-to-disordered transitions require substantially reduced energy in small nanoparticles compared with bulk materials. These previous results consistently support the low energy barrier of the crystalline-to-disordered transformation of small nanoclusters. Fluctuations between two states over a free-energy barrier are a key thermodynamic concept of classical nucleation theory. Although this concept is not excluded in the framework of nonclassical two-step nucleation (fig. S35) (*2*), only a few studies (*7*, *17*, *32*) have investigated it. The above thermodynamic description and our high-speed observations reintroduce and verify the idea that reversible and dynamic transformations can occur in nonclassical nucleation pathways.

The low energy barrier of the crystalline-to-disordered transformation can be overcome by various sources. Monomer attachment is an exergonic reaction and can deposit a relatively large amount of energy to nascent nanoclusters as thermal fluctuations and the electron beam can. We performed first-principles calculations of the energy released from binding reactions between an Au atom and hemispheroidal Au nanocrystals (Fig. 3C, figs. S36 and S37, tables S1 to S3, and supplementary materials section 5), and we evaluated whether the calculated energies are comparable to collapsing crystalline structures by using the thermal energies required to increase the temperatures of the nanocrystals to the depressed melting points (*29*–*31*). The crossover of the two energies occurs at the nanocrystal size containing 49 constituent atoms (nanocrystal area: ~1.4 nm^2) in Fig. 3C. This implies that recurrent binding of Au atoms can provide sufficient energy to small clusters to drive toward the disordered state. Experimental results that partly support this hypothesis are presented in Fig. 3, D to F; fig. S38; and movie S6, which show that the binding of a small atomic cluster (composed of ~10 atoms, ~0.7 nm^2) to a large nanocrystal induces noticeable structural transformations to the disordered state. Just after the atomic-cluster binding, the crystalline area is gradually reduced and then recovered (~9.0 nm^2 → ~3.0 nm^2 → ~10.0 nm^2). We also found that coalescence of small nanocrystals drives either or both of the nanocrystals to visit the disordered state (figs. S39 to S43 and movie S7). Therefore, reversible transformations commonly occur throughout various stages in our model system. Our system does not universally reproduce the entire scope of crystal nucleation starting from scattered monomers. However, our work reveals near-atomic scale dynamics from concentrated adatoms to the formation of a stable crystal, thereby addressing a critical step that determines the nucleation pathway in many different types of crystallization processes (supplementary materials section 6 and fig. S44).

In this study, we found that crystal nucleation of gold clusters on graphene progresses through reversible structural fluctuations between disordered and crystalline states. High-speed in situ observations of a real atomic system confirm nonclassical and dynamic natures of the nucleation process during atomic crystallization. Our findings clarify fundamental mechanisms underlying the nucleation stage of material growth, including thin-film deposition, interface-induced precipitation, and nanoparticle formation.

REFERENCES AND NOTES

1. J. J. De Yoreo *et al.*, *Science* **349**, aaa6760 (2015).
2. P. G. Vekilov, *Cryst. Growth Des.* **10**, 5007–5019 (2010).
3. D. Erdemir, A. Y. Lee, A. S. Myerson, *Acc. Chem. Res.* **42**, 621–629 (2009).
4. J. Chen *et al.*, *Science* **362**, 1135–1139 (2018).
5. M. Sleutel, J. Lutsko, A. E. S. Van Driessche, M. A. Durán-Olivencia, D. Maes, *Nat. Commun.* **5**, 5598 (2014).
6. Z. Ou, Z. Wang, B. Luo, E. Luijten, Q. Chen, *Nat. Mater.* **19**, 450–455 (2020).
7. T. H. Zhang, X. Y. Liu, *Angew. Chem. Int. Ed.* **48**, 1308–1312 (2009).
8. P. R. ten Wolde, D. Frenkel, *Science* **277**, 1975–1978 (1997).
9. L. Houben, H. Weissman, S. G. Wolf, B. Rybtchinski, *Nature* **579**, 540–543 (2020).
10. M. H. Nielsen, S. Aloni, J. J. De Yoreo, *Science* **345**, 1158–1162 (2014).
11. A. S. Barnard, N. P. Young, A. I. Kirkland, M. A. van Huis, H. Xu, *ACS Nano* **3**, 1431–1436 (2009).
12. N. D. Loh *et al.*, *Nat. Chem.* **9**, 77–82 (2017).
13. J. Yang *et al.*, *J. Am. Chem. Soc.* **141**, 763–768 (2019).
14. M. H. Hu, S. Noda, H. Komiyama, *J. Appl. Phys.* **93**, 9336–9344 (2003).
15. L. Fei *et al.*, *ACS Nano* **13**, 681–688 (2019).
16. J. Zhou *et al.*, *Nature* **570**, 500–503 (2019).
17. K. Cao *et al.*, *Nat. Chem.* **12**, 921–928 (2020).
18. B. W. Reed *et al.*, *Struct. Dyn.* **6**, 054303 (2019).
19. W. C. Lee *et al.*, *Nat. Nanotechnol.* **10**, 423–428 (2015).
20. J. Kim *et al.*, *J. Phys. Chem. Lett.* **8**, 1302–1309 (2017).
21. M. T. Beck *et al.*, *J. Solid State Chem.* **246**, 65–74 (2017).
22. Z. W. Wang, R. E. Palmer, *Nano Lett.* **12**, 5510–5514 (2012).
23. T. J. Pennycook, J. R. McBride, S. J. Rosenthal, S. J. Pennycook, S. T. Pantelides, *Nano Lett.* **12**, 3038–3042 (2012).
24. P. M. Ajayan, L. D. Marks, *Phys. Rev. Lett.* **63**, 279–282 (1989).
25. V. Petkov *et al.*, *J. Phys. Chem. C* **112**, 8907–8911 (2008).
26. L. Li *et al.*, *J. Am. Chem. Soc.* **135**, 13062–13072 (2013).
27. Y. Sun, L. Zhuang, J. Lu, X. Hong, P. Liu, *J. Am. Chem. Soc.* **129**, 15465–15467 (2007).
28. I. L. Garzón *et al.*, *Phys. Rev. Lett.* **81**, 1600–1603 (1998).
29. P. Buffat, J. P. Borel, *Phys. Rev. A* **13**, 2287–2298 (1976).
30. K. Dick, T. Dhanasekaran, Z. Zhang, D. Meisel, *J. Am. Chem. Soc.* **124**, 2312–2317 (2002).
31. W. H. Qi, M. P. Wang, *Mater. Chem. Phys.* **88**, 280–284 (2004).
32. P. W. Sutter, E. A. Sutter, *Nat. Mater.* **6**, 363–366 (2007).

ACKNOWLEDGMENTS

The authors thank A. Minor, T. Hyeon, S. Takeuchi, and S. Chung for helpful discussions. **Funding:** This work was mainly supported by the National Research Foundation of Korea (NRF) funded by the Ministry of Science and ICT (MSIT) and the Ministry of Education (MOE) under contract nos. 2016R1C1B1014940 and 2019R1F1A1059099. Work

at the Molecular Foundry was supported by the Office of Science, Office of Basic Energy Sciences, of the U.S. Department of Energy under contract no. DE-AC02-05CH11231. The authors also acknowledge multiple financial supports from the Institutes for Basic Science (IBS-R006-D1); the NRF funded by the Korean government (MSIT and MOE) under contract nos. 2017R1C1B2010434, 2017R1A5 A1015365, 2019M3E6A1064877, 2018R1A5A1025208, 2017R1A5A1014862, 2015M3C1B2052811, 2018R1D1A1B07050575, and 2020R1F1A1065856; the Samsung Science and Technology Foundation for developing the data analysis and TEM simulation methods (M.-H.K. and J.P., no. SSTF-BA1802-08); the U.S. Department of Energy, Office of Science, Office of Basic Energy Sciences, Materials Sciences and Engineering Division (DE-AC02-05-CH11231) within the Nanomachines Programs (KC1203), which supported preliminary TEM measurements; and the U.S. National Science Foundation (DMR-1807233), which provided for the development of graphene TEM supports. **Author contributions:** W.C.L., J.P., and P.E. conceived the design of the study. S.J., S.Ka., J.C., K.C.B., B.W.R., R.S.B., P.E., and W.C.L. performed in situ TEM imaging. S.J. and T.H. analyzed the data. S.-Y.H. and W.Y.K. performed first-principles calculations. J.S.K., J.H., S.Ki., J.L., K.L., M.-H.K., S.H., K.K., and A.Z. contributed to sample preparation or data analysis. S.J., T.H., S.-Y.H., J.C., K.C.B., B.W.R., S.H., P.E., J.P., and W.C.L. wrote the manuscript. All authors discussed the results and commented on the manuscript. **Competing interests:** The authors declare no competing interests. **Data and materials availability:** All data are available in the main text or the supplementary materials.

SUPPLEMENTARY MATERIALS

science.sciencemag.org/content/371/6528/498/suppl/DC1
Materials and Methods
Supplementary Text
Figs. S1 to S44
Tables S1 to S3
References (*33*–*65*)
Movies S1 to S7

15 October 2019; resubmitted 19 October 2020
Accepted 28 December 2020
10.1126/science.aaz7555

ANIMAL CULTURE

Cultural transmission of vocal dialect in the naked mole-rat

Alison J. Barker[1]*, Grigorii Veviurko[1]†, Nigel C. Bennett[2], Daniel W. Hart[2], Lina Mograby[1], Gary R. Lewin[1]*

Naked mole-rats (*Heterocephalus glaber*) form some of the most cooperative groups in the animal kingdom, living in multigenerational colonies under the control of a single breeding queen. Yet how they maintain this highly organized social structure is unknown. Here we show that the most common naked mole-rat vocalization, the soft chirp, is used to transmit information about group membership, creating distinctive colony dialects. Audio playback experiments demonstrate that individuals make preferential vocal responses to home colony dialects. Pups fostered in foreign colonies in early postnatal life learn the vocal dialect of their adoptive colonies, which suggests vertical transmission and flexibility of vocal signatures. Dialect integrity is partly controlled by the queen: Dialect cohesiveness decreases with queen loss and remerges only with the ascendance of a new queen.

The naked mole-rat (*Heterocephalus glaber*) was the first eusocial mammal to be identified (*1*) and has received much attention for an array of extreme physiological traits (*2*–*4*). Yet often overlooked are the sounds these animals make: constant peeping, chirruping, and grunting (*5*, *6*) (audio S1 and S2). Complex patterns of acoustic communication exist throughout the animal kingdom (*7*), and decades of study—notably in songbirds (*8*), bats (*9*), cetaceans (*10*), and primates (*11*)—have generated debate about the etiology of human language, with compelling evidence for anatomical (*12*), genetic (*13*), and cultural (*14*) drivers. The highly cooperative nature of naked mole-rat societies led us to investigate whether their vocalizations support social complexity.

The vocal repertoire of the naked mole-rat consists of at least 17 distinct vocalizations (*6*). The most common vocalization, the soft chip, serves as a greeting call that has been previously shown to occur in a stereotyped call-and-response (i.e., antiphonal) manner (*15*).

[1]Department of Neuroscience, Max Delbrück Center for Molecular Medicine, Berlin, Germany. [2]Mammal Research Institute, Department of Zoology and Entomology, University of Pretoria, Pretoria, Republic of South Africa.
***Corresponding author. Email: glewin@mdc-berlin.de (G.R.L.); alison.barker@mdc-berlin.de (A.J.B.)** †Present address: Department of Electrical Engineering, Mathematics and Computer Science, Delft University of Technology, Delft, Netherlands.

We recorded 36,190 soft chirps from 166 animals (seven colonies), housed in Berlin, Germany, or Pretoria, South Africa, over a period of 2 years. We developed an algorithm to automatically segment, trace, and extract acoustic features of individual soft chirps (Fig. 1A). In developing our analysis pipeline, we included established parameters for vocalization analysis (*16*) and, whenever possible, spectrogram-extracted features, which minimized variable background noise from recordings made across different locations and days. We used a type of supervised machine learning, the random forest classifier (*17*), to analyze eight soft-chirp features: three from the sound wave (pitch, Wiener entropy, and zero-crossings rate) and five from the soft-chirp spectrogram (asymmetry, peak frequency, height, duration, and slope) (Fig. 1A and fig. S1). By training the classifier with soft chirps from individual mole-rats, we found that it could reliably predict the identity of individuals within a colony (Fig. 1B and fig. S2).

Within naked mole-rat colonies, reproductive suppression of nearly all members is necessary to sustain the colony with limited food resources and leads to strong xenophobia (*18*). As such, multiple mechanisms for maintaining the social integrity of the colony and for detecting intruders might be necessary. We next tested for colony-specific signatures (*15*) by using soft chirps recorded from three colonies in Berlin (colonies B, M, and T) and a fourth colony, which has always been located in South Africa (colony D). Again, using a random forest classifier, we found that soft-chirp features were highly predictive of colony identity (Fig. 2, A and B, and figs. S3 to S5), with asymmetry and peak frequency found to be the best spectrogram-derived features for colony separation (Fig. 2, C and D) (*15*). Although soft-chirp features did not strongly predict rank, age, or sex (fig. S6), we observed a positive correlation with body size and soft-chirp pitch (supplementary text and fig. S7).

We next evaluated whether naked mole-rats recognize information communicated via soft chirps. To test this, we employed a place preference assay in which individual animals were given access to two interconnected chambers (Fig. 3A, top, and movie S1), each equipped for simultaneous audio playback and recording. Animals preferred to spend most of the allotted time in the chamber with sound presentation, regardless of whether soft chirps from their home colony or a foreign colony were played (Fig. 3A). In response to the audio playback stimulus, animals frequently vocalized with their own soft chirp, consistent with the antiphonal behavior previously described (Fig. 3B) (*15*, *19*). We observed very high response rates when animals were presented with home colony audio playbacks, much higher than and significantly different from responses to foreign colony playbacks (Fig. 3C).

Do naked mole-rats recognize individual voices from home colonies rather than colony dialects? We tested this by designing artificial stimuli, using two features: asymmetry and peak frequency (*15*). Artificial stimuli were fabricated such that our colony classifier would categorize them as belonging to "mock colony members" but they would not overlap with the vocalizations of any known individuals in the colony (fig. S8). Notably, response rates were again higher for the mock home stimulus, which suggests that naked mole-rats can distinguish colony-specific features in vocalizations (Fig. 3, D and E, and fig. S8). To test whether peak frequency or asymmetry alone were sufficient for behavioral preference, we used a pure tone of 4.5 kHz (mean colony peak

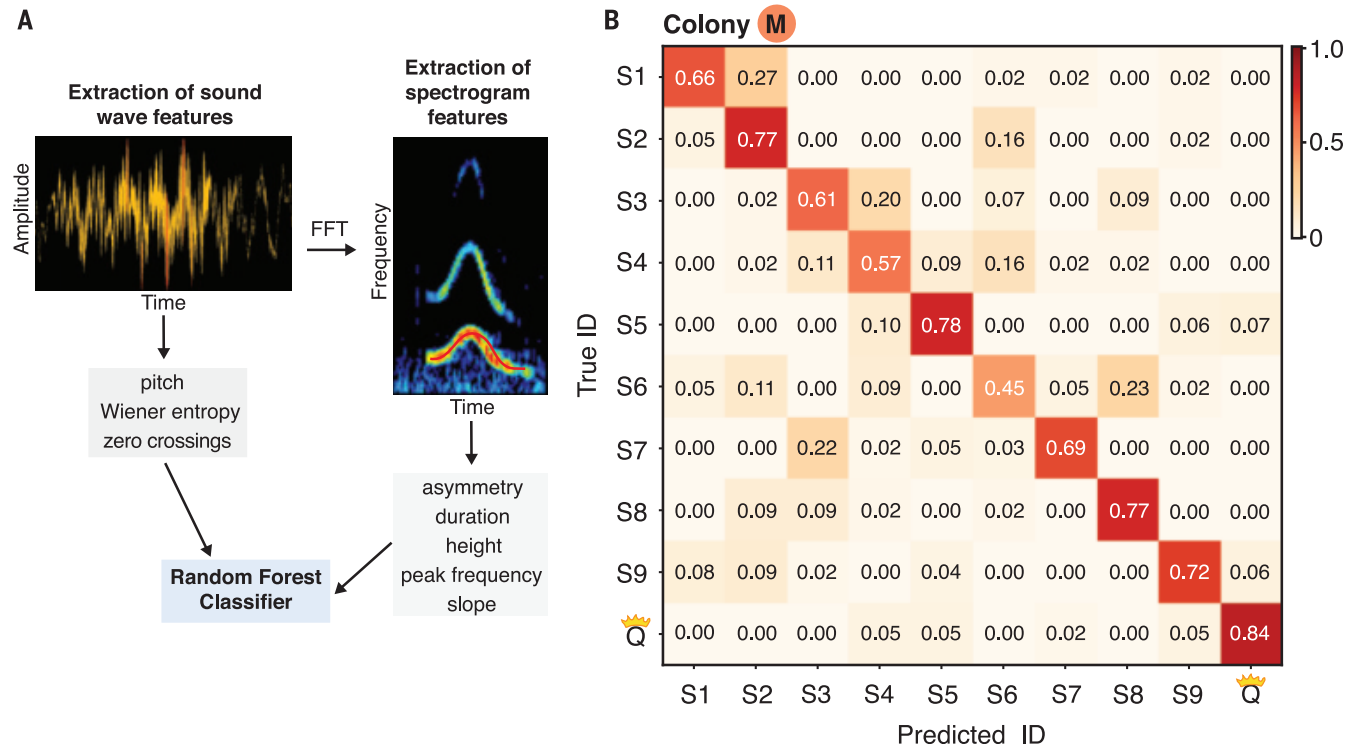

Fig. 1. Naked mole-rat soft chirps encode individual identity. (**A**) Soft-chirp analysis and classifier training workflow. FFT, fast Fourier transform. (**B**) Individuals can be identified with high accuracy using machine learning tools trained on vocal features (A). S1 to S9 represent subordinate individuals; Q represents the queen.

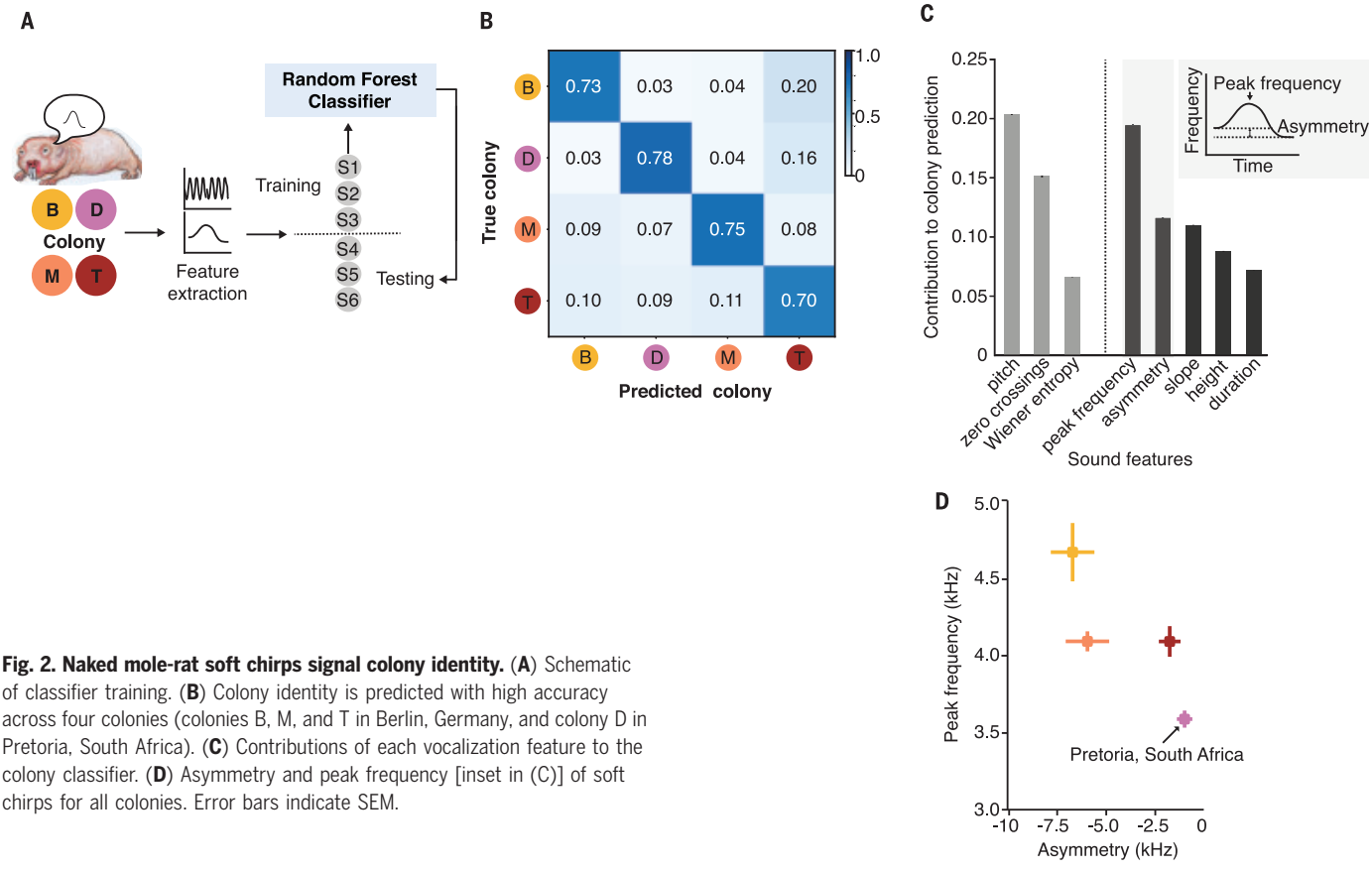

Fig. 2. Naked mole-rat soft chirps signal colony identity. (**A**) Schematic of classifier training. (**B**) Colony identity is predicted with high accuracy across four colonies (colonies B, M, and T in Berlin, Germany, and colony D in Pretoria, South Africa). (**C**) Contributions of each vocalization feature to the colony classifier. (**D**) Asymmetry and peak frequency [inset in (C)] of soft chirps for all colonies. Error bars indicate SEM.

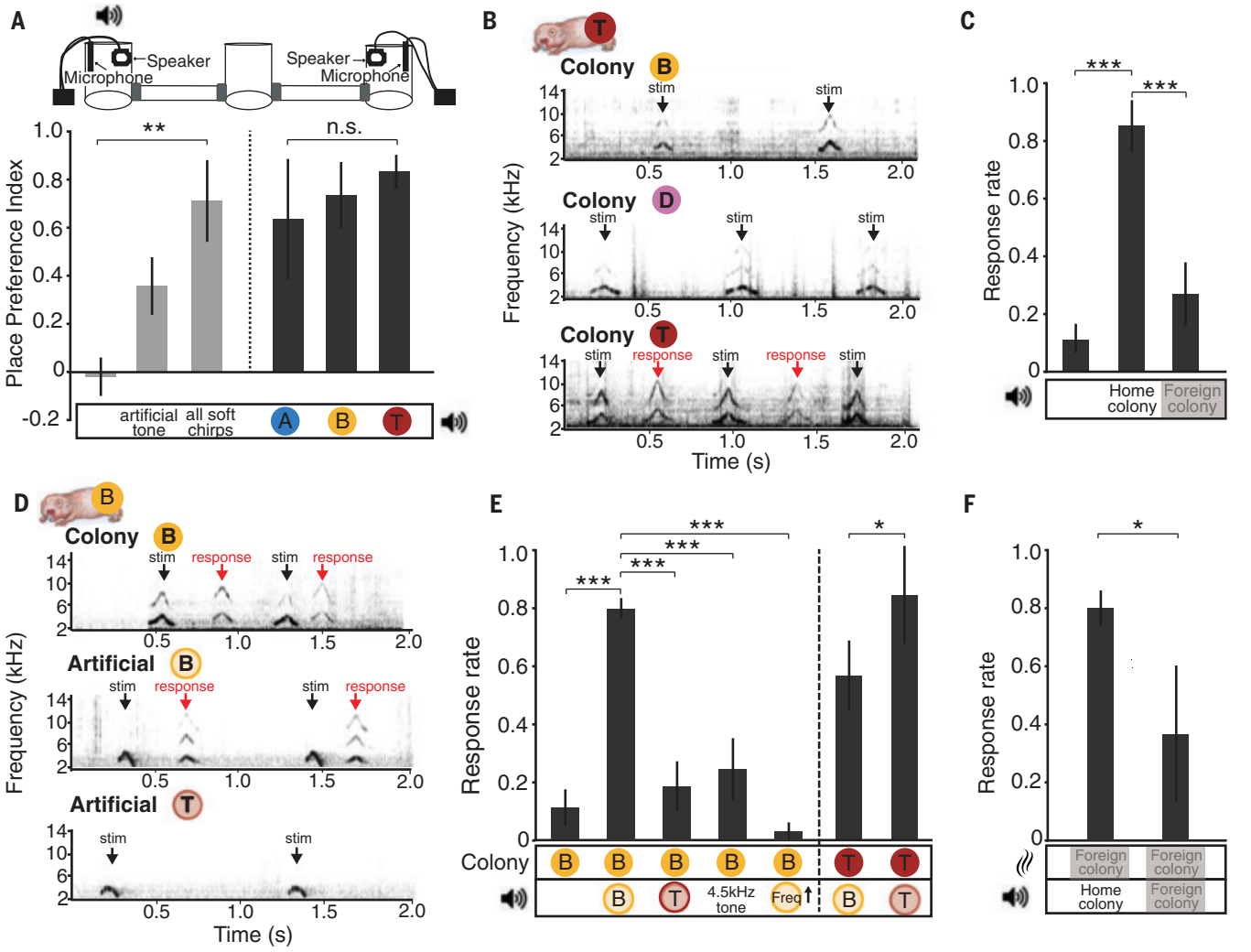

Fig. 3. Vocal response rates are modulated by colony identity. (**A**) (Top) Place preference assay setup. Individual animals were given access to two interconnected chambers, each equipped for simultaneous audio playback and recording. (Left) In a place preference assay, naked mole-rats spend more time in the chamber with sound presentation than in the chamber with silence [n = 4 animals; $N \geq 36$ trials per animal, one-way analysis of variance (ANOVA), $^{**}P < 0.005$]. (Right) No place preference to colony-specific audio playbacks was observed. n.s., not significant. Error bars indicate SEM. (**B**) Soft-chirp response rates were enhanced to home colony audio playbacks. Example responses from colony T animals are indicated. stim, stimulus. (**C**) Response rate to home colony audio playback is greater than response rate to no playback or foreign colony playback (n = 9 animals; $N \geq 36$ trials, one-way ANOVA, $^{***}P < 0.0005$). Error bars indicate SEM. (**D**) Example responses to home colony and artificial stimuli. The indicated responses are from colony B animals. (**E**) For artificially generated stimuli, soft-chirp responses to home colony–classified audio playbacks are significantly increased compared with responses to foreign colony–classified audio playbacks or when frequency and asymmetry features alone are tested (n = 4 animals in colony B and 5 animals in colony T, one-way ANOVA or unpaired t test, $^{*}P < 0.05$, $^{***}P < 0.0005$). Error bars indicate SEM. (**F**) Colony-specific response rates were present when conflicting olfactory cues (bedding from a foreign colony) were placed in the test chamber (n = 6 animals, $N \geq 36$ trials per animal, $^{*}P < 0.05$). Error bars indicate SEM. For all experiments, a minimum of N = 36 behavioral trials were performed for each animal.

frequency) and a frequency-doubled stimulus (9.0 kHz with mean colony asymmetry). We observed responses to the pure tone alone but virtually none to the frequency-doubled stimulus (Fig. 3E and fig. S8). The preferential response to home colony dialect was still found in the presence of a conflicting olfactory cue in the test chamber (Fig. 3F).

If naked mole-rats use distinct colony dialects to differentiate themselves from neighboring colonies or as a mechanism for ensuring conformity within the colony, such dialects must be maintained across generations. We cross-fostered three individuals between colonies—a nontrivial task because queens breed rarely and breeding activity cannot be synchronized across colonies. An abandoned pup (pup Mi) was cross-fostered from colony T to colony M (Fig. 4, A and D), and we simultaneously tracked two surviving foster siblings born in colony M (pups Ob and Ny; Fig. 4, B and C). In a second experiment, two orphaned pups (pups Da and Jo, colony S) were fostered into two different colonies (colony M and colony T, respectively) (Fig. 4, E to G). We observed that adult vocalizations fully develop by ~3 months of age (supplementary text and figs. S9 and S10), so we examined pup dialects at time points later than 6 months after fostering. We tested foster pup vocalizations on our colony classifier, which classified the pups as belonging to one of five test colonies (including birth and foster colonies). In all three successful foster experiments, the dialect of the new colony was adopted with correct prediction rates between 59 and 95% (Fig. 4H).

Finally, we investigated whether the queen's presence might influence the vocal signature

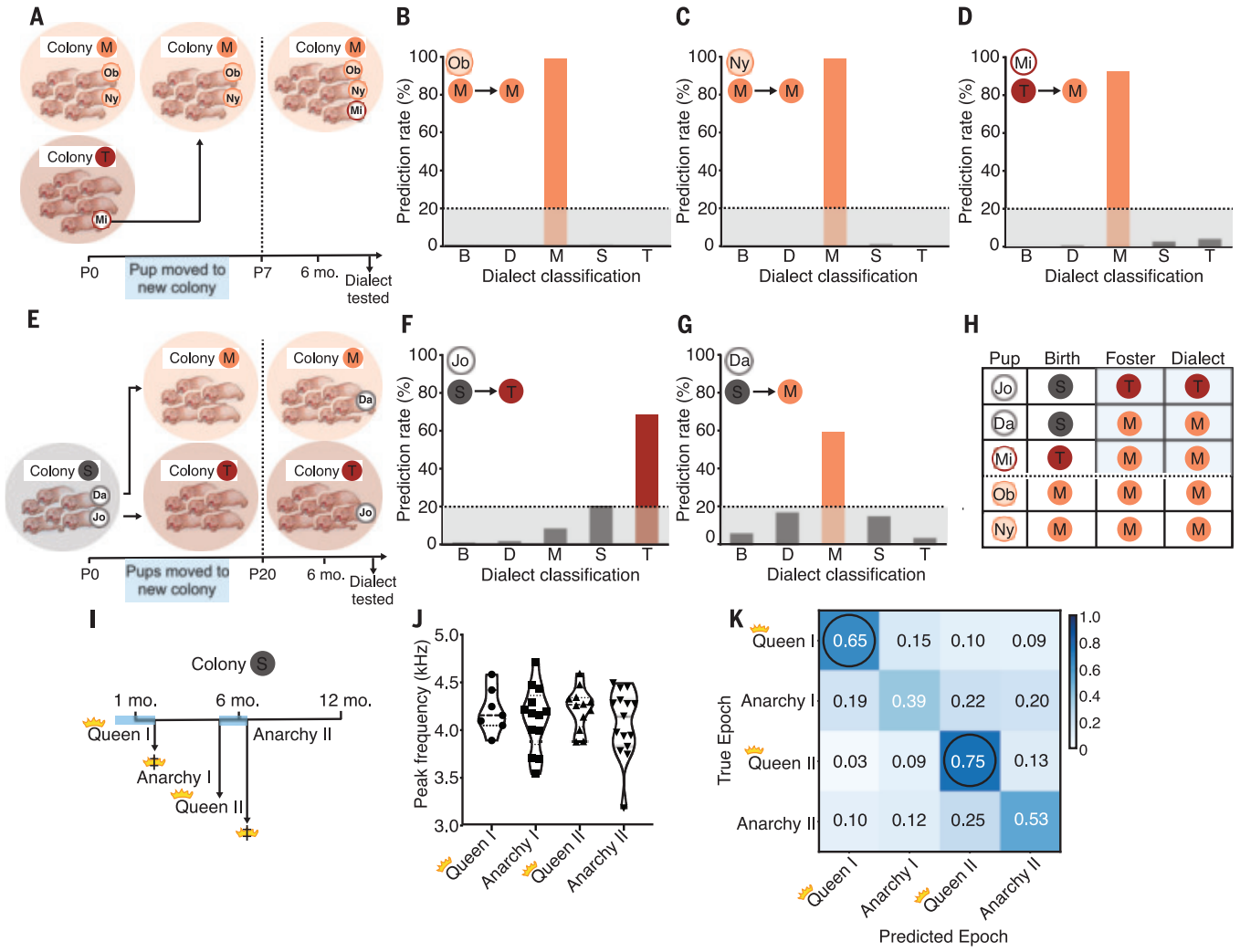

Fig. 4. Cultural transmission of colony dialects. (**A**) Schematic of first cross-fostering experiment. P0, postnatal day 0; P7, postnatal day 7. (**B** to **D**) Individual colony dialect predictions for each pup (Ny and Ob, nonfostered control pups; Mi, fostered pup). Prediction accuracies: pup Mi = 95.5%, pup Ob = 99.2%, pup Ny = 99.0%. (**E**) Schematic of second cross-fostering experiment. (**F** and **G**) Individual colony dialect predictions for foster pups Da and Jo were 59.1% and 68.4% accurate, respectively. (**H**) All fostered pups adopt the dialect of their adoptive colonies. (**I**) Timeline of social upheaval in colony S. (**J**) During anarchy periods, variability in soft-chirp frequency increases. (**K**) Colony classification accuracy decreases during anarchy periods relative to epochs with a stable queen (black circles).

of the colony (supplementary text). During the course of this study, colony S consecutively lost two queens (Fig. 4I and fig. S11), which enabled us to record soft chirps during queen epochs and subsequent periods of anarchy. Individual variability of several features, including peak frequency, was higher during periods of anarchy (Fig. 4J and fig. S12), and classification accuracy of the colony dialect decreased during periods of anarchy (Fig. 4K and fig. S12), which suggests that the presence of the queen enhances dialect cohesiveness.

Acoustic communication of social information has been observed in multiple mammalian species—bats (*9*), primates (*11*), cetaceans (*10*), pachyderms (*20*), and carnivores (*21*)—and now we expand this group to include a member of the order Rodentia. More work is needed to resolve whether naked mole-rats are capable of true production learning, as exemplified in songbirds, or whether, like many nonhuman primates, they are exceptionally good usage learners (*22*). With a simple vocal greeting, humans convey individual identity (distinctive voice) and cultural identity (dialect usage); here we show that naked mole-rats also signal social membership with dialect usage. Dialect features can be transmitted across generations, a surprising feat for a rodent species, thus supporting an accumulating body of evidence that social complexity evolved concurrently with vocal complexity.

REFERENCES AND NOTES

1. J. U. Jarvis, *Science* **212**, 571–573 (1981).
2. T. J. Park *et al.*, *Science* **356**, 307–311 (2017).
3. J. G. Ruby, M. Smith, R. Buffenstein, *eLife* **7**, e31157 (2018).
4. R. Buffenstein, S. Yahav, *J. Therm. Biol.* **16**, 227–232 (1991).
5. W. C. O. Hill, A. Porter, R. T. Bloom, J. Seago, M. D. Southwick, *Proc. Zool. Soc. London* **128**, 455–514 (1955).
6. J. W. Pepper, S. H. Braude, E. A. Lacey, P. W. Sherman, in *The Biology of the Naked Mole-Rat*, P. W. Sherman, J. U. M. Jarvis, R. D. Alexander, Eds. (Princeton Univ. Press, 1991), pp. 243–274.
7. M. S. Brainard, W. T. Fitch, *Curr. Opin. Neurobiol.* **28**, v–viii (2014).
8. A. J. Doupe, P. K. Kuhl, *Annu. Rev. Neurosci.* **22**, 567–631 (1999).
9. M. Knörnschild, *Curr. Opin. Neurobiol.* **28**, 80–85 (2014).
10. V. M. Janik, *Curr. Opin. Neurobiol.* **28**, 60–65 (2014).
11. R. M. Seyfarth, D. L. Cheney, *Curr. Opin. Neurobiol.* **28**, 5–9 (2014).
12. P. Lieberman, *Curr. Anthropol.* **48**, 39–66 (2007).
13. G. Konopka *et al.*, *Nature* **462**, 213–217 (2009).
14. R. Dunbar, *Evol. Anthropol.* **6**, 178–190 (1998).
15. S. Yosida, K. I. Kobayasi, M. Ikebuchi, R. Ozaki, K. Okanoya, *Ethology* **113**, 703–710 (2007).
16. D. Lipkind, O. Tchernichovski, *Proc. Natl. Acad. Sci. U.S.A.* **108** (suppl. 3), 15572–15579 (2011).

17. Materials and methods are available as supplementary materials.
18. M. J. O'Riain, J. U. M. Jarvis, *Anim. Behav.* **53**, 487–498 (1997).
19. S. Yosida, K. Okanoya, *Ethology* **115**, 823–831 (2009).
20. A. S. Stoeger, P. Manger, *Curr. Opin. Neurobiol.* **28**, 101–107 (2014).
21. K. E. Holekamp, S. T. Sakai, B. L. Lundrigan, *Philos. Trans. R. Soc. B* **362**, 523–538 (2007).
22. V. M. Janik, P. J. B. Slater, *Anim. Behav.* **60**, 1–11 (2000).

ACKNOWLEDGMENTS

We thank J. Reznick, U. Koch, A. Rossi, and O. Eigenbrod for helpful comments on the manuscript; G. Pflanz, N. Schrim, and A. Mühlenberg for naked mole-rat husbandry; R. Hodge for illustrations; and C. O. Lewin for supplementary movies. **Funding:** This work was supported by a grant from the European Research Council (Advanced Grant 294678) to G.R.L. and a South African Research Chair for Mammalian Behavioral Research to N.C.B. (Grant GUN64756) We thank O. Daumke for additional salary funding. **Author contributions:** This project was conceived by A.J.B. and G.R.L., who together wrote the manuscript with input from all authors. Behavioral experiments were performed by A.J.B., N.C.B., D.W.H., and L.M. Machine learning and data analysis pipelines were developed by G.V., with input from A.J.B. **Competing interests:** The authors declare no competing interests. **Data and materials availability:** All data are available in the manuscript or the supplementary materials.

SUPPLEMENTARY MATERIALS

science.sciencemag.org/content/371/6528/503/suppl/DC1
Materials and Methods
Supplementary Text
Figs. S1 to S12
References (*23*–*29*)
Movies S1 and S2
Audios S1 and S2

7 May 2020; accepted 18 November 2020
10.1126/science.abc6588

ORGANIC CHEMISTRY

Merging shuttle reactions and paired electrolysis for reversible vicinal dihalogenations

Xichang Dong[1]*, Johannes L. Roeckl[1,2]*, Siegfried R. Waldvogel[2]†, Bill Morandi[1]†

Vicinal dibromides and dichlorides are important commodity chemicals and indispensable synthetic intermediates in modern chemistry that are traditionally synthesized using hazardous elemental chlorine and bromine. Meanwhile, the environmental persistence of halogenated pollutants necessitates improved approaches to accelerate their remediation. Here, we introduce an electrochemically assisted shuttle (*e*-shuttle) paradigm for the facile and scalable interconversion of alkenes and vicinal dihalides, a class of reactions that can be used both to synthesize useful dihalogenated molecules from simple alkenes and to recycle waste material through *retro*-dihalogenation. The reaction is demonstrated using 1,2-dibromoethane, as well as 1,1,1,2-tetrachloroethane or 1,2-dichloroethane, to dibrominate or dichlorinate, respectively, a wide range of alkenes in a simple setup with inexpensive graphite electrodes. Conversely, the hexachlorinated persistent pollutant lindane could be fully dechlorinated to benzene in soil samples using simple alkene acceptors.

Vicinal dibromides and dichlorides have found widespread applications as flame retardants, pest control agents, polymers, and pharmaceuticals (*1*, *2*). They also serve as versatile synthetic intermediates in organic chemistry because of the inherent reactivity of carbon–halogen bonds (*3*, *4*). Despite these attractive features, the preparation of dihalogenated molecules still mainly relies on the use of highly reactive and corrosive halogenating reagents such as Cl_2 and Br_2, which are hazardous compounds to transport, store, and handle (*4*–*7*). Two general strategies have been commonly used to avoid the direct use of Cl_2 and Br_2. The first strategy makes use of carrier reagents such as Et_4NCl_3 or pyridinium tribromide as bench-stable surrogates. Despite their increasing stability, they still require the use of X_2 reagents for their syntheses and tend to be unstable and corrosive themselves because they are designed to readily release the corresponding X_2 reagents (*5*–*7*). The second strategy relies on the in situ generation of the active halogenating species from the reaction between halides and strong oxidants, a feature that can limit the functional group (e.g., alcohols) compatibility of these reactions (*5*–*7*). The use of strong oxidants also creates thermodynamic challenges for the development of the reverse reactions, *retro*-dihalogenations, that could be applied to remediation of persistent halogenated pollutants.

Transfer hydrofunctionalization proceeding through a shuttle catalysis (*8*) paradigm has emerged as a powerful and versatile strategy to reversibly functionalize and defunctionalize organic molecules without using or releasing hazardous reagents (*8*–*15*) such as HCN (*9*). However, catalytic and reversible transfer reactions have so far been limited to alkene monofunctionalization (*16*) reactions, which usually involve the transfer of an HX molecule (*8*, *15*). By contrast, the synthetically appealing simultaneous transfer of two functional groups in a catalytic reversible transfer difunctionalization process has remained largely elusive despite the vast synthetic potential of these reactions in organic synthesis. In particular, reactions involving the formal transfer of extremely reactive and corrosive molecules such as Cl_2 (*17*, *18*) and Br_2 from easier-to-handle, stable bulk chemicals such as inexpensive 1,2-dichloroethane and 1,2-dibromoethane would be highly desirable because of the widespread synthetic applications of dihalogenated molecules in flame retardants, pesticides, materials, and natural products (*1*, *2*, *19*) (Fig. 1A). The inherent reversibility of such a shuttle reaction would further unlock the facile *retro*-dihalogenations of end-of-life halogenated products for remediation (Fig. 1A).

The challenge in developing transfer difunctionalizations such as transfer dihalogenations originates from the catalytic approach generally used in shuttle catalysis. Transfer hydrofunctionalizations such as hydrocyanation (*9*) rely on the intermediacy of an alkyl-metal complex that readily undergoes fast and reversible β-hydride elimination, thus triggering the transfer of a hydrogen atom alongside the desired functional group (*15*) (Fig. 1B). Unfortunately, the ease of β-hydride elimination makes the selective, competitive elimination of other synthetically useful groups challenging (*20*). Furthermore, while β-hydride elimination is a fast and reversible process, the subsequent migratory reinsertion of an alkene into a metal-halogen bond is often kinetically and thermodynamically disfavored because of the high stability of these types of bonds (*6*). Thus, a mechanistically distinct approach to favor halogen transfer over hydrogen transfer is crucial to unlock this important class of transfer difunctionalization reactions.

Electrosynthesis has recently experienced a renaissance in organic chemistry because it takes advantage of readily available electrical current as a sustainable and inherently safe redox reagent (*21*–*24*). Notable advances have been made in halogenation reactions (*25*, *26*), as illustrated by an elegant example of dichlorination from Lin *et al.* (*25*). However, this reaction, as well as many other electrochemical reactions, has to be coupled to another sacrificial half-reaction, e.g., proton reduction to form hydrogen, at the counterelectrode (*23*, *24*). In addition to this limitation, current protocols can often be further limited by the use of complex reaction setups including expensive metal electrodes (*23*, *24*).

We envisaged that consecutive paired electrolysis (*27*) involving a domino reduction-oxidation cascade (*28*, *29*), a class of ideal yet comparatively rare electrochemical reactions in which both electrodes are used in the desired transformation, could provide a path to reversible, electrochemically mediated shuttle

[1]Laboratory of Organic Chemistry, Department of Chemistry and Applied Biosciences, ETH Zürich, Zürich, Switzerland. [2]Department of Chemistry, Johannes Gutenberg University, Mainz, Germany.
*These authors contributed equally to this work.
†Corresponding author. Email: bill.morandi@org.chem.ethz.ch (B.M.); waldvogel@uni-mainz.de (S.R.W.)

reactions (*e*-shuttle). We surmised that the reversible cleavage of two strong carbon-halogen bonds through a controlled electron-transfer process initiated by a simultaneous, simple reduction and oxidation of key intermediates at the cathode and anode, respectively, would unlock this transformation (Fig. 1, C and D). In our hypothesis, the single-electron reduction of the dihalide at the cathode releases the X^- anion and generates the carbon radical **1**, which is almost instantly reduced again to generate a carbanion (*30*). As a central design, the subsequent selective loss of the second X^- instead of a hydride breaks the C–X bond, releasing the alkene compound. Considering

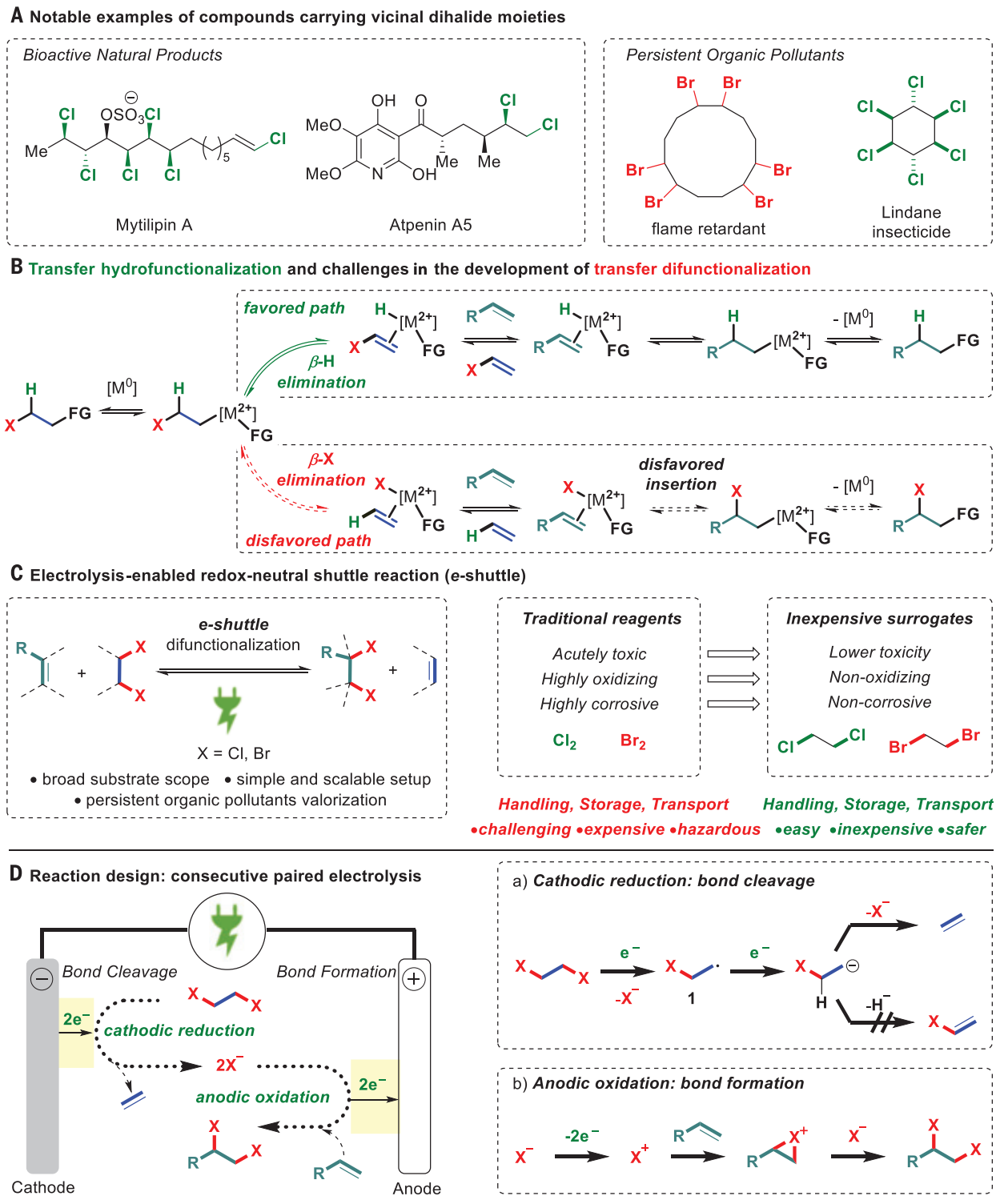

Fig. 1. Reaction design and challenges of transfer difunctionalization. (**A**) Notable examples of compounds carrying vicinal dihalide moieties. (**B**) Transfer hydrofunctionalization and challenges in the development of transfer difunctionalization. (**C**) Electrolysis-enabled redox-neutral shuttle reaction (*e*-shuttle). (**D**) Reaction design showing consecutive paired electrolysis.

that a halide anion is a much better leaving group than a hydride, the competing undesired β–H elimination, which is often the preferred pathway when alkyl-transition metal complexes are involved as intermediates, can be effectively suppressed by this electrochemical approach. The subsequent oxidation of X^- at the anode followed by reaction with the alkene delivers the desired product, which closes the cycle by reestablishing the C–X bonds in a fully isodesmic process. Precise control of the potential applied on the electrodes

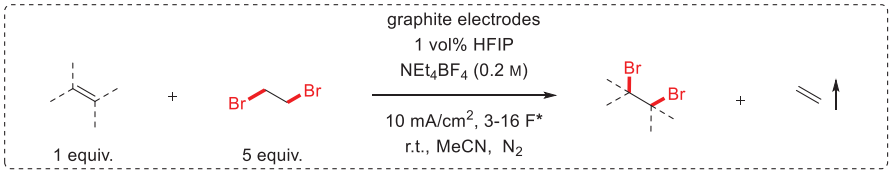

A Cyclic voltammetry studies†: Key role of HFIP

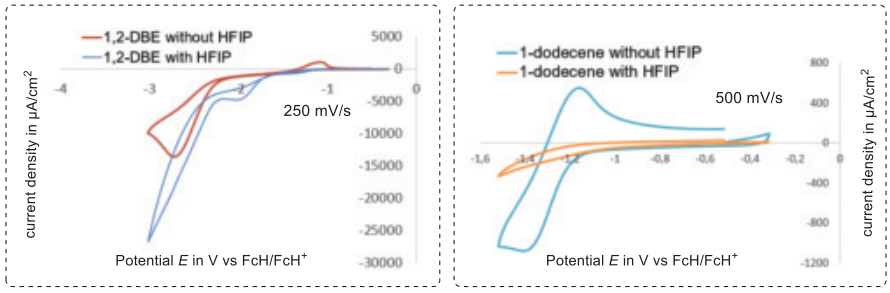

B Scope of the Br_2 shuttle reaction

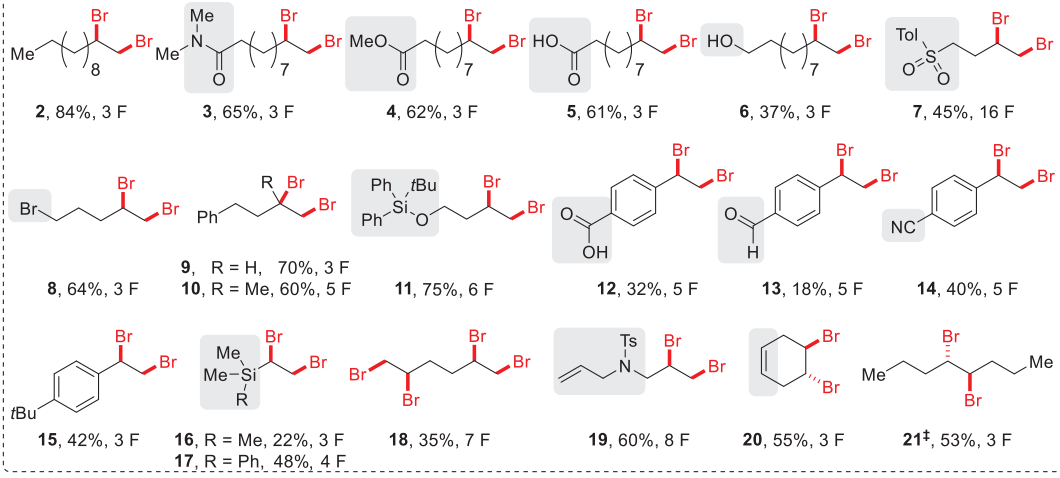

C Scale-up reaction in a beaker cell

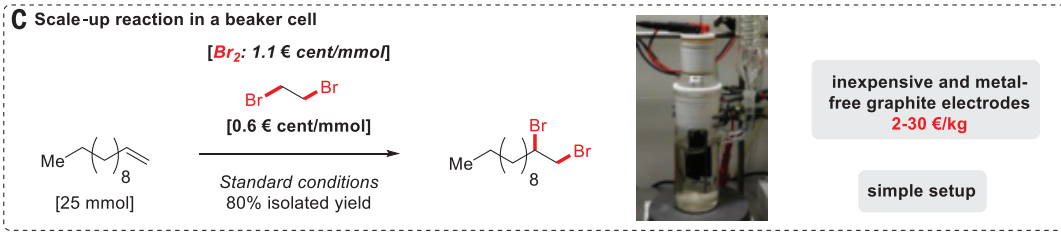

D Scope of the Br–SPh shuttle reaction

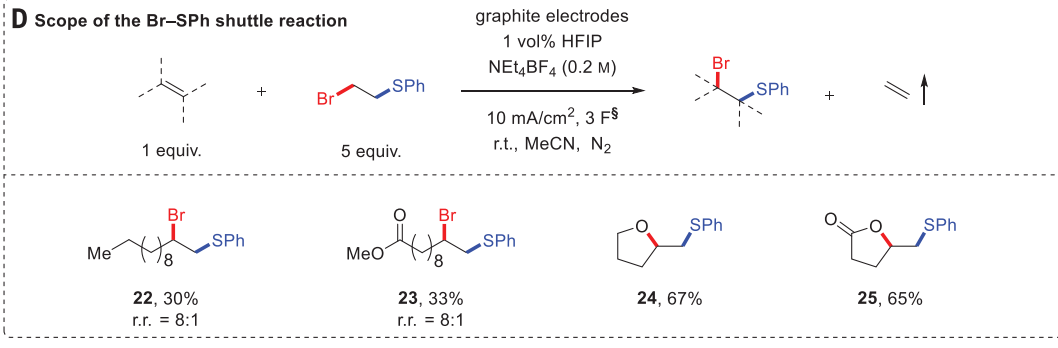

Fig. 2. Scope of the Br_2 and Br–SPh shuttle reactions. All yields are isolated yields of the products. (**A**) CV studies. (**B**) Scope of the Br_2 shuttle reaction. (**C**) Scale-up reaction in a beaker cell. (**D**) Scope of the Br–SPh shuttle reaction. *1 F equals ~62 min of electrolysis time. †Conditions for CV studies: A 5 mM solution of 1,2-DBE and 1-dodecene in MeCN using NEt_4BF_4 (0.2 M) as the supporting electrolyte at a graphite electrode with and without 1 vol % HFIP as the additive. ‡(*E*)-4-octene used as the starting material. §1 F equals ~31 min of electrolysis time. r.t., room temperature; FcH, ferrocene; r.r., regioisomeric ratio.

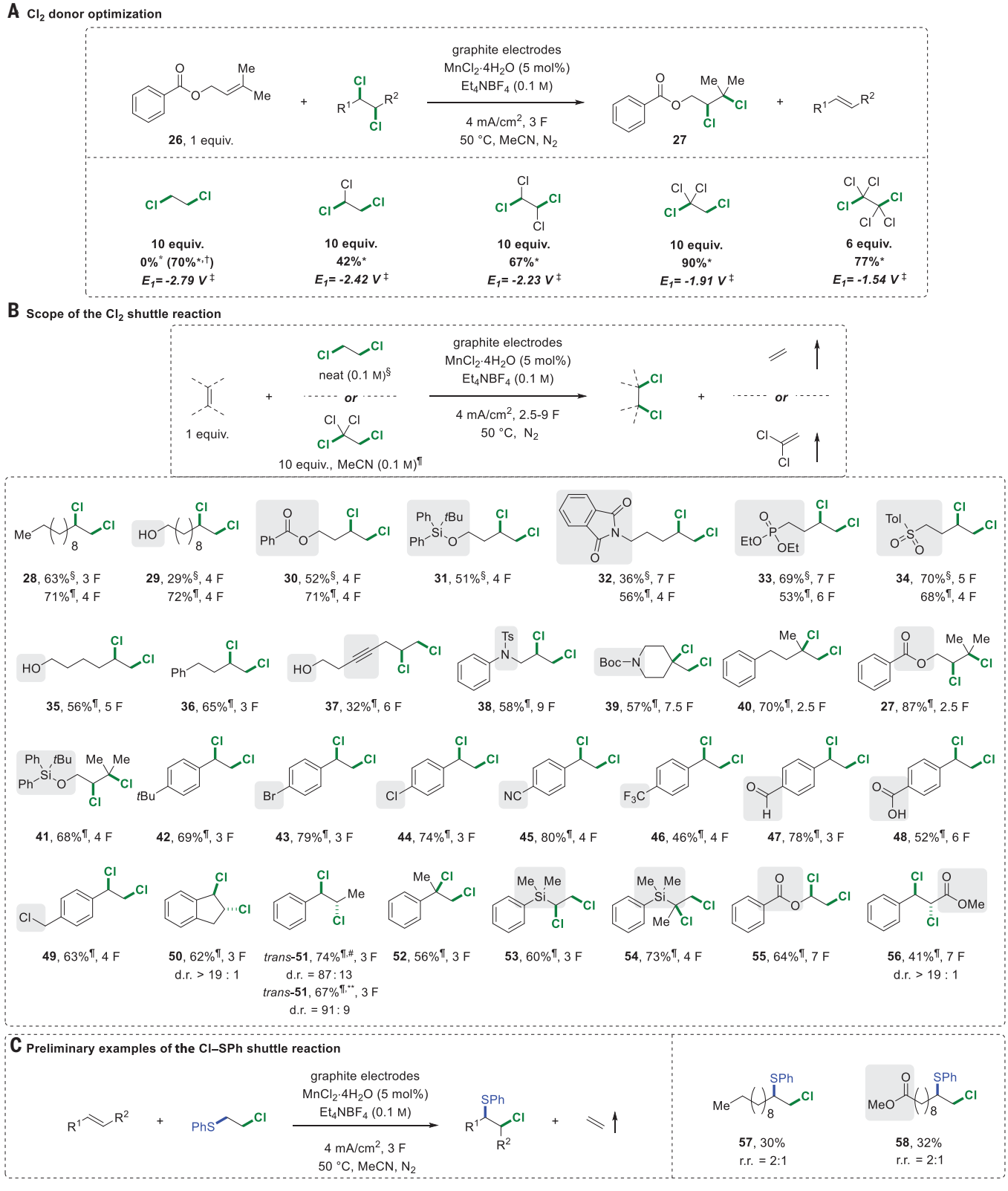

Fig. 3. Scope of the Cl_2 and Cl–SPh shuttle reactions. Here, 1 F equals ~81 min of electrolysis time. All yields are isolated yields of the products unless otherwise noted. (**A**) Cl_2 donor optimization. (**B**) Scope of the Cl_2 shuttle reaction. (**C**) Preliminary examples of the Cl–SPh shuttle reaction. *^{1}H-NMR yield with mesitylene as the internal standard. †Neat DCE (0.1 M) as the donor and 1-dodecene (1 equivalent) as the acceptor. ‡Redox potential (V versus SCE) measured for the first reduction peak at 0.2 Vs^{-1} for polychlororethanes (2 mM) in DMF + 0.1 M $(C_3H_7)_4NBF_4$ at a glassy carbon electrode according to (*38*). §Neat DCE (0.1 M) as the donor. ¶Reaction performed in MeCN (0.1 M) with 1,1,1,2-tetrachloroethane as the donor. #(*E*)-prop-1-en-1-ylbenzene used as the starting material. **(*Z*)-prop-1-en-1-ylbenzene used as the starting material. d.r., diastereomeric ratio.

and the highly tunable cell voltage would make this strategy modular and versatile with regard to the group transferred. This is an advantage over the organometallic strategy, in which each shuttle reaction relies on a completely different combination of metal and catalyst requiring independent optimization campaigns (*15*).

At the outset of our investigations, a transfer dibromination was optimized in an undivided cell using inexpensive isostatic graphite as the electrode material under constant current conditions at room temperature, a reaction setup easily accessible to nonspecialized laboratories. 1,2-Dibromoethane (DBE) was selected

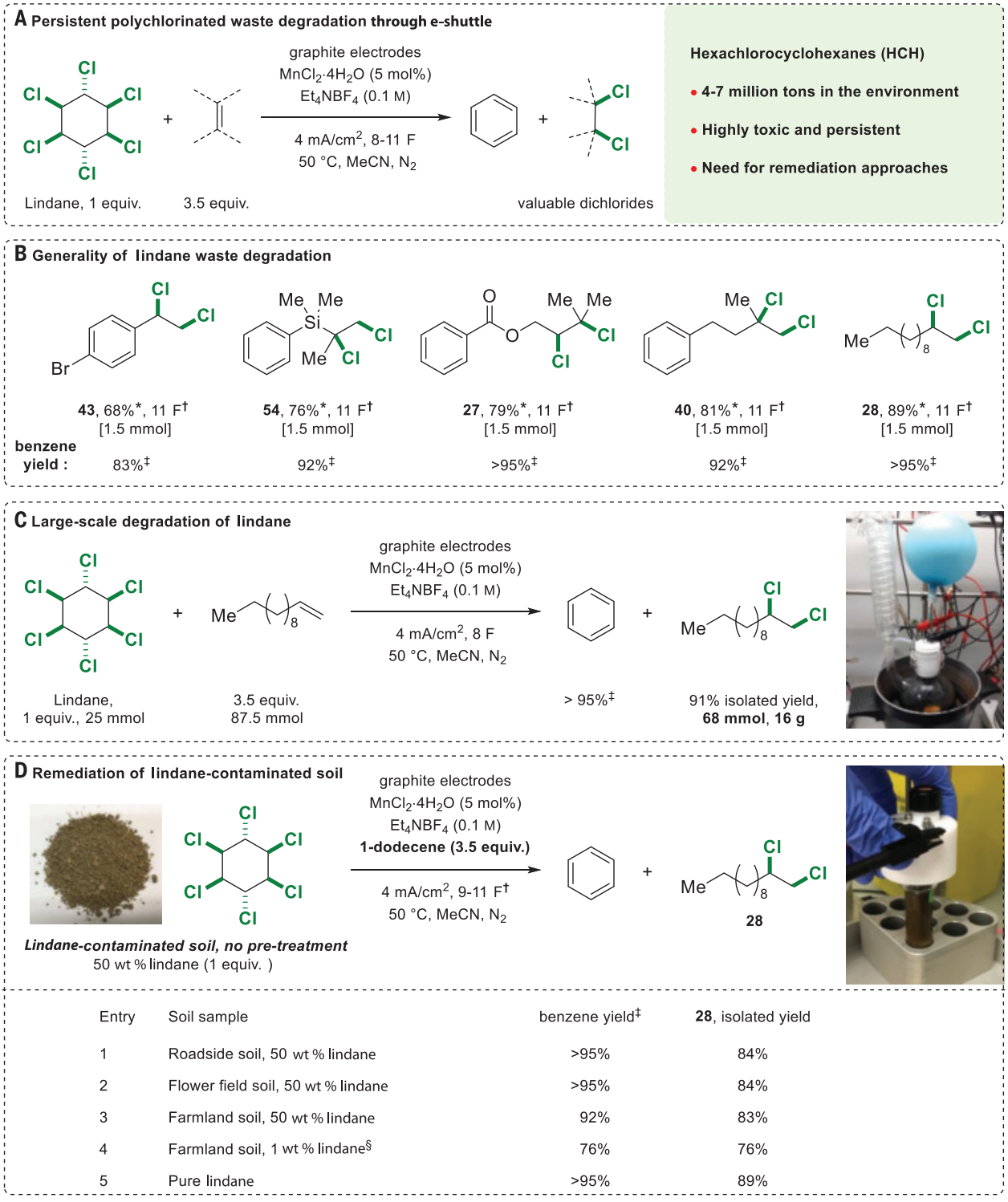

Entry	Soil sample	benzene yield‡	**28**, isolated yield
1	Roadside soil, 50 wt % lindane	>95%	84%
2	Flower field soil, 50 wt % lindane	>95%	84%
3	Farmland soil, 50 wt % lindane	92%	83%
4	Farmland soil, 1 wt % lindane§	76%	76%
5	Pure lindane	>95%	89%

Fig. 4. Application of *e*-shuttle reactions. (**A**) Persistent polychlorinated waste degradation through *e*-shuttle. (**B**) Generality of lindane waste degradation. (**C**) Large-scale degradation of lindane. (**D**) Remediation of lindane-contaminated soil. *Isolated yield. †1 F equals ~81 min of electrolysis time. ‡Yield measured by gas chromatography using mesitylene or anisole as the internal standard. §Lindane was extracted with MeCN before degradation.

as a formal Br_2 donor because it is an inexpensive and stable reagent, produced on a bulk scale, that would release gaseous ethylene as a by-product, thus providing a driving force for the shuttle process. Most commercial suppliers offer this reagent at an even lower price (per mole of Br_2 equivalents) than Br_2 itself, presumably reflecting the challenges and costs inherent to transporting and storing the volatile and corrosive Br_2 (*31*). Optimal results were obtained with 5 equivalents of 1,2-dibromoethane as the Br_2 donor, 1 volume percent (vol %) 1,1,1,3,3,3-hexafluoroisopropanol (HFIP) as a key additive (*32*), and 2 equivalents of Et_4NBF_4 as electrolyte in acetonitrile, providing the targeted 1,2-dibromide **2** in 84% yield (measured by integration of nuclear magnetic resonance spectra) when 3 F of electricity with respect to 1-dodecene was applied (Fig. 2). As indicated by cyclic voltammetry (CV) studies, the HFIP facilitates the reduction of the DBE donor and suppresses the undesired and unproductive reductive oligomerization and/or polymerization of alkene acceptors at the cathode (see Fig. 2A and figs. S31 and S32 for more details). The supporting electrolyte can be easily crystallized from the reaction mixture to be recycled.

Using this protocol, a broad range of unactivated terminal alkenes (**2**–**11**) were readily converted to the corresponding dibromide product in modest to good yields. The reaction conditions were compatible with a large variety of functional groups such as amide (**3**), ester (**4**), free carboxylic acid (**5**), primary alcohol (**6**), sulfone (**7**), and bromide (**8**). Only a small amount of the alcohol group oxidation to aldehyde was observed, confirming the mild nature of the reaction conditions. Activated alkenes, such as styrene (**12**–**15**) and vinyl silane (**16** and **17**), proved to be suitable substrates as well, albeit giving slightly lower yields because of undesired alkene oligomerization. Although hexa-1,5-diene underwent twofold 1,2-dibromination to yield the tetrabrominated product **18** in acceptable yield, selective mono-1,2-dibromination was observed for several other unconjugated dienes (**19** and **20**). (*E*)-4-Octene was smoothly dibrominated to produce the *meso*-dibromide **21** as the single diastereomer. To demonstrate the scalability and robustness of this *e*-shuttle process, the transfer bromination of 1-dodecene was readily scaled up to a 250-ml beaker cell from a 10-ml reaction vial to give 6.57 g (80% yield) of product **2** under otherwise identical reaction conditions (Fig. 2C).

Taking advantage of the reversible elimination of a –SR group (*33*), we could next also develop a transfer bromothiolation of alkenes to prepare 1,2-bromothioether derivatives, which are valuable synthetic intermediates usually accessed through multistep synthesis involving highly reactive RSBr reagents (*34*, *35*). Several terminal alkenes were successfully converted to the targeted bromothioether product under otherwise identical conditions, taking 2-bromoethyl phenyl sulfide (5 equivalents) as the PhS–Br donor (Fig. 2D). The lower yields arose from competing formation of vicinal disulfides and RS–SR, as well as alkene oligomerization. The ester (**23**) functional group was compatible. An interrupted shuttle reaction took place when pent-4-en-1-ol and pent-4-enoic acid were used as the substrates, delivering the cyclic ether (**24**) or lactone derivatives (**25**) through subsequent intramolecular nucleophilic attack, demonstrating the method's potential for the development of cascade reactions.

We next explored a transfer dichlorination reaction (Fig. 3). 1,2-Dichloroethane (DCE) was selected as the donor because it is an inexpensive bulk chemical (20 million tons/year) that is produced as a central intermediate in polyvinylchloride (PVC) production using the excess of Cl_2 gas generated during the Chlor-alkali electrolysis process (*36*). The desired dichloride **28** was obtained in 40% yield when 5 mol % of manganese(II) chloride tetrahydrate was introduced as a mediator (*25*) using an otherwise identical electrochemical setup to the dibromination protocol. The yield was further increased to 70% when DCE (~125 equivalents) was used as the solvent (*37*). Although this procedure was efficient for a wide set of terminal alkenes (**28**–**34**; Fig. 3B), it failed for more challenging 1,1,2-trisubstituted alkene **26** (Fig. 3A), a feature largely attributable to the undesired 1,2-dechlorinative decomposition of the product **27** and alkene oligomerization of the starting material through cathodic reduction. We reasoned that these two challenges could be smoothly addressed by choosing a more suitable dichloride donor. On the basis of the known reduction potentials of a large set of simple chlorinated compounds (*38*), we hypothesized that polychlorinated C2 donors, which are more readily reduced, should lead to a more favorable reaction outcome. Experimentally, an excellent correlation between the reduction potential of a series of donors was indeed observed, leading to the identification of 1,1,1,2-tetrachloroethane, a stable, noncorrosive compound, as the reagent of choice, affording the desired dichloride product **27** in 90% nuclear magnetic resonance (NMR) yield (Fig. 3A). Using this procedure, a series of monosubstituted, disubstituted, and trisubstituted alkenes participated smoothly in the 1,2-transfer dichlorination reaction, with free alcohol (**29**, **35**, and **37**), ester (**30**), imide (**32**), phosphonate (**33**), sulfone (**34**), and Ts- and Boc-protected amine moieties (**38** and **39**) proving compatible. An internal alkyne (**37**) was even partially compatible with the reaction conditions despite the minor formation of unidentified by-products. Various styrene-derived alkenes were converted to the corresponding 1,2-dichlorides in good to excellent yield (**42**–**52**), leaving the Br, Cl, CN, CF_3, CHO, and COOH functional groups untouched. Indene was diastereoselectively transformed into *trans*-1,2-dichloride **50** (diastereomeric ratio > 19:1). Both (*E*)- and (*Z*)-1-phenylpropene were converted to the *anti*-dichloride **51** in similarly high diastereoselectivity. The 1,2-dichloride compound **52**, bearing a reactive benzylic tertiary C–Cl bond, was prepared in good yield from α-methylstyrene. Several other activated alkenes, such as the silyl- and ester-substituted alkenes, also proved to be viable substrates to deliver the dichloride products (**53**–**56**), in particular, methyl cinnamate was converted to the 1,2-dichloride **56** in an excellent diastereomeric ratio (>19:1). To our delight, preliminary experiments showed that this protocol can be readily extended to the 1,2-chlorothiolation transfer reaction using the commercially available 2-chloroethyl phenyl sulfide (10 equivalents) as the donor (Fig. 3C). The lower yield can be explained by the undesired formation of RS–SR species as well as substrate oligomerization.

In contrast to traditional halogenation methods, the inherent reversibility of the *e*-shuttle strategy offers a platform to develop *retro*-dihalogenation reactions. Given the environmental persistence of several halogenated compounds produced at commodity scale, such as flame retardants and insecticides, *e*-shuttle could facilitate their recycling and valorization through *retro*-dihalogenations, which could ultimately lead to a circular economy for these important chemicals. A notable example is lindane [*gamma*-hexachlorocyclohexane (HCH)], a compound that was once used worldwide as an effective broad-spectrum insecticide in crop protection, which is now classified as a persistent organic pollutant because of its high toxicity and high persistency in the environment (*39*–*42*). Global quantities of HCH wastes still present in the environment range between 4 and 7 million tons worldwide, highlighting the pressing challenge of finding methods to recycle and remove this compound from contaminated soils (*39*). We thus questioned whether this waste material, which, among other chemical and biological approaches (*40*), can only be inefficiently degraded through normal electrochemical recycling methods (*43*–*45*), could be efficiently *retro*-dihalogenated using our *e*-shuttle strategy (Fig. 4A). Indeed, lindane, through three successive *retro*-dichlorination events, successfully transferred its six chlorine atoms to an acceptor alkene to form benzene, the fully dechlorinated by-product of lindane, alongside a dichlorinated alkane. Five illustrative alkene examples gave excellent yields up to 89% (>95% gas chromatography yield of benzene; Fig. 4B), demonstrating the

generality of this process and the possibility of accessing a wide variety of potentially useful chemicals. A scale-up experiment (87.5 mmol of alkene) further showcased the efficiency of the *retro*-dichlorination process (Fig. 4C). The exceptional functional group tolerance of our *e*-shuttle strategy made us next question whether we could successfully *retro*-dichlorinate lindane–contaminated soils through a transfer dichlorination reaction (Fig. 4D). In theory, such a process could lead to a new avenue to chemically remediate highly contaminated soils, which are mainly caused by leachates of improper disposal at landfilling or dump sites (*39*, *40*, *42*), through simultaneous synthesis of commercially relevant dichlorinated chemicals. This could provide an alternative to current industrial approaches that focus on the generation of HCl from chlorinated waste (*42*).

Artificially contaminated soils are commonly used as models in environmental chemistry to perform proof-of-concept chemical remediation experiments (*46*). Therefore, to mimic the composition of soils contaminated by high concentration of HCH, three soil samples from different locations near our university campus, i.e., roadside, flower field, and farmland, were collected and homogeneously mixed with commercially available lindane. The 50 weight % (wt %) lindane–contaminated soil could be used directly in the reaction without any preextraction or filtration, delivering both the benzene and dichloride product in excellent yields and high purity (Entries 1 to 3; Fig. 4D), a result comparable to the experiments using pure lindane (Entry 5; Fig. 4D). This result shows that our degradation process is compatible with the biological and mineral impurities present in three different soil types. Although the exact composition of environmentally relevant contaminated soils might differ from our samples (*39*, *41*, *42*), we nevertheless believe that these positive preliminary results using a variety of soil samples support the feasibility of this approach. A much lower lindane-soil ratio of 1 wt % was extracted with the reaction solvent before the degradation to also afford good yields for both benzene (76%) and dichloride (76%, Entry 4; Fig. 4D). This alternative preextraction protocol acts as a further proof-of-concept that might help in the design of larger-scale remediation processes in which undesired soil contamination with electrolytes and Mn catalysts can be prevented. The large-scale feasibility of an extraction approach has been demonstrated by the successful treatment of ~70,000 tons of HCH-contaminated soils in the Netherlands in a full-scale soil-washing plant, which achieved HCH removal efficiency of >99.7% (*42*).

Collectively, these preliminary results serve as a proof-of-principle for the direct remediation of lindane-contaminated soils using *e*-shuttle methodology.

REFERENCES AND NOTES

1. K. L. Kirk, "Persistent polyhalogenated compounds: biochemistry, toxicology, medical applications, and associated environmental issues," in *Biochemistry of the Elemental Halogens and Inorganic Halides* (Springer, 1991), pp. 191–238.
2. M. M. Häggblom, I. D. Bossert, "Halogenated organic compounds: A global perspective," in *Dehalogenation: Microbial Processes and Environmental Applications* (Springer, 2003) pp. 3–29.
3. S. Patai, *The Chemistry of The Carbon–Halogen Bond: Part 1* (Wiley, 1973).
4. I. Saikia, A. J. Borah, P. Phukan, *Chem. Rev.* **116**, 6837–7042 (2016).
5. M. Eissen, D. Lenoir, *Chem. Eur. J.* **14**, 9830–9841 (2008).
6. A. J. Cresswell, S. T.-C. Eey, S. E. Denmark, *Angew. Chem. Int. Ed.* **54**, 15642–15682 (2015).
7. W.-J. Chung, C. D. Vanderwal, *Angew. Chem. Int. Ed.* **55**, 4396–4434 (2016).
8. B. N. Bhawal, B. Morandi, *ACS Catal.* **6**, 7528–7535 (2016).
9. X. Fang, P. Yu, B. Morandi, *Science* **351**, 832–836 (2016).
10. X. Fang, B. Cacherat, B. Morandi, *Nat. Chem.* **9**, 1105–1109 (2017).
11. S. K. Murphy, J.-W. Park, F. A. Cruz, V. M. Dong, *Science* **347**, 56–60 (2015).
12. D. A. Petrone *et al*., *J. Am. Chem. Soc.* **139**, 3546–3557 (2017).
13. W. Chen, J. C. L. Walker, M. Oestreich, *J. Am. Chem. Soc.* **141**, 1135–1140 (2019).
14. P. Yu, A. Bismuto, B. Morandi, *Angew. Chem. Int. Ed.* **59**, 2904–2910 (2020).
15. B. N. Bhawal, B. Morandi, *Angew. Chem. Int. Ed.* **58**, 10074–10103 (2019).
16. M. Beller, J. Seayad, A. Tillack, H. Jiao, *Angew. Chem. Int. Ed.* **43**, 3368–3398 (2004).
17. K. Sakai, K. Sugimoto, S. Shigeizumi, K. Kondo, *Tetrahedron Lett.* **35**, 737–740 (1994).
18. M. L. Ho, A. B. Flynn, W. W. Ogilvie, *J. Org. Chem.* **72**, 977–983 (2007).
19. G. W. Gribble, *Acc. Chem. Res.* **31**, 141–152 (1998).
20. R. H. Crabtree, *The Organometallic Chemistry of the Transition Metals* (Wiley, ed. 5, 2009).
21. M. Yan, Y. Kawamata, P. S. Baran, *Chem. Rev.* **117**, 13230–13319 (2017).
22. J. C. Siu, N. Fu, S. Lin, *Acc. Chem. Res.* **53**, 547–560 (2020).
23. J. L. Röckl, D. Pollok, R. Franke, S. R. Waldvogel, *Acc. Chem. Res.* **53**, 45–61 (2020).
24. A. Wiebe *et al*., *Angew. Chem. Int. Ed.* **57**, 5594–5619 (2018).
25. N. Fu, G. S. Sauer, S. Lin, *J. Am. Chem. Soc.* **139**, 15548–15553 (2017).
26. Y. Yuan *et al*., *iScience* **12**, 293–303 (2019).
27. Y. Mo *et al*., *Science* **368**, 1352–1357 (2020).
28. M. F. Hartmer, S. R. Waldvogel, *Chem. Commun.* **51**, 16346–16348 (2015).
29. D. Pollok, S. R. Waldvogel, *Chem. Sci.* **11**, 12386–12400 (2020).
30. J. Casanova, L. Eberson, "Electrochemistry of the carbon–halogen bond," in *The Chemistry of The Carbon-Halogen Bond: Part 1*, S. Patai, ed. (Wiley, 1973), pp. 979–1047.
31. D. M. Hill, "Safety review of bromine-based electrolytes for energy storage applications," Report 1 (2018); http://energystorageicl.com/wp-content/uploads/2018/04/DNV-GL-Safety-Review-of-Bromine-Based-Electrolytes-for-Energy-Storage-Applications.pdf.
32. L. Schulz, S. R. Waldvogel, *Synlett* **30**, 275–286 (2019).
33. S. E. Denmark, W. R. Collins, M. D. Cullen, *J. Am. Chem. Soc.* **131**, 3490–3492 (2009).
34. E. Schneider, *Chem. Ber.* **84**, 911–916 (1951).
35. J. Drabowicz, P. Kiełbasiński, M. Mikołajczyk, "Synthesis of sulphenyl halides and sulphenamides," in *Sulfenic Acids and Derivatives*, S. Patai, ed. (Wiley, 1990), pp. 221–292.
36. C. Hoffmann, J. Weigert, E. Esche, J.-U. Repke, *Chem. Eng. Sci.* **214**, 115358 (2020).
37. Y. Liang, F. Lin, Y. Adeli, R. Jin, N. Jiao, *Angew. Chem. Int. Ed.* **58**, 4566–4570 (2019).
38. B. Huang, A. A. Isse, C. Durante, C. Wei, A. Gennaro, *Electrochim. Acta* **70**, 50–61 (2012).
39. J. Vijgen, B. de Borst, R. Weber, T. Stobiecki, M. Forter, *Environ. Pollut.* **248**, 696–705 (2019).
40. P. Bhatt, M. S. Kumar, T. Chakrabarti, *Crit. Rev. Environ. Sci. Technol.* **39**, 655–695 (2009).
41. K. Walker, D. A. Vallero, R. G. Lewis, *Environ. Sci. Technol.* **33**, 4373–4378 (1999).
42. M. Vega, D. Romano, E. Uotila, "Lindane (persistent organic pollutant) in the EU" [Directorate General for Internal Policies. Policy Department C: Citizens' Rights and Constitutional Affairs. Petitions (PETI) PE 571.398, 2016].
43. S. Rondinini, A. Vertova, "Electroreduction of halogenated organic compounds," in *Electrochemistry for the Environment*, C. Comninellis, G. Chen, ed. (Springer, 2010), pp. 279–306.
44. J. P. Merz, B. C. Gamoke, M. P. Foley, K. Raghavachari, D. G. Peters, *J. Electroanal. Chem.* **660**, 121–126 (2011).
45. E. T. Martin, C. M. McGuire, M. S. Mubarak, D. G. Peters, *Chem. Rev.* **116**, 15198–15234 (2016).
46. E. Morillo, J. Villaverde, *Sci. Total Environ.* **586**, 576–597 (2017).
47. G. R. Fulmer *et al*., *Organometallics* **29**, 2176–2179 (2010).
48. J. Liu, Q. Ren, X. Zhang, H. Gong, *Angew. Chem. Int. Ed.* **55**, 15544–15548 (2016).
49. A. K. Macharla, R. C. Nappunni, N. Nama, *Tetrahedron Lett.* **53**, 1401–1405 (2012).
50. S. Lethu, S. Matsuoka, M. Murata, *Org. Lett.* **16**, 844–847 (2014).
51. J. Long *et al*., *Synlett* **30**, 181–184 (2019).
52. G. W. Kabalka, K. Yang, N. K. Reddy, C. Narayana, *Synth. Commun.* **28**, 925–929 (1998).
53. K. Yubata, H. Matsubara, *Tetrahedron Lett.* **60**, 1001–1004 (2019).
54. X. Xia, P. H. Toy, *Beilstein J. Org. Chem.* **10**, 1397–1405 (2014).
55. W. Chen *et al*., *Chem. Eur. J.* **22**, 9546–9550 (2016).
56. A. Chassepot *et al*., *Chem. Mater.* **24**, 930–937 (2012).
57. N. S. Martins, E. E. Alberto, *New J. Chem.* **42**, 161–167 (2018).
58. W. E. Billups *et al*., *J. Org. Chem.* **67**, 4436–4440 (2002).
59. K. M. Redies, T. Fallon, M. Oestreich, *Organometallics* **33**, 3235–3238 (2014).
60. R. Campagne, F. Schäkel, R. Guillot, V. Alezra, C. Kouklovsky, *Org. Lett.* **20**, 1884–1887 (2018).
61. D. Lexa *et al*., *J. Am. Chem. Soc.* **112**, 6162–6177 (1990).
62. L. Benati, P. C. Montevecchi, P. Spagnolo, *Tetrahedron* **49**, 5365–5376 (1993).
63. X. Marset, G. Guillena, D. J. Ramón, *Chem. Eur. J.* **23**, 10522–10526 (2017).
64. R. M. Denton, X. Tang, A. Przeslak, *Org. Lett.* **12**, 4678–4681 (2010).
65. A. J. Cresswell, S. T.-C. Eey, S. E. Denmark, *Nat. Chem.* **7**, 146–152 (2015).
66. J. C. Sarie, J. Neufeld, C. G. Daniliuc, R. Gilmour, *ACS Catal.* **9**, 7232–7237 (2019).
67. H. Egami *et al*., *J. Org. Chem.* **81**, 4020–4030 (2016).
68. V. Wedek, R. Van Lommel, C. G. Daniliuc, F. De Proft, U. Hennecke, *Angew. Chem. Int. Ed.* **58**, 9239–9243 (2019).
69. E. W. Tan, B. Chan, A. G. Blackman, *J. Am. Chem. Soc.* **124**, 2078–2079 (2002).
70. J. Wei, S. Liang, L. Jiang, Y. Mumtaz, W.-B. Yi, *J. Org. Chem.* **85**, 977–984 (2020).
71. L. Benati, L. Capella, P. C. Montevecchi, P. Spagnolo, *Tetrahedron* **50**, 12395–12406 (1994).
72. P. Sanllehí *et al*., *Chem. Commun.* **53**, 5441–5444 (2017).
73. J. M. Lopchuk *et al*., *J. Am. Chem. Soc.* **139**, 3209–3226 (2017).
74. K. Yuan, J.-F. Soulé, V. Dorcet, H. Doucet, *ACS Catal.* **6**, 8121–8126 (2016).
75. J. C. Siu, J. B. Parry, S. Lin, *J. Am. Chem. Soc.* **141**, 2825–2831 (2019).
76. R. L. Nyland II, Y. Xiao, P. Liu, C. L. Freel Meyers, *J. Am. Chem. Soc.* **131**, 17734–17735 (2009).
77. K. Yasui, K. Fugami, S. Tanaka, Y. Tamaru, *J. Org. Chem.* **60**, 1365–1380 (1995).
78. D. Song, S. Cho, Y. Han, Y. You, W. Nam, *Org. Lett.* **15**, 3582–3585 (2013).
79. Y.-Y. Ren, X. Zheng, X. Zhang, *Synlett* **29**, 1028–1032 (2018).

ACKNOWLEDGMENTS

We thank M. Zesiger, the NMR service, the Molecular and Biomolecular Analysis Service (MoBiAS), and ETH Zürich for

technical assistance; SusInnoScience (JGU Mainz) for support; S. Makai for assistance with gas chromatography–mass spectrometry headspace analysis and helpful discussions; E. Falk for reproducing one of the lindane-soil experiments; S. Makai, E. Falk, B. Bhawal, and T. Delcaillau for sharing chemicals; and the whole Morandi group for critical proofreading of this manuscript. **Funding:** This project received funding from the European Research Council under the European Union's Horizon 2020 research and innovation program (Shuttle Cat, Project ID: 757608) and the ETH Zürich. X.D. acknowledges the Marie Skłodowska-Curie Action (HaloCat, Project ID: 886102) for a postdoctoral fellowship. J.L.R. is a recipient of a DFG fellowship through the Excellence Initiative by the Graduate School Materials Science in Mainz (GSC 266). **Author contributions:** B.M. and X.D. conceived the project. X.D. and J.L.R. designed and performed all the synthetic studies. S.W. and B.M. supervised the research. All authors contributed to the writing and editing of the manuscript. **Competing interests:** The authors declare no competing interests. **Data and materials availability:** All experimental data are available in the main text or the supplementary materials.

SUPPLEMENTARY MATERIALS

science.sciencemag.org/content/371/6528/507/suppl/DC1
Materials and Methods
Figs. S1 to S41
Tables S1 to S16
NMR Spectra
References (*47*–*79*)

16 October 2020; accepted 30 December 2020
10.1126/science.abf2974

TROPICAL CYCLONES

Recent migration of tropical cyclones toward coasts

Shuai Wang* **and Ralf Toumi**

Poleward migrations of tropical cyclones have been observed globally, but their impact on coastal areas remains unclear. We investigated the change in global tropical cyclone activity in coastal regions over the period 1982–2018. We found that the distance of tropical cyclone maximum intensity to land has decreased by about 30 kilometers per decade, and that the annual frequency of global tropical cyclones increases with proximity to land by about two additional cyclones per decade. Trend analysis reveals a robust migration of tropical cyclone activity toward coasts, concurrent with poleward migration of cyclone locations as well as a statistically significant westward shift. This zonal shift of tropical cyclone tracks may be mainly driven by global zonal changes in environmental steering flow.

Tropical cyclones are one of the most devastating natural disasters in terms of their average destructiveness and annual frequency affecting coastal regions. There are ~100-year records of tropical cyclone activity in some regions (*1*, *2*), but only since 1982 have tropical cyclones been monitored globally by satellites. Poleward migration of the locations of tropical cyclone maximum intensity in the past 40 years has been reported in the global "best-track" data (*3*) and is projected to continue regionally in the 21st century (*4*). This poleward migration has been traced back to the poleward shift of tropical cyclone formation, which is speculated to be linked to an anthropogenically forced tropical circulation expansion (*5*). These trends could change the coastal tropical cyclone risk in the future (*4*). However, the poleward migration of the locations of tropical cyclone formation and peak intensity by themselves may not necessarily indicate a change in coastal tropical cyclone risk directly, because these locations are commonly too far away to generate an impact on the coasts. The changes in coastal tropical cyclone activity and landfall frequency are a central and perhaps ultimate concern.

A tropical cyclone landfall is conventionally defined as the intersection of the surface center of a tropical cyclone with a coastline (*6*). To date, there has been no firm evidence of global trends of the frequency of tropical cyclones with maximum wind speed above the hurricane-force wind (64 knots) at landfall (*7*). However, a "near miss" or "indirect-hit" tropical cyclone track can also cause damage; for example, Sandy in 2012 and Dorian in 2019 skirted along the U.S. coast for a considerable time before making landfall. Investigating the trend of tropical cyclones entering coastal regions is therefore essential to better understand tropical cyclone risk.

Here we consider tropical cyclones, defined by the lifetime maximum intensity (LMI) reaching at least 34 knots (see supplementary materials), during the period 1982–2018. This is the period for which we have the highest confidence in the quality of data and its completeness in global basins (*8*). The poleward migration of tropical cyclone activity was first found at LMI (*3*). The annual mean distance of the locations of LMI to the nearest land (Fig. 1A) also shows an evident and statistically significant decreasing trend of −32 ± 31 km per decade (table S1). The fraction of annual tropical cyclones entering coastal regions, defined as the offshore area with a distance to the nearest land less than 200 km (Fig. 1B), shows a robust increase of 2.2 ± 1.9% per decade (table S1). We also find positive trends of the

Department of Physics, Imperial College London, London SW7 2BU, UK.
***Corresponding author. Email: shuai.wang@imperial.ac.uk**

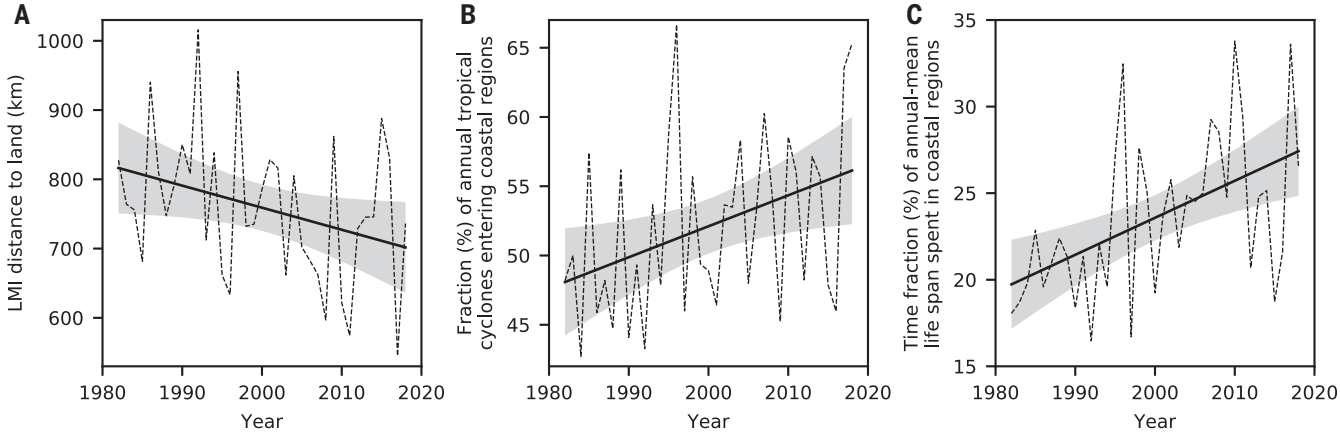

Fig. 1. Landward migration of global tropical cyclone activity. (**A**) Time series of annual-mean distance to land of the locations of lifetime maximum intensity (LMI). (**B**) As in (A), but for the fraction of annual tropical cyclones entering coastal regions. (**C**) As in (A), but for the time fraction of annual-mean life span spent in coastal regions. Dashed lines are historical data; solid lines are linear trends, with shaded areas denoting 95% confidence intervals.

annual mean lifetime fraction that tropical cyclones spend in coastal regions, at a rate of 2.1 ± 1.2% per decade globally, and in the Northern and Southern hemispheres of 2.1 ± 1.6% and 2.1 ± 1.9% per decade, respectively (table S1). The consistently positive contribution from both hemispheres (table S1) to the three global trends shown in Fig. 1 suggests that the increase of tropical cyclone activity in coastal regions is a global phenomenon, although regional differences between basins are evident.

The trend of the frequency of coastal tropical cyclones increases very significantly with proximity to land by one cyclone per decade per 1000 km (Fig. 2 and table S2). There are ~2 ± 2 additional tropical cyclones per decade in the 200-km coastal region globally (Fig. 2). Consistent with this, the fraction of annual tropical cyclones entering coastal regions (fig. S1A) and the annual-mean lifetime fraction that tropical cyclones spend in coastal regions (fig. S1B) increase with proximity to land. The statistical significance remains by excluding short-lived storms (*9*) and using an alternative set of tropical cyclone records (table S3). These clear increases in trend with reduced distance-to-land threshold suggest a global-scale landward migration of tropical cyclone activity.

Considering the geometry of global land-sea distribution, zonal and/or meridional shifts of tropical cyclone locations may lead to a change of tropical cyclone activity in coastal regions. Our analysis shows that from 1982–1999 to 2000–2018, the epochal mean tropical cyclone location in the global basins migrated not only poleward but also westward (Table 1). The globally epochal poleward and westward shifts are both statistically significant. If we measure the track shift in terms of degrees, the zonal shift is considerably larger than the meridional change. Tropical cyclone activity is being shifted westward in the West Pacific, East Pacific, and North and South Indian Ocean. These four basins account for ~75% of global tropical cyclones for 1982–2018, which accounts for the global mean westward track shifts. There are eastward track shifts in the South Pacific and no significant zonal shifts in the North Atlantic. These basin-wise changes in tropical cyclone locations can also be seen in the density change of tropical cyclone locations between the two epochs (fig. S2).

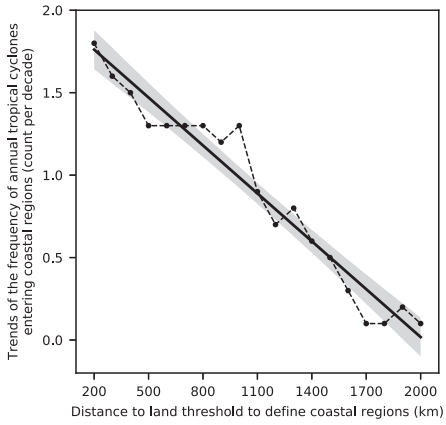

Fig. 2. Increasing trend of global tropical cyclone activity in coastal regions when reducing the distance-to-land threshold for coastal region definition. Changes in trends of the frequency of global annual tropical cyclones entering coastal regions are shown as a consequence of reducing the distance-to-land threshold from 2000 km to 200 km at 100-km intervals. The dashed line, solid line, and shading show the historical data, linear trend, and 95% confidence interval of the trend, respectively. On average there are 45 cyclones per year reaching coastal regions within 200 km of land.

We do not find any statistically significant global change in cyclone zonal translation velocity, duration, or zonal shifts of cyclone genesis (table S4). The lack of regionally significant zonal genesis location change is different from a reported poleward shift of genesis in the Pacific Ocean basins (*10*). The relative changes in meridional cyclone translation velocity in the second epoch agree with the meridional track shifts in all the basins.

Tropical cyclone tracks are primarily determined by the environmental steering flow and genesis location (*11*, *12*). We find significant enhancement of westward steering at a global scale in all basins except the North Indian Ocean (Table 1). Consistent general circulation patterns are confirmed in all three reanalysis products (fig. S3, A to C). The global mean change in zonal steering (+0.3 m s^{-1}; Table 1) is about 11% of the global mean zonal steering speed (2.6 m s^{-1} in ERA5 reanalysis; fig. S3) and global mean cyclone zonal translation speed (2.7 m s^{-1}). The West Pacific, East Pacific, and South Indian Ocean show both westward track shift and enhanced westward environmental steering between the epochs. The West Pacific is the only basin that shows a consistent link among seasonal westward steering enhancement, larger westward cyclone velocity, and westward track shift. This robust linkage to seasonal mean environmental conditions may be due to the considerably larger fraction of storm days in the season in the West Pacific relative to the other basins (*13*).

An environment with reduced vertical wind shear and/or increased potential intensity is favorable for tropical cyclone development (*14*, *15*) and may also contribute to geographical shifts of tropical cyclone locations (*3*). We find a significant relative decrease in vertical wind shear from the east to west globally (Fig. 3), which is confirmed in individual basins with reanalysis products (fig. S4, A to F). The South Pacific is the only basin where neither steering flow nor vertical wind shear fully explains the regional eastward track shift. However, we do find a relative increase in potential intensity to the east and a decrease to the west in that basin (fig. S4L). In the North Atlantic, the shear weakens only in the central part of the basin (fig. S4C) with no zonal change in either steering (Table 1) or potential intensity (fig. S4I), which is consistent with the absence of a significant zonal track shift. Further analysis reveals that the zonal potential intensity change is primarily modulated by the variation of the atmospheric convective available potential energy (fig. S5).

Given the dominant role of steering flow in tropical cyclone tracks (*12*) and a larger epochal relative change of steering (Table 1) than wind shear (Fig. 3) in our analysis, it is very likely that the westward shift of cyclone tracks is mainly due to the enhanced westward steering. Anomalous westward steering may increase tropical cyclone frequency in the west

Table 1. Changes in mean tropical cyclone location and deep-layer steering flow between the periods 1982–1999 and 2000–2018. The seasonal mean steering flow is calculated from the reanalysis product ERA5. The meridional steering flow is not shown because the absolute mean epochal change is less than 0.1 m s^{-1} in all regions. Statistical significance is indicated in bold at the 95% confidence interval. The differences are calculated globally, in the hemispheres (NHEM, Northern Hemisphere; SHEM, Southern Hemisphere), and in the individual basins (WPAC, West Pacific; EPAC, East Pacific; NATL, North Atlantic; NIO, North Indian Ocean; SIO, South Indian Ocean; SPAC, South Pacific).

	Global	NHEM	SHEM	WPAC	EPAC	NATL	NIO	SIO	SPAC
Westward (degrees longitude)	**+0.8 ± 0.2**	**+1.0 ± 0.3**	**+0.4 ± 0.3**	**+1.6 ± 0.4**	**+1.3 ± 0.7**	−0.1 ± 0.5	**+2.7 ± 0.4**	**+1.4 ± 0.5**	**−1.6 ± 0.6**
Poleward (degrees latitude)	**+0.3 ± 0.1**	**+0.2 ± 0.1**	**+0.6 ± 0.2**	**+0.5 ± 0.2**	**+0.4 ± 0.2**	**−0.3 ± 0.3**	**−0.8 ± 0.3**	**+0.6 ± 0.2**	**+0.5 ± 0.3**
Zonal steering (m s^{-1})	**+0.3 ± 0.3**	+0.2 ± 0.3	+0.4 ± 0.6	**+0.4 ± 0.4**	**+0.4 ± 0.3**	+0.1 ± 0.3	−0.1 ± 0.3	+0.3 ± 0.5	+0.5 ± 0.7

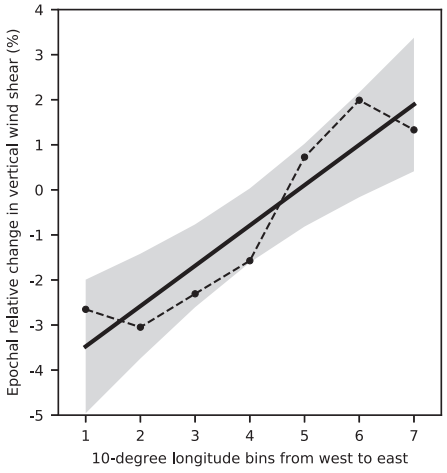

Fig. 3. Epochal change in the global-mean basin-wise climate condition as a function of longitude. The climate condition shown here is calculated as the relative change in vertical wind shear in the second epoch, 2000–2018, with respect to that in the first epoch, 1982–1999. The vertical wind shear is extracted from the reanalysis product ERA5. The mean vertical wind shear is calculated in seven of the 10° longitude bins, from west to east, in all the basins. The black dashed line shows the mean relative change in the seven longitude bins. The solid line shows the linear fit with ordinary least-squares regression. The shading denotes the 95% confidence interval of the fit.

of the basins, and relatively reduced vertical wind shear provides a further favorable environment for cyclones there. The quantitative contribution of the three environmental factors needs further exploration.

Climate modes such as the El Niño–Southern Oscillation (ENSO) and Pacific Decadal Oscillation (PDO), considered as measures of mainly internal unforced variability, can modulate tropical cyclone activities (*16*–*19*) and global atmospheric circulation in the tropics (*20*, *21*). We find that ENSO has a very limited impact on annual trends. However, the PDO may substantially contribute to the trends in the Northern Hemisphere (table S1). The epochal steering flow change is similar to the steering difference between PDO warm and cold phases (fig. S3, D to F). The PDO index had a phase change in 1998 (*5*), which also separates the first and second epochs (pre- and post-2000) in our analysis into a warm and cold PDO phase, respectively.

Given no strong trend of global annual frequency of tropical cyclones (*22*), an increasing trend of annual coastal cyclone fraction agrees with a rising frequency of coastal tropical cyclones shown here. The lifetime fraction trend in Fig. 1C seems to agree with a recently reported global slowdown of tropical cyclone translation speed (*23*) because the annual mean tropical cyclone duration has not changed significantly during the period 1982–2018 (table S4). However, this causal hypothesis needs to be confirmed, as changes in cyclone moving speed are disputed (*24*).

We find statistically significant landward migration of tropical cyclone activity. The lack of a statistically significant trend of actual landfall (+1 ± 2 cyclones per decade globally) may be due to the rapid intensity reduction before and during landfall. Major tropical cyclones have decayed more rapidly after LMI (*25*). This could stabilize the annual frequency of landfall defined by a fixed intensity threshold. Thus, the lack of a global trend of annual mean landfall frequency, as has been previously reported (*7*) and confirmed in our analysis, may not be contradictory to the increase in tropical cyclone activity in coastal regions reported here.

Long-term zonal migration of tropical cyclones, as found in our analysis, has been previously shown directly or indirectly in some individual basins for different metrics. In the West Pacific, westward migration of the tropical cyclone maximum intensity locations was reported (*26*), which was related to the strengthened tropical Pacific Walker circulation driven by the zonally enhanced sea surface temperature gradient. No detectable trend of U.S. landfall hurricane frequency has emerged (*22*). There has been a decreasing trend of landfall frequency by severe tropical cyclones in eastern Australia (*2*). In the North Indian Ocean, the reduction of local wind shear over the Arabian Sea has made tropical cyclone development more favorable, and this may continue in the future (*27*).

The relatively limited length of global tropical cyclone observations, limitations of climate modeling, and possible association with the PDO limit our ability to attribute tropical cyclone migration toward coasts to anthropogenic forcing. However, we note that global epochal westward shifts are still present when considering only PDO-neutral years (table S5). The West Pacific LMI distance to land, fraction of coastal cyclones, and coastal time fraction trends since 1950 are still significant after the PDO is removed (table S1). This suggests that factors other than the PDO are also important. It is argued that greenhouse gas emissions have contributed to the observed changes in regional distribution of tropical cyclones since 1980, and yet these trends may not persist in the 21st century (*28*).

The enhanced westward tropical cyclone steering may also be consistent with Hadley circulation expansion. The PDO phase change and Hadley circulation expansion are related (*20*, *21*). The poleward migration of cyclone locations has also been related to the anomalous sinking and rising motions due to the meridional expansion of the Hadley circulation (*5*). Long-term zonal shifts of tropical precipitation emerge in atmospheric reanalysis data (*29*). The Walker circulation dominates the large-scale zonal motion in the tropics. An attempt has been made to establish a link between the covariability of tropical cyclone genesis locations and both the Hadley and Walker circulations in the West Pacific (*30*). The combined Walker and Hadley circulation variation is a plausible avenue for future study to understand the global tropical cyclone changes presented here. The considerable impacts of coastal tropical cyclones warrant further study of the changes in coastal tropical cyclone activity, as identified here, and its future projections and the consequent change in risk.

REFERENCES AND NOTES

1. J. C. L. Chan, K.-S. Liu, M. Xu, Q. Yang, *Int. J. Climatol.* **32**, 1946–1950 (2012).
2. J. Callaghan, S. B. Power, *Clim. Dyn.* **37**, 647–662 (2011).
3. J. P. Kossin, K. A. Emanuel, G. A. Vecchi, *Nature* **509**, 349–352 (2014).
4. J. P. Kossin, K. A. Emanuel, S. J. Camargo, *J. Clim.* **29**, 5725–5739 (2016).
5. S. Sharmila, K. J. E. Walsh, *Nat. Clim. Chang.* **8**, 730–736 (2018).
6. NOAA, Glossary of National Hurricane Center Terms; www.nhc.noaa.gov/aboutgloss.shtml.
7. J. Weinkle, R. Maue, R. Pielke Jr., *J. Clim.* **25**, 4729–4735 (2012).
8. K. R. Knapp, M. C. Kruk, *Mon. Weather Rev.* **138**, 1459–1473 (2010).
9. C. W. Landsea, G. A. Vecchi, L. Bengtsson, T. R. Knutson, *J. Clim.* **23**, 2508–2519 (2010).
10. A. S. Daloz, S. J. Camargo, *Clim. Dyn.* **50**, 705–715 (2018).
11. L. Wu, B. Wang, *J. Clim.* **17**, 1686–1698 (2004).
12. J. C. L. Chan, *Annu. Rev. Fluid Mech.* **37**, 99–128 (2005).
13. B. Wang, Y. Yang, Q. H. Ding, H. Murakami, F. Huang, *Geophys. Res. Lett.* **37**, L07704 (2010).
14. K. A. Emanuel, *Nature* **401**, 665–669 (1999).
15. M. Ting, J. P. Kossin, S. J. Camargo, C. Li, *Sci. Rep.* **9**, 7795 (2019).
16. S. J. Camargo, A. W. Robertson, A. G. Barnston, M. Ghil, *Geochem. Geophys. Geosyst.* **9**, Q06V05 (2008).
17. J. P. Kossin, S. J. Camargo, M. Sitkowski, *J. Clim.* **23**, 3057–3076 (2010).
18. S. J. Camargo, A. W. Robertson, S. J. Gaffney, P. Smyth, M. Ghil, *J. Clim.* **20**, 3654–3676 (2007).
19. H. A. Ramsay, S. J. Camargo, D. Kim, *Clim. Dyn.* **39**, 897–917 (2012).
20. R. J. Allen, M. Kovilakam, *J. Clim.* **30**, 6329–6350 (2017).
21. P. W. Staten, J. Lu, K. M. Grise, S. M. Davis, T. Birner, *Nat. Clim. Chang.* **8**, 768–775 (2018).
22. T. Knutson *et al.*, *Bull. Am. Meteorol. Soc.* **100**, 1987–2007 (2019).
23. J. P. Kossin, *Nature* **558**, 104–107 (2018).
24. M. Yamaguchi, J. C. L. Chan, I. J. Moon, K. Yoshida, R. Mizuta, *Nat. Commun.* **11**, 47 (2020).
25. S. Wang, T. Rashid, H. Throp, R. Toumi, *Geophys. Res. Lett.* **47**, (2020).
26. D.-S. R. Park, C.-H. Ho, J.-H. Kim, *Environ. Res. Lett.* **9**, 014008 (2014).
27. H. Murakami, G. A. Vecchi, S. Underwood, *Nat. Clim. Chang.* **7**, 885–889 (2017).
28. H. Murakami *et al.*, *Proc. Natl. Acad. Sci. U.S.A.* **117**, 10706–10714 (2020).
29. M. P. Byrne, A. G. Pendergrass, A. D. Rapp, K. R. Wodzicki, *Curr. Clim. Change Rep.* **4**, 355–370 (2018).
30. H. Zhao, J. Zhang, P. J. Klotzbach, S. Chen, *J. Clim.* **32**, 8167–8179 (2019).

ACKNOWLEDGMENTS

We thank C. Landsea, two anonymous reviewers, and K. Emanuel for helpful comments. **Funding:** Supported by the UK-China Research and Innovation Partnership Fund through the Met Office Climate Science for Service Partnership (CSSP) China as part of the Newton Fund. **Author contributions:** S.W. and R.T. conceived the study. S.W. performed the analysis. Both authors discussed the results and jointly contributed to writing the manuscript. **Competing interests:** The authors declare no competing interests. **Data and materials availability:** The tropical

cyclone best-track data can be downloaded from the National Centers for Environmental Information website (www.ncdc.noaa.gov/ibtracs/index.php). The ERA5, MERRA, and NCEP/NCAR reanalysis data are available at the European Centre for Medium-Range Weather Forecasts (www.ecmwf.int/en/forecasts/datasets/reanalysis-datasets/era5), the NASA Modeling and Assimilation Data and Information Services Center (https://gmao.gsfc.nasa.gov/reanalysis/MERRA-2/), and the NOAA Physical Sciences Laboratory (https://psl.noaa.gov/data/reanalysis/reanalysis.shtml), respectively.

SUPPLEMENTARY MATERIALS

science.sciencemag.org/content/371/6528/514/suppl/DC1

Materials and Methods
Figs. S1 to S6
Tables S1 to S5
References (*31*–*40*)

26 March 2020; accepted 30 November 2020
10.1126/science.abb9038

CATALYSIS

In situ manipulation of the active Au-TiO_2 interface with atomic precision during CO oxidation

Wentao Yuan[1]*, Beien Zhu[2,3]*, Ke Fang[1]*, Xiao-Yan Li[3,4], Thomas W. Hansen[5]†, Yang Ou[1], Hangsheng Yang[1], Jakob B. Wagner[5]†, Yi Gao[2,3]†, Yong Wang[1]†, Ze Zhang[1]

The interface between metal catalyst and support plays a critical role in heterogeneous catalysis. An epitaxial interface is generally considered to be rigid, and tuning its intrinsic microstructure with atomic precision during catalytic reactions is challenging. Using aberration-corrected environmental transmission electron microscopy, we studied the interface between gold (Au) and a titanium dioxide (TiO_2) support. Direct atomic-scale observations showed an unexpected dependence of the atomic structure of the Au-TiO_2 interface with the epitaxial rotation of gold nanoparticles on a TiO_2 surface during carbon monoxide (CO) oxidation. Taking advantage of the reversible and controllable rotation, we achieved in situ manipulation of the active Au-TiO_2 interface by changing gas and temperature. This result suggests that real-time design of the catalytic interface in operating conditions may be possible.

Supported nanoparticles (NPs) are widely used as catalysts for heterogeneous reactions (*1*–*7*). Their catalytic activities can depend on the interfaces between the NPs and their substrates, because the most-active sites in many reactions are located at the perimeter interface (PI) (*7*–*15*), as is the case for the Au-TiO_2 PI in CO oxidation (*14*–*16*). Recent in situ experiments indicate that refacetting of NPs and surface reconstructions of the substrates can occur in reactive environments (*17*–*25*), but little is known about the dependence of the intrinsic interface on the surrounding environment (*26*). Although structural changes of the interface induced by the electron beam (e-beam) have been reported (*26*–*28*), it is unclear whether the intrinsic interface changes in reactive environments and whether the catalytic interface can be manipulated with atomic precision during reactions (*29*–*32*).

[1]State Key Laboratory of Silicon Materials and Center of Electron Microscopy, School of Materials Science and Engineering, Zhejiang University, Hangzhou, 310027 China. [2]Interdisciplinary Research Center, Zhangjiang Laboratory, Shanghai Advanced Research Institute, Chinese Academy of Sciences, Shanghai, 201210 China. [3]Key Laboratory of Interfacial Physics and Technology, Shanghai Institute of Applied Physics, Chinese Academy of Sciences, Shanghai, 201800 China. [4]University of Chinese Academy of Sciences, Beijing, 100049 China. [5]DTU Nanolab, Technical University of Denmark, DK-2800, Kgs. Lyngby, Denmark.
*These authors contributed equally to this work.
†Corresponding author. Email: yongwang@zju.edu.cn (Y.W.); gaoyi@zjlab.org.cn (Y.G.); thwh@dtu.dk (T.W.H.); jabw@dtu.dk (J.B.W.)

In this work, we used environmental transmission electron microscopy (ETEM) to monitor the Au-TiO_2 interface in real time. We observed that Au NPs strongly anchored on TiO_2 (001) surfaces rotate epitaxially during CO oxidation. Theoretical calculations indicate that this rotation was induced by the change of O_2 adsorption coverage at the PI and demonstrate the change of electronic structure related to the activity of the PI before and after the rotation. Furthermore, through control of the interfacial O_2 by adjusting the reaction environment, we achieved in situ manipulation of the active Au-TiO_2 interface.

The experiments were performed in a spherical aberration (Cs)–corrected environmental transmission electron microscope (FEI Titan 80-300 ST) equipped with a heating holder (DENSsolutions Wildfire S3). To avoid the e-beam–induced reconstruction of the interface, as reported in previous in situ studies (*26*–*28*), we used a low e-beam dose (6.45×10^{-1} to 8.73×10^{-1} A/cm^2) and a Gatan OneView complementary metal-oxide semiconductor camera to obtain atomic in situ images of the intrinsic interface structure based on previous results (*26*). We used impregnation and annealing approaches to load Au NPs (diameter: 4 to 8 nm) on TiO_2 nanosheets with dominant (001) surfaces (length: ~30 nm; thickness: ~5 nm) (*33*–*36*). The very strong Au-TiO_2 (001) interaction suppressed the sintering of Au NPs (*37*). A low oxygen pressure (~10^{-3} mbar) was first introduced into the ETEM setup to compensate for the e-beam–induced oxygen loss of TiO_2 nanocrystals. This addition did not change the structures of Au NPs and TiO_2 (001) surfaces, as shown in a recent work (*26*).

A high-resolution TEM (HRTEM) image of the Au-TiO_2 (001) interface structure is shown in Fig. 1A, viewed along the TiO_2 [010] direction. The TiO_2 (-101) lattice spacings measured 0.37 nm, and the Au (111) lattice spacings were 0.24 nm. The interface structure featured atomic steps between TiO_2 (001) and Au (111) crystal planes. The in situ TEM observation showed that this interface structure was stable and did not change after long-term (~20 min) annealing at 500°C. An image (Fig. 1B) of the atomic structure of the Au-TiO_2 interface of the same NP at 6.5 mbar O_2, three orders of magnitude higher than in the low–oxygen pressure environment, shows that the (-101) lattice fringes are still clearly visible for TiO_2. The Au NP exhibited two sets of lattice fringes with ~0.24-nm spacings that we assigned to the Au (-111) and (111) planes.

A perfect epitaxial relationship was found at the interface between the Au NP and the TiO_2 (001) surface—i.e., Au (111) // TiO_2 (001) (Au [01-1] // TiO_2 [010]; also see Fig. 1D)—we refer to this configuration as $S^{//}$. Compared with the interface structure depicted in Fig. 1A, the interface at high oxygen pressure became atomically smooth and formed a semicoherent interface. The periodic misfit dislocations can be identified at the interface (Fig. 1B) with an extra Au (-111) plane appearing every for two TiO_2 (-101) planes. The different interface structures observed at different oxygen pressures indicate that the Au-TiO_2 nanocatalyst changed its interface structure with changing O_2 pressure.

To mimic the reaction condition of CO oxidation, CO was injected into the system, and the O_2 level was adjusted such that the ratio of O_2 volume to CO volume was 1 to 2 ($V_{O_2} : V_{CO} = 1 : 2$), with a total pressure of 4.4 mbar. The HRTEM image of the Au-TiO_2 interface after exposure to the reaction condition for ~3 min (Fig. 1C) shows that the interface structure changed further in response to the more-reducing environment. We kept the e-beam off between collecting the images in Fig. 1, B and C, thus excluding any e-beam effect on the interfacial changes. The disappearance of two-dimensional (2D) Au NP lattice fringes shows that the [01-1] zone axis of the Au NP was no longer parallel to the direction of observation (TiO_2 [010]). Only 1D

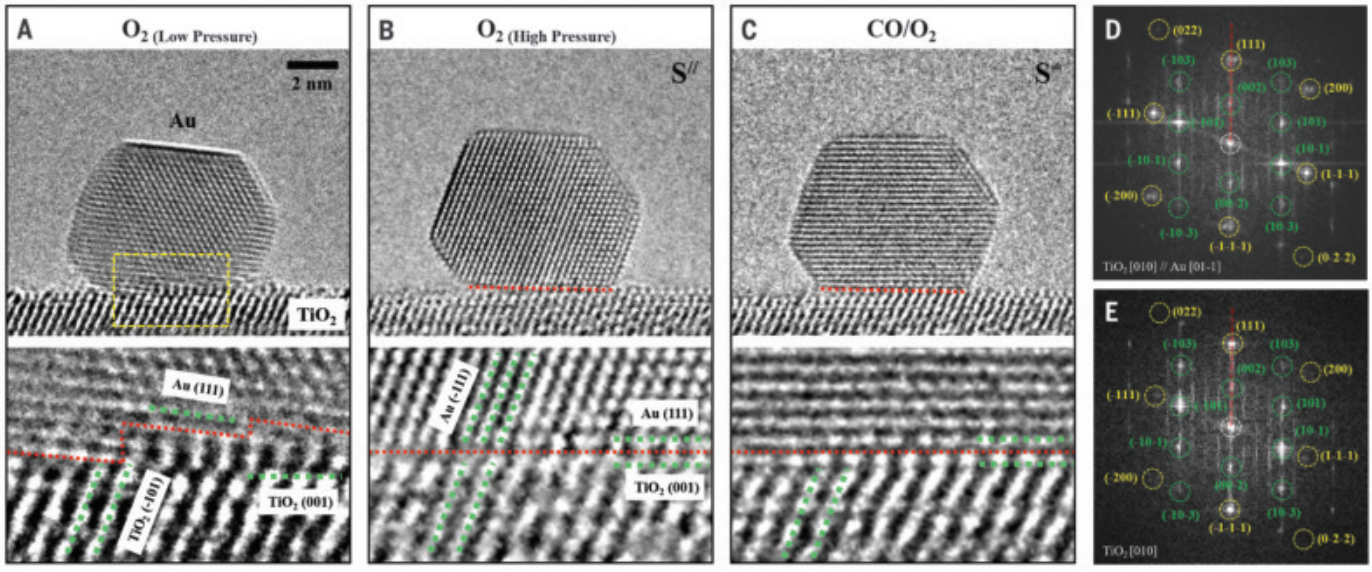

Fig. 1. The tunable Au-TiO_2 (001) interface under different gas environments (side view). The temperature is held at 500°C. (**A** to **C**) (Top) Cs-corrected ETEM images of a Au NP supported on a TiO_2 (001) surface in (A) a low-pressure oxygen (10^{-3} mbar) environment, (B) a high-pressure oxygen (6.5 mbar) environment, and (C) a CO oxidation (total pressure: 4.4 mbar, $V_{O_2} : V_{CO} = 1 : 2$) environment. (Bottom) Corresponding enlarged images of the Au-TiO_2 interfaces [marked by the yellow rectangle in (A)]. Red and green dotted lines indicate the Au-TiO_2 interface and facet, respectively. (**D** and **E**) FFT patterns of the HRTEM images of Au-TiO_2 in (B) and (C), respectively. The FFT spots of Au and TiO_2 are labeled by the yellow and green dashed circles, respectively.

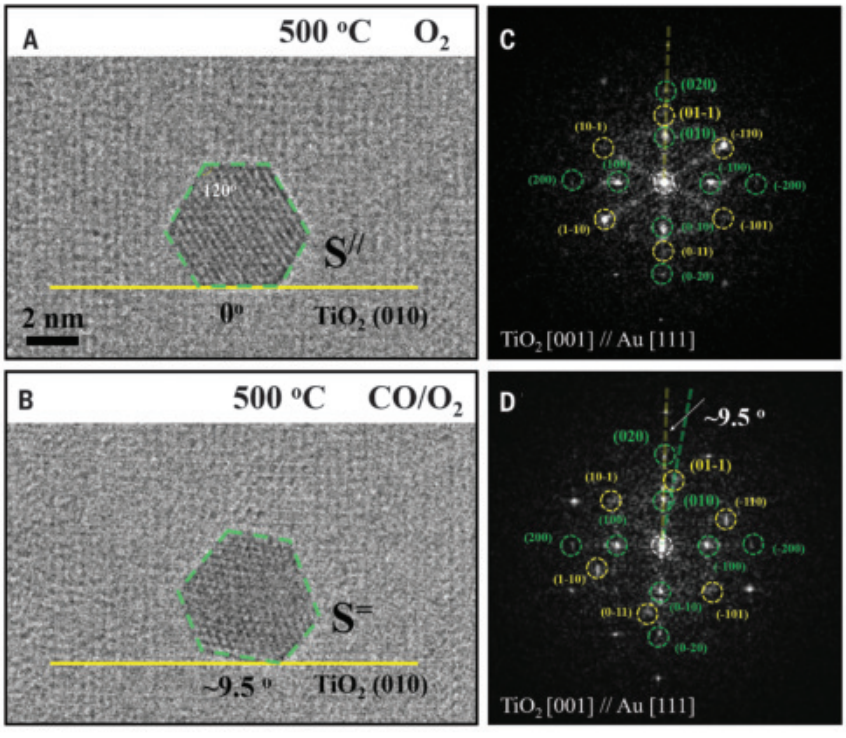

Fig. 2. Rotation of a Au NP on a TiO_2 (001) surface in different environments (top view). (**A** and **B**) ETEM images show the structural evolution of the Au-TiO_2 (001) nanocatalyst from an oxygen environment [(A), 5 mbar] to a reactive environment [(B), 500°C, 5 mbar, $V_{O_2} : V_{CO} = 1 : 2$)]. (**C** and **D**) FFT patterns of the Au-TiO_2 catalyst in (A) and (B), respectively. The FFT spots of Au and TiO_2 are labeled by the yellow and green dashed circles, respectively.

Au (111) lattice fringes could be identified—the interface remained atomically smooth with Au (111) attached to TiO_2 (001)—this configuration is referred to as $S^{=}$.

Because the lattice fringes of the whole Au NP (as opposed to only part of it) changed in our observation, we can exclude the possibility that this behavior is induced by surface reconstructions of the Au NP. Note that (i) the TiO_2 crystal lattice showed negligible changes in Fig. 1B relative to Fig. 1C, so the TiO_2 substrate remained immobile during the reaction process (Fig. 1, B and C), and (ii) the Au (111) planes remained parallel to the TiO_2 (001) surface during the rotation (Fig. 1, B to E). Thus, we conclude that from $S^{//}$ to $S^{=}$, the Au NP rotated along the axis (Au [111]) perpendicular to the TiO_2 (001) surface (i.e., epitaxial rotation), consistent with the findings of the top-view experiments (see below in Fig. 2). For comparison, if the Au NP rolls along another axis, the Au (111) planes will tilt at an angle to the TiO_2 (001) surface, as demonstrated in the schematic in fig. S1. All of the results described above support an epitaxial rotation of a Au NP on a TiO_2 surface, induced by environmental change, which suggests that the atomic configuration of the Au-TiO_2 interface could be manipulated by controlling external environments.

The top-view observations were obtained to help quantify the rotation angle. Figure 2 shows top-view TEM images of another Au NP

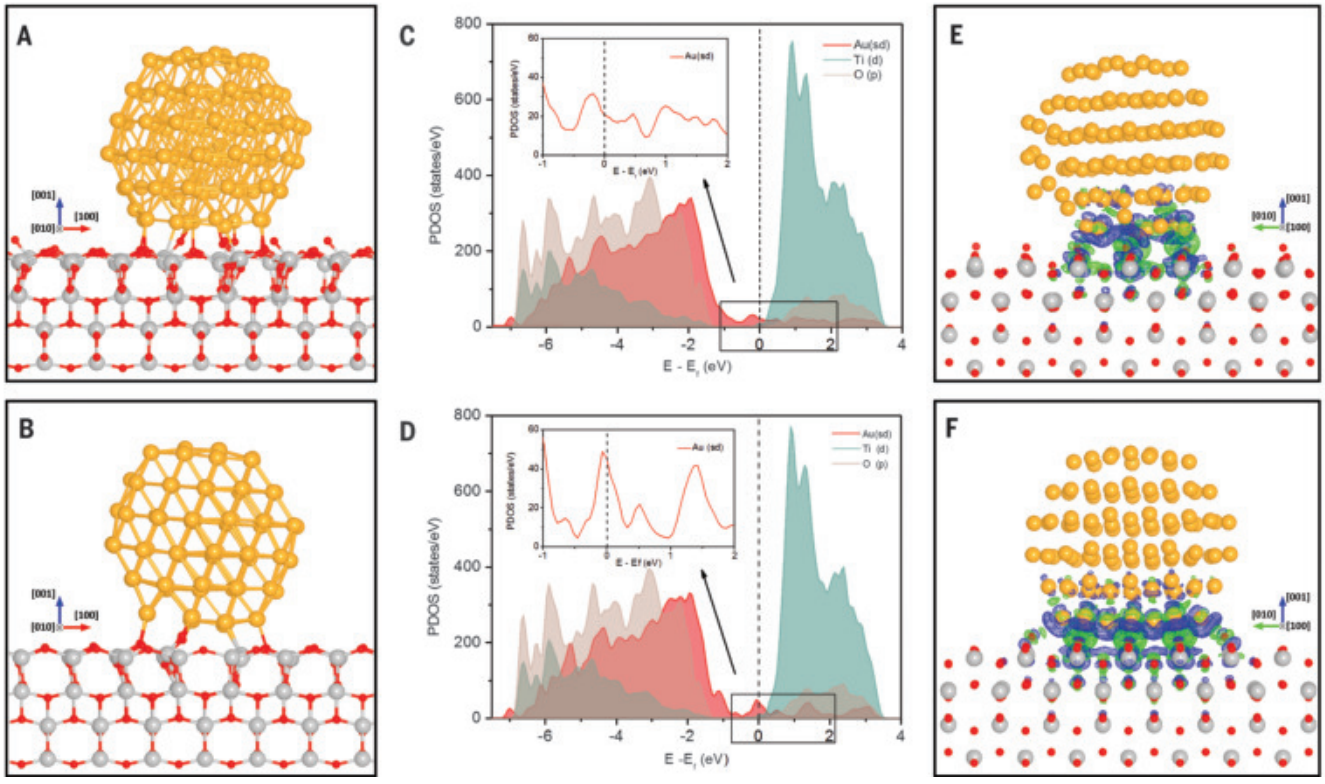

Fig. 3. Electronic structure analysis of the supported Au_{116} cluster with $S^{=}$ and $S^{//}$ configurations. (**A** and **B**) Side view of the theoretically identified $S^{//}$ and $S^{=}$ configurations of Au_{116}/TiO_2 (001). (**C** and **D**) Density of states of the supported Au_{116} cluster. PDOS, projected density of states; E, energy; E_f, Fermi energy. (**E** and **F**) 3D charge-density difference of the supported Au clusters with an isosurface value of 0.002 e/bohr^3. Green, gaining electrons; blue, losing electrons. Images in (A), (C), and (E) are $S^{=}$ configurations; those in (B), (D), and (F) are $S^{//}$ configurations.

located on a TiO_2 nanosheet. To reduce the contrast interference of the overlapping Au and TiO_2, the sample was slightly tilted off the zone axis of TiO_2 [001]. The (100) and (010) lattice fringes of TiO_2 could still be identified (yellow lines indicate (010) planes in Fig. 2). The projection of the Au NP was approximately hexagonal with the ~120° interior angles, which indicates that the observation direction was very close to the Au [111] zone axis. The fast Fourier transform (FFT) pattern in Fig. 2C verified that the epitaxial relationship was consistent with that of the side-view result {Au [111] // TiO_2 [001] and Au (01-1) // TiO_2 (010)}, although some spots of Au were less bright owing to the slightly tilted sample and the TiO_2 substrate interference. The hexagonal Au projection could serve as a very good reference for identifying the in-plane rotation. At 500°C under 5 mbar O_2 pressure, a hexagonal side was parallel to the TiO_2 (010) lattice fringes ($S^{//}$; Fig. 2A). At the same temperature, with the addition of CO, the hexagonal Au NP rotated, and the hexagonal side was no longer parallel to the TiO_2 (010) lattice fringes ($S^{=}$; Fig. 2B). The measured rotation angle was ~9.5°, quantified by comparison of Fig. 2B with Fig. 2A and confirmed by the FFT pattern in Fig. 2D.

Density functional theory (DFT) calculations were performed to obtain insight into rotation behavior in different environments. A truncated octahedral cluster (Au_{116}) was used as a model for the face-centered-cubic Au NP. The gold cluster was deposited on a TiO_2 slab, and the contact interface is TiO_2 (001) and Au (111), on the basis of ETEM observations. The $S^{//}$ was first modeled as a reference (Fig. 3B), according to the featured 2D crystal lattice of the Au cluster viewed along the TiO_2 [010] direction (Fig. 1B). A sequence of test configurations was set up by the clockwise and counterclockwise rotation of the reference Au cluster at small angles (fig. S2). The energy calculation results showed that without O_2 adsorption, $S^{//}$ became energetically unfavorable, 0.3 eV less stable than the most-stable configuration. The Au NP of the most-stable one (Figs. 3A and 1C) has 1D lattice fringes and was identified as the $S^{=}$ observed in our experiments. The rotation angle between this configuration and the $S^{//}$ was ~8° (fig. S2), which is near that of the experimental measurements (~9.5°; Fig. 2, C and D).

The effect of O_2 adsorption was investigated by calculating its adsorption coverage (θ) at the PI of modeled $S^{//}$ and $S^{=}$, respectively, by combining the DFT-calculated adsorption energy (E_{ads}) and the Fowler-Guggenheim adsorption isotherm (details in the supplementary materials). Under the experimental condition (500°C, 5 mbar O_2), O_2 barely adsorbed at the PI of $S^{=}$ ($\theta_{S^{=}} = 0.08$), whereas $\theta_{S^{//}} = 0.31$. The total O_2 adsorption energies at the PI of $S^{//}$ and $S^{=}$ are −4.42 and −0.77 eV, respectively, which caused $S^{//}$ to be 3.35 eV more stable than $S^{=}$ in such a condition. Similar results were obtained using a truncated-octahedral Au_{79} cluster as well (supplementary materials). When CO molecules were introduced, they consumed the O_2 at the interface (*38*). Direct effects of CO adsorption on the rotation could be excluded because CO does not prefer the perimeter site (*39*), but CO adsorbed on the Au NP could easily react with the O_2 at the PI to form CO_2 (fig. S6) (*39*, *40*). As the coverage of interfacial O_2 molecules decreased, the stability of $S^{//}$ decreased and the Au NP rotated to $S^{=}$ (see Figs. 1 and 2).

The density of states of the two configurations (Fig. 3, C and D) showed that occupied orbitals of Au upshifted toward the Fermi level from Au_{116}-$S^{=}$ to Au_{116}-$S^{//}$, so Au_{116}-$S^{//}$ would lose electrons more readily than Au_{116}-$S^{=}$ and would bond more strongly with O_2. Charge-density difference calculations also showed that the interfacial Au atoms of Au_{116}-$S^{//}$ lost

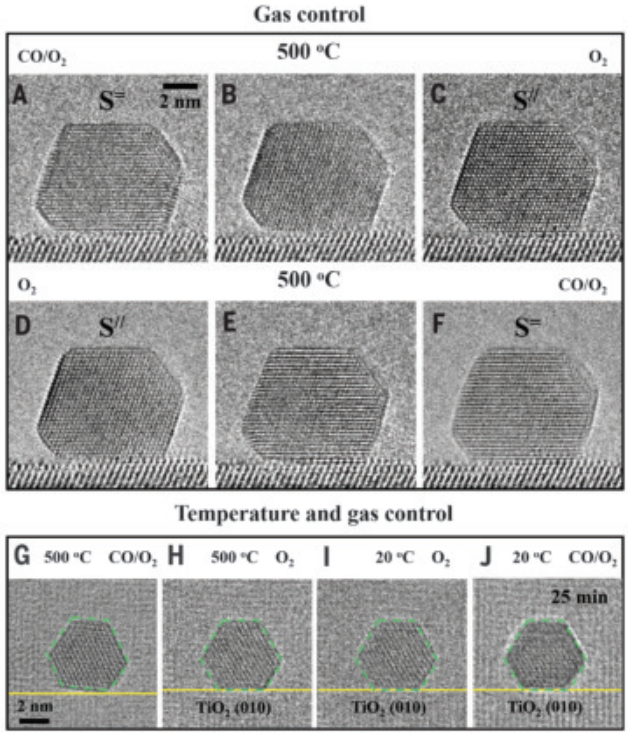

Fig. 4. Manipulating Au-TiO_2 (001) interface configurations through environment-dependent rotation. (**A** to **C**) Side-view ETEM images show the structural evolution of the Au-TiO_2 (001) nanocatalyst [(A) and (C); (B) is the snapshot between (A) and (C)] from a reactive environment [(A), total pressure: 4.4 mbar, $V_{O_2} : V_{CO} = 1 : 2$)] to an oxygen environment [(C), 1 mbar]. (**D** to **F**) Side-view ETEM images show the structural evolution of the Au-TiO_2 (001) nanocatalyst [(D) and (F); (E) is the snapshot between (D) and (F)] from an oxygen environment [(D), 4 mbar] to a reactive environment [(F), 5 mbar, $V_{O_2} : V_{CO} = 1 : 3$)]. The temperature is held at 500°C. (**G** to **J**) Top-view ETEM images show the structural evolution of the Au-TiO_2 (001) nanocatalyst under different temperatures. Images in (G) and (H) were acquired at 500°C [(G), reactive environment, 5 mbar, ($V_{O_2} : V_{CO} = 1 : 2$); (H), oxygen environment, 5 mbar]; images in (I) and (J) were acquired at 20°C [(I), oxygen environment, 5 mbar; (J), reactive environment, 5 mbar, $V_{O_2} : V_{CO} = 1 : 2$)]. The image in (J) was captured after 25 min of exposure to a reactive environment.

more electrons than those of Au_{116}-$S^{=}$ (enlarged blue region in Fig. 3, E and F). The Bader charge calculations also showed that the number of Au^{+} ions with larger positive charges (>0.1*e*, where *e* is the elementary charge) at the interface increased from four ($S^{=}$) to nine ($S^{//}$). Previous studies have shown that the Au^{+} sites can help the adsorption and activation of O_2 at the PI (*40*), which explains why $S^{//}$ can adsorb more O_2 and also indicates that enhanced catalytic activity could be realized by tuning PI with $S^{//}$.

The discovery of NP rotation showed that the structure of an active interface could be controlled during catalytic reactions. As illustrated in Figs. 1 and 2, tuning could be carried out by changing the reactive gas environments. To further confirm the tunability, we periodically stopped injecting CO during the CO oxidation reaction. Notably, when we stopped injecting CO and reverted to an O_2 environment (1 mbar; the image in Fig. 4A was acquired a few minutes after that in Fig. 1C), a reverse change from $S^{=}$ to $S^{//}$ was observed (Fig. 4, A to C). When the O_2 pressure changed from 1 mbar (Fig. 4C) to 4 mbar, the interface structure showed no notable change (Fig. 4D). In Fig. 4, D to F, we reintroduced CO, and rotation from $S^{//}$ to $S^{=}$ was observed again (the intermediate stages during the rotations are presented as Fig. 4, B and E, respectively). A typical rotation process can be seen in movie S1, and more cases are shown in figs. S7 to S10. These results show the reversibility of the dynamic response of the Au-TiO_2 (001) interface to the external environment at high temperature.

To exploit the promoted activity of the $S^{//}$ interface, it would be necessary to fix the interfacial configuration in the application. Additional top-view observations showed that the rotation of the Au NP in CO and O_2 reactive environments was temperature dependent. Unlike the reversible rotation behavior at 500°C (Fig. 4, G and H; images acquired after that in Fig. 2B), the rotation of Au NP caused by the gas environment change could be frozen by cooling to 20°C. When the Au NP was cooled from 500° to 20°C (Fig. 4, H to I) in oxygen, the $S^{//}$ state was preserved. At 20°C, CO injection did not induce rotation of the Au NP, and the $S^{//}$ state remained unchanged during the 25-min observation (Fig. 4J) in CO and O_2 reactive environments. These results indicate that the $S^{//}$ configuration is fixed during low-temperature CO oxidation. After raising the temperature to 500°C, the dynamic change between $S^{//}$ and $S^{=}$ was observed again. Thus, the combination of gas control and temperature control enabled us to achieve interface tunability at the atomic level. These results indicate various approaches toward in situ control, which may lead to the design of distinctive catalysts.

REFERENCES AND NOTES

1. A. Corma, P. Serna, *Science* **313**, 332–334 (2006).
2. G. J. Hutchings, *J. Catal.* **96**, 292–295 (1985).
3. P. Munnik, P. E. de Jongh, K. P. de Jong, *Chem. Rev.* **115**, 6687–6718 (2015).
4. M. Haruta, *J. Catal.* **115**, 301–309 (1989).
5. A. S. K. Hashmi, G. J. Hutchings, *Angew. Chem. Int. Ed.* **45**, 7896–7936 (2006).
6. D. A. Panayotov, A. I. Frenkel, J. R. Morris, *ACS Energy Lett.* **2**, 1223–1231 (2017).
7. M. Valden, X. Lai, D. W. Goodman, *Science* **281**, 1647–1650 (1998).
8. A. A. Herzing, C. J. Kiely, A. F. Carley, P. Landon, G. J. Hutchings, *Science* **321**, 1331–1335 (2008).
9. B. Hvolbæk *et al*., *Nano Today* **2**, 14–18 (2007).
10. W. Karim *et al*., *Nature* **541**, 68–71 (2017).
11. W. Gao, Z. D. Hood, M. Chi, *Acc. Chem. Res.* **50**, 787–795 (2017).
12. Y. Suchorski *et al*., *Nat. Mater.* **17**, 519–522 (2018).
13. D. Widmann, R. J. Behm, *Acc. Chem. Res.* **47**, 740–749 (2014).
14. I. X. Green, W. Tang, M. Neurock, J. T. Yates Jr.., *Science* **333**, 736–739 (2011).
15. T. Fujitani, I. Nakamura, *Angew. Chem. Int. Ed.* **50**, 10144–10147 (2011).
16. M. Haruta, *CATTech* **6**, 102–115 (2002).
17. E. de Smit *et al*., *Nature* **456**, 222–225 (2008).
18. P. L. Hansen *et al*., *Science* **295**, 2053–2055 (2002).
19. K. F. Kalz *et al*., *ChemCatChem* **9**, 17–29 (2017).
20. T. Uchiyama *et al*., *Angew. Chem. Int. Ed.* **50**, 10157–10160 (2011).
21. S. B. Vendelbo *et al*., *Nat. Mater.* **13**, 884–890 (2014).
22. H. Yoshida *et al*., *Science* **335**, 317–319 (2012).
23. W. Yuan *et al*., *Science* **367**, 428–430 (2020).
24. W. Yuan *et al*., *Nano Lett.* **16**, 132–137 (2016).
25. B. Zugic *et al*., *Nat. Mater.* **16**, 558–564 (2017).
26. Y. Kuwauchi, H. Yoshida, T. Akita, M. Haruta, S. Takeda, *Angew. Chem. Int. Ed.* **51**, 7729–7733 (2012).
27. P. Liu *et al*., *Nanoscale* **11**, 11885–11891 (2019).
28. Y. Kuwauchi *et al*., *Nano Lett.* **13**, 3073–3077 (2013).
29. T. Akita, M. Kohyama, M. Haruta, *Acc. Chem. Res.* **46**, 1773–1782 (2013).
30. J. J. Liu, *ChemCatChem* **3**, 934–948 (2011).
31. D. S. Su, B. Zhang, R. Schlögl, *Chem. Rev.* **115**, 2818–2882 (2015).
32. F. F. Tao, P. A. Crozier, *Chem. Rev.* **116**, 3487–3539 (2016).
33. H. G. Yang *et al*., *Nature* **453**, 638–641 (2008).
34. X. Han, Q. Kuang, M. Jin, Z. Xie, L. Zheng, *J. Am. Chem. Soc.* **131**, 3152–3153 (2009).
35. N. Zheng, J. Fan, G. D. Stucky, *J. Am. Chem. Soc.* **128**, 6550–6551 (2006).
36. G. Li *et al*., *Prog. Nat. Sci-Mater.* **31**, 1–13 (2021).
37. W. Yuan *et al*., *Angew. Chem. Int. Ed.* **57**, 16827–16831 (2018).
38. Y. Chen, P. Crawford, P. Hu, *Catal. Lett.* **119**, 21–28 (2007).
39. Y. Gao, N. Shao, Y. Pei, Z. Chen, X. C. Zeng, *ACS Nano* **5**, 7818–7829 (2011).
40. Z.-P. Liu, X.-Q. Gong, J. Kohanoff, C. Sanchez, P. Hu, *Phys. Rev. Lett.* **91**, 266102 (2003).

ACKNOWLEDGMENTS

Funding: We acknowledge the financial support of the National Natural Science Foundation of China (52025011, 92045301, 91645103, 51390474, 11574340, 21773287, 51801182, 11604357, 51872260, and 51971202), the Zhejiang Provincial Natural Science Foundation (LD19B030001), and the Fundamental Research Funds for the Zhejiang Provincial Universities (2019XZZX003-01). B.Z. thanks the Youth Innovation Promotion Association of CAS. The computations were performed at the National Supercomputer Center in Guangzhou (NSCC-GZ) and in Shanghai. W.Y. thanks the China Postdoctoral Science Foundation (2020T130578 and 2020M671714). **Author contributions:** Y.W. initiated the project.

Y.W., Y.G., and J.B.W. supervised the project. W.Y., K.F., and T.W.H. conducted the ETEM experiments. K.F. and Y.O. prepared the samples. B.Z. and X.-Y.L. performed the calculations. H.Y. and Z.Z. participated in the analysis and discussion. **Competing interests:** The authors declare no competing interests. **Data and materials availability:** All data needed to evaluate the conclusions in the paper are present in the paper, the supplementary materials, or the Cambridge Crystallographic Data Centre (deposition numbers: 2044905 to 2044938).

SUPPLEMENTARY MATERIALS

science.sciencemag.org/content/371/6528/517/suppl/DC1
Materials and Methods
Supplementary Text
Figs. S1 to S10
Table S1
References (*41*–*48*)
Movie S1

17 August 2020; accepted 4 January 2021
10.1126/science.abe3558

VACCINES

MAIT cell activation augments adenovirus vector vaccine immunogenicity

Nicholas M. Provine[1]*, Ali Amini[1], Lucy C. Garner[1], Alexandra J. Spencer[2], Christina Dold[3], Claire Hutchings[4], Laura Silva Reyes[3], Michael E. B. FitzPatrick[1], Senthil Chinnakannan[4], Blanche Oguti[3], Meriel Raymond[3], Marta Ulaszewska[2], Fulvia Troise[5,6], Hannah Sharpe[2], Sophie B. Morgan[7], Timothy S. C. Hinks[7], Teresa Lambe[2], Stefania Capone[8], Antonella Folgori[8], Eleanor Barnes[1,2,4], Christine S. Rollier[3], Andrew J. Pollard[3], Paul Klenerman[1,4]*

Mucosal-associated invariant T (MAIT) cells are innate sensors of viruses and can augment early immune responses and contribute to protection. We hypothesized that MAIT cells may have inherent adjuvant activity in vaccine platforms that use replication-incompetent adenovirus vectors. In mice and humans, ChAdOx1 (chimpanzee adenovirus Ox1) immunization robustly activated MAIT cells. Activation required plasmacytoid dendritic cell (pDC)–derived interferon (IFN)–α and monocyte-derived interleukin-18. IFN-α–induced, monocyte-derived tumor necrosis factor was also identified as a key secondary signal. All three cytokines were required in vitro and in vivo. Activation of MAIT cells positively correlated with vaccine-induced T cell responses in human volunteers and MAIT cell–deficient mice displayed impaired CD8$^+$ T cell responses to multiple vaccine-encoded antigens. Thus, MAIT cells contribute to the immunogenicity of adenovirus vectors, with implications for vaccine design.

Mucosal-associated invariant T (MAIT) cells are unconventional T cells that recognize microbe-derived metabolites of vitamin B2 biosynthesis such as 5-(2-oxopropylideneamino)-6-D-ribitylaminouracil (5-OP-RU) (*1*). However, MAIT cells can also be activated by cytokines and thereby respond to viruses, which do not synthesize vitamin B2. In vivo, MAIT cells respond to influenza virus to amplify early local immune responses and protect against lethal infection (*2*–*4*). We hypothesized that the ability of MAIT cells to augment early immune responses may play a key role in viral vector vaccine immunogenicity. Replication-incompetent adenovirus (Ad) vectors are highly potent vaccine platforms for many human diseases (*5*). They have recently been licensed for use against the Ebola virus (*6*) and show promise for severe acute respiratory syndrome coronavirus 2 (SARS-CoV-2) infection (*7*, *8*). We sought to determine whether such vectors activate MAIT cells and whether this affects vaccine immunogenicity.

To determine whether MAIT cells respond to Ad vectors, we stimulated human peripheral blood mononuclear cells (PBMCs) with Ad5 and chimpanzee adenovirus Ox1 (ChAdOx1), which are leading SARS-CoV-2 candidate vaccines (*7*, *8*). ChAdOx1 induced dose-dependent up-regulation of CD69, granzyme B, and interferon (IFN)–γ by MAIT cells (Fig. 1, A to C, and fig. S1, A to D), whereas Ad5 only weakly activated MAIT cells. This activation was confirmed using the MR1–5-OP-RU tetramer to identify MAIT cells (fig. S1E).

Species C–derived Ad vectors have been shown to poorly stimulate innate immune responses as compared with non–species C vectors (*9*–*11*). We tested the relative ability of three species C vectors (Ad5, Ad6, and ChAdN13) and five non–species C vectors (Ad24, Ad35, ChAd63, ChAd68, and ChAdOx1) (fig. S1F) to activate MAIT cells. After stimulation, we observed greater average activation by non–species C vectors as compared with species C vectors (Fig. 1, D and E).

We next tested the ability of Ad vectors to activate MAIT cells in vivo. Intramuscular (i.m.) ChAdOx1 immunization of C57BL/6J mice strongly induced up-regulation of CD69 and granzyme B by MAIT cells, whereas Ad5 induced significantly weaker activation (Fig. 1, F and G, and fig. S2, A to C). We also observed significant up-regulation of CD69 on MAIT cells 1 day after immunization of human volunteers with a candidate ChAdOx1 vaccine (Fig. 1H and fig. S3, A to C). Plasma IFN-γ levels markedly increased after vaccination (fig. S3D), as seen in nonhuman primates (*10*). This increase correlated with levels of MAIT cell activation (Fig. 1I).

To investigate the pathways involved, RNA sequencing (RNA-seq) of MAIT cells was performed. Eighty-four genes were significantly up-regulated in human MAIT cells after vaccination (Fig. 2A and data S1). Gene set enrichment analysis (GSEA) (*12*) identified the strong induction of type I IFN, interleukin (IL)–1 family, IL-12 family, and IL-2 family signaling pathways (Fig. 2B). Changes in post-vaccination plasma IFN-α or CCL2, an IFN-regulated chemokine (*13*), strongly correlated with MAIT cell activation (Fig. 2C and fig. S3, D and E). Comparison of genes up-regulated in MAIT cells after human vaccination, vaccination of mice, or in vitro stimulation showed a high degree of overlap. Ninety-eight percent of vaccine–up-regulated genes in humans were up-regulated in at least one of the other two conditions, and 63% were up-regulated in both (Fig. 2D; fig. S4, A and B; and data S2 to S4). GSEA on murine MAIT cells and in vitro–stimulated human MAIT cells identified similar enrichment of these cytokine signaling pathways (fig. S4, C and D).

In vitro inhibition of type I IFN signaling reduced MAIT cell IFN-γ production by >50% (Fig. 2E). Blockade of IL-18 (an IL-1 family member) or IL-12 also reduced MAIT cell activation. By contrast, blockade of IL-15 (an IL-2 family member) had no effect (Fig. 2F and fig. S5A). MAIT cell activation by Ad vectors was independent of T cell receptor signaling (fig. S5B) (*2*, *3*).

To understand the cellular origins of these critical cytokines, we examined the cell populations transduced by Ad5 and ChAdOx1. Monocytes or conventional dendritic cells were the major transduced population by both vectors [>80% of green fluorescent protein–expressing (GFP$^+$) cells] (fig. S5, C to F). ChAdOx1 also efficiently transduced CD123$^+$ plasmacytoid dendritic cells (pDCs), whereas Ad5 did not (fig. S5F) (*11*). Notably, depletion of CD123$^+$ pDCs resulted in a significant (67%) reduction in IFN-γ production by MAIT cells (Fig.

[1]Translational Gastroenterology Unit, Nuffield Department of Medicine, University of Oxford, Oxford, UK. [2]Jenner Institute, University of Oxford, Oxford, UK. [3]Oxford Vaccine Group, Department of Paediatrics, University of Oxford, and the National Institute for Health Research (NIHR) Oxford Biomedical Research Centre, Oxford, UK. [4]Peter Medawar Building for Pathogen Research, University of Oxford, Oxford, UK. [5]Nouscom, SRL, Rome, Italy. [6]Ceinge Biotechnologie Avanzate, Naples, Italy. [7]Respiratory Medicine Unit, Nuffield Department of Medicine – Experimental Medicine, University of Oxford, Oxford, UK. [8]ReiThera, SRL, Rome, Italy.
***Corresponding author. Email: nicholas.provine@ndm.ox.ac.uk (N.M.P.); paul.klenerman@ndm.ox.ac.uk (P.K.)**

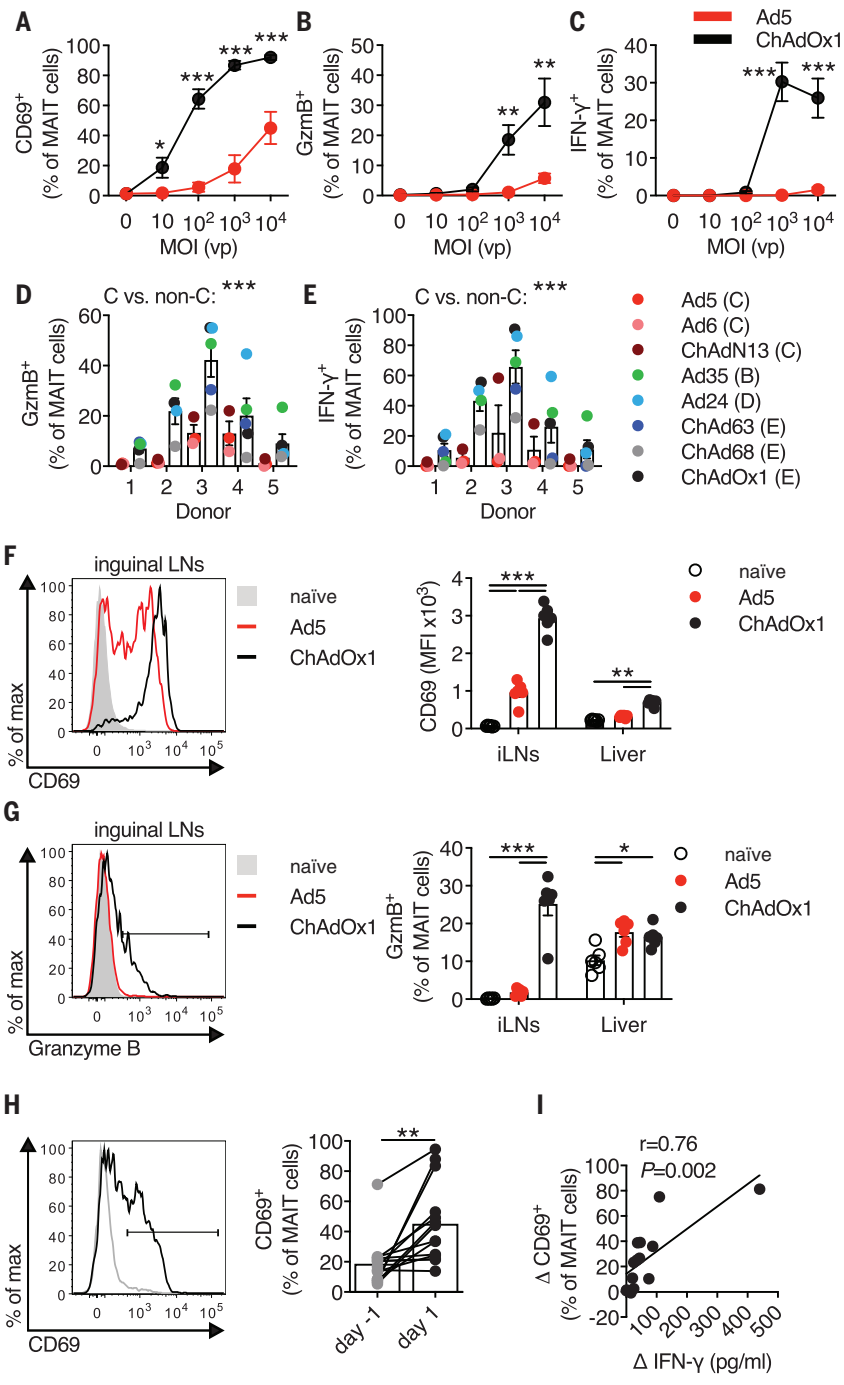

Fig. 1. Activation of human and murine MAIT cells by adenovirus vectors. (**A** to **C**) Human PBMCs (n = 9 donors; four experiments) were stimulated with Ad5-GFP or ChAdOx1-GFP [multiplicity of infection (MOI) = 0 to 10^4 vp (viral particles)]. MAIT cell CD69 (A), granzyme B (GzmB) (B), and IFN-γ (C) expression was measured after 24 hours. (**D** and **E**) Human PBMCs (n = 5 donors; two experiments) were stimulated with the indicated vectors (species in parentheses). MAIT cell GzmB (D) or IFN-γ (E) expression was measured after 24 hours. C, species C; non-C, non–species C. (**F** and **G**) C57BL/6J mice (n = 6 mice per group; representative of two experiments) were immunized intramuscularly (i.m.) with 10^8 IU (infectious units) of Ad5-GFP or ChAdOx1-GFP. Inguinal lymph node (iLN) and liver MAIT cell CD69 (F) and GzmB (G) expression was measured after 24 hours. (**H** and **I**) Healthy human volunteers (n = 14) were immunized with a 5 × 10^{10} vp dose of ChAdOx1 MenB.1. (H) MAIT cell CD69 expression 1 day before and 1 day after immunization. (I) Pearson correlation of change in plasma IFN-γ levels after vaccination with the change in MAIT cell CD69 expression. *P < 0.05; **P < 0.01; ***P < 0.001. Unpaired t test [(A) to (C)], two-way analysis of variance (ANOVA) [(D) and (E)], one-way ANOVA with Sidak correction for multiple comparisons [(F) and (G)], or Wilcoxon rank-sum test (H). Symbols indicate average response [(A) to (C)] or individual mice or volunteers [(D) to (I)]. Mean ± SEM is shown.

2G) and reduced IFN-α levels by >99% after ChAdOx1 stimulation (Fig. 2H).

Depletion of CD14$^+$ monocytes significantly reduced MAIT cell activation after ChAdOx1 stimulation (Fig. 2I and fig. S5G) and abrogated the secretion of IL-18 (Fig. 2J). The cathepsin B–NLRP3 inflammasome pathway (*14*) was the source of IL-18 in response to ChAdOx1 (fig. S6). Thus, pDC-derived IFN-α and monocyte-derived IL-18 play critical roles in activating MAIT cells in response to Ad vectors. Ad5 induced negligible amounts of IFN-α (fig. S7, A and B) (*10*, *11*). Despite transducing monocytes, Ad5 did not induce IL-18 or IL-12p70 (fig. S7, C and D). By contrast, ChAdOx1 induced robust production of IFN-α and IL-18.

Although IFN-α/β and IL-18 together induced production of IFN-γ by MAIT cells in PBMC culture, this was not seen using isolated CD8$^+$ T cells [~75% of human MAIT cells express CD8 (*15*)] (Fig. 3A), despite the induction of CD69 (fig. S8A). Depletion of monocytes reduced MAIT cell IFN-γ production after stimulation with IFN-α and IL-18 (fig. S8B). The addition of monocytes rescued the response (Fig. 3B). Conditioned supernatant or the provision of PBMCs across a transwell significantly rescued MAIT cell IFN-γ production (Fig. 3C and fig. S8C), suggesting the presence of a soluble, monocyte-derived, IFN-α–dependent signal. Unexpectedly, IFN-α–treated monocytes secreted tumor necrosis factor (TNF) (Fig. 3D and fig. S8D). Additionally, TNFR2 signaling pathways were strongly induced in stimulated MAIT cells (fig. S8, E to G). Thus, we investigated whether TNF was the IFN-α–dependent intermediary signal. Addition of TNF or an anti-TNFR2 agonist to isolated CD8$^+$ T cells stimulated with IFN-α and IL-18 enhanced MAIT cell IFN-γ production by >300% (Fig. 3E and fig. S8H). Addition of an anti-TNF antibody (adalimumab) inhibited MAIT cell IFN-γ production in response to IFN-α and IL-18 stimulation or to conditioned supernatant (fig. S8, I and J). TNF blockade using either adalimumab or recombinant TNFR2-Fc fusion protein (etanercept), but not a control antibody (vedolizumab), inhibited IFN-γ production by MAIT cells in response to ChAdOx1 (Fig. 3F). Depletion of monocytes reduced ChAdOx1-induced TNF production by 94% (Fig. 3G). Ad5 induced minimal TNF (fig. S8K), consistent with the poor ability to stimulate IFN-α (fig. S7A).

These data suggest a model in which pDC-derived IFN-α acts directly and indirectly via induction of TNF by monocytes (with IL-18) to activate MAIT cells in response to ChAdOx1 (fig. S9). To test this model in vivo, wild-type (WT) C57BL/6J, *Il18rap*$^{-/-}$, *Ifnar*$^{-/-}$, and *Tnfrsf1a*$^{-/-}$ *Tnfrsf1b*$^{-/-}$ mice were immunized with ChAdOx1. MAIT cells from these animals were then

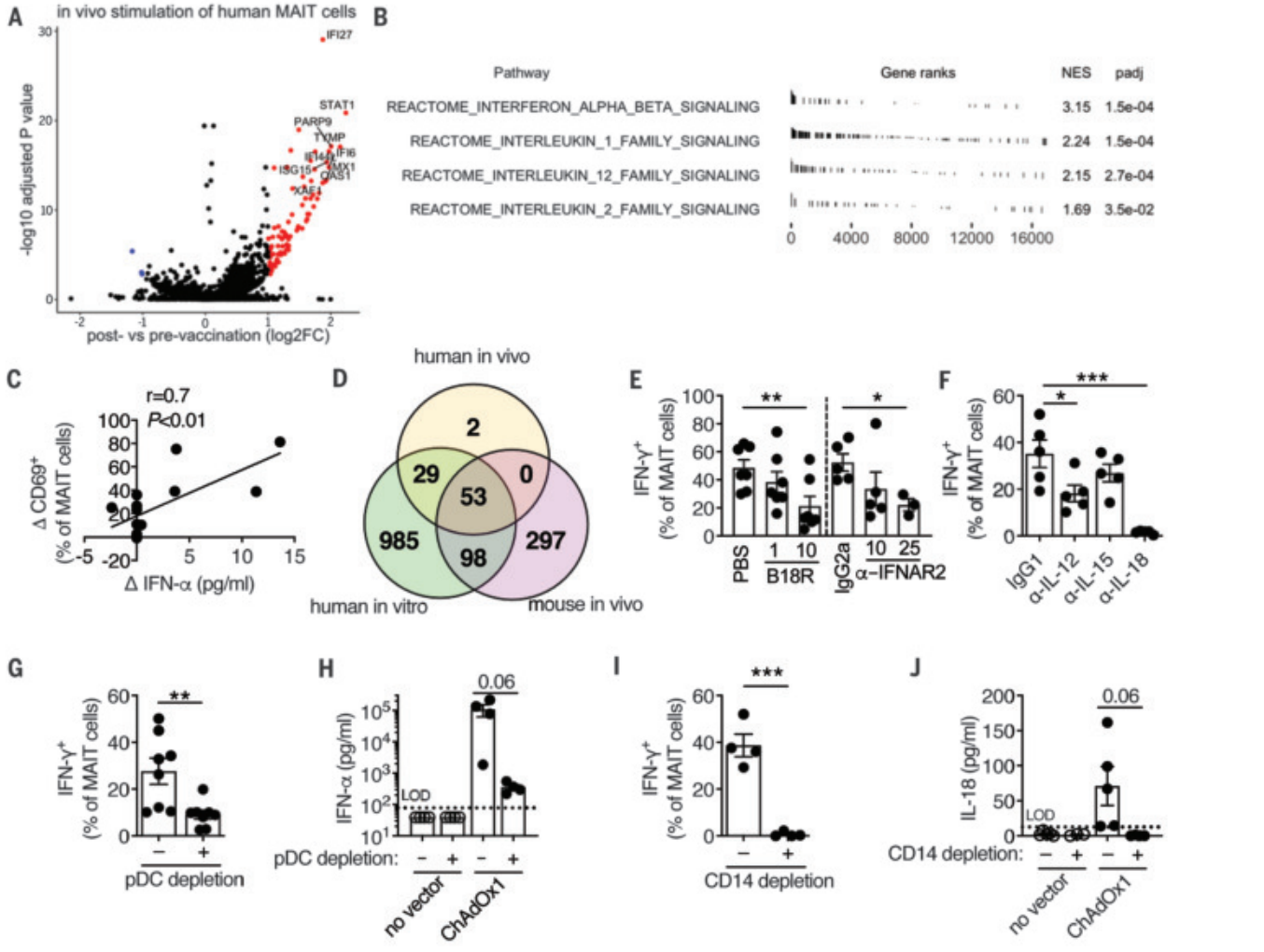

Fig. 2. Activation of MAIT cells by adenovirus vectors requires pDC-derived IFN-α and monocyte-derived IL-18. (**A** and **B**) Gene expression analysis of MAIT cells isolated from the PBMCs of human volunteers 1 day before and 1 day after vaccination with ChAdOx1 MenB.1 (n = 14 vacinees). (A) Volcano plot of differentially expressed genes [$\log_2$ fold change (FC) > 1, adjusted P < 0.05]. The top 10 up-regulated genes are annotated. (B) Selected cytokine signaling pathways from the Reactome database enriched by GSEA. NES, normalized enrichment score. (**C**) Pearson correlation of change in plasma IFN-α level after vaccination with the change in MAIT cell CD69 expression. (**D**) Overlap of genes up-regulated in MAIT cells from ChAdOx1-vaccinated volunteers ("human in vivo"), from human PBMCs stimulated with ChAdOx1 ("human in vitro"), and from the draining inguinal LNs of ChAdOx1-vaccinated mice ("mouse in vivo"). (**E** and **F**) Human PBMCs were stimulated with ChAdOx1-GFP, and the following inhibitors were used: vaccinia virus–derived type I IFN antagonist B18R (1 or 10 μg/ml; n = 7 donors; three experiments) or anti-IFNAR2 antibody (10 or 25 μg/ml; n = 5 or 3 donors; two or one experiments, respectively) (E); or anti-IL-12, anti-IL-15, or anti-IL-18 antibodies (10 μg/ml; n = 5 donors; two experiments) (F). MAIT cell IFN-γ expression was measured after 24 hours. PBS, phosphate-buffered saline. (**G** and **H**) PBMCs were depleted of CD123$^+$ pDCs or left untreated and stimulated with ChAdOx1-GFP. MAIT cell IFN-γ expression (n = 8 donors; three experiments) (G) or levels of IFN-α in the cell culture supernatant (n = 4 donors; one experiment) (H) were measured after 24 hours. (**I** and **J**) PBMCs were depleted of CD14$^+$ monocytes or left untreated and stimulated with ChAdOx1-GFP. MAIT cell IFN-γ expression (n = 4 donors; two experiments) (I) or IL-18 levels in the supernatant (n = 4 donors; three experiments) (J) were measured after 24 hours. *P < 0.05; **P < 0.01; ***P < 0.001. Repeated-measures one-way ANOVA with Dunnett correction [(E) and (F)] or unpaired t test [(G) to (J)]. Symbols indicate individual donors. Mean ± SEM is shown.

analyzed by RNA-seq (fig. S10, A and B, and data S5 to S8). Principal components analysis identified a strong gradient of activation, where MAIT cells from *Ifnar*$^{-/-}$ mice were most similar to those from naïve animals, and MAIT cells from *Tnfrsf1a*$^{-/-}$*Tnfrsf1b*$^{-/-}$ and *Il18rap*$^{-/-}$ mice had intermediate transcriptional profiles (Fig. 3, H and I). The effector genes *Cd69* (at both the gene and protein level), *Cxcl10*, *Cxcl11*, *Ccl5*, and *Gzmb* were all regulated along this gradient (fig. S10, C and D). Other genes (such as *Cxcl9*) were only regulated by TNF signaling (fig. S10D). In total, 51% of the genes induced by vaccination were regulated by one or more of these cytokine pathways, and 11% were co-regulated by two or more of these pathways (Fig. 3J and data S9). Thus, TNF, IL-18, and especially type I IFN play a critical role in vivo in Ad vector–induced MAIT cell activation.

Human volunteers showed a significant increase in IFN-γ–producing T cells after ChAdOx1 boosting immunization (Fig. 4A). The degree of expansion positively correlated with MAIT cell activation (Fig. 4B). To determine whether this was a causal relationship, WT and *Mr1*$^{-/-}$ mice, which lack MAIT cells (*16*), were used (fig. S11, A to C). After vaccination with ChAdOx1 expressing an optimized hepatitis C virus (HCV) antigen (*17*), *Mr1*$^{-/-}$ mice had significantly reduced frequencies of HCV-specific CD8$^+$ T cells compared with WT mice (Fig. 4C and fig. S11D). No significant defect in HCV-specific CD4$^+$ T cells was observed (fig. S11E). We also observed defects in the CD8$^+$

T cell responses of *Mr1*$^{-/-}$ mice vaccinated with the candidate SARS-CoV-2 vaccine, ChAdOx1-nCoV-19 (Fig. 4D and fig. S11F) (*7*). WT and *Mr1*$^{-/-}$ mice were then given a homologous ChAd63-ovalbumin (OVA) prime-boost immunization (fig. S11G) (*18*). *Mr1*$^{-/-}$ mice displayed reduced OVA-specific CD8$^+$ T cell responses after both priming and boosting (Fig. 4, E and F). Differences in the microbiome (*19*) or general immunodeficiency of *Mr1*$^{-/-}$ mice did not explain these differences in immunogenicity (fig. S12).

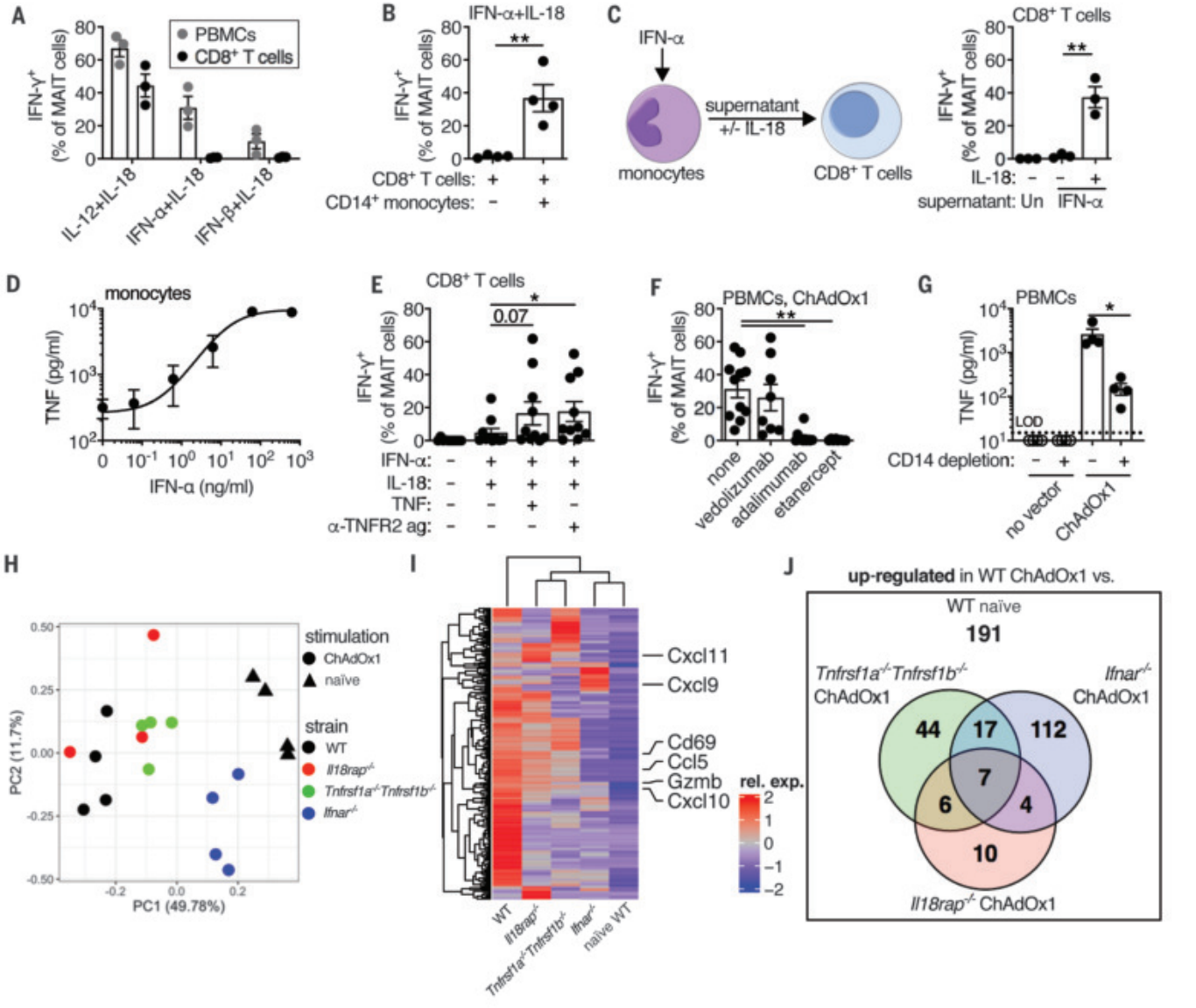

Fig. 3. IFN-α acts directly and indirectly through the induction of TNF to activate MAIT cells. (**A**) Human PBMCs or purified CD8$^+$ T cells (n = 3 donors; one experiment) were stimulated with the indicated cytokines (50 ng/ml). MAIT cell IFN-γ expression was measured after 24 hours. (**B**) Purified CD8$^+$ T cells with or without CD14$^+$ monocytes (n = 4 donors; one experiment) were stimulated with IFN-α and IL-18 (50 ng/ml). MAIT cell IFN-γ expression was measured after 24 hours. (**C**) Purified monocytes (n = 3 donors; one experiment) were stimulated with IFN-α (50 ng/ml) or left untreated. After 24 hours, supernatants were transferred with or without IL-18 (50 ng/ml) to autologous purified CD8$^+$ T cells. MAIT cell IFN-γ expression was measured after 24 hours. (**D**) TNF production by IFN-α–treated CD14-purified monocytes was measured after 24 hours (n = 3 donors; one experiment). (**E**) Purified CD8$^+$ T cells (n = 10 donors; four experiments) were stimulated with IFN-α and IL-18 with or without TNF (50 ng/ml) or anti-TNFR2 agonist antibody (2.5 μg/ml). MAIT cell IFN-γ expression was measured after 24 hours. (**F**) PBMCs were stimulated with ChAdOx1, and the following inhibitors were added: vedolizumab (anti-α4β7 integrin antibody, n = 8 donors; two experiments), adalimumab (anti-TNF antibody, n = 11 donors; three experiments), or etanercept (TNFR2-Fc fusion protein, n = 8 donors; two experiments) (10 μg/ml). MAIT cell IFN-γ expression was measured after 24 hours. (**G**) PBMCs with or without CD14 depletion were stimulated with ChAdOx1. Concentration of TNF in the supernatant was measured after 24 hours (n = 4 donors; one experiment). (**H** to **J**) C57BL/6J (n = 4), *Il18rap*$^{-/-}$ (n = 3), *Tnfrsf1a*$^{-/-}$*Tnfrsf1b*$^{-/-}$ (n = 4), or *Ifnar*$^{-/-}$ (n = 4) mice were immunized i.m. with 10^8 IU of ChAdOx1-GFP. Naïve C57BL/6J mice (n = 4) were used as a control. After 24 hours, MAIT cells were isolated from the iLNs and sorted for RNA-seq (one experiment). (H) Principal components analysis. (I) Heatmap of the up-regulated differentially expressed genes ($\log_2$ FC > 1, adjusted P < 0.05) between MAIT cells from ChAdOx1-immunized and naïve C57BL/6J mice, with all other groups shown for comparison. (J) Overlap of the genes up-regulated ($\log_2$ FC > 1, adjusted P < 0.05) in MAIT cells from ChAdOx1-immunized and naïve C57BL/6J mice, and the genes up-regulated in MAIT cells from ChAdOx1-immunized C57BL/6J mice as compared to each of the ChAdOx1-immunized knockout strains. *P < 0.05; **P < 0.01. Unpaired t test [(B), (C), and (G)], repeated-measures one-way ANOVA with Dunnett correction [(E) and (F)]. Symbols indicate individual donors. Mean ± SEM is shown.

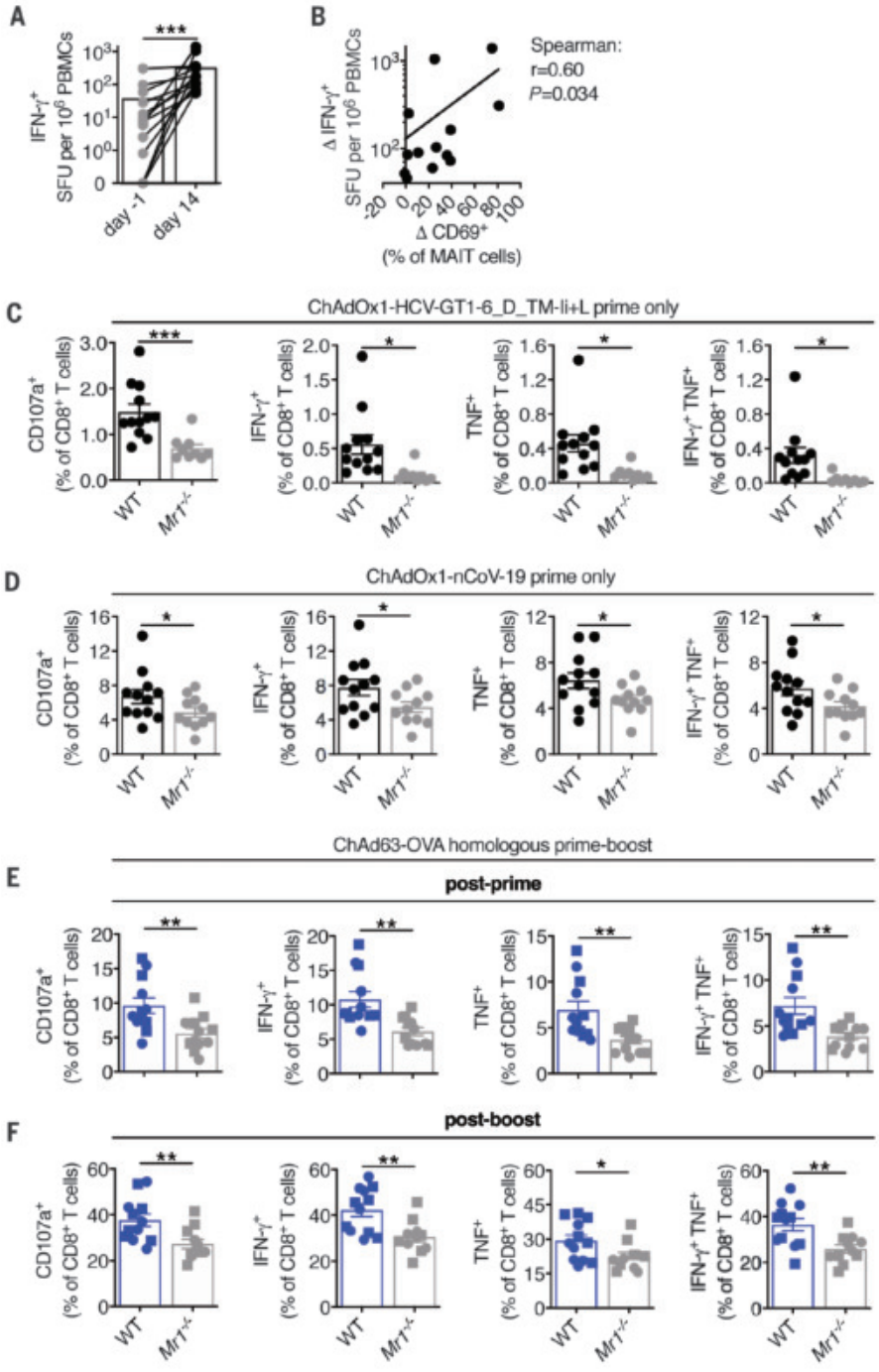

Fig. 4. Impact of MAIT cell deficiency on T cell responses after ChAdOx1 or ChAd63 immunization. (**A**) Frequency of IFN-γ–producing PBMCs measured by peptide enzyme-linked immunospot (ELISPOT) in ChAdOx1 MenB.1 vaccinated volunteers before boost (n = 14) or day 14 after boost (n = 13). SFU, spot forming units. (**B**) Spearman rank correlation analysis of the change in MAIT cell CD69 expression from before boost to day 1 after boost versus the increase in IFN-γ–producing PBMCs from before boost to day 14 after boost. (**C**) C57BL/6J (n = 12) or *Mr1*$^{-/-}$ (n = 9) mice were immunized i.m. with 10^8 IU of ChAdOx1-HCV-GT1-6_D_TM-li+L (two experiments). On day 16, HCV-specific CD107a$^+$, IFN-γ$^+$, TNF$^+$, or IFN-γ$^+$TNF$^+$ CD8$^+$ T cell responses were measured. (**D**) C57BL/6J (n = 12) or *Mr1*$^{-/-}$ (n = 11) mice were immunized i.m. with 10^8 IU of ChAdOx1-nCoV-19 (two experiments). On day 13, SARS-CoV-2 spike-specific CD107a$^+$, IFN-γ$^+$, TNF$^+$, or IFN-γ$^+$TNF$^+$ CD8$^+$ T cell responses were measured. (**E** and **F**) C57BL/6J (n = 12) or *Mr1*$^{-/-}$ (n = 12, n = 11 after boost) were primed i.m. with 10^7 IU of ChAd63-OVA and boosted intravenously on day 28 with 10^8 IU (squares) or 10^9 IU (circles) of ChAd63-OVA. SIINFEKL-specific CD107a$^+$, IFN-γ$^+$, TNF$^+$, or IFN-γ$^+$TNF$^+$ CD8$^+$ T cell responses were measured either 3 weeks after prime (E) or 3 weeks after boost (F). *P < 0.05; **P < 0.01; ***P < 0.001. Wilcoxon rank-sum test (A) or two-way ANOVA [(C) to (F)]. Symbols indicate individual volunteers or mice. Mean ± SEM is shown.

MAIT cells can sense the diversity of the Ad vector–induced innate immune activation landscape (e.g., IFN-α, TNF, IL-18), integrating these signals to augment vaccine-induced CD8$^+$ T cell immunity. The blend of signals required to maximally trigger MAIT cells described here includes a critical pathway via type I IFN–dependent TNF release, relies on cross-talk between two distinct populations of transduced cells, and varies between adenovirus serotypes. Our data, coupled with studies in the lung (*4*, *20*, *21*), support a model that places MAIT cells in a critical bridging position between innate and adaptive immunity. The mechanism by which MAIT cell activation promotes antigen-specific CD8$^+$ T cell responses remains to be defined. However, local production of chemokine CXC10 represents a promising candidate as it can promote CD8$^+$ T cell priming (*22*).

It is notable that the activation of MAIT cells is tightly linked to the immunogenicity of adenovirus vectors. This technology has emerged as a potent platform for T cell immunogenicity in clinical trials for HIV (*23*) and as vaccines for emerging viruses such as Ebola (*6*) and SARS-CoV-2 (*7*, *8*). This knowledge can be harnessed to improve the design of these vaccines against major pathogens and cancers.

REFERENCES AND NOTES

1. N. M. Provine, P. Klenerman, *Annu. Rev. Immunol.* **38**, 203–228 (2020).
2. L. Loh *et al.*, *Proc. Natl. Acad. Sci. U.S.A.* **113**, 10133–10138 (2016).
3. B. van Wilgenburg *et al.*, *Nat. Commun.* **7**, 11653 (2016).
4. B. van Wilgenburg *et al.*, *Nat. Commun.* **9**, 4706 (2018).
5. A. Vitelli *et al.*, *Expert Rev. Vaccines* **16**, 1241–1252 (2017).
6. European Medicines Agency, New vaccine for prevention of Ebola virus disease recommended for approval in the

European Union, press release (29 May 2020); www.ema.europa.eu/en/documents/press-release/new-vaccine-prevention-ebola-virus-disease-recommended-approval-european-union_en.pdf.
7. P. M. Folegatti *et al.*, *Lancet* **396**, 467–478 (2020).
8. F.-C. Zhu *et al.*, *Lancet* **396**, 479–488 (2020).
9. K. M. Quinn *et al.*, *J. Clin. Invest.* **125**, 1129–1146 (2015).
10. J. E. Teigler, M. J. Iampietro, D. H. Barouch, *J. Virol.* **86**, 9590–9598 (2012).
11. M. J. Johnson *et al.*, *J. Immunol.* **188**, 6109–6118 (2012).
12. A. Subramanian *et al.*, *Proc. Natl. Acad. Sci. U.S.A.* **102**, 15545–15550 (2005).
13. S. A. Samarajiwa, S. Forster, K. Auchettl, P. J. Hertzog, *Nucleic Acids Res.* **37** (suppl. 1), D852–D857 (2009).
14. V. Hornung *et al.*, *Nat. Immunol.* **9**, 847–856 (2008).
15. L. C. Garner, P. Klenerman, N. M. Provine, *Front. Immunol.* **9**, 1478 (2018).
16. E. Treiner *et al.*, *Nature* **422**, 164–169 (2003).
17. T. Donnison *et al.*, *Vaccine* **38**, 5036–5048 (2020).
18. A. Gola *et al.*, *Sci. Transl. Med.* **10**, eaap9128 (2018).
19. A. Varelias *et al.*, *J. Clin. Invest.* **128**, 1919–1936 (2018).
20. A. Meierovics, W.-J. C. Yankelevich, S. C. Cowley, *Proc. Natl. Acad. Sci. U.S.A.* **110**, E3119–E3128 (2013).
21. A. I. Meierovics, S. C. Cowley, *J. Exp. Med.* **213**, 2793–2809 (2016).
22. V. Peperzak *et al.*, *J. Immunol.* **191**, 3025–3036 (2013).
23. D. H. Barouch *et al.*, *Lancet* **392**, 232–243 (2018).

ACKNOWLEDGMENTS

We thank H. Ferry and L. Hardy for assistance with cell sorting; S. Slevin, C.-P. Hackstein, and C. Willberg for critical discussions; M. Salio and V. Cerundolo for the *Mr1*$^{-/-}$ mice; J. Rehwinkel for the *Ifnar*$^{-/-}$ mice; M. Esposito, H. Al-Mossawi, L. Ni Lee, and T. Donnison for reagents; the NIH Tetramer Facility for the MR1 tetramers; and all of the volunteers for sample donation and participation in the trial. **Funding:** N.M.P. is supported by an Oxford-UCB Postdoctoral Fellowship. A.A. is supported by a Wellcome Clinical Training Fellowship (216417/Z/19/Z). L.C.G. is supported by a Wellcome PhD Studentship (109028/Z/15/Z). M.E.B.F. is supported by an Oxford-Celgene Doctoral Fellowship. S.B.M. and T.S.C.H. are supported by the Wellcome Trust (211050/Z/18/Z and 211050/Z/18/A). E.B. is supported by the Medical Research Council (STOP-HCV and MR/R014485/1), an NIHR Senior Fellowship, the NIHR Biomedical Research Centre (Oxford), and the UKRI/NIHR through the UK Coronavirus Immunology Consortium (UK-CIC). C.S.R. is supported by the NIHR Biomedical Research Centre and is a Jenner Institute Investigator. A.J.P. is supported by the NIHR Oxford Biomedical Research Centre and is an NIHR Senior Investigator. P.K. is supported by the Wellcome Trust (WT109965MA), the NIHR Biomedical Research Centre (Oxford), the UKRI/NIHR through the UK Coronavirus Immunology Consortium (UK-CIC), and an NIHR Senior Fellowship. The ChAdOx1 MenB.1 clinical trial is funded by the Medical Research Council DPFS (MRM0076931). The views expressed are those of the authors and not necessarily those of the NHS, the NIHR, or the Department of Health. **Author contributions:** N.M.P. and P.K. designed the project. N.M.P., A.J.S., C.D., T.S.C.H., E.B., C.S.R., A.J.P., and P.K. designed the experiments. N.M.P., A.A., L.C.G., A.J.S., C.D., C.H., L.S.R., M.E.B.F., M.U., H.S., and S.B.M. performed the experiments. S.C., B.O., M.R., F.T., T.L., S.C., A.F., E.B., C.S.R., and A.J.P. provided samples and reagents. All authors contributed to the writing and editing of the manuscript. **Competing interests:** C.D., C.S.R., and A.J.P. are named inventors on a patent application in the field of meningococcal vaccines. A.J.P. waives his rights under any patent. P.K. is a named inventor on a patent application in the field of cancer vaccines. **Data and materials availability:** All gene expression data are deposited in the Gene Expression Omnibus under GSE158835. All data are available in the manuscript or the supplementary materials.

SUPPLEMENTARY MATERIALS

science.sciencemag.org/content/371/6528/521/suppl/DC1
Materials and Methods
Figs. S1 to S12
Tables S1 and S2
References (*24*–*44*)
MDAR Reproducibility Checklist
Data S1 to S9

1 May 2019; resubmitted 20 July 2020
Accepted 19 November 2020
10.1126/science.aax8819

GEOLOGY

Early plant organics increased global terrestrial mud deposition through enhanced flocculation

Sarah S. Zeichner[1]*, Justin Nghiem[1], Michael P. Lamb[1], Nina Takashima[1], Jan de Leeuw[1], Vamsi Ganti[2,3], Woodward W. Fischer[1]

An irreversible increase in alluvial mudrock occurred with the Ordovician-Silurian evolution of bryophytes, challenging a paradigm that deep-rooted plants were responsible for this landscape shift. We tested the idea that increased primary production and plant organics promoted aggregation of clay into flocs in rivers and facilitated mud deposition on floodplains. In experiments, we observed that clay readily flocculated for organic and clay concentrations common to modern rivers, yielding settling velocities three orders of magnitude larger than those without organics. Using a transport model, we found that flocculation substantially increased mud deposition, resulting in muddier floodplains. Thus, organic-induced flocculation may have been more critical than deep-rooted plants in the proliferation of muddy floodplains.

The Paleozoic evolution and proliferation of terrestrial plants has been connected with changes in soil and atmospheric chemistry and increased land primary productivity and organic carbon deposition (*1*). Correspondingly, the stratigraphic record contains a major first-order change in the construction of river floodplain deposits (*2*). A recent study quantified an Ordovician-Silurian increase in alluvial mudrock—that is, siliciclastic rock consisting of at least 50% mud-sized particles—which occurred concurrently with the evolution of early plants (Fig. 1A) (*3*). However, these data presented an apparent paradox. One explanation could be that the proliferation of plants led to mud production, yet the sedimentary record contains abundant mudrock throughout Earth's history, albeit in marine paleoenvironments before early Paleozoic time (*4*). Further, this increase in alluvial mudrock predated the evolution of large rooted plants and forests (Fig. 1A) (*3*, *5*). Early plants were small in size (~1 cm tall; inset of Fig. 1A) and lacked the deep rooting (*1*) that was likely necessary for floodplain binding through rooting and flow baffling (*6*). We hypothesized that these plants instead could have increased mudrock prevalence through a molecular mechanism: The rise in terrestrial organic material associated with early plants would drive mud flocculation in rivers and, in consequence, enhance mud settling and deposition on river floodplains. Plant polymers are not uniquely capable of binding sediment—previous work demonstrated the presence of sedimentary structures built by pre-Silurian terrestrial microbiota (*7*). However, the proliferation of early plants dramatically increased the productivity of the land surface and thereby the flux of organic polymers in terrestrial environments—both the polymers produced directly by the plants themselves as well as those generated and further modified by the rich associated microbial communities (*1*, *5*).

Flocculation is the process of binding of individual particles into larger aggregates called "flocs" (Fig. 1B) and is known to promote the deposition of clay and silt (i.e., mud) within estuarine and marine environments (*8*). Flocculation can substantially increase mud settling velocities (*9*), and growing evidence suggests that mud flocculation occurs in modern rivers (*10*) (Fig. 1B). Therefore, an increase in the ability to flocculate fluvial sediment has the potential to cause a major rise in alluvial mud deposition rates.

Flocculation in freshwater is associated with the presence of organics (*9*) because they—particularly polymers—facilitate particle binding interactions (*11*). Laboratory studies found that combinations of primary particles and polymers could lead to variable levels of flocculation (*9*, *12*). However, these studies did not directly measure the effect of polymer-clay combinations on floc settling velocity. Evidence for widespread flocculation in natural rivers came from an analysis of suspended sediment concentration-depth profiles, which showed systematically larger settling velocities compared with theoretical expectations for sediment smaller than 40 μm in diameter (*10*). Thus, flocculation appears to be a primary control on mud settling in modern fluvial environments, but the specific roles of organic matter in driving flocculation in rivers have remained unclear.

We conducted 83 flume experiments with distinct combinations of model organic polymers (xanthan gum and guar gum) and clay minerals (smectite and kaolinite) (inset of Fig. 2A) to quantify the role of organic material in determining mud settling rates in freshwater

[1]Division of Geological and Planetary Sciences, California Institute of Technology, Pasadena, CA, USA. [2]Department of Geography, University of California, Santa Barbara, Santa Barbara, CA, USA. [3]Department of Earth Science, University of California, Santa Barbara, Santa Barbara, CA, USA.
***Corresponding author. Email: szeichner@caltech.edu**

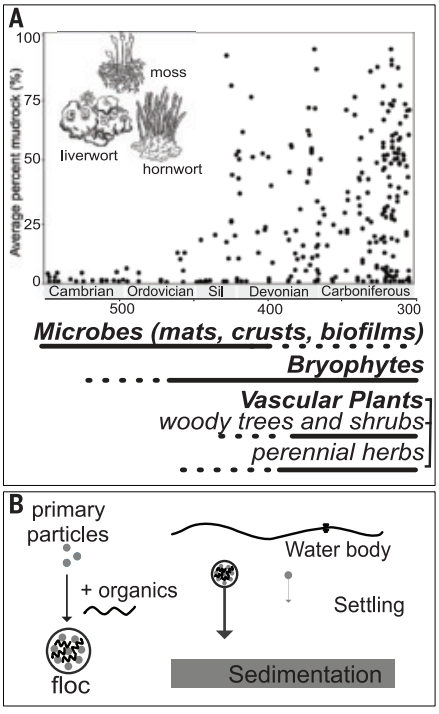

Fig. 1. Mudrock abundance, plant evolution, and flocculation. (**A**) Average percent mudrock for alluvial deposits over time, adapted from (*3*), shown alongside ranges of key evolutionary events in early plant evolution (*1*). The amount of alluvial mudrock increased with proliferation of early diverging plant lineages (e.g., bryophytes, including liverworts, hornworts, and mosses). Solid lines indicate the ranges for landscape occupation of different biological groups derived from the fossil record, whereas dashed lines indicate intervals of lesser occupational importance. Sil, Silurian. (**B**) Organic polymers (black squiggles) can bind primary clay particles (gray dots) together into flocs (black circles), which increases their settling velocities and sedimentation rates. The size of the arrow indicates increased settling velocities driven by larger particle aggregate size upon flocculation.

rivers (*13*). The experiments had constant turbulent Reynolds numbers, volumetric sediment concentrations of ~0.1 g/liter, and low ionic strength, similar to natural rivers (table S1) (*13*). Although these abiotic variables can also affect flocculation, particularly in marine and estuarine settings (*12*), our goal was to isolate the effect of organics on freshwater flocculation. We performed experiments in a fixed-volume stirred-batch reactor within a light-sensitive box (inset of Fig. 2A). For each experiment, we mixed specific proportions of clay and organic polymer, fully suspended the sediment in the water, and then captured time-lapse photographs of suspended sediment once the turbulent mixing was stopped. We calibrated the time-series absorbance data to derive sediment concentration (fig. S2) and regressed the concentration data on time to calculate settling velocities (Fig. 2A) (*13*).

We observed that organic polymers had a substantial, varied, and nonlinear effect on clay flocculation and settling velocity. All experiments with organic polymers formed visible flocs (fig. S1), which settled significantly faster than primary unflocculated clay particles [primary particle median diameter (D_{50}) = 1 μm; settling velocity ($w_{s,unflocculated}$) = 2.205 × 10^{-6} m/s; p = 0.004] (Fig. 2B) (*13*). Generally, floc settling velocities increased with organic concentrations (table S2) (*13*). Guar gum was a more effective flocculant compared with xanthan gum (p = 0.004), likely because of its charge and branched structure, which increased the number of possible cross-links between clays and organics. Together, guar gum and smectite formed the largest flocs with the fastest settling velocities (w_s ~ 10^{-3} m/s; p = 0.001) (Fig. 2B), even when mixed with kaolinite. Additional particle-tracking experiments using humic acids and kaolinite also yielded readily observable flocs and settling velocities of ~1 × 10^{-3} m/s—albeit at much higher sediment concentrations (*13*). Settling velocities from our floc experiments deviated substantially from Stokes' settling velocity predictions (*14*) for clay primary particles by up to three orders of magnitude (Fig. 2, B and C) and instead yielded velocities expected for medium to coarse silt [diameter (D) = 20 to 63 μm].

Our experimental results were consistent with data from previous experiments that characterized freshwater flocculation for similar combinations of clay with organic polymers, and they demonstrated, both qualitatively and quantitatively (Fig. 2C) (*9*, *15*), the optimal conditions for flocculation (Fig. 2B). The results also agreed with previous measurements of freshwater floc settling velocities from activated sludge (*16*) and natural sediment from rivers (Fig. 2C) (*16*–*19*). In particular, the guar-smectite experiments produced settling velocities consistent with those estimated in rivers by inversion of suspended sediment concentration-depth profiles (Fig. 2, B and C) (*10*).

The mineralogical and organic materials found in rivers can be more complex than those that we simulated in our experiments. However, we found that interactions between clays with charged interlayers and charged branched polymers can produce settling velocities like those observed in rivers (w_s ~ 10^{-4} to 10^{-3} m/s) (*10*), even if we added other clays like kaolinite to the mixture. Experiments without organics or with low organic concentrations did not produce enhanced settling velocities (Fig. 2B and fig. S1); these conditions are atypical for modern rivers. Likewise, the presence of silt common to rivers would further increase floc settling velocities compared with those measured in our experiments (*20*). Although we used idealized, chemically well-defined

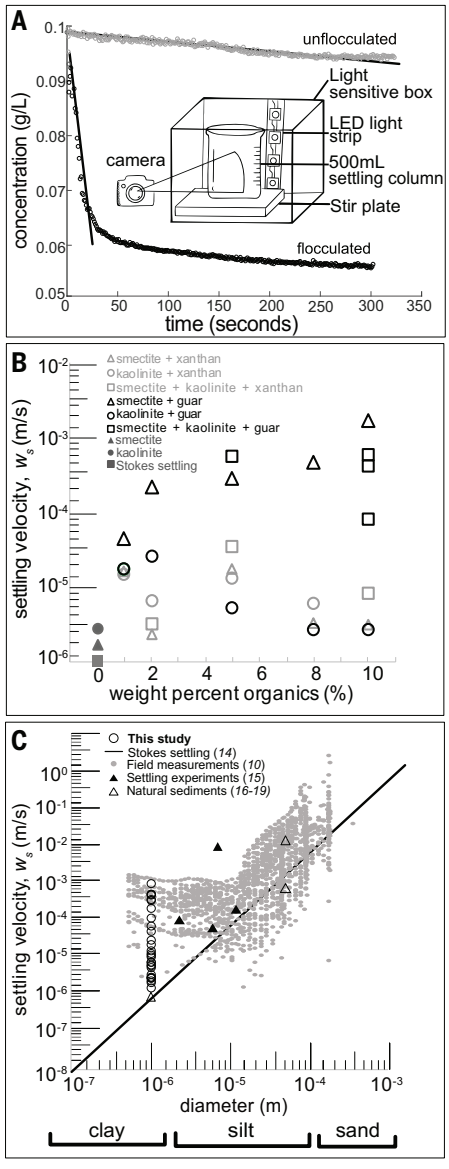

Fig. 2. Experimental results. (**A**) Suspended sediment concentration as a function of time from an example experiment with smectite control (gray) compared with an experiment of 5 wt % guar gum with smectite (black). Floc settling velocity was determined from the rate of concentration change over time, as shown by the fit black line (*13*). The inset shows the experimental setup. LED, light-emitting diode. (**B**) Settling velocities measured from our experiments as a function of weight percent organics for different combinations of clays and organics compared with the Stokes' settling rate for primary (unflocculated) particles (*14*). (**C**) Settling velocities from our experiments and previous work as a function of primary particle diameter and the Stokes' prediction for unflocculated particles (*14*). Previous studies include settling experiments with clay and organic polymers comparable to our experiments (*15*), experiments with natural sediments (*16*–*19*), and settling velocities from modern rivers inverted from concentration-depth profiles (*10*).

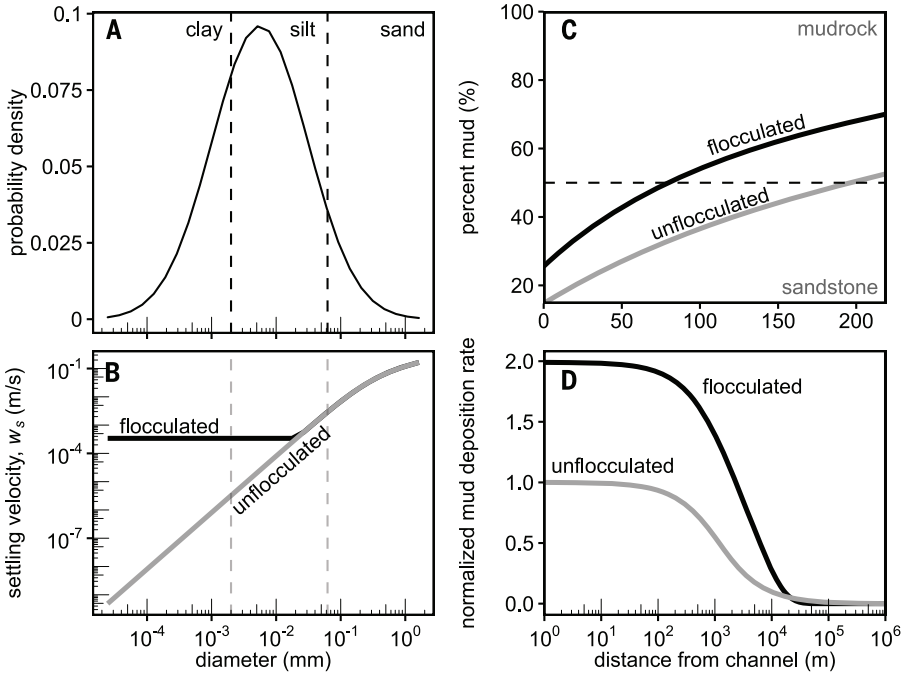

Fig. 3. Floodplain sediment transport model. (**A**) Grain-size distribution of sediment supplied from the channel onto the floodplain, approximately scaled after the Mississippi River (*13*). (**B**) Settling velocities used in the model for flocculated and unflocculated scenarios. (**C**) Results for the percentage of mud in the proximal floodplain, classified as mudrock and sandstone. (**D**) Mud deposition rate as a function of distance from the channel, normalized by the rate at the channel edge for the unflocculated case.

polymers, these polymers have comparable structures and functional groups to a range of plant-derived materials (*13*), including those found in modern plant cell walls (*21*), and are thought to have remained relatively consistent throughout plant evolution (*22*). This similarity supported the notion that organics play an important role in mud sediment transport in rivers, and vice versa.

We used a one-dimensional (1D) advection-settling analytical model to study the effect of organic-driven flocculation on overbank floodplain deposition, scaled roughly after the Mississippi River (Fig. 3) (*13*) as an example of the deep channeled, low-gradient single-threaded rivers common before and after the Silurian period (*23*). Model results showed systematically higher mud abundance relative to that of sand across the floodplain width in a flocculated scenario compared with an unflocculated scenario (26% mud for flocculated compared with 15% for unflocculated near the channel; Fig. 3C). For the flocculated case, we assumed that particles with $D < 20$ μm settled at a rate of 0.34 mm/s (Fig. 3B), similar to observations from rivers (*10*, *13*). Mud abundances in the flocculated case exceeded 50%—the definition of mudrock—everywhere beyond ~80 m of the channel edge. Both scenarios predicted predominantly mud deposition beyond ~200 m of the channel because this is beyond the advection-settling length for sand in our model (Fig. 3C) (*13*). Notably, flocculation also caused twofold-higher mud deposition rates at kilometer-scale distances from the channel (Fig. 3D). These model results can be generalized to any river system by changing the overbank water discharge, sediment concentration, and the sediment size distribution (fig. S4) (*13*). Although changing parameter values affected the mud deposition rate and the transition location from sandstone to mudrock, the general result of flocculation resulting in muddier overbank deposition held for all scenarios (*13*).

Our results have substantial implications for the proliferation of fluvial mudrock. The model predicted that flocculation results in muddier channel banks (Fig. 3C), which can increase bank cohesion and reduce the channel lateral migration rates (*24*). Slower lateral migration rates, in turn, limit the width of sandy channel-belt deposits (*25*). Furthermore, muddier channel-proximal deposits can cause channel narrowing, restrict braiding, and decrease channel sinuosity (*24*), all of which limit the extent of sandy channel-belt deposits. When this deposition pattern is spatially superposed over time as channels aggrade and migrate laterally, these feedbacks should produce overall muddier floodplains than predicted by our simple model that lacked channel dynamics. At the larger basin scale, increased rates of mud deposition kilometers from the channel owing to flocculation (Fig. 3D) will make mud preservation overall more likely, with lower chances of reworking by fluvial or aeolian processes (fig. S3) (*13*, *26*). In addition, the rates of lateral migration relative to channel switching, or avulsion, determine the stacking pattern and preservation of channel-belt sandstone bodies (*25*). Thus, slower lateral migration rates not only reduce the extent of individual sandstone bodies but also shift the alluvial architecture to a pattern characterized by mudrock with isolated sandstone bodies (fig. S3) (*13*, *25*). By contrast, the architecture of Precambrian alluvial deposits is characterized by laterally extensive sandstone bodies with substantial amalgamation and low mudrock preservation (*3*, *27*–*29*)—features indicative of high rates of channel lateral migration, relative to channel avulsion (*26*).

Our experiments illustrate how plant-associated organics can cause flocculation and substantially increase the settling velocity of mud in freshwater rivers, resulting in muddier floodplains. This coupling between organic carbon and mud transport and deposition has important implications for carbon cycling and sequestration. The proliferation of early land plants in terrestrial ecosystems during the Ordovician and Silurian periods increased the amount of primary production and the burial flux of organic material by at least an order of magnitude (*30*). This increase in the amount of organic matter in terrestrial environments would have generated a diverse suite of polymeric molecules, both through direct synthesis from plants as well as the microbial communities that thrive on plant-derived organic matter (*31*). Together, all these polysaccharides would drive the binding of fine sediment particles. Thus, a natural correlate of a plant-driven flocculation mechanism would have been an increase in organic carbon content in fluvial deposits associated with the increase in mudrock in those deposits. Although only a few examples are suitable for comparison, and total organic carbon (TOC) might be lower on average in older rocks owing to preservation biases, existing geochemical data supported the idea that pre-Ordovician rivers had lower TOC contents and thus relatively less effective mud flocculation (and sandier floodplains). Proterozoic alluvial rocks with low mudrock abundances have commensurately low TOC (e.g., Nonesuch Formation, which has <1% alluvial mudrock and <1% TOC) (*32*). By contrast, alluvial rocks postdating the evolution of land plants have both greater mudrock abundances and greater TOC concentrations within those mudrocks (e.g., lower Carboniferous Hørybreen/Mormien Formation, which has up to 28% mudrock and 11 to 30% TOC) (*3*, *33*). These trends are consistent with the hypothesis that plant proliferation, with its commensurate rise in primary production and terrestrial organic carbon fluxes, could have

contributed substantially to the abrupt and irreversible early Paleozoic increase in alluvial mudrocks (*3*). Likewise, the processes of flocculation and enhanced settling of mud onto floodplains outlined an efficacious mechanism for organic carbon burial in ancient and modern alluvial systems.

REFERENCES AND NOTES

1. C. K. Boyce, J.-E. Lee, *Annu. Rev. Earth Planet. Sci.* **45**, 61–87 (2017).
2. D. Long, in *Fluvial Sedimentology—Memoir 5*, A. D. Miall Ed. (Canadian Society of Petroleum Geologists, 1978), pp. 313–341.
3. W. J. McMahon, N. S. Davies, *Science* **359**, 1022–1024 (2018).
4. N. S. Davies, M. R. Gibling, *Earth Sci. Rev.* **98**, 171–200 (2010).
5. W. W. Fischer, *Science* **359**, 994–995 (2018).
6. R. Hadley, "Influence of riparian vegetation on channel shape, northeastern Arizona" (Geological Survey Professional Paper 424–C, U.S. Government Printing Office, 1961), pp. 30–31.
7. S. McMahon, J. Parnell, *J. Geol. Soc. London* **175**, 716–720 (2018).
8. F. Maggi, thesis, Delft University of Technology (2005).
9. G. Zhang, H. Yin, Z. Lei, A. H. Reed, Y. Furukawa, *J. Geophys. Res. Oceans* **118**, 3473–3489 (2013).
10. M. P. Lamb *et al*., *Nat. Geosci.* **13**, 566–570 (2020).
11. E. R. Sholkovitz, *Geochim. Cosmochim. Acta* **40**, 831–845 (1976).
12. Y. Furukawa, A. H. Reed, G. Zhang, *Geochem. Trans.* **15**, 1–9 (2014).
13. See supplementary materials.
14. G. G. Stokes, *Trans. Cambridge Philos. Soc.* **9**, 8–106 (1851).
15. X. L. Tan, G. P. Zhang, H. Yin, A. H. Reed, Y. Furukawa, *Int. J. Sediment Res.* **27**, 473–485 (2012).
16. J. Námer, J. J. Ganczarczyk, *Water Res.* **27**, 1285–1294 (1993).
17. W. Lick, H. Huang, R. Jepsen, *J. Geophys. Res.* **98**, 10279 (1993).
18. Q. Q. Shang, H. W. Fang, H. M. Zhao, G. J. He, Z. H. Cui, *Int. J. Sediment Res.* **29**, 471–480 (2014).
19. V. Wendling *et al*., *J. Soils Sediments* **15**, 1991–2003 (2015).
20. D. Tran, K. Strom, *Cont. Shelf Res.* **138**, 81–94 (2017).
21. M. Pauly, K. Keegstra, *Curr. Opin. Plant Biol.* **13**, 305–312 (2010).
22. Z. A. Popper, *Curr. Opin. Plant Biol.* **11**, 286–292 (2008).
23. V. Ganti, A. C. Whittaker, M. P. Lamb, W. W. Fischer, *Proc. Natl. Acad. Sci. U.S.A.* **116**, 11652–11657 (2019).
24. M. G. A. Lapôtre, A. Ielpi, M. P. Lamb, R. M. E. Williams, A. H. Knoll, *J. Geophys. Res. Earth Surf.* **124**, 2757–2777 (2019).
25. D. J. Jerolmack, D. Mohrig, *Geology* **35**, 463–466 (2007).
26. V. Ganti, E. A. Hajek, K. Leary, K. M. Straub, C. Paola, *Geophys. Res. Lett.* **47**, 1–10 (2020).
27. D. Winston, in *Fluvial Sedimentology—Memoir 5*, A. D. Miall, Ed. (Canadian Society of Petroleum Geologists, 1978), pp. 343–359.
28. E. Cotter, in *Fluvial Sedimentology—Memoir 5*, A. D. Miall, Ed. (Canadian Society of Petroleum Geologists, 1978), pp. 361–383.
29. A. Ielpi *et al*., *Sediment. Geol.* **372**, 140–172 (2018).
30. D. Edwards, L. Cherns, J. A. Raven, *Palaeontology* **58**, 803–837 (2015).
31. M. V. Cheshire, *J. Soil Sci.* **28**, 1–10 (1977).
32. J. R. Hatch, G. B. Morey, *Am. Assoc. Pet. Geol. Bull.* **69**, 1208–1216 (1985).
33. E. Dallmann *et al.*, in *Lithostratigraphic Lexicon of Svalbard: Review and Recommendations for Nomenclature Use: Upper Palaeozoic to Quaternary Bedrock*, W. K. Dallman, Ed. (Norsk Polarinstitutt, 2004), pp. 29–65.
34. S. S. Zeichner, J. Nghiem, M. P. Lamb, N. Takashima, J. de Leeuw, V. Ganti, W. W. Fischer, szeichner/Flocs-Code-and-Models: flocs1.1. Zenodo (2020); https://doi.org/10.5281/zenodo.4033293.

ACKNOWLEDGMENTS

We thank T. Ulizio and M. Douglas for help with the experiments and valuable input. **Funding:** This work was made possible with support from the Caltech Discovery Fund (W.W.F. and M.P.L.), David and Lucile Packard Foundation (W.W.F.), American Chemical Society Petroleum Research Fund (W.W.F.), National Science Foundation Graduate Research Fellowship Program (S.S.Z.), and Troy Tech High School Program (N.T.). **Author contributions:** Methodology, Formal analysis, Software, Writing, Visualization: S.S.Z.; Software, Formal analysis, Writing, Visualization: J.N.; Conceptualization, Supervision, Funding acquisition: M.P.L.; Methodology, Writing – review & editing: J.d.L.; Validation, Data curation: N.T.; Formal analysis, Writing – review & editing: V.G.; Conceptualization, Supervision, Funding acquisition: W.W.F. **Competing interests:** We have no competing interests. **Data and materials availability:** All data are available in the main text or the supplementary materials. All code for image processing, statistical analyses, and the 1D sedimentation model is available at Zenodo (*34*).

SUPPLEMENTARY MATERIALS

science.sciencemag.org/content/371/6528/526/suppl/DC1
Materials and Methods
Figs. S1 to S4
Tables S1 and S2
References (*35*–*50*)

27 May 2020; accepted 21 December 2020
10.1126/science.abd0379

ETH zürich

Professor of Food Systems Economics and Policy

→ The Department of Environmental Systems Science (www.usys.ethz.ch) at ETH Zurich invites applications for a full professorship focusing on the economic and political choices as well as the governance of food systems.

→ Successful candidates are expected to pursue an excellent research programme linking food chains to environmental conditions as well as to socio-economic and policy choices, across a range of spatial and institutional scales, and contributing to create more sustainable and resilient food and agricultural systems. Application and development of innovative methods and approaches for such food system are particularly welcome. The new professor is expected to have a strong background in agricultural and food economics, policy sciences, behavioural sciences, or related fields, to have an international track record in research, and to be motivated and experienced teachers. Teaching duties will include undergraduate (German or English) and graduate level courses (English) at the interface between economics, agriculture, food production, distribution, consumption and policy.

→ **Please apply online: www.facultyaffairs.ethz.ch**

→ Applications should include a curriculum vitae, a list of publications, a statement of future research and teaching interests, and a description of the three most important achievements. The letter of application should be addressed **to the President of ETH Zurich, Prof. Dr. Joël Mesot. The closing date for applications is 28 February 2021.** ETH Zurich is an equal opportunity and family friendly employer, strives to increase the number of women professors, and is responsive to the needs of dual career couples.

utmb Health

Working together to work wonders.

MOLECULAR BACTERIOLOGY AND IMMUNOLOGY FACULTY POSITIONS

The Department of Microbiology & Immunology at the University of Texas Medical Branch (UTMB), Galveston, is seeking to recruit tenure-track faculty in Bacteriology and Immunology at the academic rank of **Assistant**, **Associate** or **Full Professor** with MD, PhD, DVM or equivalent degrees.

The preferred research areas of **bacteriology** include bacterial genomics/proteomics, virulence, structure-function relationships, antibiotic resistance, host-pathogen interactions with a focus on cell signaling, the role of the microbiota in disease outcomes, and vaccine development using novel platforms.

The preferred research areas of **immunology** include the molecular basis of innate and adaptive immunity and studies of human T and B cells in response to infectious diseases. Emphasis may be on either basic or pathogen-elicited immunities during acute as well as chronic diseases.

The successful candidates should be highly productive based on their past accomplishments and have either an established record of extramural funding or have the potential to establish robust, funded research programs in the desired research areas. The successful applicants should be amenable to collaborative studies with other investigators studying the pathogenesis of infectious diseases, as well as teaching and mentoring graduate and medical students. Salary and academic rank are commensurate with experience, and excellent benefits and start-up packages are offered. The department has recently recruited five highly successful faculty members from across the nation at the level of Assistant or Associate Professor.

UTMB, a member of Texas Medical Center, has many highly collaborative research centers and institutes, including the fields of vaccine development, tropical diseases, biodefense and emerging infectious diseases, aging, women's health, translational science and structural biology. Its state-of-the-art core facilities include one of two NIH-funded national biocontainment laboratories (Galveston National Laboratory) with excellent infrastructure to conduct research at BSL2, -3 and -4 on diverse animal models of infectious diseases, as well as arthropod containment facilities to study the transmission of vector-borne diseases. The Department of Microbiology & Immunology, with 36 full-time faculty, is ranked among the top of its peer departments in NIH funding. Interested candidates should apply via the UTMB careers website at **https://www.utmb.edu/hr/careers requisition# 2100260**.

Each application should include a cover letter, current Curriculum Vitae, and a statement of current and future research interests.

Complete applications should be addressed to: Dr. Tian Wang (**ti1wang@utmb.edu**) and Dr. Ashok Chopra (**achopra@utmb.edu**), co-chairs, Faculty Search Committee, Department of Microbiology and Immunology, UTMB.

UTMB Health strives to provide equal opportunity employment without regard to race, color, religion, age, national origin, sex, gender, sexual orientation, gender identity/expression, genetic information, disability, veteran status, or any other basis protected by institutional policy or by federal, state or local laws unless such distinction is required by law. As a VEVRAA Federal Contractor, UTMB Health takes affirmative action to hire and advance women, minorities, protected veterans and individuals with disabilities.

BNU Seeking Top Talents in Systems Science

Feel free to contact us:

Website: http://sss.bnu.edu.cn
Email: sss@bnu.edu.cn
Address: School of Systems Science, Beijing Normal University, No. 19, XinJieKouWai St., Haidian District, Beijing, P.R.China 100875

Beijing Normal University (BNU), as a venerable and dynamic institution, has a long-held tradition of partnering with leading academic institutions from around the world. Noted for its culturally rich and diverse environment, BNU endeavors to become a leader of higher education in China, Asia and even the world.

The School of Systems Science (SSS) at BNU advocates interdisciplinary research in systems science through collaboration with other disciplines in natural, social, technical and economic sciences inside and outside BNU. Having such a uniquely collaborative environment together with outstanding research facilities, SSS aspires to excel internationally in the field of Systems Science.

In 2018, SSS will establish an International Science Center for Complex Systems on the Zhuhai campus of BNU in southern China. This center aims at the frontiers of scientific research and technical innovation, specifically in the formation mechanism of human decision making behavior and its neural mechanism, together with data analysis of human behavior and artificial intelligence (including swarm intelligence). By mobilizing its top experts to lead key research projects in cooperation with talents around the world, this science center is expected to become an international platform for systems science development as well as an interface between academia, industry and governmental authorities.

In order to carry out cutting-edge research in systems science, SSS intends to expand its research team. Its current research portfolio includes, but is not limited to the following fields:

i. The fundamental theories of complex system.

ii. Social and economic system.

iii. The life ecosystem and the self-organizing behavior of brain and cognition.

iv. Multi-agent system and evolutionary algorithm.

v. Information technology of artificial intelligence systems.

vi. The science of science.

I Think the Next Century Will Be the Century of Complexity.

––Stephen Hawking, 2000.

SSS sincerely welcomes famous scholars, academic leaders, promising young scholars and postdocs in interdisciplinary areas of systems science. The applicant is expected to have a doctoral degree in relevant orientation, a solid research foundation and outstanding research findings in the above-mentioned fields, with great potential for being an excellent teacher and tutor, at the same time an excellent team player in interdisciplinary collaboration.

BNU will place each successful applicant in a proper position according to his/her academic background, research interests and teaching plan, and provide him/her with competitive salary, sufficient start-up fund, necessary laboratory and office space, and other reasonable supports. During the employment, BNU will evaluate each faculty member's capacity and potential and provide the best opportunities for vocational development in line with the international conventions and common practices in academic circles.

Over the years, SSS has made great contributions to the sustainable development of systems science in and outside China. Faced with the complex social and technological challenges, SSS will resume its effort to solve scientific problems in nature and society. By integrating many different yet relevant disciplines and building the international advanced research center of complex systems, SSS strives to cultivate high-level interdisciplinary talents so as to generate new knowledge, new minds, and new technologies that will promote the creation of a shared future for mankind. In time, SSS will become a crucial education and innovation incubator for big data, artificial intelligence, future brain and intellectual education.

SSS cordially welcomes job applicants and visiting scholars with expertise in systems science and related areas. The school also welcomes research and education collaboration from China and the rest of world.

Science Careers helps you advance your career. Learn how!

- Register for a free online account on **ScienceCareers.org**.
- Search hundreds of job postings and find your perfect job.
- Sign up to receive e-mail alerts about job postings that match your criteria.
- Upload your resume into our database and connect with employers.
- Watch one of our many webinars on different career topics such as job searching, networking, and more.
- Download our career booklets, including Career Basics, Careers Beyond the Bench, and Developing Your Skills.
- Complete an interactive, personalized career plan at "my IDP."
- Visit our Employer Profiles to learn more about prospective employers.
- Read relevant career advice articles from our library of thousands.

Visit **ScienceCareers.org** today — all resources are free

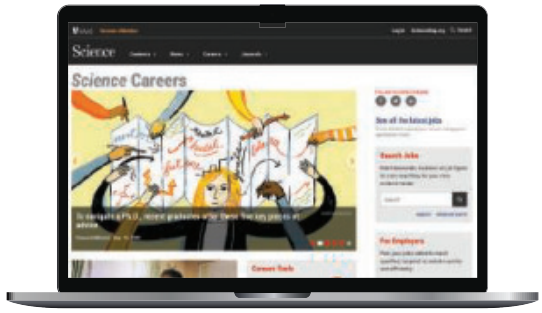

SCIENCECAREERS.ORG

ScienceCareers
FROM THE JOURNAL SCIENCE AAAS

EPFL

Tenure Track Faculty Position in Catchment Science and Engineering

at the Ecole polytechnique fédérale de Lausanne (EPFL)

The EPFL School of Architecture, Civil and Environmental Engineering (ENAC) invites applications for a tenure track Assistant Professor of **Catchment Science and Engineering**, located within the Institute of Environmental Engineering (Institut d'ingénierie de l'environnement, IIE).

The professor will be a member of EPFL's Alpine and Polar Environment Research Center (ALPOLE), based at Sion in the Swiss Canton of Valais. Sion, in the heart of the Swiss Alps, is in close proximity to mountainous zones where effects of climate change on natural and urbanized environments are unmistakable.

Catchments are natural integrators of processes that span a range of scientific disciplines, and occur on multiple spatial and temporal scales. Climate change-induced modifications of catchment hydrology are well established, in contrast to concomitant changes in, e.g., geomorphological, biogeochemical and ecological functioning. Understanding these changes and the linkages between them involves a cross-disciplinary focus on different physical and biological systems occurring in impacted catchments.

We welcome applicants whose vision in catchment research extends across scales and disciplines, using a range of investigative tools including theory, modeling, data science, laboratory experiments and field measurements. As part of ALPOLE, the appointee will have excellent opportunities to work on mountainous and polar environments.

We seek an outstanding individual who will lead an internationally recognized research program that leverages the opportunities offered by EPFL. The professor will be committed to excellence in undergraduate and graduate level teaching, and will contribute to the Environmental Engineering program, which emphasizes basic and translational research as the foundation for environmental adaption and engineering design.

EPFL is a growing and well-funded institution fostering excellence and diversity. It is well equipped with experimental and computational infrastructure, and offers a fertile environment for research collaboration between various disciplines. The EPFL environment is multilingual and multicultural, with English serving as a common interface. EPFL offers internationally competitive start-up resources, salaries and benefits. Besides its main Lausanne campus, EPFL operates antenna sites across Western Switzerland, in Fribourg, Geneva, Neuchâtel and Sion.

The following documents are requested in PDF format: cover letter including a statement of motivation, curriculum vitae, publication list, concise statements of research and teaching interests (up to 5 pages for each) as well as the names and addresses (including emails), of at least three references (contacted for shortlisted applicants).

Applications should be uploaded to the EPFL recruitment web site:

https://facultyrecruiting.epfl.ch/position/28737536

Formal evaluation of the applications will begin on **March 1, 2021**. The search will continue until the position is filled.

Further enquiries should be made to the Chair of the Search Committee:
Prof. D. Andrew Barry
Director of the Environmental Engineering Institute
E-mail: searchcase@epfl.ch

Additional information on EPFL: www.epfl.ch/en, www.epfl.ch/schools/enac, www.epfl.ch/schools/enac/research/environmental-engineering-institute-iie, www.epfl.ch/schools/enac/research/environmental-engineering-institute-iie/alpole-en, www.epfl.ch/schools/enac/education/environmental

EPFL is an equal opportunity employer and a family friendly university. It is committed to increasing the diversity of its faculty, and strongly encourages women to apply.

EPFL

Tenure Track Faculty Position in Environmental Adaptation

at the Ecole polytechnique fédérale de Lausanne (EPFL)

The EPFL School of Architecture, Civil and Environmental Engineering (ENAC) invites applications for a tenure track Assistant Professor of **Environmental Adaptation, with an emphasis on cryospheric biosystems**, located within the Institute of Environmental Engineering (Institut d'ingénierie de l'environnement, IIE).

The professor will be a member of EPFL's Alpine and Polar Environment Research Center (ALPOLE), based at Sion in the Swiss Canton of Valais. Sion, in the heart of the Swiss Alps, is in close proximity to mountainous zones where effects of climate change on natural and urbanized environments are unmistakable.

Physical changes (e.g., loss of permafrost) in alpine and polar environments affect adaptive strategies and resilience of cryospheric biological systems. Adaptations can occur across multiple scales, include ecological and evolutionary processes, and influence cryospheric ecosystem functioning. These changes are mediated by biota including microbial communities, fungi and plants, with associated alterations to nutrient and carbon cycling. The appointee will build on state-of-the-art life-science tools to relate climate-induced trends and variability (e.g., temperature and hydrological regime changes) to changes in terrestrial ecosystem biodiversity, productivity and functioning.

We welcome applications from experimentalists (laboratory or field) whose research interests extend across scales, and who employ a range of investigative tools. Rapidly developing laboratory tools ranging from genomics to phenomics will enable new insights into adaptive strategies, and open up research perspectives on metabolism, bioprospection and biotechnology, as well as biosensor development. Of interest also are field studies that utilize traditional and modern approaches (e.g., autonomous sensor networks, data fusion/model integration) to understand ecosystem functioning and services. As part of ALPOLE, the appointee will have excellent opportunities for interdisciplinary collaborations that target mountainous and polar environments.

We seek an outstanding individual who will lead an internationally recognized research program that leverages the opportunities offered by EPFL. The professor will be committed to excellence in undergraduate and graduate level teaching, and will contribute to the Environmental Engineering program, which emphasizes basic and translational research as the foundation for environmental adaption and engineering design.

EPFL is a growing and well-funded institution fostering excellence and diversity. It is well equipped with experimental and computational infrastructure, and offers a fertile environment for interdisciplinary research collaboration. The EPFL environment is multilingual and multicultural, with English serving as a common interface. EPFL offers internationally competitive start-up resources, salaries and benefits. Besides its main Lausanne campus, EPFL operates antenna sites across Western Switzerland, in Fribourg, Geneva, Neuchâtel and Sion.

The following documents are requested in PDF format: cover letter including a statement of motivation, curriculum vitae, publication list, concise statements of research and teaching interests (up to 5 pages for each statement) as well as the names and addresses, including emails, of at least three references (contacted for shortlisted candidates).

Applications should be uploaded to the EPFL recruitment web site:

https://facultyrecruiting.epfl.ch/position/28737537

Formal evaluation of the applications will begin on **March 1, 2021**. The search will continue until the position is filled.

Further enquiries should be made to the Chair of the Search Committee:
Prof. D. Andrew Barry
Director of the Environmental Engineering Institute
E-mail: searchenvadaptation@epfl.ch

Additional information on EPFL: www.epfl.ch/en, www.epfl.ch/schools/enac, www.epfl.ch/schools/enac/research/environmental-engineering-institute-iie, www.epfl.ch/schools/enac/research/environmental-engineering-institute-iie/alpole-en, www.epfl.ch/schools/enac/education/environmental

EPFL is an equal opportunity employer and a family friendly university. It is committed to increasing the diversity of its faculty, and strongly encourages women to apply.

By **Julia Gala de Pablo**

When life happens

I couldn't believe my luck. It was December 2018, I was finishing up my Ph.D. in the United Kingdom, and a professor whose work I admired had invited me to interview for a postdoc position in his lab in Japan. I was excited about experiencing a completely different research environment. The Zoom interview, during my holiday visit to my family in Spain, went well. Until this stage of my life, every year had been better than the last, and I was sure 2019 would be the same.

Then, in April, my mother told me about some weird symptoms she was experiencing. My family likes to travel, so we thought perhaps she had contracted a tropical disease. "Have you submitted your thesis yet?" she asked me. "Almost, mum," I said. She seemed to be holding back. But I was focused on finishing my experiments and the final edits on my thesis, so I brushed away my concerns.

A week later, the doctors had an update: They had found a shadow on the x-ray. It was lung cancer. I spent the next 2 months torn between my research and my family as I submitted my thesis and prepared for my defense, scheduled for mid-July, while my mother started radiation and immunotherapy treatment. My Ph.D. supervisor encouraged me to take all the time I needed to be with my mom, and I made three short visits home. But my expectations for myself pulled me back to lab. In the meantime, we learned that the cancer had spread throughout my mother's body, including to her brain.

"I will never forgive myself for losing precious time with my mother."

Yet my scientific commitments still had a grip on me. I was set to attend a big conference in New Zealand in early July, where I would present my Ph.D. results, meet with members of the Japanese research group I hoped to join, and broaden my job hunt in case that position didn't work out. I had secured travel grants to cover the costs. Flights were bought, accommodations booked. My mother even told me she was jealous I was going to such an amazing location.

But on my way to the airport, I crumbled. Instead of New Zealand, I flew back to Madrid. Soon after, it was confirmed: The cancer was stage 4, it was everywhere, and it was unstoppable. My mother had 1 or 2 years left, the doctors said.

I postponed my Ph.D. defense. My mother asked whether I could get a job in Madrid, but nothing fit my research area and funding was scarce. The Japanese funding agency awarded my fellowship, but I didn't know whether I should go. I had another opportunity in London—closer than Japan, but still too far. Meanwhile—in just 3 weeks—my mother's prognosis changed to 1 year, then months, weeks, days. Cancer beat my mother at the end of July.

I will never forgive myself for losing precious time with my mother between that first call in April and that day in early July when I finally moved back home to help care for her. I thought I had more time and I didn't. I had never slowed down before, knowing what it takes to secure an academic position. You need to publish. You need to present at international conferences. You need to secure grants and fellowships. You need to get cited. Passing up any opportunity felt like slipping back down the mountain, away from the big prizes at the top.

Losing my mother put things into perspective for me. I saw the humane side of science in the understanding and flexibility offered by my Ph.D. and postdoc supervisors and the funding agencies as I juggled my personal and professional needs and timelines. And the work I missed during my time away felt insignificant. I defended my thesis in mid-September and moved to Tokyo to start my new life.

For me, last year felt like a walk in the park compared with 2019. But I know that many people's 2020 and 2021 may feel like my 2019, with struggles and losses competing with career goals. Please, take my advice: If your loved ones need you now, be there for them. Science will be waiting when you return. Prioritize yourself and your family. Prioritize well-being. Prioritize your mental health. Remember that life is what happens while you are making plans. ■

Julia Gala de Pablo is a postdoctoral fellow at the University of Tokyo. Send your career story to SciCareerEditor@aaas.org.

ILLUSTRATION: ROBERT NEUBECKER

CALL FOR PAPERS

SPJ
SCIENCE PARTNER JOURNALS

Energy Material Advances

Energy Material Advances is an online-only, Open Access journal published in affiliation with **Beijing Institute of Technology (BIT)** and distributed by the **American Association for the Advancement of Science (AAAS)**. The journal publishes, research articles, review articles, short communications, perspectives, and editorials. *Energy Material Advances* covers multiple fields from cutting-edge material to energy science, investigating theoretical, technological as well as engineering aspects.

Submit your research to *Energy Material Advances* today!

Learn more at **spj.sciencemag.org/energymatadv**

The Science Partner Journal (SPJ) program was established by the American Association for the Advancement of Science (AAAS), the nonprofit publisher of the *Science* family of journals. The SPJ program features high-quality, online-only, Open Access publications produced in collaboration with international research institutions, foundations, funders and societies. Through these collaborations, AAAS furthers its mission to communicate science broadly and for the benefit of all people by providing top-tier international research organizations with the technology, visibility, and publishing expertise that AAAS is uniquely positioned to offer as the world's largest general science membership society.

Visit us at: **spj.sciencemag.org**

@SPJournals **@SPJournals**

OPEN ACCESS

ARTICLE PROCESSING CHARGES WAIVED UNTIL JULY 2023

UNDERSTANDING DYNAMIC ECOSYSTEMS

AAAS | ANNUAL MEETING

AAAS, publisher of the *Science* family of journals, thanks the sponsors of the virtual 2021 AAAS Annual Meeting:

Arizona State University
Host University

This Study Shows.
A Wiley podcast.

Canada

AAAS Science & Technology Policy Fellowships, American Academy of Arts & Sciences, Defense Threat Reduction Agency, Food and Drug Administration, Harvard University Press, Japan Association of Communication for Science and Technology, Japan Science and Technology Agency, Japan Society for the Promotion of Science, Library of Congress, Congressional Research Service, MIT Press, National Institute of Justice, National Institute of Neurological Disorders and Stroke, National Science Policy Network, Princeton University Press, *Science* Journals, University of Washington

As of January 5, 2021

The 2021 Annual Meeting will convene entirely online, February 8-11 with pre-recorded videos available starting January 18. Join us!

Meeting registration and program now available online.

aaas.org/meetings | #AAASmtg